Imperial College London
Department of Chemical Engineering

Multiscale Simulation of Slip Flow and Adsorption in Carbon Nanopores

Daniel A. Ross

Submitted in partial fulfilment of the requirements for the degree of
Doctor of Philosophy in Chemical Engineering of Imperial College London
and the Diploma of Imperial College London, July 2017

Declaration

I hereby declare that the materials contained herein are my own work and any other work has been appropriately referenced. I further declare that this work has not been submitted in its entirety or in part to any other academic institution for the award of any degree or diploma.

Daniel Ross
Department of Chemical Engineering
Imperial College London

Date: July 2017

The copyright of this thesis rests with the author and is made available under a Creative Commons Attribution Non-Commercial No Derivatives licence. Researchers are free to copy, distribute or transmit the thesis on the condition that they attribute it, that they do not use it for commercial purposes and that they do not alter, transform or build upon it. For any reuse or redistribution, researchers must make clear to others the licence terms of this work.

Abstract

Molecular dynamics and the lattice Boltzmann method (LBM) are combined as part of a multiscale procedure for translating information from nanoscopic molecular simulations up to the level of continuum models. The larger scales attainable with LBM allow for the scale-up of nanoscale phenomena, observed in individual pores, to larger complex porous structures. One such phenomena is that of slip flow, quantified by a slip length, whereby fluid in contact with a solid surface exhibits a non-zero velocity.

Initially, adsorption and pore filling mechanisms in carbon nanotubes and graphitic slit pores with varying sizes are investigated. The fluids of interest are water, utilising the TIP4P model, and n-heptane, modelled with the OPLS-AA forcefield. Models are validated against experimental literature for macroscopic properties as functions of temperature at a pressure of 1 bar. The final densities in the pores are shown to be highly dependent on the level of packing of the fluids, which in turn depends on the surface-fluid wettability. As such, the fluid density varies drastically with relatively small changes in the pore dimensions.

The friction coefficient, which is proportional to the inverse of the slip length, is calculated for each equilibrated system. This is shown to be independent of separation for flat surfaces. However, with increasing confinement and wettability, large deviations are observed due to enhanced fluid densities. There is also a clear relationship between the slip length and curvature that differs depending on whether the surface is concave or convex.

Finally, two methods of implementing a slip boundary condition into LBM are presented and compared with analytical solutions to the Navier-Stokes equations for flows in channels and pipes. These are a specular-bounce-back combination boundary and an on-site velocity boundary. The latter is found to be preferable for implementation of slip in complex geometries, however further work is still required.

Acknowledgements

I would like to extend my fullest gratitude to both Professor Erich Müller of Imperial College London and Dr Edo Boek of Queen Mary University of London for their supervision and guidance, as well as their unprecedented patience.

I would also like to thank both the EPSRC and Shell Research Limited, UK, for funding this work. Particular thanks to Dr Roger Cracknell of Shell for his continued assistance and for making this project possible.

Further, I would not have been able to complete this work without the support of Dr Christine Seifried and Dr Emily Chapman, who were always available for an all too frequent tea break. I would also like to thank Dr Nathan Welch, Katie Welch, and Dr Ruien Hu for sharing some stronger drinks than tea. In addition, thank you to Jason Law, along with those mentioned above, for helping me to keep my sanity.

Finally, thanks to all the people in the Complex Fluids group at Imperial, including Dr Farrel Gray, Dr Saurabh Shah, Rebecca Liyanage, and JJ Cen.

‘A strange game. The only winning move is not to play.’

WarGames 1983

‘Holy Belgium. How much longer?’

Zaphod Beeblebrox I, President of the Galaxy

Contents

Declaration i

Abstract i

Acknowledgements v

1 Introduction 1

1.1 Objectives 1

1.2 Publications and conferences 2

1.2.1 Publications 2

1.2.2 Conferences 3

2 Background theory 5

2.1 Introduction 5

2.2 Engine deposits 5

2.2.1 Overview 7

2.2.2 Effects of intake-valve deposits 10

2.2.3 Intake valve deposits composition and structure 11

2.3 Modelling 12

2.3.1 Molecular modelling techniques 13

2.3.2 Molecular dynamics 19

2.3.3 Continuum scale modelling techniques 21

2.3.4 Lattice Boltzmann method 26

2.3.5 Hybrid models 27

2.4 Slip 28

2.4.1 Definition 28

2.4.2 Literature review 29

3 Models for molecular simulations 39

3.1 Introduction 39

3.2 GROMACS 39

3.2.1 Version and generalities 40

3.2.2 Non-bonded interactions 40

3.2.3 Periodic boundary conditions 42

3.2.4 Bonded interactions 46

3.2.5 Forces calculation 47

3.2.6 Integration 48

3.2.7 Ensembles 49

3.2.8 Energy minimisation 49

3.2.9 Thermostat 50

3.2.10 Barostat 52

3.2.11 Example workflow 53

3.3 Water 54
3.3.1 Choice of model 54
3.3.2 Model description 57
3.4 Straight chain hydrocarbons 58
3.4.1 Choice of model 58
3.4.2 Model description 62
3.5 Solid surfaces 63
3.5.1 Modelling solid walls 64
3.5.2 Pistons 68

4 Adsorption in nanopores via molecular simulation 69

4.1 Introduction 69
4.2 Objectives 70
4.3 Methodology 70
4.3.1 Pore specification 71
4.3.2 Density calculation 74
4.3.3 Surface tension 78
4.3.4 Adsorption process 79
4.3.5 Adsorption from a bulk liquid phase 80
4.3.6 Adsorption from a bulk gas phase 82
4.4 Discussion 86
4.4.1 Density calculation 86
4.4.2 Surface tension 95

4.4.3 Liquid adsorption against a vacuum 99

4.4.4 Gas adsorption against a vacuum 142

4.4.5 Water isobars 158

4.4.6 n-Heptane isobars 161

4.5 Conclusions 163

5 Calculation of slip lengths and friction coefficients via molecular simulation 171

5.1 Introduction 171

5.2 Objectives 173

5.3 Methodology 173

5.3.1 Non-equilibrium slip calculation 176

5.3.2 Equilibrium slip calculation 180

5.4 Discussion 183

5.4.1 Water at 300 K 183

5.4.2 n-Heptane at 300 K 188

5.4.3 Water at 400 K 191

5.4.4 n-Heptane at 400 K 193

5.5 Conclusions 195

6 Lattice Boltzmann implementation of slip parameter 199

6.1 Introduction 199

6.1.1 Lattice gas cellular automata (LGCA) 200

6.1.2 Boltzmann equation 202

6.1.3 Model 204
6.1.4 Boundary conditions 210
6.1.5 Periodic boundaries 211
6.1.6 Bounce-back boundaries 212
6.2 Literature review 213
6.3 Objectives 220
6.4 Methodology 221
6.5 Discussion 225
6.5.1 Specular-bounce-back boundary condition 225
6.5.2 Velocity boundary condition 231
6.6 Conclusions 239

7 Conclusion **241**

7.1 Future work 244

Bibliography **245**

Appendices **267**

A Models for molecular simulations 267
B Calculation of slip lengths and friction coefficients via molecular simulation 271
C Adsorption in nanopores via molecular simulation 275

List of Tables

2.1 Elementary composition of IVDs in wt%. 12

2.2 Comparison of molecular modelling techniques. 15

2.3 Comparison of continuum scale modelling techniques. 23

4.1 Pore dimensions for all graphitic pores investigated herein. 72

6.1 Slip lengths in straight geometries calculated using LBM with specular bounce-back combination boundary condition. Boundaries are in alignment with the grid. 227

6.2 Slip lengths in cylindrical geometries calculated using LBM with specular bounce-back combination boundary condition. 229

6.3 Slip lengths in straight geometries calculated using LBM with velocity boundary condition. Boundaries are in alignment with the grid. 233

6.4 Slip lengths in cylindrical geometries calculated using LBM with velocity boundary condition. 237

6.5 Slip lengths in diagonal geometries calculated using LBM with velocity boundary condition. Boundaries are 45° out of alignment with the grid. 238

A.1 Simulation options for use with GROMACS. 268

A.2 Summary of non-bonded interactions. 269

A.3 Summary of bonded interactions. 270

List of Figures

2.1 Carbonaceous deposits on an intake-valve. 9

2.2 Left: Poiseuille flow profile with no-slip. Right: Poiseuille flow profile with slip. 29

2.3 Possible definitions of surface location. Solid and fluid atoms are the large and small circles respectively. The surfaces are indicated by dashed lines as follows (left to right): Centre of solid-surface atoms; Solid-fluid minimum in Lennard-Jones potential; Solid-solid minimum in Lennard-Jones potential; Midpoint between solid and fluid peaks in density profile (ρ); Hydrodynamic boundary. . . . 31

3.1 Lennard-Jones potential. 41

3.2 Periodic system representation in two dimensions. 43

3.3 Common periodic unit cells, from left to right: Cubic, rhombic dodecahedral and parallelepiped. 43

3.4 Ryckaert-Bellemans dihedral potential. Dashed: general shape. Solid: specifically 4-carbon dihedral in n-heptane 48

3.5 Viscosity of water calculated using the TIP4P model, alongside experimental data (IAPWS 1997). Ref 1: Yongli et al. (2007). Ref 2: Markesteijn et al. (2012). Ref 3: González and Abascal (2010) . 55

3.6 Self-diffusion coefficient for water calculated using the TIP4P model, alongside experimental data (Dietrich 2002). Ref 1: Mahoney and Jorgensen (2001). Ref 2: Watanabe and Klein (1989). Ref 3: English (2005) 56

3.7 Layout of the TIP4P water model. 58

3.8 Viscosity of n-heptane calculated using the OPLS-AA forcefield, alongside experimental data (Dymond and O/ye 1994). Ref 1: Zhao et al. (2008). Ref 2: Zahariev et al. (2014)*. Ref 3: Zahariev et al. (2014)**. *Nosé-Hoover thermostat and Parrinello-Rahman barostat. **Berendsen thermostat and barostat. 59

3.9 Self-diffusion coefficient for n-heptane calculated using the OPLS-AA forcefield, alongside experimental data (Fishman 1955) (Moore and Wellek 1974). Ref 1: Smolyanitsky et al. (2013). Ref 2: Zahariev et al. (2014)*. Ref 3: Zahariev et al. (2014)**. *Nosé-Hoover thermostat and Parrinello-Rahman barostat. **Berendsen thermostat and barostat. 60

3.10 Equilibrium structure of the n-heptane model. 62

3.11 Armchair carbon nanotube. 64

4.1 Orthographic (side on) view of an equilibrated film (approx. 6 nm wide) of n-heptane at 440 K used for determining the vapour pressure curve. 75

4.2 Orthographic (side on) view of an equilibrated film (approx. 3 nm wide) of water at 440 K used for determining the vapour pressure curve. 75

4.3 Orthographic (side on) view of a 2 nm slit pore attached to two reservoirs filled with n-heptane. (a) Before the reservoirs have been equilibrated, n-heptane has been added from an equilibrated system at the correct temperature and pressure. (b) After the reservoirs have equilibrated at 300 K and 1 bar. (c) After the barricade has been removed and the pore has completely filled. The fluid in the top image looks slightly different due to molecules having been made whole for the image creation. Molecules in the other two images have been left broken by the periodic boundaries. 81

4.4 Orthographic (side on) view of a 2 nm slit pore attached to two reservoirs filled with water. (a) Before the reservoirs have been equilibrated, water has been added from an equilibrated system at the correct temperature and pressure. (b) After the reservoirs have equilibrated at 300 K and 1 bar. (c) After the barricade has been removed and the pore has completely filled. The fluid in the top image looks slightly different due to molecules having been made whole for the image creation. Molecules in the other two images have been left broken by the periodic boundaries. 82

4.5 Orthographic (side on) view of a 2 nm slit pore adjacent to a single gas phase n-heptane reservoir spanning the periodic boundary. The pore is barricaded whilst the reservoir equilibrates. The reservoir is larger than the portion shown in this image. 83

4.6 Orthographic (side on) view of a 2 nm slit pore adjacent to a single gas phase water reservoir spanning the periodic boundary. The pore is barricaded whilst the reservoir equilibrates. The reservoir is larger than the portion shown in this image. 83

4.7 Saturated vapour pressure curve for TIP4P water. Ref 1: Lisal et al. (2001). Ref 2: Shen et al. (*NIST Standard Reference Simulation Website*). Ref 3: Vega and De Miguel (2007). Experiments: Wagner and Pruss (2002). 87

4.8 Saturated vapour pressure curve for OPLS-AA n-heptane. Ref 1: Chen and Siepmann (1999). Experiments: Span (2000). 88

4.9 Density profile of saturated water along two phase system. Zero corresponds to the centre of the box. The arrows indicate the direction of increasing temperature, from 300 K to 450 K in increments of 10 K. 89

4.10 Density profile of saturated n-heptane along two phase system. Zero corresponds to the centre of the box. The arrows indicate the direction of increasing temperature, from 300 K to 440 K in increments of 10 K. 90

4.11 Liquid-vapour coexistence curve for TIP4P water. Ref 1: Lisal et al. (2001). Ref 2: Shen et al. (*NIST Standard Reference Simulation Website*). Ref 3: Vega and De Miguel (2007). Experiments: Wagner and Pruss (2002). 91

4.12 Liquid-vapour coexistence curve for OPLS-AA n-heptane. Ref 1: Chen and Siepmann (1999). Experiments: Span (2000). 92

4.13 Density-temperature isobar for TIP4P water at 1 bar. Experiments: Wagner and Pruss (2002). 93

4.14 Density-temperature isobar for OPLS-AA n-heptane at 1 bar. Experiments: Span (2000). 94

4.15 Surface tension for TIP4P water. The dashed line indicates experimental data. Ref 3: Vega and De Miguel (2007). Ref 4: Sides et al. (1999). Experiments: IAPWS (1994). The TIP4P/2005 and the TIP4P-Ew re-parameterisations presented in references 3 and 4 are for the purpose of comparison between models. 96

4.16 Surface tension for OPLS-AA n-heptane and other straight chain hydrocarbons for comparison. Dashed lines indicate experimental data. Ref 2: Mendoza et al. (2008). Experiments: heptane and hexane: Somayajulu (1988); butane: Calado et al. (1978), Coffin and Maass (1928); propane: Baidakov and Sulla (1985); ethane: Soares et al. (1986), Leadbetter et al. (1964), Katz et al. (1939). 97

4.17 Orthographic (side on) view of liquid water at 300 K filling a 2.01 nm slit pore after 0, 100, 150, and 1,980 ps. 100

4.18 Liquid water at 300 K filling various slit pores. a) Pore density against time. b) Comparison between pore fill time and the mean density calculated over the final 500 ps of (a). The labels correspond to the density extremes in the smallest pores. The matching pore geometries are shown in figure 4.25. c) Pore density * pore length against time, for use in calculating initial fill rate of pore. d) Initial and secondary rates of adsorption, extracted from (c). The lengths stated in (d) are the equivalent pore penetration lengths, given that the fluid were to enter the pore in a plug fashion at the same local density as the final pore density. 101

4.19 Liquid water at 300 K filling various cylindrical pores. a) Pore density against time. b) Comparison between pore fill time and the mean density calculated over the final 500 ps of (a). The labels correspond to the density extremes in the smallest pores. The matching pore geometries are shown in figure 4.25. c) Pore density * pore length against time, for use in calculating initial fill rate of pore. d) Initial and secondary rates of adsorption, extracted from (c). The lengths stated in (d) are the equivalent pore penetration lengths, given that the fluid were to enter the pore in a plug fashion at the same local density as the final pore density. 102

4.20 Liquid water at 300 K filling the outside of various cylindrical pores. a) Pore density against time. b) Comparison between pore fill time and the mean density calculated over the final 500 ps of (a). The labels correspond to the density extremes in the smallest pores. The matching pore geometries are shown in figure 4.25. c) Pore density * pore length against time, for use in calculating initial fill rate of pore. d) Initial and secondary rates of adsorption, extracted from (c). The lengths stated in (d) are the equivalent pore penetration lengths, given that the fluid were to enter the pore in a plug fashion at the same local density as the final pore density. 103

4.21 Average molecules of water within slit (top) and cylindrical (bottom) pores, after equilibration, at 300 K (liquid). 105

4.22 Snapshots of liquid water at 300 K filling a 0.7 nm slit pore. . . . 106

4.23 Snapshots of liquid water at 300 K filling a 3 nm slit pore. 106

4.24 Snapshots of liquid water at 300 K filling a 10 nm slit pore. 106

4.25 Orthographic (end on) views of slit (left) and cylindrical (right) pores filled with water. The carbon surface atoms are shown as spheres of radius σ_{ss} whilst the water is shown in skeletal form as bonds only. The depth of each pore has been cut to 8 nm for image comparison purposes. The numbering corresponds to the labelled points in figures 4.18 and 4.19 and capture significant fluid phases present in the smallest pores. Left: 1) 0.7 nm, 2) 0.8 nm, 3) 0.9 nm, 4) 1.1 nm, 5) 1.3 nm. Right: 1) 0.81 nm, 2) 0.94 nm, 3) 1.08 nm, 4) 1.21 nm, 5) 1.34 nm. 108

4.26 Density profiles of water, at 300 K, (top) inside and outside cylindrical pores and (bottom) inside slit pores. Calculated from a separate 5 ns simulation after the reservoirs have been removed and the pore made periodic. 110

4.27 Mean water reservoir density over pore filling process for 0.7-10 nm slit pores. $t = 0$ ps is the point at which the barrier is removed. Densities have been normalised by the equilibrium bulk density. . 112

4.28 Mean water reservoir density over pore filling process for 0.81-10.03 nm cylindrical pores. $t = 0$ ps is the point at which the barrier is removed. Densities have been normalised by the equilibrium bulk density. 113

4.29 Snapshots of liquid water at 300 K filling a 0.81 nm cylindrical pore, coloured based on proximity to solid surface: 0-0.6 nm: blue; 0.6-1 nm: green; 1-1.4 nm: yellow; 1.4+ nm: as reservoir fluid. . . 115

4.30 Snapshots of liquid water at 300 K filling a 0.94 nm cylindrical pore, coloured based on proximity to solid surface: 0-0.6 nm: blue; 0.6-1 nm: green; 1-1.4 nm: yellow; 1.4+ nm: as reservoir fluid. . . 115

4.31 Snapshots of liquid water at 300 K filling a 1.08 nm cylindrical pore, coloured based on proximity to solid surface: 0-0.6 nm: blue; 0.6-1 nm: green; 1-1.4 nm: yellow; 1.4+ nm: as reservoir fluid. . . 116

4.32 Snapshots of liquid water at 300 K filling a 2.94 nm cylindrical pore, coloured based on proximity to solid surface: 0-0.6 nm: blue; 0.6-1 nm: green; 1-1.4 nm: yellow; 1.4+ nm: as reservoir fluid. . . 116

4.33 Snapshots of liquid water at 300 K filling a 10.03 nm cylindrical pore, coloured based on proximity to solid surface: 0-0.6 nm: blue; 0.6-1 nm: green; 1-1.4 nm: yellow; 1.4+ nm: as reservoir fluid. . . 117

4.34 Orthographic (side on) view of liquid n-heptane at 300 K filling a 2 nm slit pore after 0, 10, 34, and 1,980 ps. 119

4.35 Liquid n-heptane at 300 K filling various slit pores. a) Pore density against time. b) Comparison between pore fill time and the mean density calculated over the final 500 ps of (a). The labels correspond to the density extremes in the smallest pores. The matching pore geometries are shown in figure 4.45. c) Pore density * pore length against time, for use in calculating initial fill rate of pore. d) Initial and secondary rates of adsorption, extracted from (c). The lengths stated in (d) are the equivalent pore penetration lengths, given that the fluid were to enter the pore in a plug fashion at the same local density as the final pore density. 121

4.36 As in figure 4.35 (a), separated into groups, based on the shape of the data. 122

4.37 Liquid n-heptane at 300 K filling various cylindrical pores. a) Pore density against time. b) Comparison between pore fill time and the mean density calculated over the final 500 ps of (a). The labels correspond to the density extremes in the smallest pores. The matching pore geometries are shown in figure 4.45. c) Pore density * pore length against time, for use in calculating initial fill rate of pore. d) Initial and secondary rates of adsorption, extracted from (c). The lengths stated in (d) are the equivalent pore penetration lengths, given that the fluid were to enter the pore in a plug fashion at the same local density as the final pore density. 123

4.38 As in figure 4.35 (a), separated into groups, based on the shape of the data. 124

4.39 Liquid n-heptane at 300 K filling the outside of various cylindrical pores. a) Pore density against time. b) Comparison between pore fill time and the mean density calculated over the final 500 ps of (a). The labels correspond to the density extremes in the smallest pores. The matching pore geometries are shown in figure 4.45. c) Pore density * pore length against time, for use in calculating initial fill rate of pore. d) Initial and secondary rates of adsorption, extracted from (c). The lengths stated in (d) are the equivalent pore penetration lengths, given that the fluid were to enter the pore in a plug fashion at the same local density as the final pore density. 125

4.40 Average molecules of n-heptane within slit (top) and cylindrical (bottom) pores, after equilibration, at 300 K (liquid). 126

4.41 Snapshots of liquid n-heptane at 300 K filling a 0.7 nm slit pore. . 128

4.42 Snapshots of liquid n-heptane at 300 K filling a 1.8 nm slit pore. . 128

4.43 Snapshots of liquid n-heptane at 300 K filling a 3 nm slit pore. . . 128

4.44 Snapshots of liquid n-heptane at 300 K filling a 10 nm slit pore. . 129

4.45 Orthographic (end on) views of slit (left) and cylindrical (right) pores filled with n-heptane. The carbon surface atoms are shown as spheres of radius σ_{ss} whilst the n-heptane is shown in skeletal form as bonds only. The depth of each pore has been cut to 8 nm for image comparison purposes. The numbering corresponds to the labelled points in figures 4.35 and 4.37 and capture significant fluid phases present in the smallest pores. Left: 1) 0.7 nm, 2) 1 nm, 3) 1.1 nm, 4) 1.4 nm, 5) 1.5 nm, 6) 1.8 nm. Right: 1) 0.81 nm, 2) 1.08 nm, 3) 1.34 nm, 4) 1.61 nm, 5) 1.74 nm, 6) 2.01 nm. . 130

4.46 Density profiles of n-heptane, at 300 K, (top) inside and outside cylindrical pores and (bottom) inside slit pores. Calculated from a separate 5 ns simulation after the reservoirs have been removed and the pore made periodic. 131

4.47 Comparison between the n-heptane reservoir density and the pore density for a selection of slit pores. $t = 0$ ps is the point at which the barrier is removed and the density has been normalised by the equilibrium bulk density. 132

4.48 Mean n-heptane reservoir density over pore filling process for 0.7-10 nm slit pores. $t = 0$ ps is the point at which the barrier is removed. Densities have been normalised by the equilibrium bulk density. 133

4.49 Snapshots of liquid n-heptane at 300 K filling a 0.81 nm cylindrical pore, coloured based on proximity to solid surface: 0-0.6 nm: blue; 0.6-1 nm: green; 1-1.4 nm: yellow; 1.4+ nm: as reservoir fluid. . . 136

4.50 Snapshots of liquid n-heptane at 300 K filling a 1.34 nm cylindrical pore, coloured based on proximity to solid surface: 0-0.6 nm: blue; 0.6-1 nm: green; 1-1.4 nm: yellow; 1.4+ nm: as reservoir fluid. . . 137

4.51 Snapshots of liquid n-heptane at 300 K filling a 2.01 nm cylindrical pore, coloured based on proximity to solid surface: 0-0.6 nm: blue; 0.6-1 nm: green; 1-1.4 nm: yellow; 1.4+ nm: as reservoir fluid. . . 137

4.52 Snapshots of liquid n-heptane at 300 K filling a 2.81 nm cylindrical pore, coloured based on proximity to solid surface: 0-0.6 nm: blue; 0.6-1 nm: green; 1-1.4 nm: yellow; 1.4+ nm: as reservoir fluid. . . 138

4.53 Snapshots of liquid n-heptane at 300 K filling a 2.94 nm cylindrical pore, coloured based on proximity to solid surface: 0-0.6 nm: blue; 0.6-1 nm: green; 1-1.4 nm: yellow; 1.4+ nm: as reservoir fluid. . . 139

4.54 Snapshots of liquid n-heptane at 300 K filling a 3.61 nm cylindrical pore, coloured based on proximity to solid surface: 0-0.6 nm: blue; 0.6-1 nm: green; 1-1.4 nm: yellow; 1.4+ nm: as reservoir fluid. . . 139

4.55 Snapshots of liquid n-heptane at 300 K filling a 10.03 nm cylindrical pore, coloured based on proximity to solid surface: 0-0.6 nm: blue; 0.6-1 nm: green; 1-1.4 nm: yellow; 1.4+ nm: as reservoir fluid. . . 140

4.56 N-heptane reservoir and pore densities for a selection of cylindrical pores. $t = 0$ ps is the point at which the barrier is removed. Reservoir and pore densities have been normalised by the equilibrium bulk density. 141

4.57 Mean n-heptane reservoir density over pore filling process for 0.81-10.03 nm cylindrical pores. $t = 0$ ps is the point at which the barrier is removed. Densities have been normalised by the equilibrium bulk density. 141

4.58 Orthographic (side on) view of vapour phase water at 400 K filling a 2 nm slit pore after 0 and 4,800 ps. The final image is of the same fluid filling a 5 nm slit pore, after 4,800 ps. 143

4.59 Pore density against time for water at 400 K (gas) filling various slit pores. 143

4.60 Pore density against time for water at 400 K (gas) filling various cylindrical pores. 144

4.61 Pore density against time for water at 400 K (gas) filling the outside of various cylindrical pores. 144

4.62 Average density of water within slit (top) and cylindrical (bottom) pores, after equilibration, at 400 K (gas). The dashed line is the bulk fluid density. 145

4.63 Average molecules of water within slit (top) and cylindrical (bottom) pores per unit surface area, after equilibration, at 400 K (gas). 146

4.64 Density profiles of water, at 400 K, (top) inside and outside cylindrical pores and (bottom) inside slit pores. Calculated from a separate 5 ns simulation after the reservoirs have been removed and the pore made periodic. 147

4.65 Orthographic (side on) view of vapour phase n-heptane at 400 K filling a 2 nm slit pore after 0, 4,000, and 34,800 ps. 148

4.66 Orthographic (side on) view of vapour phase n-heptane at 400 K filling a 5 nm slit pore after 1,420 and 19,800 ps. 149

4.67 Pore density against time for n-heptane at 400 K (gas) filling various slit pores. 149

4.68 Pore density against time for n-heptane at 400 K (gas) filling various cylindrical pores. 150

4.69 Pore density against time for n-heptane at 400 K (gas) filling the outside of various cylindrical pores. 150

4.70 Density profiles of n-heptane, at 400 K, (top) inside and outside cylindrical pores and (bottom) inside slit pores. Calculated from a separate 5 ns simulation after the reservoirs have been removed and the pore made periodic. 152

4.71 Average density and time taken to reach 95 % full for n-heptane within slit (top) and cylindrical (bottom) pores, after equilibration, at 400 K (gas). 153

4.72 Average molecules of n-heptane within slit (top) and cylindrical (bottom) pores, after equilibration, at 400 K (gas). 154

4.73 Snapshots of liquid n-heptane at 400 K filling a 0.7 nm slit pore. . 155

4.74 Snapshots of liquid n-heptane at 400 K filling a 1.8 nm slit pore. . 155

4.75 Snapshots of liquid n-heptane at 400 K filling a 2 nm slit pore. . . 155

4.76 Snapshots of liquid n-heptane at 400 K filling a 3 nm slit pore. . . 155

4.77 Snapshots of liquid n-heptane at 400 K filling a 10 nm slit pore. . 155

4.78 Snapshots of liquid n-heptane at 400 K filling a 0.94 nm cylindrical pore, coloured based on proximity to solid surface: 0-0.6 nm: blue; 0.6-1 nm: green; 1-1.4 nm: yellow; 1.4+ nm: as reservoir fluid. . . 156

4.79 Snapshots of liquid n-heptane at 400 K filling a 2.01 nm cylindrical pore, coloured based on proximity to solid surface: 0-0.6 nm: blue; 0.6-1 nm: green; 1-1.4 nm: yellow; 1.4+ nm: as reservoir fluid. . . 156

4.80 Snapshots of liquid n-heptane at 400 K filling a 2.94 nm cylindrical pore, coloured based on proximity to solid surface: 0-0.6 nm: blue; 0.6-1 nm: green; 1-1.4 nm: yellow; 1.4+ nm: as reservoir fluid. . . 157

4.81 Snapshots of liquid n-heptane at 400 K filling a 10.03 nm cylindrical pore, coloured based on proximity to solid surface: 0-0.6 nm: blue; 0.6-1 nm: green; 1-1.4 nm: yellow; 1.4+ nm: as reservoir fluid. . . 157

4.82 Adsorption isobars of TIP4P water at 1 bar inside slit (top) and cylindrical (bottom) pores. The temperature is rescaled by the bulk fluid boiling point (365.5 K). 159

4.83 Adsorption isobars of n-heptane at 1 bar inside slit (top) and cylindrical (bottom) pores. The temperature is rescaled by the bulk fluid boiling point (371.5 K). 162

5.1 Cross section of equilibrated system of water inside a carbon nanotube, before removal of the reservoirs. 174

5.2 Density profile along the length of the pore initially (solid) and after several time steps once filled back up to equilibrium value (dashed) for water (top) and n-heptane (bottom) in 10 nm slit (left) and cylindrical (right) pores. The z-position has been shifted, such that zero is the location of the end of the pore prior to removal of the reservoirs and addition of periodicity. 175

5.3 Example of geometries studied here. From left to right: Fluid inside carbon nanotube. Fluid outside of carbon nanotube. Fluid inside graphitic slit pore. 176

5.4 Friction coefficient calculated using equation 5.10, for water at 300 K, inside and outside of a carbon nanotube. The central dataset is for water between two flat surfaces. The lines of fit shown are used to find the constants in equations 5.22. 184

5.5 Comparison between EMD and NEMD slip lengths, for water at 300 K, calculated using equation 5.11 and equations 5.2 and 5.3 respectively. The lines are the fits from the EMD method and are equivalent to those in figure 5.4. NEMD results only exist for the inside and flat cases as there is no simple analytical solution to the Navier-Stokes equation for the outside case. 187

5.6 Friction coefficient calculated using equation 5.10, for n-heptane at 300 K, inside and outside of a carbon nanotube. The central dataset is for water between two flat surfaces. The lines of fit shown are used to find the constants in equations 5.22. 189

5.7 Comparison between EMD and NEMD slip lengths, for n-heptane at 300 K, calculated using equation 5.11 and equations 5.2 and 5.3 respectively. The lines are the fits from the EMD method and are equivalent to those in figure 5.4. NEMD results only exist for the inside and flat cases as there is no simple analytical solution to the Navier-Stokes equation for the outside case. 190

5.8 Friction coefficient calculated using equation 5.10, for water at 400 K, inside and outside of a carbon nanotube. The central dataset is for n-heptane between two flat surfaces. The lines of fit shown are used to find the constants in equation 5.22. 192

5.9 EMD slip lengths, for water at 400 K, calculated using equation 5.11. The lines are the fits from the EMD method and are equivalent to those in figure 5.4. 193

5.10 Friction coefficient calculated using equation 5.10, for n-heptane at 400 K, inside and outside of a carbon nanotube. The central dataset is for n-heptane between two flat surfaces. The lines of fit shown are used to find the constants in equation 5.22. 194

5.11 EMD slip lengths, for n-heptane at 400 K, calculated using equation 5.11. The lines are the fits from the EMD method and are equivalent to those in figure 5.4. 195

6.1 The two-dimensional FHP model and its unit velocity vectors (adapted from Sukop and Thorne (2013)). 201

6.2 The D2Q9 model lattice (adapted from Sukop and Thorne (2013)). 205

6.3 The D3Q19 model lattice. 206

6.4 The streaming process on a D2Q9 lattice (adapted from Cercignani (1969)). 208

6.5 The collision process on a D2Q9 lattice (adapted from Cercignani (1969)). 208

6.6 The movement of particles in periodic boundaries (adapted from Succi (2001)). 211

6.7 The process of mid-plane bounce back movement in D2Q9 model (adapted from Sukop and Thorne (2013)). 213

6.8 The process of specular reflection at boundaries in the D2Q9 model. 221

6.9 The specular reflection bounce-back combination boundary condition for the cases of a channel 45° out of alignment with the lattice and a straight channel. Red dots and the surrounding red lines indicate the discretised location of the solid boundary. The dashed line indicates the represented surface. 222

6.10 Sample of geometries used in LBM flow calculations. Red signifies solid nodes whilst grey signifies fluid nodes. (Left) 20 lu wide channel 45° out of alignment. (Bottom right) 20 lu wide channel aligned with lattice. (Top right) 11 lu and 10 lu diameter cylindrical geometries. 224

6.11 Discretised cylindrical geometries, 10 lu (top) and 11 lu (bottom) diameters, with central node either on grid (left) or mid-grid (right). 225

6.12 Velocity profiles, in straight geometries, calculated from LBM with specular-bounce-back combination boundary condition (marks) and the fit to Navier-Stokes (equation 5.4)(solid lines). From bottom to top for each channel width: $C_s = 0$, 0.8, and 0.95. 227

6.13 Velocity profiles, in cylindrical geometries, calculated from LBM with specular-bounce-back combination boundary condition (marks) and the fit to Navier-Stokes (equation 5.5)(solid lines). From bottom to top for each cylinder diameter: $C_s = 0$, 0.8, and 0.95. . . . 228

6.14 Error from Navier-Stokes as a function of cylinder diameter for three values of the slip coefficient. 230

6.15 Calculated (marks) slip length and prediction from equation 6.25 (solid lines) as a function of cylinder diameter for three values of the slip coefficient. 231

6.16 Velocity profiles, in straight geometries, calculated from LBM with velocity boundary condition (marks) and the fit to Navier-Stokes (equation 5.4)(solid lines). From bottom to top for each channel width: $u_{wall} = 0$, 0.0001, and 0.0002 lu ts^{-1}. 232

6.17 Velocity profiles, in cylindrical geometries, calculated from LBM with velocity boundary condition (marks) and the fit to Navier-Stokes (equation 5.5)(solid lines). From bottom to top for each cylinder diameter: $u_{wall} = 0$, 0.0001, and 0.0002 lu ts^{-1}. 234

6.18 Error from Navier-Stokes as a function of cylinder diameter for three values of the wall velocity. 235

6.19 Calculated (marks) slip length and prediction from equation 5.5 (solid lines) as a function of cylinder diameter for three values of the wall velocity. 236

6.20 Velocity profiles, in straight geometries 45° out of alignment with the lattice, calculated from LBM with velocity boundary condition (marks) and the fit to Navier-Stokes (equation 5.4)(solid lines). From bottom to top for each channel width: $u_{wall} = 0$, 0.0001, and 0.0002 lu ts^{-1}. 238

C.1 Liquid water at 300 K filling various slit pores. a) Pore density against time. 276

C.2 Liquid water at 300 K filling various slit pores. b) Comparison between pore fill time and the mean density calculated over the final 500 ps of (a). The labels correspond to the density extremes in the smallest pores. The matching pore geometries are shown in figure 4.25. 277

C.3 Liquid water at 300 K filling various slit pores. c) Pore density * pore length against time, for use in calculating initial fill rate of pore. 278

C.4 Liquid water at 300 K filling various slit pores. d) Initial and secondary rates of adsorption, extracted from (c). The lengths stated in (d) are the equivalent pore penetration lengths, given that the fluid were to enter the pore in a plug fashion at the same local density as the final pore density. 279

C.5 Liquid water at 300 K filling various cylindrical pores. a) Pore density against time. 280

C.6 Liquid water at 300 K filling various cylindrical pores. b) Comparison between pore fill time and the mean density calculated over the final 500 ps of (a). The labels correspond to the density extremes in the smallest pores. The matching pore geometries are shown in figure 4.25. 281

C.7 Liquid water at 300 K filling various cylindrical pores. c) Pore density * pore length against time, for use in calculating initial fill rate of pore. 282

C.8 Liquid water at 300 K filling various cylindrical pores. d) Initial and secondary rates of adsorption, extracted from (c). The lengths stated in (d) are the equivalent pore penetration lengths, given that the fluid were to enter the pore in a plug fashion at the same local density as the final pore density. 283

C.9 Liquid water at 300 K filling the outside of various cylindrical pores. a) Pore density against time. 284

C.10 Liquid water at 300 K filling the outside of various cylindrical pores. b) Comparison between pore fill time and the mean density calculated over the final 500 ps of (a). The labels correspond to the density extremes in the smallest pores. The matching pore geometries are shown in figure 4.25. 285

C.11 Liquid water at 300 K filling the outside of various cylindrical pores. c) Pore density * pore length against time, for use in calculating initial fill rate of pore. 286

C.12 Liquid water at 300 K filling the outside of various cylindrical pores. d) Initial and secondary rates of adsorption, extracted from (c). The lengths stated in (d) are the equivalent pore penetration lengths, given that the fluid were to enter the pore in a plug fashion at the same local density as the final pore density. 287

C.13 Liquid n-heptane at 300 K filling various slit pores. a) Pore density against time. 288

C.14 Liquid n-heptane at 300 K filling various slit pores. b) Comparison between pore fill time and the mean density calculated over the final 500 ps of (a). The labels correspond to the density extremes in the smallest pores. The matching pore geometries are shown in figure 4.45. 289

C.15 Liquid n-heptane at 300 K filling various slit pores. c) Pore density * pore length against time, for use in calculating initial fill rate of pore. 290

C.16 Liquid n-heptane at 300 K filling various slit pores. d) Initial and secondary rates of adsorption, extracted from (c). The percentage ranges in (d) are of the final maximum fluid density in the pore. . 291

C.17 As in figure C.13 (a), separated into groups, based on the shape of the data. 292

C.18 As in figure C.13 (a), separated into groups, based on the shape of the data. 293

C.19 As in figure C.13 (a), separated into groups, based on the shape of the data. 294

C.20 As in figure C.13 (a), separated into groups, based on the shape of the data. 295

C.21 Liquid n-heptane at 300 K filling various cylindrical pores. a) Pore density against time. 296

C.22 Liquid n-heptane at 300 K filling various cylindrical pores. b) Comparison between pore fill time and the mean density calculated over the final 500 ps of (a). The labels correspond to the density extremes in the smallest pores. The matching pore geometries are shown in figure 4.45. 297

C.23 Liquid n-heptane at 300 K filling various cylindrical pores. c) Pore density * pore length against time, for use in calculating initial fill rate of pore. 298

C.24 Liquid n-heptane at 300 K filling various cylindrical pores. d) Initial and secondary rates of adsorption, extracted from (c). The percentage ranges in (d) are of the final maximum fluid density in the pore. 299

C.25 As in figure C.21 (a), separated into groups, based on the shape of the data. 300

C.26 As in figure C.21 (a), separated into groups, based on the shape of the data. 301

C.27 As in figure C.21 (a), separated into groups, based on the shape of the data. 302

C.28 As in figure C.21 (a), separated into groups, based on the shape of the data. 303

C.29 Liquid n-heptane at 300 K filling the outside of various cylindrical pores. a) Pore density against time. 304

C.30 Liquid n-heptane at 300 K filling the outside of various cylindrical pores. b) Comparison between pore fill time and the mean density calculated over the final 500 ps of (a). The labels correspond to the density extremes in the smallest pores. The matching pore geometries are shown in figure 4.45. 305

C.31 Liquid n-heptane at 300 K filling the outside of various cylindrical pores. c) Pore density * pore length against time, for use in calculating initial fill rate of pore. 306

C.32 Liquid n-heptane at 300 K filling the outside of various cylindrical pores. d) Initial and secondary rates of adsorption, extracted from (c). The percentage ranges in (d) are of the final maximum fluid density in the pore. 307

Chapter 1

Introduction

1.1 Objectives

The main goal of this work is to create a scale-up procedure for translating information from molecular simulations up to the continuum scale in order to study flow in nano-pores. This goal is achieved by combining molecular dynamics and Lattice Boltzmann simulations.

As part of the process for reaching this goal, appropriate pores and fluid models for molecular simulation are selected for initial testing of the procedure.

The mechanisms of adsorption of sample fluids are investigated and relationships between the pore density, fluid arrangement, pore shapes, and pore sizes are found.

Once pore densities are known, the slip length is found along with its relationship with curvature using molecular dynamics.

Knowing the slip length, the Lattice Boltzmann boundary condition for solid surfaces is adapted in order to be able to exhibit slip. The proposed methods are tested in straight, cylindrical, and off-grid straight channels.

The intended application of this work is in the description of transport and adsorption of fuel components in carbonaceous engine deposits that form on the back of intake valves in internal combustion engines. The cycle of the engine, coupled with the large range of temperatures experienced, can result in continuous adsorption and desorption of fuel components that affect the fuel-air ratio and cause in undesirable performance issues.

The focus here is on the transport of water and n-heptane in carbon nanotubes (CNTs) and graphitic slit pores, however the procedure, observations, and results can also be applied to any nanoporous system, including gas shales.

1.2 Publications and conferences

Below is a list of published scientific journal articles and conference reports published up to the presentation of this thesis.

1.2.1 Publications

Li, X., Ross, D. A., Trusler, J. P. M., Maitland, G. C., and Boek, E. S. (2013). "Molecular dynamics simulations of CO2 and brine interfacial tension at high temperatures and pressures". *Journal of Physical Chemistry B* 117.18, pp. 5647–5652. DOI: 10.1021/jp309730m

Ross, D. A. and Boek, E. S. (2016). "Molecular Dynamics Simulations of Slip on Curved Surfaces". *Oil & Gas Science and Technology Revue d'IFP Energies nouvelles* 71.4. Ed. by C. David and N. Sallee, p. 46. DOI: http://dx.doi.org/10.2516/ogst/2016004

1.2.2 Conferences

Presentations

Multiscale Simulation of the transport of Hydrocarbons in Porous Engine Deposits. Joint CCP5-RSC Workshop on Advances in Theory and Simulation of non-Equilibrium Systems. 26-27 June 2013. Imperial College London.

Molecular Dynamics Simulations of Slip Flow in Nanopores. IOP: The Physics of Soft and Biological Matter. 14-16 April 2013. Homerton College, Cambridge.

Simulating Fluid Transport in Nano-pores. Shell Amsterdam Centennial Conference "Rock & Fluid Physics: Academic and Industrial Perspectives". 15-17 September 2014. Shell Technology Centre, Amsterdam.

Molecular Dynamics Simulations of Slip on Curved Surfaces. LowPerm2015. 9-11 June 2015. IFP Energies nouvelles, Paris.

Posters

Multi-scale Simulation of the Transport of Hydrocarbons in Porous Engine Deposits. QCCSRC annual review meeting. 28-30 January 2013. Imperial College London.

Multi-scale Simulation of the Transport of Hydrocarbons in Porous Engine Deposits. Shell Tech Foresight. 6 June 2013. Imperial College London.

Molecular Dynamics Simulations of Slip Flow in Nanopores. ChemEngDayUK 2014. 7-8 April 2014. The University of Manchester.

Slip Flow in Nanopores. CDT Festival of Science 2014. 13 June 2014. Imperial College London.

Chapter 2

Background theory

2.1 Introduction

In this chapter the motivation for this thesis is discussed along with the background, methods, and literature. First engine deposits are introduced, followed by a comparison of pore-scale and continuum-scale modelling techniques. Molecular dynamics (MD) for nanometre scale systems is discussed along with Lattice Boltzmann methods (LBM) for larger scale (nanometre, to metre, to kilometres) systems. Additionally hybrid models are briefly discussed. Finally the concept of slip is introduced and some existing literature is discussed. Further comparisons between these works and literature values can be found in later chapters.

2.2 Engine deposits

There is an ever increasing trend in recent years towards reducing emissions amongst consumers for reasons such as vehicle tax, based on CO_2 emissions, and public opinion. This, coupled with the unquenchable desire for ever increasing engine performance, has led to boundless areas of ongoing research into products

and fuel additives that can enhance consumer satisfaction and meet increasing emission standards.

In this pursuit of increased engine performance and emissions control, there are many improvements that can be made to the already highly engineered design of internal combustion engines. But there are also contributing factors which are less mechanical and more chemical, such as fuel composition and the composition of any fluids used within the engine including lubricating oils. The unrestricted flow of air within the engine is an important factor as well as maintaining the correct fuel/air ratios in the combustion chamber and intake system.

One contributor to adverse effects in engines are engine deposits. These are the thick black, almost soot like, substances one would find coating all surfaces if one were to dismantle a used engine. One may initially assume this is a normal and unavoidable ramification of incomplete combustion, which is difficult to avoid, and that the effect on engine operation is negligible (especially considering these deposits are much smaller than a millimetre thick). However, it is a well known fact that cleaning an engine completely of these deposits can result in reduced emissions. Yue et al. (2012) performed experiments on light-duty engines in Beijing, China. The authors found, upon removal of deposits, a surprising reduction in hydrocarbon and carbon monoxide emissions of on average 29.4% and 35.5% respectively. This is arguably an inflated value compared to western societies where technology is more developed and these deposits are not as voluminous. In many countries these deposits can be very large, for instance in emerging markets such as India, where the most up-to-date technologies are not affordable and price is generally a larger contributing factor to buyers' choices than emissions.

Fuel additives exist on the market which are able to remove engine deposits from the intake system, however these come at a cost of increased combustion chamber deposits (Kalghatgi 1995). For this reason, amongst others, it is important to understand with as much detail as possible the chemistry involved in all types of

deposits in order to justify the removal of one type at the expense of build up of another.

2.2.1 Overview

Engine deposits are heterogeneous carbonaceous residues which accumulate within internal combustion engines believed to form as a result of incomplete combustion and the thermal cracking of lube oil contaminants (Zerda et al. 1999). The formation of these deposits result in many negative implications for engine performance and emissions, such as increased likelihood of knocking, slower response to acceleration and adverse emission changes (Pinto Da Costa et al. 2011).

Engine deposits can accumulate on all internal surfaces of the engine and can be classed under three categories:

- Fuel system deposits.
- Combustion chamber deposits.
- Intake system deposits.

Intake system deposits, specifically those accumulating on the intake-valves, are discussed in detail herein. However, a brief overview of each category is given for the sake of completeness. Nonetheless, the works presented herein have relevance and applicability to all forms of carbonaceous deposits.

The most concerning fuel system deposits are located in the fuel-metering devices such as the fuel injector or carburettor in older vehicles. Since almost all new vehicles use fuel injection as opposed to a carburettor, due to increased power and torque, better drivability and emission control (Kalghatgi 1990), mainly fuel injection shall be discussed here. Incidentally, the main reason for the switch from

carburettors to fuel injection was due to political pressures to reduce fuel consumption and pollution of unburnt hydrocarbons and oxides of nitrogen. Deposits can build up in the narrow annular region at the tip of the injector, restricting fuel flow rate and upsetting the fuel spray pattern (Kalghatgi 1990).

Combustion chamber deposits contribute to knocking, which can damage the engine. This is when the autoignition of fuel, due to sufficiently high temperature and pressure ahead of the flame front, changes the nature of the reaction in the engine from an orderly progressive burning to an explosion. In this case, the ignition of fuel occurs in a shorter time than the time for which the flame front usually crosses the chamber. The name comes from the sound heard from the engine as this happens.

A fuel's ability to resist knock is measured by it's octane number and corresponds to the percentage of isooctane in a mixture with n-heptane that has an equivalent autoignition point. A higher number indicates that the fuel can withstand a higher compression ratio before autoignition occurs. Regular unleaded petrol has a typical octane number of 87, whereas premium fuels can have octane numbers in the range of 92-99 and are generally more expensive than their regular counterparts. As long as the minimum octane number requirement for the engine is achieved, the choice of fuel will make little difference to an engine's performance.

During use, the quantity of deposits within the engine increases, these deposits stabilise after roughly 15,000 to 25,000 km (9,000 to 15,000 miles) (Heywood 1988). At this point the engines octane requirement increases by 1 to 13 octane numbers, typically 5 octane numbers (Heywood 1988). The compression ratio also increases, however it has less of an effect on the octane requirement. When stable, the amount of deposits per cylinder is in the range 0.3 to 1 cm^3, which corresponds to an increased compression ratio of 0.1 (Heywood 1988). A study by Benson (1975) found that the octane requirement increase (ORI) was mostly caused by deposits on the cylinder head, about two-thirds of the total ORI (Benson 1975).

The presence of engine deposits results in incomplete combustion of the fuel, increasing emissions of CO by 35.5% on average and hydrocarbons by 29.4% on average compared to a clean, without deposits, engine (Yue et al. 2012).

In the intake system, deposits can form on the surfaces of the port and on the intake-valves; an example of deposit build up on an intake valve can be seen in figure 2.1. Of fuel injection techniques, port fuel injection (PFI) has now become standard (Lumley 1999). In PFI, the fuel is usually injected into the intake manifold, where the air entering the engine is directed to each cylinder, directly behind the intake-valves. In this case, liquid fuel is deposited on the back of the intake-valve (and surrounding port walls), this fuel then evaporates rapidly due to the hot surfaces. This contributes to deposit formation on the valve tulip, the curved surface on the back of the valve. The fluid film can also result in cleaning of the deposit in circumstances where deposit control additives are added to the fuel. Valve deposit levels can increase upon increasing the inlet air temperature, as the liquid fraction on the valve is reduced leading to a reduction in this washing action (Kalghatgi 1990). However, the deposits that wash off the intake-valve are often deposited on the inner surfaces of the combustion chamber, increasing combustion chamber deposit formation (Kalghatgi 1995).



Figure 2.1: Carbonaceous deposits on an intake-valve.

Further contributors to intake-valve deposits include:

- Blow-back occurring after the start of the compression stroke, whilst the valve is still closing (Kalghatgi 1990).
- Higher alkene content in the fuel (Kalghatgi 1990).
- Alcohol and cat-cracked components (Kalghatgi 1990).
- Increased valve surface temperatures (very high surface temperatures, above the film boiling limit, lead to a reduction in deposit formation) (Kalghatgi 1990).
- Engine oil degradation (Diaby et al. 2009).
- Exhaust gas recirculation EGR (Diaby et al. 2009).

Another factor which affects deposit formation on the intake-valve are fuel properties, for instance aromatics content, which changes the nature of the deposit and mean molecular weight (Kalghatgi 1990).

2.2.2 Effects of intake-valve deposits

Deposits on the intake-valve can have the following affects on the engine performance:

- Increased NO_x emissions at part throttle, due to either an increased combustion rate or a difference in level of residual gases (Kalghatgi 1990).
- Power loss, due to reduction of flow to engine at wide open throttle caused by deposits restricting flow. Also due to disrupted swirl, which many engines depend on for faster combustion (Kalghatgi 1990).

- Drivability problems such as hesitation (non-continuous power during acceleration) and poor throttle response during warm up. This is probably due to adsorption of unevaporated fuel resulting in excessively lean mixtures during cold start (Kalghatgi 1990) .

From the literature it seems that deposits on the intake-valve have little to no effect on the ORI. In the intake system, it seems that the ridge deposits have the largest effect in cases when the inlet system deposits do contribute to ORI (Kalghatgi 1990). In this case, where the inlet system deposits do contribute to ORI, it is possible that this is due to the affect they have on inlet flow characteristics, which ultimately affect the turbulent heat transfer at the wall (Kalghatgi 1990). The general conclusion is that ORI can increase or decrease due to the effects of intake-valve deposits, but the amount varies from engine to engine, and even chamber to chamber in the same engine, to the point where the overall effect is negligible.

2.2.3 Intake valve deposits composition and structure

Zerda et al. (2001) found that combustion chamber deposits (CCD), removed from the cylinder heads, are more porous than deposits on the piston tops. Intake-valve (IVD) deposits were found to be similarly less porous than combustion chamber deposits.

They also found that the typical pore size responsible for the majority of the internal surface area in their engine deposit samples was approximately 0.5 nm. They also presented TEM images to back up this result, which showed clearly identifiable graphitic structures along with large amorphous structures. Although not discussed directly, the image presented shows that many of the pores are of slit type, but some overall curvature can be seen.

In a study by Pinto Da Costa et al. (2009), where one IVD and two CCD samples

were considered, the pore size distribution (PSD) was determined. One CCD sample was taken from a bench mounted engine and the other CCD and IVD were from a scrapyard Ford Fiesta 1.2L engine. Here the authors assumed that the deposits could be modelled as activated carbon, with a slit-shaped pore geometry. Ethane absorption measurements were carried out at temperatures between 278 K and 298 K and pressures up to 25 bar. A maximum temperature of 450 K was used in outgassing the samples prior to adsorption experiments. Grand canonical Monte Carlo simulations were used to generate the PSD assuming ideal graphite slit pores. The PSDs show peaks at around 10 and 40 Å. These confirm the results by Zerda et al. (1999), that IVDs are less porous than CCDs. A large internal surface area was found, in the approximate range 100-300 m^2/g and the primary contributors to this are the smaller pores.

The elementary composition of intake valve deposits, from various references, is shown in table 2.1.

Table 2.1: Elementary composition of IVDs in wt%.

Component	C	O	N	H	Zn	S	Fe	Ca	P	Pb	Cu
Ref 1*	74.5	2.5	1.9	6.7	2.9	1.5	1.4	1.5	0.9	0.4	0.288
Ref 2†	59.1	15.6	3.8	6.0	1.9	–	–	3.5	0.9	–	–
Ref 2†	73.6	9.7	1.9	7.4	1.9	–	–	1.5	0.7	–	–
Ref 2†	71.1	11.0	1.6	9.7	1.2	–	–	1.9	1.3	–	–

* Pinto Da Costa et al. (2011). Scrapyard samples from a Ford Fiesta 1.2L engine. Zn, Mg and Ca are elements from the lubricating oil.
† Esaki et al. (1990). Three different engines tested under different operating conditions. The first two results are for a 1600 cc engine, running at 6000 rpm for 1000 hr and 200,000 cycles respectively. The third result is for a 2000 cc engine running at on-road conditions for 100 hr. Zn, Ca and P are elements from oil additives.

2.3 Modelling

The size and highly nano-porous nature of intake-valve deposits make them ideal for molecular modelling; Whereby each molecule is explicitly represented, and atomic and molecular interactions are considered, such that the simulated topol-

ogy is a realistic representation of the system to be studied. However the time-scales that exist in engines, approximately 50 μs per complete cycle, cannot currently be viewed on the scale of molecular simulations. This is where continuum scale techniques come in, which can deal with much longer time periods in the range of seconds. Unfortunately, these continuum scale techniques work by effectively coarse-graining in some way or another. This means that the interfacial physics are no longer recovered, but explicitly applied based on assumptions of macroscopic surface properties.

The main goal of these works is to extract macroscopic properties such as slip length from molecular simulation and to import these as parameters into a larger scale continuum modelling technique. Therefore, it is important to choose the correct modelling techniques for both scales.

2.3.1 Molecular modelling techniques

There is a large selection of molecular modelling techniques available, each with its own advantages and limitations. The technique chosen for this study should be able to accurately model, in a realistic way, the transport of fluid when in contact with a solid boundary. For this reason, there needs to be a way of defining a solid surface, which would act differently from a liquid or vapour medium.

The solid boundary needs to be defined explicitly, in order to realistically introduce a source of friction. It would also need to be parameterised in such a way that it accurately represents a nanopore or nanochannel present in a carbonaceous engine deposit.

There would also need to be existing parametrised models available for both the solid surface and any fluids of interest in this study, and for any future works, i.e. straight chain hydrocarbons and water.

Results should be generated within a reasonable time frame of days/weeks and

data sets of results should include simulation areas of 1000-10,000 nm^3 over time scales of 1-10 ns. This would correspond to tens to hundreds of thousands of molecules.

Naturally, it must also be possibly to calculate the slip length in the chosen technique, either by averaging over velocities and positions of explicit molecules and extrapolating, or by some other method, including calculating friction at the surfaces and relating this to a slip length.

Any intramolecular interactions and collisions with other atoms would need to be solved, as opposed to being resolved stochastically, in order for quantitative values for friction and slip length to be calculated.

There would be no need to include breaking or formation of bonds as no reactions are expected in any of the applications discussed earlier in this chapter. This means that no subatomic interactions need be solved.

Table 2.2 lists some of the main molecular modelling techniques along with a short summary of their advantages, disadvantages, and applications. This table is used in selecting a technique that matches closest the requirements given above. Details of the chosen technique, along with the parameterisation of the molecular models used in this study, are given in chapter 3.

Table 2.2: Comparison of molecular modelling techniques.

Modelling technique	Description	Advantages	Disadvantages	Applications
Density functional theory (DFT) and Quantum mechanics (QM)	Total energy of a system is found from the electron density which is calculated via functionals (i.e. functions of functions). Here the electron density is a function of space and time.	Very detailed description of a system without requiring fitting to experimental data. There also exists a QM/MD hybrid that allows calculation of properties similar to classical MD.	Generally only able to investigate single atoms or molecules, unless using a QM/MD hybrid or similar.	Computing the electronic structure of matter. Parameterising models of molecules or atoms for use in MD of MC. Computing molecular structures and model reactions.
Molecular dynamics (MD)	Evolution of the system occurs in real time. Trajectories of molecules determined by Newton's equations of motion.	Realistic representation of the transport of molecules. Velocities and positions change naturally with time, so transport properties can be calculated.	Molecules may be trapped in a small number of low energy conformations, unable to escape due to large energy barriers. Possibles solutions involve running many simulations with different initial conditions or by simulating annealing during the equilibration process	Determination of transport properties such as viscosity. Calculation of dynamic, structural, and thermodynamic properties.

Monte Carlo (MC)	Generates system states based on Boltzmann probabilities, where new states are chosen at random and accepted based on whether they have a smaller free energy than the previous state.	Good for low density fluids at equilibrium. Unlike MD, in MC the random moves can easily overcome energy barriers. Able to vary the number of particles throughout a simulation. Generally easier to implement than MD.	Relies on equilibrium conditions and as such only static quantities can be studied.	Calculation of structural and thermodynamic properties.
Langevin dynamics	Here a solvent is simulated implicitly by adding two force terms to the Newton's second law in MD. The term consists of a friction coefficient for the solvent representing viscous drag and a random force, associated with thermal motion. When the friction coefficient is chosen to be small, then Langevin dynamics becomes MD with a Langevin thermostat.	Solute no longer explicitly considered, meaning a reduction in simulation time and as such longer simulations can be performed. Langevin thermostatting works well when simulating a gas phase system, as a build up of translational momentum is avoided, unlike with other thermostatting methods. See section 4.3.6 for details on this.	Because of the stochastic nature of Langevin dynamics and the Langevin thermostat, momentum transfer is not preserved. Thus, diffusion coefficients are incorrect.	Used in simulations of complicated systems, such as linear polymers where the relaxation time is long as as such the total simulation time required is long.

Multi-particle collision dynamics (MPC) or Stochastic rotation dynamics (SRD)	A coarser grained MD. Here timesteps are either collision or streaming steps. During collisions new velocities are chosen randomly whilst conserving momentum and energy. On streaming steps the fluid behaves as an ideal gas and move according to their velocities.	Simulations are less computationally expensive, due to calculation of intermolecular potentials at every step is not required.	Solid boundaries are difficult to implement and surface friction is chosen rather than determined.	Dynamics of large molecules, such as polymers or large biomolecules, in solution. For looking at relatively large systems of particles where the individual motion of atoms is not important.

Dissipative particle dynamics (DPD)	Similarly to MD, particles move according to Newton's equations of motion. Particles represent clusters of molecules. The force on a particle is calculated from the sum of the conservative (soft interaction between two particles), dissipative (representing viscosity, dependant on relative positions and velocities of two particles) and random (thermal fluctuations) forces.	Mesoscale simulation method. Longer time-scales and dimensions than MD. Can be a good stepping stone between MD and LB, since the fluid particles are not restricted to lattice sites. More flexible than LB and much faster than MD.	Structure of fluid and wall particles are lost in coarse-graining. Momentum transfer and diffusion happen on roughly the same time-scale, whereas in a real fluid momentum transfer is $O(10^3)$ times larger. This leads to viscosities which are much lower than in real fluids. Fine tuning of the model is required in order to achieve more realistic transport properties. Interactions with wall particles require explicitly specifying the amount of slip.	Used in understanding mesoscale systems, similar to the applications of LB.

2.3.2 Molecular dynamics

From the list of techniques described in table 2.2, molecular dynamics has been chosen for studying adsorption and transport in engine deposits, and in similar nano-porous systems on the molecular scale. This is due to its ability to accurately calculate transport properties of a system with a relatively large number of molecules. Although the system size and time-scale is more restricted than in other techniques, the higher accuracy generated from explicitly including molecular structure is necessary in these works.

First introduced in the late 1950s by Alder and Wainwright (Alder and Wainwright 1959), Molecular dynamics has proven to be a crucial and powerful tool in a boundless range of disciplines and applications.

MD has been used to better understand many areas of physical chemistry, biology and used in the design of highly porous materials such as catalysts. Some ongoing areas of soft matter research include investigations into protein interactions, rheology, flow (Koplik et al. 1989) (Thompson and Robbins 1989), wetting, imbibition (Stukan et al. 2010), capillary condensation (Peterson et al. 1988) (Heffelfinger et al. 1988), diffusive transport, surface tension calculations (Li et al. 2013) (Kuznetsova and Kvamme 2002) (Matsumoto and Kataoka 1988) and adsorption to name but a few.

In MD atoms are modelled as either hard or soft spherical particles, which interact with each other via some potential (typically Lennard-Jones). Time is discretised, such that forces, velocities, and positions are recalculated at set intervals. Forces between atoms are calculated from the potential function, based on the distance between a pair of atoms within range of each other. The total force experienced by each atom is then the sum of all the pairwise interactions. Once this force is known, given the original position and velocity of the atom is also known, the new velocity and position after the discrete time-step is obtained via solving

Newton's second law. This calculation is performed at each time-step and is enough to result in some evolution of the system. The minimum requirements to define and perform a simple microcanonical (constant energy) MD simulation are: the size of an atom, the strength of interactions between pairs of atoms, and a function of these two quantities for calculating the potential between atom pairs.

Additional features can be integrated into the model beyond this basic system. for instance, expanding from individual atoms to multi-atom molecules. When making this addition, more parameters are required in order to model intra-molecular interactions. This includes defining how the distance between bonded atoms is maintained and whether or not they can stretch and oscillate. When three or more atoms make up a molecule, one must also consider how atoms not directly bonded together, but existing in the same molecule, should interact. This includes how the angle between these atoms are to be maintained. Once four atoms constitute a linear molecule, the dihedral angle must also be considered. In all of these cases it is possibly to simply constrain these bond lengths and angles or to allow them to oscillate harmonically or in some other way.

Atoms may also in reality have some charge or polarity. In these cases, there is an additional force term which can be found from Coulomb's law.

Furthermore, the temperature of the system can be controlled by weakly coupling the velocities of the atoms in the system, or by applying some random external force.

In the most basic case, if allowed to run for many time-steps, eventually the system would become so spread out that atoms or molecules are no longer interacting with each other. To prevent this, periodic boundary conditions can be implemented. In this way, any molecule leaving one side of a simulation cell would re-enter at the opposite side. Given that the simulation cell is large enough to prevent a molecule interacting with itself, or with another molecule twice, this

results in an effectively infinite system without an infinite computing requirement.

Beyond this, one can add additional fluids and phases to the system. Liquid and gas phases may require different methods of temperature coupling due to the difference in density. Solids can be modelled in several ways, including implicit surfaces, atoms "frozen" in place, and many-atom molecules than span across periodic boundaries.

This is just a short summary of MD and more detail, including the MD package used herein and the algorithms employed, is given in chapter 3.

2.3.3 Continuum scale modelling techniques

As previously discussed, the goal of this work is to create a procedure for moving from molecular simulations up to the continuum scale for studying flow in nano-pores. Once parameters are extracted from molecular simulations, these are input into a suitable continuum technique, such that transport of fluid in complex nano-porous geometries can be simulated. This model is then able to imitate the important aspects of nano-porous flow whilst still being able to simulate large complicated systems for times reaching seconds.

The requirements for a suitable continuum modelling technique are now discussed. The technique would have to have a suitable method of introducing multiple phases. Initially, only solid and fluid phases are required, however it should be possible to extend the model to have separate fluid phases, including gas and liquid phases coexisting.

The model would have to have a simple method of introducing slip boundary conditions between solid and fluid phases. The slip should be implemented in a way that the amount of slip can be specified locally, such that the relationship between slip length and curvature can be included.

It would also need to be quick to converge to a meaningful result and be able to deal with large complex geometries made up of 10s to 100s of individual pores.

Table 2.3 lists some of the main continuum modelling techniques along with a short summary of their advantages, disadvantages, and applications. This table is used in selecting a technique that matches closest the requirements given above. Details of the chosen technique, as well as the implementation and verification, are given in chapter 6.

Table 2.3: Comparison of continuum scale modelling techniques.

Modelling technique	Description	Advantages	Disadvantages	Applications
Lattice Boltzmann Methods (LBM)	A kinetic approach to CFD, which involves solving the discrete Boltzmann transport equation. Instead of numerically solving conservation equations involving complex partial differential equations, LBM models the fluid element as a system composed of virtual particles moving on a discrete lattice mesh. Each element has a set of distribution functions which represent the probability of finding a particle with a particular position and momentum.	Easy to implement complex boundary conditions, including moving boundaries such as in the case of a suspension of solids. Scales well on massively parallel architectures, including GPUs. Multiphase flow is easily implemented. Works well for non-Newtonian flows.	Numerical instability occurs when the flow rate approaches the speed of sound, such as in aerodynamic applications. Square mesh is used, so unable to increase accuracy in specific areas without increasing the mesh density everywhere. Relatively unproven in comparison to Navier-Stokes solvers, due to being currently less adopted. Some versions are unreliable for problems involving compressibility.	Works well in most problems which Navier-Stokes solvers are used for. Additionally, works especially well for multiphase and multicomponent flows. Complex porous systems, such as in micro-scale reservoir flow calculations.

Finite Difference Method (FDM)	Domain is discretized into a Cartesian grid and the partial differential equations are approximated using 1st or 2nd order truncated Taylor expansions. The error of this approximation is then either $O(\Delta x^2)$ or $O(\Delta x)$. Solutions are found only at grid points.	Easy to implement. Functions can be made higher order easily. Easy to implement efficiently for geometries which align with the grid. Easy to segment the regular shaped grid for parallel computing	Runs into problems when curved boundaries are involved. Difficult to adapt the simulation mesh. Generally families of mesh lines are parallel to each other and only intercept other families once, i.e. a parallelepiped mesh.	Used in relatively easy problems which involve simple or complex geometries.
Finite Element Analysis (FEA)	Just like in FDM the domain is discretized, however now the domain can be divided into triangular or rectangular grid segments.	Works well in problems where the domain changes, since the mesh can change with the shape of the domain. Also useful in situations where the required precision changes across the domain. Curved and complex geometries are handled naturally. Functions can be made higher order easily.	Requires advanced mathematical expertise to implement, thus it is harder to implement than FDM or FVM. Boundary conditions can be difficult to formulate. Usually more computationally taxing in comparison to FDM or FVM.	Used in a range of CFD applications, which require a higher order of approximation than FVM, with efficient and accurate results.

Finite Volume Methods (FVM)	Unlike in FDM, here the conservation equations are solved in integral form (as opposed to differential form), such that they can be solved for a finite volume rather than point. Here fluxes of conserved variables into and out of the volume are calculated. Variables are generally placed at the centres of cells rather than at nodes.	Like FEA, FVM does not require a structured grid. Similarly, the mesh can be refined at key points in the domain, for higher accuracy. Curved and complex geometries are handled naturally. Conserves mass rigorously, unlike in FDM.	Unlike FEA, in FVM the functions cannot be made higher order easily.	Used in a range of CFD applications with efficient and accurate results. Works better than FVM for convection-dominated PDEs.
Spectral Methods	Considers entire domain for approximating partial differential equations, not just the two adjacent points and the point itself. Uses fast Fourier transforms to solve the resulting equations.	Extremely high accuracy, effectively infinite order accuracy. Uses global functions as opposed to local functions. More computationally efficient than FDM once implemented for a given domain. Able to handle coarser grids than FDM.	Difficult to implement. There is a loss of accuracy for complicated domains. Doesn't work well when shock is involved.	The methods fit well to global weather modelling and homogeneous turbulence problems. Can be used for similar applications to the above methods, as long as the domain isn't complicated. Works well for long time simulations and where quantities vary a lot over space or time.

2.3.4 Lattice Boltzmann method

Finite Volume Method (FVM) is a good all-round performer, which is easy to implement and mass is rigorously conserved. In addition curved and complicated geometries, such as those to be studied herein, present no problems for this method.

Nonetheless, the Lattice Boltzmann Method (LBM) has been chosen for this work. The reason for this is partially due to the existing code available for adaptation, already implemented for GPU computing. The GPU implementation of LBM is much faster than its CPU counterpart, whilst a GPU costs a fraction of the price of a computing cluster. The GPU implementation used in this study was developed by Gray and Boek (2016) and can be run on almost any personal computer with a GPU. Using high end GPUs result in extremely fast calculations. Boek et al. (2014) performed a single phase flow field and permeability calculation on a 700x700x1400 mesh porous rock sample micro-CT image on two computing systems. They compared the calculation, using two similar codes each developed within the group, on a high-end dual CPU system with a 4-GPU workstation. The latter was 97% faster, converging in only 10 minutes as opposed to 6 hours.

The existing CPU code is able to run multiphase simulations, which is a key requirement for further work involving the study of adsorption in engine deposits and similar systems.

In addition to the ease of availability of the LBM code and its high computational performance, LBM was chosen for it's ease of editing boundary conditions. The default behaviour in LBM is to use a "bounce-back" boundary condition for fluids in contact with solid surfaces. In this way, the distribution of virtual particles moving into the solid surface at any time-step is added to the distribution in the opposite direction on the same node at the next time-step. This results in a no-slip condition at the interface, where the fluid velocity is zero.

Two methods are studied here. The first being a combination of specular reflection and bounce-back. The second method involves applying a velocity directly to the fluid in contact with the surface that is proportional to the shear rate at the surface. This way the slip length is maintained constant through this varying velocity boundary condition, since it is equal to $u/\left(\mathrm{d}u/\mathrm{d}x\right)$.

An in depth discussion into LBM, as well as some insight into the mathematical workings of the model, is given in chapter 6.

2.3.5 Hybrid models

There have been several attempts at creating hybrid models between MD and CFD. O'Connell and Thompson (1995) developed one of the first MD-Continuum hybrid models, which used MD at interfaces, within 5 nm, and a finite difference method in the bulk regions. The Navier-Stokes equation solved in the finite difference approximation was a simplification for unidirectional flow and no pressure gradients or driving force. The model included an overlap region between MD and the continuum model in order to achieve continuity of stress and a consistent velocity field. This is achieved by relaxing, through constraint dynamics, the average momentum of particles in the overlap region to that of the corresponding continuum fluid element. The velocity boundary condition for the continuum model is found by averaging over the velocity components of the MD particles in the vicinity of the interface. The outermost MD particles within the overlap region have a constant external field applied, in order to spatially terminate the MD domain and to fix the density in this region. They found that for Couette flow test case the results matched well with both the MD and Navier-Stokes solutions. This method is limited to cases where there is no mass or energy exchange across the hybrid interface.

The issue with this method is that it still requires a relatively computationally expensive MD simulation within 5-10 nm of a solid surface, including the overlap

region. The pore sizes of intake-valve deposits are circa 1-4 nm, so this method would not be applicable in this case. Additionally, the objective of this work is to be able to model a large complex porous geometry, which even with larger pores would still be impractical with this method. This method also does not extend the time simulated beyond the level of MD, which would be nanoseconds.

More recently Smith et al. (2012) developed a control volume representation of molecular dynamics, in which the formulas of Irving and Kirkwood (1950) are integrated over a finite cubic volume of molecular dimensions. The final appearance of which has the same form as Reynolds' transport theorem applied to a discrete system. An advantage of this method is that it ensures conservation laws are satisfied.

2.4 Slip

2.4.1 Definition

Considering a fluid flowing over a solid surface, the no-slip boundary condition states that the tangential component of the fluid velocity equals that of the solid at the surface (Thompson and Robbins 1989). This condition can be used in the Navier-Stokes equations, for instance in channel flow, in order to develop a Poiseuille flow profile. This is an essential part of understanding continuum flow at the macroscopic scale, however at the nanoscale, where the Knudsen number is particularly large in many cases, an unexpected phenomenon occurs. It turns out that for low density fluids flowing in nanopores, the tangential velocity at a stationary solid surface is not always zero. This effect is enhanced when the walls of a nanopore are atomistically smooth, and can be present even for liquids. In order to quantify this "slip" a new parameter is defined, the "slip-length". This slip-length, b, and its influence on the velocity profile and the fluid velocity at

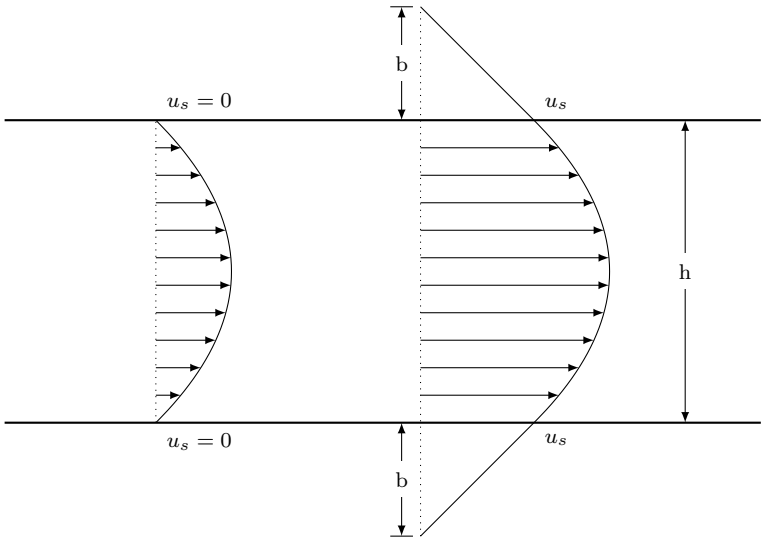


Figure 2.2: Left: Poiseuille flow profile with no-slip. Right: Poiseuille flow profile with slip.

the surface, u_s, is shown in figure 2.2 for a channel of height h.

The Knudsen number is a dimensionless parameter defined as the ratio of the mean free path, l to a characteristic length scale H:

$$Kn = \frac{l}{H}. \tag{2.1}$$

In most cases discussed here, the characteristic length scale is the width of a slit pore containing fluid. The value of the Knudsen number dictates what sort of flow should be considered. Roy et al. (2003) describe the different regimes of fluid flow depending on the Knudsen number and are as follows: Continuum flow ($0 > Kn < 10^{-3}$), slip flow ($10^{-3} < Kn < 10^{-1}$), transition flow ($10^{-1} < Kn < 10^{1}$) and free-molecule flow ($10^{1} < Kn$).

2.4.2 Literature review

There have been extensive works employing MD simulations to study slip; a selected sample include the following studies: Koplik et al. (1989), Barrat and Bocquet (1999), Cieplak et al. (2001), Galea and Attard (2004), Sokhan et al.

(2001), Sokhan et al. (2002), Kannam et al. (2013), and Hansen et al. (2011).

Koplik et al. (1989) performed molecular dynamics simulations of flow of a simple Lennard-Jones fluid confined between two solid walls with molecular structure. An acceleration was applied in a direction parallel to the walls, forcing the fluid to flow in one dimension. The aim was to investigate the appearance of a slip length, which was found at low fluid densities. The slip length was extracted from simulations by extrapolating a parabolic fit of velocity and stress to the wall. The Maxwell definition of slip length, ζ, was used:

$$b = u/\frac{\partial u}{\partial z} \tag{2.2}$$

where u is the average tangential velocity at the surface between the wall and fluid and $\partial u/\partial z$ is the shear rate at the wall.

An obvious problem with this equation is where exactly is the surface located; This problem is more evident on the nanoscale, where the size of the molecules are relatively large when compared to the system size. Koplik defined the surface location as being the centre of the inner wall layer, but other definitions may be of more use. In this work the location of the surface is consistently defined as the point $\sigma_{sf}/2$ away from the centre of the innermost wall particles. This is of course a fairly arbitrary choice of location and other possible ways of defining the surface exist. For instance, Barrat and Bocquet (1999) use the hydrodynamic surface whilst some choose to define the surface as the point half way between adjacent solid and fluid peaks in the density profile.

It is important when transferring parameters such as slip length to Lattice Boltzmann simulations later on that the location of the surface is defined in the same way as when the parameters were calculated. Figure 2.3 shows some possible surface location definitions.

In addition to Poiseuille flow, Koplik et al. (1989) also simulated Couette flow

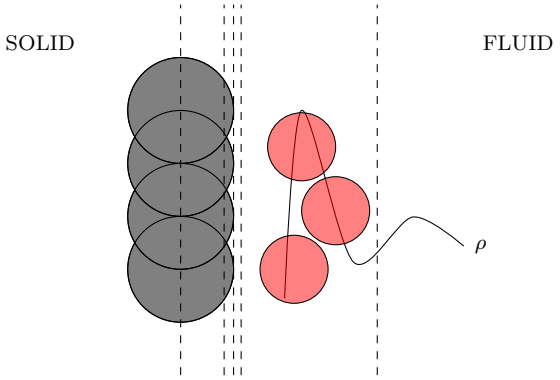


Figure 2.3: Possible definitions of surface location. Solid and fluid atoms are the large and small circles respectively. The surfaces are indicated by dashed lines as follows (left to right): Centre of solid-surface atoms; Solid-fluid minimum in Lennard-Jones potential; Solid-solid minimum in Lennard-Jones potential; Midpoint between solid and fluid peaks in density profile (ρ); Hydrodynamic boundary.

for the same system. This time instead of applying an acceleration to the fluid particles, the two walls are given opposing constant velocities. The slip length is calculated in the same way as for Poiseuille flow and the results matched with the Poiseuille flow case. Although some of the methods used have been since improved upon, this paper remains a good reference for slip flow and a flow-independent slip-length boundary condition.

Some main conclusions drawn from the work of Koplik et al. (1989) are that the slip length increases as the fluid density drops and that the same slip length is found for both Poiseuille and Couette flow, which points towards the slip length being a material property.

The manuscript also looked at the dynamics of the moving contact lines between immiscible fluids when an acceleration is applied to the fluids. The interactions between fluids were varied through use of adjustable “pseudocharges”, which prevented mixing between the phases. The conclusion found was that a breakdown of the no-slip condition, even for dense fluids, occurs in the case of a moving contact line. Their reasoning for this observation is that each fluid is individually attracted to the wall, but with high shear rates the natural adherence is

overcome. A compromise is reached between some slip and high but finite shear.

Barrat and Bocquet (1999) used molecular dynamics simulations to investigate the effect of wettability on the slip length. This was done by varying a fluid-substrate interaction coefficient which is multiplied by the attractive long range term of a 12-6 Lennard-Jones type potential. The coefficient was varied between 0.5 and 1, in effect using a smaller attractive term than the usual Lennard-Jones interactions. Typically their simulations used solid slabs with separation $h = 18\sigma$ and 10,000 atoms; the dimensions in x and y were $L_x = L_y = 20\sigma$. They found that slip lengths exceeded 30 molecular diameters for a contact angle of 140°, corresponding to very low wettability, or non-wetting, and an interaction coefficient of 0.5. This wettability is comparable with mercury on glass. In all cases tested the slip length was no less than 1 molecular diameter, which corresponds to a flow enhancement of approximately 1.5 in comparison with a no-slip case in a tube. Similarly, for the highly non-wetting case, the flow enhancement is 14. The flow enhancement, E, is calculated from the following equation for a cylinder:

$$E = \frac{Q_{slip}}{Q_{no-slip}} = \left(1 + \frac{8b}{D}\right) \tag{2.3}$$

where Q_{slip} is the observed flow rate and $Q_{no-slip}$ is the expected flow rate without slip. D is the diameter of the cylinder.

Cieplak et al. (2001) performed a similar study to Barrat and found that the slip length is independent of the channel width and the nature of the flow. Like Barrat, they also showed that even high density fluid exhibits appreciable slip upon weakening wall-fluid traction. Finally they found that the slip at low density is strongly linked to the fluid organisation in the vicinity of the walls, governed by the fluid-solid interactions. Their interactions were modelled in a similar way to Barrat. Both studies found that the slip length increased with decreased interaction parameter, decreased density, and decreased pressure.

Galea and Attard (2004) studied the effect of atomic roughness on the slip length during shear flow. The fluid properties and interaction parameters were kept constant whilst the sizes and spacing of the solid surface atoms were varied, maintaining constant packing fraction. They performed simulations of a confined Lennard-Jones fluid in Couette flow. The important conclusion is that the boundary fluid exhibits zero velocity for commensurate structures and that the slip length can increase with roughness, contrary to intuition.

Sokhan et al. (2002) performed simulations of Poiseuille flow in cylindrical carbon nanopores; extending from their previous study of slit carbon nanopores (Sokhan et al. 2001). They found a large slip length in both the cylindrical and slit pores when considering simple fluids.

Ho et al. (2011) presented simulation results which confirmed the presence of liquid water slip on even hydrophilic surfaces. They theorised that the distribution of water molecules within the contact layer at equilibrium is responsible for this. When preferential adsorption sites exist that are sufficiently close to each other, water migration from one to the next can occur without requiring hopping events and hydrodynamic liquid slip occurs.

The authors also suggested that hydrophilic nanoporous membranes could be designed which permit atomic-scale sliding of contact water molecules via the inclusion of a sufficient amount of preferential adsorption sites. Possible ways of achieving this could be via atomic-scale etching, molecular grafting, or by integrating nanoparticles on the surface.

Chen et al. (2014) calculated the slip dependence on curvature directly by measuring the velocity profile of fluid surrounding rotating cylinders, fitting it to the Navier-Stokes equation, and extrapolating to get a slip length. They used a simple, single atom, Lennard-Jones fluid. They found that the slip length at a flat wall, given the same atomic interactions, is the same as for all other cases, including curved and rotating boundaries.

Kannam et al. (2013) discussed the issues of using non-equilibrium molecular dynamics methods for calculation of the slip length and develop a method for calculating the slip length via equilibrium MD. They observe in the literature that data for slip of water is scattered over 5 orders of magnitude for nanotubes of diameter 0.81-10 nm. In this case a parabolic flow profile fit only works for channels above 5 nm in diameter. Their equilibrium MD method involves determining the friction coefficient, λ and then using the following relation to calculate the slip length from the ratio of the shear viscosity, μ, to λ:

$$b = \frac{\mu}{\lambda}. \tag{2.4}$$

Kannam et al. (2017) highlighted some of the challenges with modelling fluid flow and slip of water in CNTs. Specifically the authors refer to the scattering of results in the literature of over 2-5 orders of magnitude for measured flow rates in both experiments and simulations.

The authors point out that the flow velocity profiles taken from the literature have very small fluid velocity gradients, which makes the slip length extraction difficult and unreliable. In NEMD studies, the range of velocities observed between the centre and surface of the CNTs is less than the statistical errors obtained in the velocity profiles. As such, it is difficult to calculate the fluid viscosity and as such confirm whether or not the fluid viscosity remains the same as in the bulk. The authors continue to note that literature values for pore-radius-dependent effective viscosity are scattered over two orders of magnitude.

They also discuss further issues with NEMD methods of calculating the slip length, including limited simulation time, necessity for high external fields, and possible intrinsic limitations MD. Further, they mention other challenges such as choosing molecular potential energy functions, handling of electrostatic forces, ambiguity of tube diameter definition, tube entrance and exit effects, confined

fluid density effects, direct thermostatting of confined fluid, and plug-like flow making slip length extrapolation difficult. This reference is also a good general review of literature surrounding slip of water in carbon nanotubes.

Knowing the shear viscosity from standard techniques, one only requires finding the friction coefficient; a method for this is described by Hansen et al. (2011). In brief, the method involves calculating the centre of mass velocity autocorrelation function for a slab of fluid within one molecular diameter of the wall, $C_{uu}(t) = \langle u_{slab}(0)u_{slab}(t)\rangle$. The slab velocity-force cross correlation function is also calculated,$C_{uF_z}(t) = \langle u_{slab}(0)F_z(t)\rangle$, and then the friction coefficient is found by solving the following equation in Laplace space:

$$\widetilde{C}_{uF_z}(s) = -\widetilde{\lambda}(s)\widetilde{C}_{uu}(s). \tag{2.5}$$

The resulting friction coefficient is highly dependent on the choice of slab thickness and different trials must be conducted before finding an appropriate value. They also found that for channels with a width smaller than 7σ, approximately 2.4 nm for $\sigma = 0.34$ nm, the friction coefficient was channel-width dependent.

Ramos-Alvarado et al. (2016) reported that the implementation of this method is problematic for water and requires a large number of simulations to achieve a reliable value of the friction coefficient. Due to this, and coupled with the long post-processing time, low reliability of the results, and low consistency, this method is disregarded as a potential method for calculating the friction coefficient in this work.

Ramos-Alvarado et al. (2016) also performed a comparison of three other equilibrium methods; The Bocquet and Barrat (2013), Petravic and Harrowell (2007), and Huang and Szlufarska (2014) methods. In all cases the SPC/E water model was used in conjunction with a surface consisting of three graphene layers on each side of the fluid resulting in a slit pore. The length and width of the channel was

kept constant at $L = 6.39$ nm and $W = 6.39$ nm whilst the channel height was varied between $H = 3 - 8$ nm. Simulations were performed at 300 K for a total time of 1 ns.

They found that the methods by Bocquet and Barrat (2013) and Petravic and Harrowell (2007) are hindered by the noisiness involved in the evaluation of the force time-correlation function, whilst the method of Huang and Szlufarska (2014) provided smoother calculations. All three methods were found to have significant advantages over other methods including shorter post-processing times and more consistent results. The method of Bocquet and Barrat (2013) is the method of choice for the calculations in chapter 5.

Petravic and Harrowell (2007) pointed out issues with the Bocquet and Barrat (2013) method of calculating the friction coefficient and presented an alternative equilibrium theory of the friction associated with the confined fluid and showed how this is related to the intrinsic interfacial friction. They showed that for an amorphous liquid-like wall the friction coefficient, calculated using Bocquet and Barrat method, was no longer constant with separation in the slab case even though NEMD calculations show otherwise. Amorphous surfaces are not testing in the current work and as such no comment can be made on the applicability of this method in those cases.

Falk et al. (2010) used this method for investigating fast water transport in carbon nanotubes. They found a strong curvature dependence of the friction coefficient, with extremely low friction in the smallest tubes.

The same curvature dependence of the friction coefficient has been found for systems involving decane, ethanol and octamethylcyclotetrasiloxane (Falk et al. 2012). One exception is in the case of decane, which shows a significant reduction in the friction coefficient for small slab separations. This is due to the strong layering of decane at the solid surface. These layers influence each other and form stable domains which impact the decane structure at the surface and thus

the decane/graphene commensurability. In the cylindrical cases, the stiff chain structure of the decane molecules results in an orientation that is preferentially parallel to the cylindrical walls. This orientation becomes less preferential as the radius of curvature increases. This is also in agreement with works from Supple and Quirke (2005). The works cited above suggest that the simple functional relationship between friction coefficient and radius of curvature shown here is not applicable for more complicated molecules. Although, it may be appropriate for simulating systems where most surfaces have some curvature, or for relatively large surface separations (> 6 nm).

Michaelides (2016) developed an experimental technique to measure water flow through carbon nanotubes. Flow measurements in boron nitride, a material that forms nanotubes with a similar atomic structure to that of carbon, nanotubes were also made. The method involves two reservoirs of water separated by a water-tight membrane pierced by an individual nanotube. The pressure is raised on one reservoir and the flow rate is measured by monitoring how jets of water emerging from the nanotube displaced polystyrene nano-particles suspended in the low-pressure water reservoir. Flow rates were typically 1 femtolitre per second. They found that the narrower the tube, the less friction there is. However, for the boron nitride nanotubes, the friction was much higher than in the carbon nanotubes even with their similar structures.

Srivastava et al. (2011) compared the structure of water in graphite and mica slit pores and found that in the former case the first fluid layer is more like a two-dimensional liquid. In the mica pores, the fluid in the first layer is orientationally ordered to a limited degree in a hexatic phase.

In order to discuss the relevant literature based around the lattice Boltzmann method, an introduction to the method and some background is first needed. The literature review for this larger scale simulation technique can be found in chapter 6, in section 6.2.

Chapter 3

Models for molecular simulations

3.1 Introduction

The fluid models used for MD simulations are defined and discussed in this chapter. First the MD package is introduced, and the choice of specific algorithms is justified. This is followed by specification of the fluid and solid interaction parameters. Finally, the choice of surface structure is explained, along with how system pressure is maintained for heterogeneous systems, such as during adsorption and equilibration simulations.

A full list of simulation options and interaction parameters, along with links to input/output files for this work, can be found in Appendix A.

3.2 GROMACS

In this section the molecular dynamics algorithm is introduced and somewhat briefly explained for context when fluid/solid model specifications presented.

3.2.1 Version and generalities

The MD code used in this study is a pre-existing software package known as GROMACS (Hess et al. 2008), which is available under the GNU Lesser General Public License version 2.1. It was originally developed in the Department of Biophysical Chemistry, University of Groningen, in 1991. Since 2001, the code has been maintained by the GROMACS development teams at the Royal Institute of Technology and Uppsala University. The core development is currently undertaken by David van der Spoel, Erik Lindahl and Berk Hess. The version used here is version 4.6.5, with Intel MPI version 5.1 for parallel computing, and without GPU acceleration.

The GROMACS package includes the means to perform molecular dynamics simulations and energy minimisation. It also includes systems for post processing of results to obtain parameters of common interest. A full list of contributors as well as more detail of the workings of the GROMACS package can be found in the GROMACS manual, available online (Spoel et al. 2013). The GROMACS manual also includes many methods that are not described here, as only the fundamentals and methods applicable to this study have been described.

3.2.2 Non-bonded interactions

Lennard-Jones potential.

In order to calculate the force on any atom an equation for the potential is needed. There are several models for the potential between two non-bonded particles, most of which factor in a repulsion term, a dispersion term (attractive term), and a Coulomb term. The repulsion and dispersion terms are usually combined together in what is known as the van der Waals forces. These are generally expressed analytically as either a Lennard-Jones 12-6 potential or a Buckingham

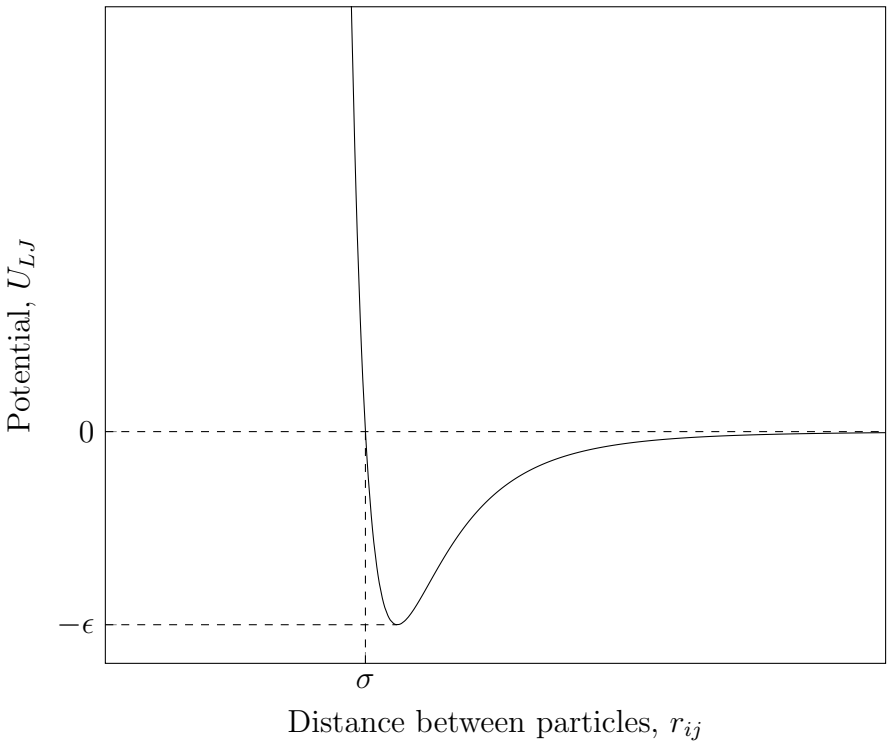


Figure 3.1: Lennard-Jones potential.

exp-6 potential. The most commonly used is the Lennard-Jones potential, the form of which is shown in equation 3.1 and figure 3.1, where in regions of negative gradient the interactions are repulsive and in regions of positive gradient the interactions are attractive.

$$U_{LJ} = 4\epsilon \left[\left(\frac{\sigma}{r_{ij}} \right)^{12} - \left(\frac{\sigma}{r_{ij}} \right)^{6} \right] \tag{3.1}$$

Here ϵ is the potential well depth, σ is the distance at which the potential is zero and r_{ij} is the distance between neighbouring particles. Given σ, the distance at which the potential is minimum is $r_m = 2^{1/6}\sigma$. The Buckingham potential has a more realistic repulsion term, but is more computationally expensive.

As seen in figure 3.1, the LJ potential tails off to zero at a relatively short distance of a few molecular diameters. In order to reduce computational time a cut-off distance, beyond which the potential is taken to be zero, is usually implemented. An additional correction is used in order to account for forces beyond this cut-off.

Forces beyond the cut-off are always attractive and as such without a dispersion correction term the pressure would be underestimated.

For Lennard-Jones interactions, and in most potential models, two parameters σ and ϵ are required. These can be specified for every interacting pair or calculated from the same species interaction parameters. This is done using the Lorentz-Bethelot rules, where σ_{ij} is calculated using an arithmetic average and ϵ_{ij} using a geometric average:

$$\sigma_{ij} = \frac{1}{2}(\sigma_{ii} + \sigma_{jj}) \tag{3.2}$$

$$\epsilon_{ij} = \sqrt{\epsilon_{ii}\epsilon_{jj}} \tag{3.3}$$

3.2.3 Periodic boundary conditions

In order to counter surface effects periodic boundary conditions are implemented, such that any atom crossing one of the system boundaries re-enters at the opposite boundary. A simple way to represent this is that all atoms in the system cell are replicated in all dimensions and infinite number of times, as shown in figure 3.2. In this way, an effectively infinite system is modelled without requiring infinite computation power.

The easiest shape to imagine for a unit cell of a periodic box is a cube. However, other shapes can be used which may be more efficient. For instance, simulations involving the cylindrical pores described later in this chapter use a parallelepipeds where $\alpha = \beta = 90°$ and $\gamma = 120°$. This results in a 13% volume saving (and thus computational saving) for the same minimum image distance compared to a simple cuboid unit cell. This shape can also be thought of as a hexagonal based prism. For bulk fluid simulations a rhombic dodecahedral unit cell can be used and has a volume saving of 29%. However, since computation time is generally

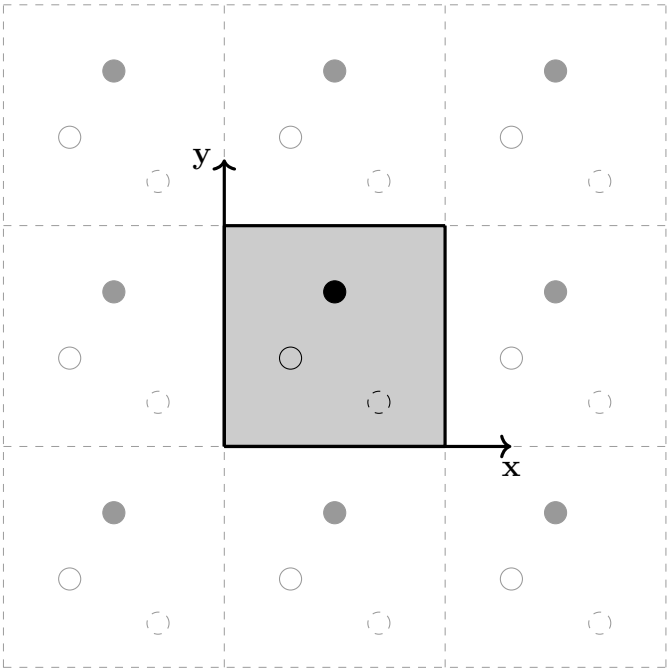


Figure 3.2: Periodic system representation in two dimensions.

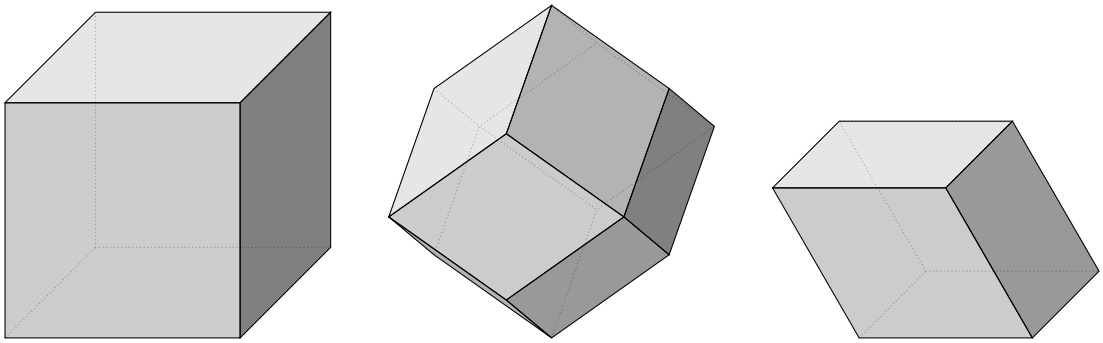


Figure 3.3: Common periodic unit cells, from left to right: Cubic, rhombic dodecahedral and parallelepiped.

not an issue for bulk fluid simulations a simple cubic box is used herein. These common box sizes are shown in figure 3.3.

The minimum size of a simulation cell is set by the minimum-image convention. This means that the distance between a pair of periodic boundaries must be larger than two times the cut-off radius for interactions, such that no atom can interact twice directly with different images of the same atom. In the case of large molecules this should be extended such that no part of a single molecule can interact with multiple images of another molecule. Additionally, the simulation

cell should be larger than the characteristic length scale of the features of interest within the system.

Coulomb interactions

Coulomb interactions are long-range electrostatic interactions between non-bonding pairs due to charges. The coulomb potential for point charges, $U_c(r_{ij})$, is given by:

$$U_c(r_{ij}) = \frac{1}{4\pi\epsilon_0}\frac{q_i q_j}{\epsilon_r r_{ij}} \tag{3.4}$$

where ϵ_0 is the permittivity of free space, ϵ_r is the relative dielectric constant and is equal to 1, q_i and q_j are the electric charges of two interacting point charges.

These interactions are of very long range, typically spanning far beyond the simulation cell. A proper accounting of these interactions requires sums over all adjacent periodic images. In the case of a cell with an index vector of $\boldsymbol{n} = (n_x, n_y, n_z)$, the total electrostatic energy of N particles is given by this slowly converging sum:

$$U_c = \frac{1}{8\pi\epsilon_0}\sum_{n_x}\sum_{n_y}\sum_{n_z}\sum_{i}^{N}\sum_{j}^{N}\frac{q_i q_j}{\boldsymbol{r}_{ij,\boldsymbol{n}}} \tag{3.5}$$

where the $i = j$ terms should be omitted in the origin cell only.

In all cases discussed in these works, the Particle-mesh Ewald (PME) method (Di Pierro et al. 2015) is used for the calculation of electrostatic interactions. In the Ewald summation method the slow-converging interaction potential sum is split into quick-converging direct and reciprocal terms and a constant term. The direct term represents the short-range interactions whilst the reciprocal term represents the long-range interactions.

PME is an improved performance version of Ewald summation, where the reciprocal sum is calculated by assigning charges to a grid and then Fourier transforming this and summing over the grid in k-space. The advantage of this is that the algorithm scales with $NlogN$ as opposed to N^2 with regular Ewald summation.

More details of both Ewald summation and PME can be found in the gromacs manual (Spoel et al. 2013).

Long-range VDW interactions

Van der Waals interactions are small, but not zero, beyond the cut-off. Due to this, energies and pressures will always be underestimated since the cut-off is large enough such that all repulsive forces are encompassed and only attractive forces are omitted. To counter this, long-range corrections to the dispersion term are required, as shown in equation 3.6.

$$U_{lr} = \frac{N^2}{2V} \int_0^\infty 4\pi r^2 g\left(r\right) \left(U\left(r\right) - U_{cut}\left(r\right)\right) \mathrm{d}r \tag{3.6}$$

Here U_{lr} is the long-range contribution to the potential, U_{cut} is the potential with a cut-off applied, N is the number of particles, V is the system volume and $g\left(r\right)$ is the radial distribution function. If $g(r)$ is assumed to be 1 beyond the cut-off, equation 3.6 reduces to:

$$U_{lr} = -\frac{8\pi N^2 \epsilon \sigma^6 r_c^{-3}}{3V}. \tag{3.7}$$

This correction is only applied in situations where the system is homogeneous, such as for density and viscosity calculations. For many of the systems explored within this study this is not the case.

In general, when it is obvious that the system is not homogeneous this correction

has not been used, for example the adsorption and slip calculations. In some cases, the cut-off has been increased in order to minimise the effect of these missing long-range interactions on the properties of interest, such as for vapour-liquid equilibrium calculations of water. The same calculation has been performed for n-heptane using a Particle-Mesh Ewald method described below. The reasons for these choices are given in section 4.3.2.

In later versions of GROMACS, namely version 5.0.0 onwards, the Lennard-Jones Particle-Mesh Ewald (LJ-PME) (Wennberg et al. 2013) method has been introduced for handling long-range van der Waals interactions. This works in a similar way to the long-range coulomb interactions calculations described above. This has not been used in these works, unless stated otherwise, due to a lack of prevalence of this version at the time of these works.

3.2.4 Bonded interactions

Bonded interactions are between atoms that are in the same molecule and are of the four categories: Bond stretching (2-body), bond angle (3-body), and dihedral angle (4-body).

Bond stretching

Bond stretching is handled using a harmonic potential:

$$U_b(r_{ij}) = \frac{1}{2} k_{ij}^b \left(r_{ij} - b_{ij}\right)^2 \tag{3.8}$$

where k_{ij}^b is the force constant between the two bonded atoms i and j and b_{ij} is the specified bond length.

Bond bending

Bond angles are dealt with using a harmonic angle potential:

$$U_a(\theta_{ijk}) = \frac{1}{2}k^{\theta}_{ijk}(\theta_{ijk} - \theta^0_{ijk})^2 \tag{3.9}$$

where k^{θ}_{ijk} is the force constant on the angle between three atoms i, j and k and θ^0_{ijk} is the specified bond angle.

Bond twisting

The dihedral angle defines the angle between planes of two bonds. It is a 4-body interaction and as such is only applicable for molecules that have at least 4 atoms bonded in series. Here the Ryckaert-Bellemans function, see figure 3.4, is used for calculating the proper dihedral potential, $U_{rb}(\phi_{ijkl})$:

$$U_{rb}(\phi_{ijkl}) = \sum_{n=0}^{5} C_n \left(cos\left(\phi_{ijkl} - 180\right)\right)^n \tag{3.10}$$

where ϕ_{ijkl} is the angle between planes formed by the bonded atoms ijk and jkl.

3.2.5 Forces calculation

The force on any atom, $\boldsymbol{F}_i$, is the sum of the forces between non-bonded atom pairs plus the forces due to bonded interactions. The forces are found from the derivative of the potential with respect to position:

$$\boldsymbol{F}_i = -\frac{\partial U}{\partial \boldsymbol{r}_i}. \tag{3.11}$$

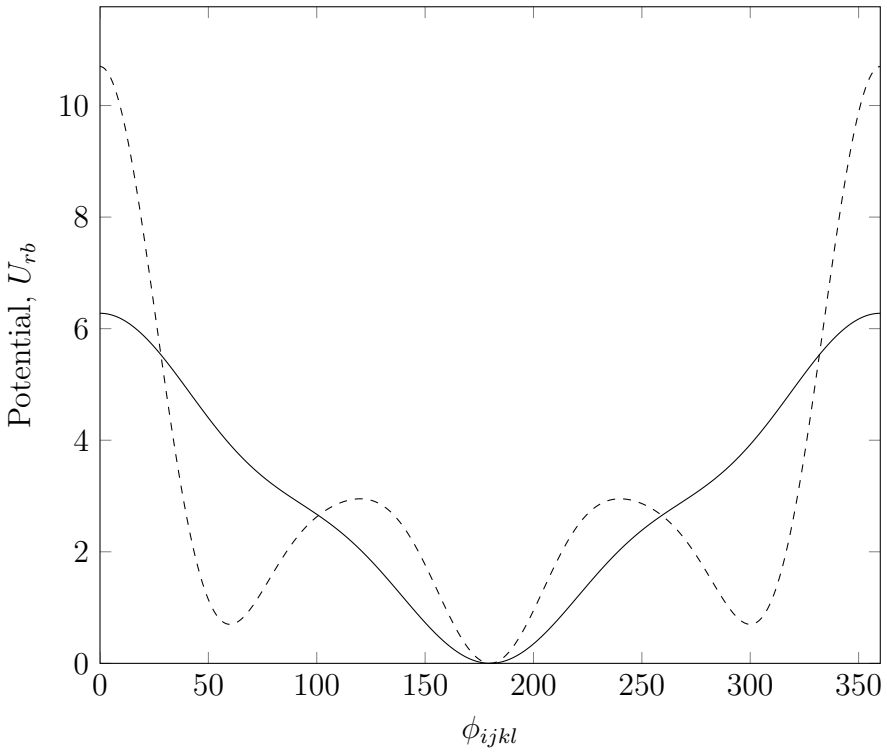


Figure 3.4: Ryckaert-Bellemans dihedral potential. Dashed: general shape. Solid: specifically 4-carbon dihedral in n-heptane

Once all the forces are known, the configuration can be updated by calculating the movement of atoms by numerically solving Newton's equations of motion:

$$\frac{\mathrm{d}^2\boldsymbol{r}_i}{\mathrm{d}t^2} = \frac{\mathrm{d}\boldsymbol{v}_i}{\mathrm{d}t} = \frac{\boldsymbol{F}_i}{m_i}. \tag{3.12}$$

3.2.6 Integration

The MD algorithm works by solving the equations of motion at discrete time intervals, as such an appropriate method of integrating equation 3.12 is required. For this, the leap-frog integrator is used. The velocity Verlet algorithm (Verlet 1967) provides more accurate integration with temperature and/or pressure coupling at the cost of computing time (as twice as many communications are made), however in these works only the leap-frog integrator is used. Both the Verlet and leap-frog methods produce identical trajectories in the absence of temperature and/or pressure coupling.

The leap-frog algorithm uses the positions $\boldsymbol{r}$ at time t to calculate the forces $\boldsymbol{F}(t)$ and velocities $\boldsymbol{v}$ are calculated at time $t - \frac{1}{2}\Delta t$ for use in the following relations:

$$\boldsymbol{v}(t + \frac{1}{2}\Delta t) = \boldsymbol{v}(t - \frac{1}{2}\Delta t) + \frac{\Delta t}{m}\boldsymbol{F}(t) \tag{3.13}$$

$$\boldsymbol{r}(t + \Delta t) = \boldsymbol{r}(t) + \Delta t \boldsymbol{v}(t + \frac{1}{2}\Delta t) \tag{3.14}$$

3.2.7 Ensembles

The simulation can be in one of many ensembles which are defined by specifying three macroscopic parameters that are to be kept constant. An example is the isothermal-isobaric ensemble, NPT, where N stands for constant number of particles, P is constant pressure and T is constant temperature. Another common ensemble for extracting results after equilibration is the canonical ensemble, NVT, where V means the volume is kept constant instead of the pressure. Similarly, instead of constant temperature a microcanonical ensemble, NVE, has constant energy.

The methods of maintaining isobaric and isothermal conditions are described in sections 3.2.9 and 3.2.10 respectively.

3.2.8 Energy minimisation

The first step of any simulation (after specification of molecule topologies, coordinates, and velocities) is energy minimisation. In this, the arrangement of particles are varied in order to minimise the total energy of the system. The reason for this is to avoid the simulation "blowing-up" due to excessively large forces resulting from a starting configuration very far from equilibrium.

Algorithms used for energy minimisation include the method of steepest decent

and the conjugate gradient method. The first method is fast converging to a point close to the local minimum, whilst the latter is faster at reaching much closer to the local minimum, but performs slower when far away from the minimum. In this study the method of steepest decent is used, as the computational time spent during energy minimisation is negligible in comparison to other stages of the simulation process.

In brief, the method of steepest decent involves systematically moving down the steepest local energy gradient. This is done in steps using the partial derivatives of the potential energy with respect to all coordinates, which is equal to the negative of the forces. The step size is adjusted to increase speed of convergence, however no information from previous steps are used.

3.2.9 Thermostat

Given a system of N atoms, with N_{df} degrees of freedom, the temperature of the system is:

$$T = \frac{2E_{kin}}{kN_{df}} \tag{3.15}$$

where E_{kin} is the total kinetic energy and k is the Boltzmann constant. The total kinetic energy can be found using:

$$E_{kin} = \frac{1}{2}\sum_{i=1}^{N} m_i v_i^2 \tag{3.16}$$

where m_i and v_i are the mass and velocity of atom i. N_{df} is usually $3N - N_c - 3$ when the centre of mass motion is removed, where N_c is the number of constraints present in the system.

Typically the temperature is specified as a constant in most MD simulations,

i.e. either a NVT or NPT ensemble as opposed to NVE. In these cases there are several ways to maintain the system temperature, including velocity scaling methods and stochastic Langevin method.

Velocity-rescaling

For most cases in these works a velocity-rescaling thermostat (Bussi et al. 2007) has been chosen (not to be confused with the strong coupling method by the same name). This is a weak temperature coupling method, in that system variables are relaxed towards the correct value, rather than in a strong coupling method whereby variables are set to give the exact value. In this, all the velocities in the system are rescaled by some factor at each time step. This scaling factor is chosen such that the following is true:

$$\mathrm{d}E_{kin} = \left(\bar{E}_{kin} - E_{kin}\right)\frac{\mathrm{d}t}{\tau} + 2\sqrt{\frac{E_{kin}\bar{E}_{kin}}{N_{df}}}\frac{\mathrm{d}W}{\sqrt{\tau}} \tag{3.17}$$

where E_{kin} is the total kinetic energy, $\bar{E}_{kin}$ is the average kinetic energy at the target temperature, and τ is an arbitrary time constant, chosen to be 0.1 ps. $\mathrm{d}W$ is a Wiener noise using the Itoh convention (Gardiner 1985), the purpose of which is to ensure the correct kinetic energy distribution and thereby the correct canonical ensemble. Without the stochastic term (the second term on the right hand side) equation 3.17 reduces to that of the Berendsen thermostat.

The Nosé-Hoover thermostat (Hoover 1985) is another popular thermostat for equilibrium runs, however that is not used here as the velocity-rescaling method is more efficient at relaxing the system to the target temperature whilst still producing the correct canonical ensemble. The velocity-rescaling thermostat is also shown to be more ergodic than the Nosé-Hoover thermostat (Bussi et al. 2007). Notwithstanding, the choice between these two thermostats has little effect on results, as seen through experience.

Langevin thermostat

In some cases, where a gas is present, the Langevin thermostat has been used. This has been done to avoid accumulation of errors for overall translation of the system, which can occur in most temperature scaling thermostats, especially when the system involves multiple phases in a rapidly changing configuration. More detail on this is given in section 4.3.6.

This method is principally stochastic dynamics as opposed to MD, although with the right parameters it can be considered as MD with stochastic temperature-coupling.

Here a friction term, $m_i\gamma_i$, where γ_i is the collision frequency, and a noise term, $\mathring{\boldsymbol{r}}_i$, is added to Newton's equations of motion, such that:

$$m_i \frac{\mathrm{d}^2 \boldsymbol{r}}{\mathrm{d}t^2} = -m_i\gamma_i \frac{\mathrm{d}\boldsymbol{r}_i}{\mathrm{d}t} + \boldsymbol{F}_i(\boldsymbol{r}) + \mathring{\boldsymbol{r}}_i. \tag{3.18}$$

A value of 0.5 ps^{-1} has been chosen for γ, since this is only used as a thermostat rather than a stochastic dynamics method, which is sufficiently small compared to the time scales present in the system.

3.2.10 Barostat

The pressure tensor is calculated in the following way:

$$\boldsymbol{P} = \frac{2}{V}\left(\frac{1}{2}\sum_i^N m_i \boldsymbol{v}_i \otimes \boldsymbol{v}_i + \frac{1}{2}\sum_{i<j} \boldsymbol{r}_{ij} \otimes \boldsymbol{F}_{ij}\right) \tag{3.19}$$

where the first term within the parenthesis is the kinetic energy tensor and the second term is the negative virial tensor.

Since the pressure is related to the system volume, it can be controlled by varying the box dimensions. In all cases herein this is done isotropically. The pressure can be controlled using Berendsen (Berendsen et al. 1984) or Parrinello-Rahman (Parrinello and Rahman 1981) barostats. Berendsen is the most efficient way to scale the box for pressure coupling, however this does not yield a correct thermodynamic ensemble and is generally only used during equilibration steps when the initial pressure is far from the equilibrium value. In these works the initial box size is chosen to be close to the equilibrium value in all cases and as such Parrinello-Rahman method is used for pressure scaling throughout for simplicity. In this method, no instantaneous scaling takes place. During data collection simulations, involving pressure scaling, this is the method of choice.

3.2.11 Example workflow

The general procedure for performing simulations involves three main steps: Energy minimisation, equilibration and a result run; However more complicated systems require more steps, in these cases more details are given in their respective sections. The minimum requirement before energy minimisation is a set of coordinates for particles in the system and a topology file which describes the interactions between bonded and non-bonded pairs of particles. An index file is generated from the topology and coordinates; This keeps track of the index of groups of particles, which can be assigned with different constraints. Where no velocities already exist, initial velocities are taken from a Maxwell-Boltzmann distribution.

After energy minimisation has finished, the result is a set of coordinates which represent a local minimum in the energy of a system given that the temperature of the system is zero. This new set of coordinates can be used directly in equilibration and result runs.

3.3 Water

3.3.1 Choice of model

Where water has been simulated, the TIP4P (Transferable Intermolecular Potential, 4 Points) model has been used. The reason only a single water model has been used throughout is to maintain consistency between results. This is important for the adsorption and slip results, reported in chapters 4 and 5 respectively, as the filled pore density is taken directly from the adsorption results for use in the friction calculations.

There are a multitude of water models reported in the literature, the main ones being: SPC, SPC/E, TIP3P, TIP4P and its variants. The TIP4P model was chosen for its well roundedness, in that it reproduces the exact liquid density of water at standard conditions (Jorgensen et al. 1983) as well as having closely matching structural properties to experimental values (Zielkiewicz 2012).

The SPC/E model is also a typical water model of choice for its computational efficiency and its accuracy. However, the work of Kiss and Baranyai (2011) showed that the SPC/E model was limited in describing vapour phase properties. In contrast, they found that the TIP4P family of models provided qualitatively correct results in the gas phase. The author also highlighted the SPC/E and TIP3P models' efficacy to form erroneous structures even in the bulk liquid phase, which weaken the reliability of studies involving SPC/E or TIP3P water even in the liquid phase.

Vega and De Miguel (2007) calculated the surface tension of various water models, including the new generation of TIP4P-like models including TIP4P/Ew, TIP4P/Ice, and TIP4P/2005, using a test-area method. They showed that, even though most models do not quantitatively reproduce the correct surface tension of water, the TIP4P/2005 model gave fairly good agreement over the entire range

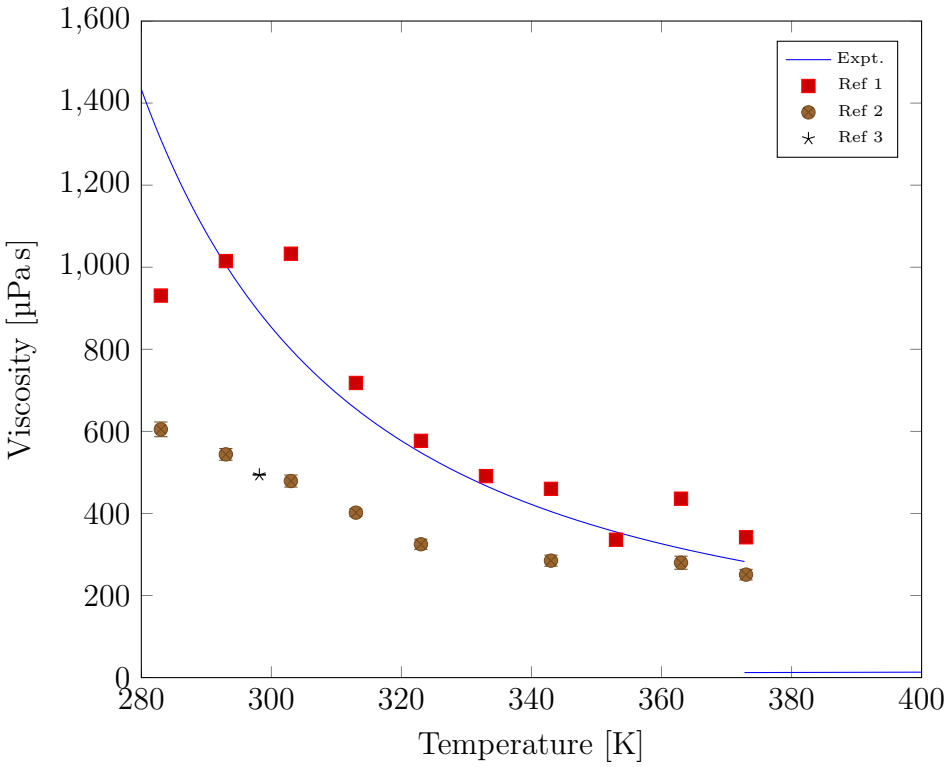


Figure 3.5: Viscosity of water calculated using the TIP4P model, alongside experimental data (IAPWS 1997). Ref 1: Yongli et al. (2007). Ref 2: Markesteijn et al. (2012). Ref 3: González and Abascal (2010)

of vapour-liquid coexistence temperatures. Even so, the original TIP4P model did perform better than the SPC and TIP3P models in reproducing the surface tension. All models underestimated the surface tension across the entire range of temperatures. The TIP4P model was found to exhibit a critical temperature 8% lower than the experimental value, whereas TIP4P/2005 was only 1% lower. In these works, all adsorption and slip simulations are performed at at least 100 K below the models critical temperature and as such TIP4P is considered to be sufficient in this regard. However, the TIP4P/2005 model is generally superior for many parameters (Abascal and Vega 2005).

Previous to their work on surface tension, Vega et al. (2006) used Gibbs-Duhem methodology, developed by Kofke (1993), to calculate the saturated vapour pressures of water. Their results show that TIP4P water overestimates the saturated vapour pressure of water whilst other variants of the TIP4P model, including TIP4P/2005, underestimate this. Both models provide results which are equally

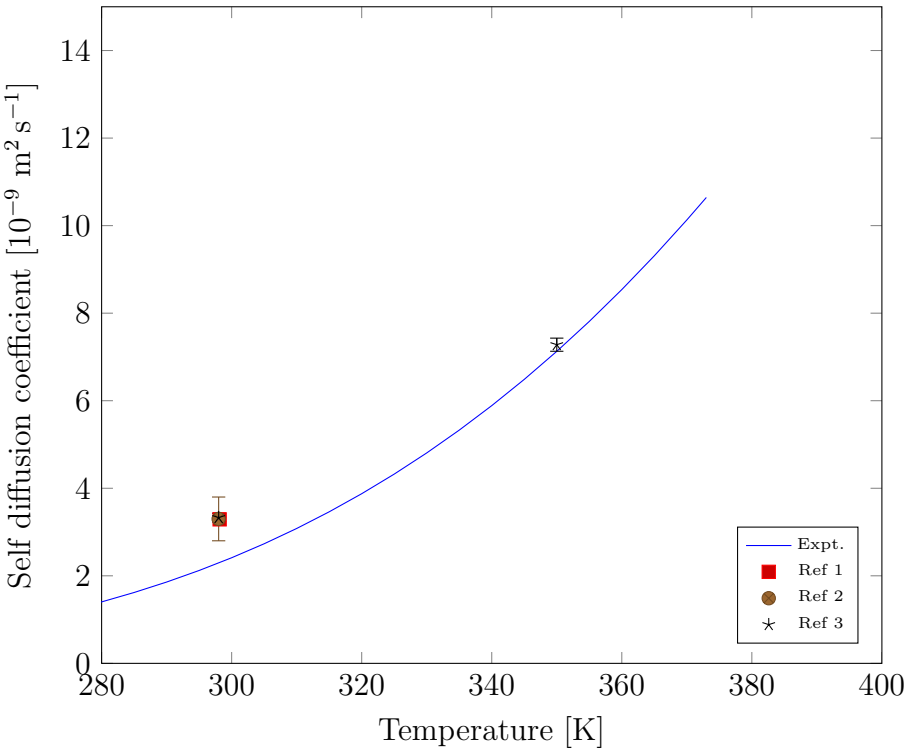


Figure 3.6: Self-diffusion coefficient for water calculated using the TIP4P model, alongside experimental data (Dietrich 2002). Ref 1: Mahoney and Jorgensen (2001). Ref 2: Watanabe and Klein (1989). Ref 3: English (2005)

distant from the experimental values.

The TIP4P vapour-liquid coexistence curve, along with saturated vapour pressures and surface tension, found in these works is presented in section 4.3.2.

One of the objectives of this work is to investigate the adsorption of fluid in slit and cylindrical pores. The rates of adsorption and the comparability of these to real life media depends partly on the intrinsic rate of mobility of the fluid (the diffusion coefficient) and on the viscosity of the models used. For this reason, these properties should be matched well by the chosen model. Figures 3.5 and 3.6 show the viscosity and diffusion coefficients for TIP4P water as a function of temperature at atmospheric pressure and comparison is made with the experimental literature.

The diffusion coefficient matches well with the experimental data, whilst there is a range of viscosities reported in the literature for the TIP4P model, though

the majority of the literature predicts an underestimated viscosity in the lower temperature ranges. This lower viscosity may result in faster rates of adsorption reported in chapter 4.

3.3.2 Model description

The TIP4P water model is a rigid planar four-site interaction potential. The bond lengths and angles are constrained to an exact value rather than being allowed to oscillate as in equations 3.8 and 3.9. In order to constrain the atom's positions the SETTLE (Miyamoto and Kollman 1992) algorithm is used. In this, only two parameters are required: the oxygen-hydrogen and the hydrogen-hydrogen distances. It is possible to use TIP4P as a flexible model, however in these works it is always rigid. For both rigid and flexible water, the full set of parameters for water is shown in tables A.2 and A.3.

The negative charge, that would otherwise be on the oxygen atom to balance the partial negative charges on the hydrogen atoms, is shifted to a dummy atom located between the oxygen and hydrogen atoms. The location of the dummy site, x_D, is determined from the positions of the oxygen, x_O, and hydrogen, x_{H1} and x_{H2}, atoms in the following way:

$$x_D = x_O + a(x_{H1} - x_O) + b(x_{H2} - x_O) \tag{3.20}$$

where $a = b = 0.128012065$ in the case of TIP4P water. The structure of the TIP4P water model is shown in figure 3.7.

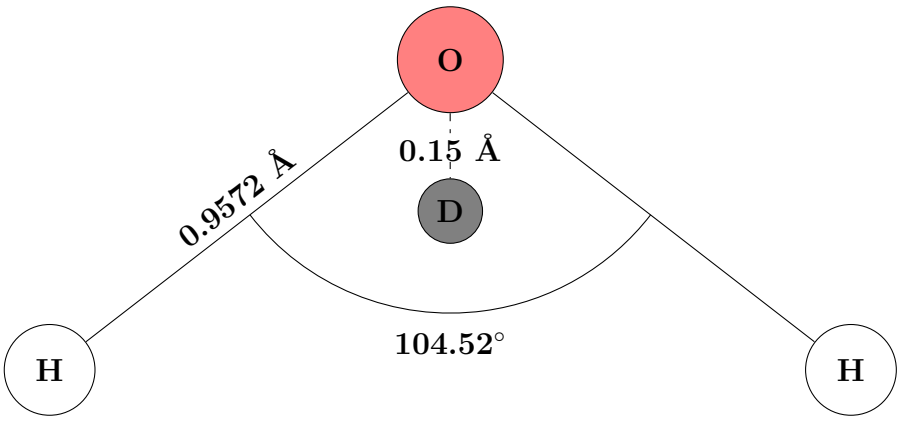


Figure 3.7: Layout of the TIP4P water model.

3.4 Straight chain hydrocarbons

3.4.1 Choice of model

When it comes to simple straight chain hydrocarbons, there are much fewer models for any given molecule than there are for water.

The reason for this is that water looks deceptively simple, but in fact is full of complications, stemming from its electrostatic interactions causing it to be highly polarisable. Coupled with this, there is a trade-off between computational efficiency and model complexity when describing water.

Unlike water, alkanes are much less polar and their interactions are dominated by van der Waals and intramolecular forces.

One of the most commonly used force field for simulating organic liquids in molecular simulations is the Optimized Potentials for Liquid Simulations (OPLS) force field (Jorgensen and Tirado-Rives 1988), which includes both united-atom (UA) and all-atom (AA) parametrisation. Here, AA refers to models where the hydrogen atoms are explicitly handled, whereas in UA models they are included within the parametrisation of the carbon atom. UA models are therefore more computationally efficient, whilst losing some structural information.

Alternatives to the OPLS force field include: CHARMM22 (MacKerell et al.

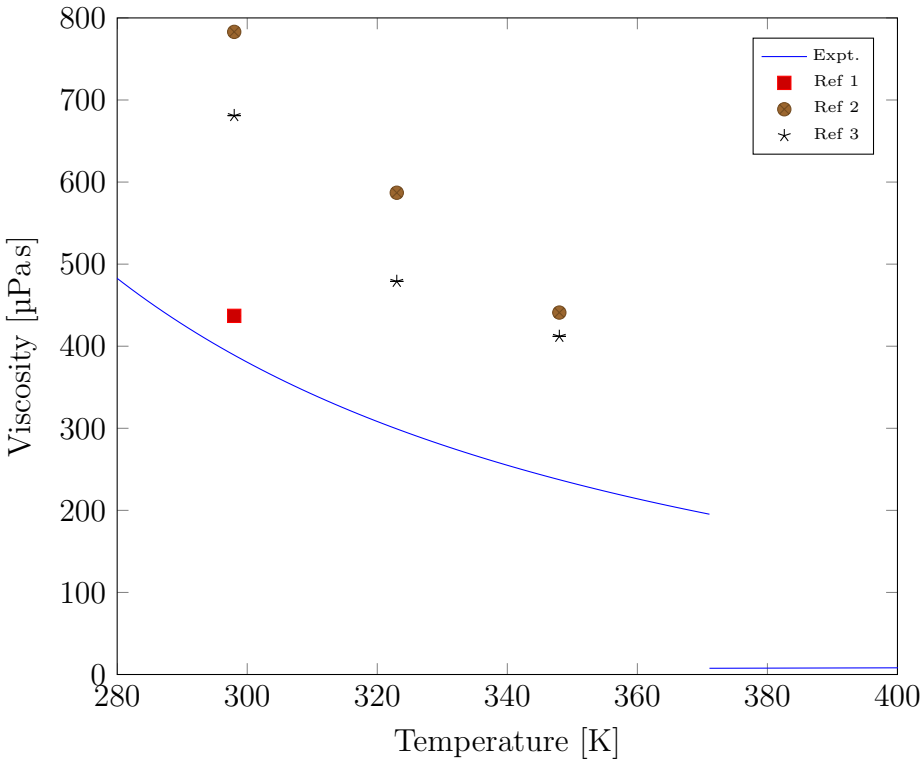


Figure 3.8: Viscosity of n-heptane calculated using the OPLS-AA forcefield, alongside experimental data (Dymond and O/ye 1994). Ref 1: Zhao et al. (2008). Ref 2: Zahariev et al. (2014)*. Ref 3: Zahariev et al. (2014)**. *Nosé-Hoover thermostat and Parrinello-Rahman barostat. **Berendsen thermostat and barostat.

1998), Amber param96 (Cornell et al. 1995), COMPASS (Sun 1998), GROMOS 43A1 (Scott et al. 1999), TraPPE (Martin and Siepmann 1998), and UFF (Rappe et al. 1992), to name but a few.

Martin (2006) compared the ability of these forcefields to reproduce vapor-liquid coexistence curves and liquid densities. They found that, amongst the force fields tested, TraPPE-UA was best for reproducing liquid results, followed closely by CHARMM. Vapour densities were best reproduced by Amber. Amber, GROMOS, and OPLS-AA provided similar quality results for liquid properties. Of the above listed force fields that performed well, only OPLS, CHARMM, and Amber modelled all atoms explicitly, including hydrogens.

Dysthe et al. (2000) investigated the ability of seven different united-atom models of four different alkanes to reproduce transport properties. All models underesti-

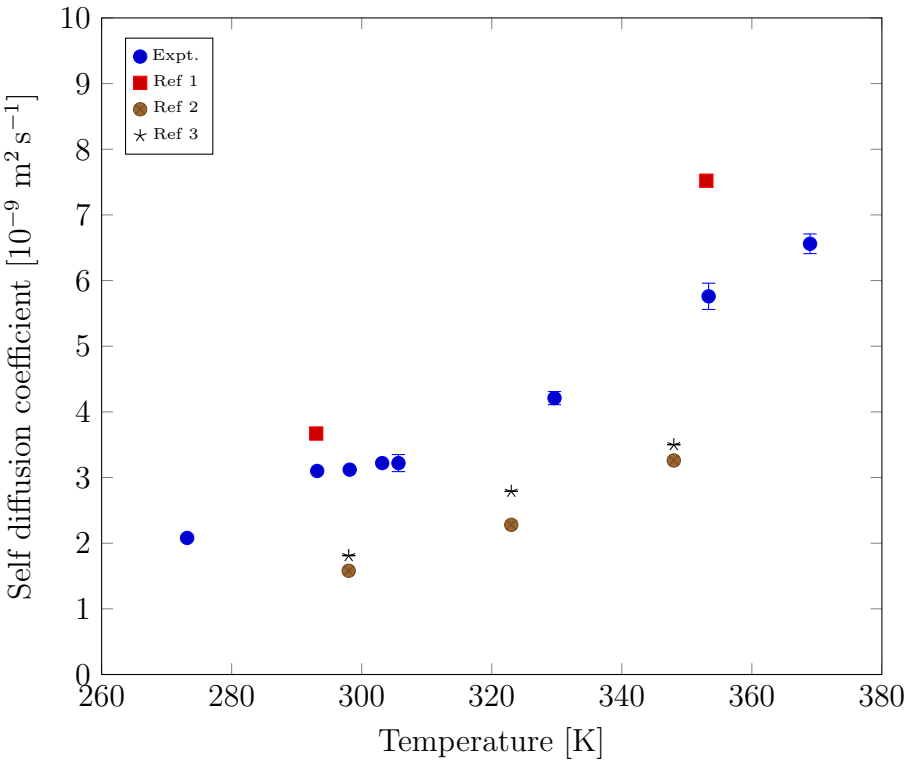


Figure 3.9: Self-diffusion coefficient for n-heptane calculated using the OPLS-AA forcefield, alongside experimental data (Fishman 1955) (Moore and Wellek 1974). Ref 1: Smolyanitsky et al. (2013). Ref 2: Zahariev et al. (2014)*. Ref 3: Zahariev et al. (2014)**. *Nosé-Hoover thermostat and Parrinello-Rahman barostat. **Berendsen thermostat and barostat.

mated viscosities by up to 80% and overestimated diffusion coefficients by up to 250%. This effect is most noticeable at higher densities and lower temperatures.

McCabe et al. (2003) compared UA and AA models and found that the predicted viscosities for the AA model of short perfluoralkanes were in excellent agreement with experimental data, whilst again the UA model underpredicted the Newtonian viscosity. They also calculated diffusion coefficients and found that the AA model produces lower self-diffusion coefficients than the UA model.

The reason for these UA models' inability to reproduce transport properties is easy to see when looking at the physical representation of these coarse-grained models. Coarse-graining infers a loss in structural information, which leads to an effective smoothing of the molecule's surface. This smoothing causes less intermolecular friction, which in turn increases the ease of transport. At higher

densities there is an increase in molecular packing, leading to a increased frictional contribution to the transport properties of which these models cannot reproduce. Similarly, at lower temperatures the fluid is less able to free itself from being entangled with other molecules, and as such structure plays an important role.

Caleman et al. (2012) compared the OPLS-AA force field and the generalized Amber force field (GAFF) for properties such as: Density, Enthalpy of vaporisation, heat capacities, surface tension, isothermal compressibility, volumetric expansion coefficient, and dielectric constant. They found that overall the OPLS-AA force field performs somewhat better than GAFF, however both force fields had issue reproducing surface tension and dielectric constants. In general the surface tension was underestimated. Zubillaga et al. (2013) later improved upon the method used by Caleman et al. (2012) to determine the surface tension. The method was improved by accounting for the long-range Lennard-Jones contributions, that are not encompassed by the short-range cut-off, via an Ewald summation. This method produced surface tensions that were still in general underestimated, but by a lesser degree.

Since the interest of this work is mainly on slip and adsorption, any model chosen would need to have a realistic structure, as any loss of resolution in the model has a large impact on transport and formational properties, as described above. In these works, the OPLS-AA force field has been chosen for modelling straight chain alkanes.

As is the case for water, it is also important that viscosity and diffusion coefficients are well represented by the model for n-heptane. Figures 3.5 and 3.6 show the viscosity and diffusion coefficients for OPLS-AA n-heptane as a function of temperature at atmospheric pressure and comparison is made with the experimental literature.

Again, a range of viscosities are reported in the literature for the OPLS-AA model. This is likely due to the method of calculation, as for instance non-

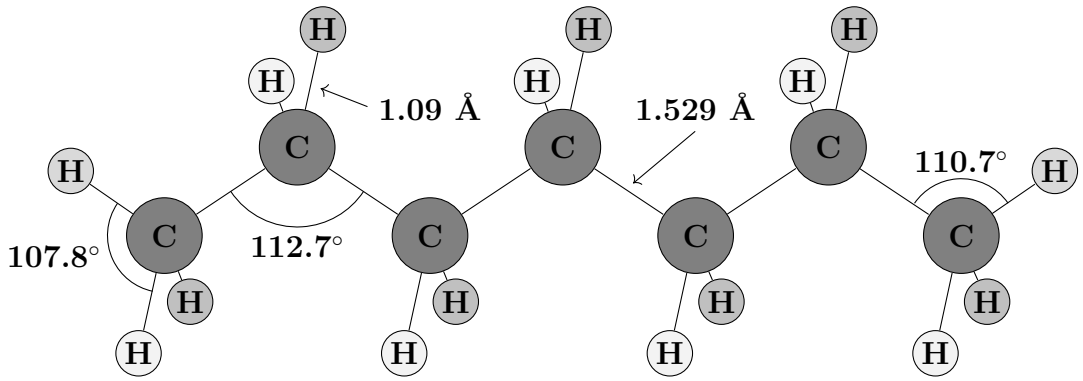


Figure 3.10: Equilibrium structure of the n-heptane model.

equilibrium viscosity calculations are subject to driving force limitations that may influence results. This is discussed more in section 5.3.1. In general the viscosity is overestimated by the model, which may result in slower rates of adsorption reported in chapter 4.

The self-diffusion coefficient is generally underestimated by the OPLS-AA model, as reported in the literature. Again, this may contribute to slower than expected rates of adsorption.

3.4.2 Model description

For straight chain hydrocarbons, namely n-heptane here, the OPLS-AA force-field (Jorgensen and Tirado-Rives 1988) is used. All hydrogen atoms are handled in the same way, whilst there are separate sets of parameters for end group carbon atoms and chain carbon atoms. The model is summarised in tables A.2 and A.3.

In this all-atom model for n-heptane, all carbon-carbon bonds are able to stretch and bend, as described in equations 3.8 and 3.9. Bond twisting is handled using equation 3.10 for all 4-atom sets. Bonds with hydrogen atoms are constrained at a set distance, as these bonds would otherwise oscillate at high frequencies, requiring a much smaller time-step than with constrained bonds. The structure of the n-heptane model is shown in figure 3.10.

3.5 Solid surfaces

Based on the discussion given in section 2.2.3, a graphitic structure has been chosen for solid surfaces. Although the majority of the literature models engine deposits as a series of slit pores, in these works the effect of surface curvature on fluid transport is also investigated. As such, it is necessary to develop a methodology for calculating this in a way which minimises the possibility of external influence, such as shear rate effects and method of imposing flow.

The simplest way to vary curvature in a single system would be to apply some varying surface curvature along a channel, such as a sinusoidal wave, resembling corrugation. By then applying a driving force to the fluid, one could measure the slip length as a function of local curvature. However, this requires a very large system to be simulated over a long time period in order to gain a sufficient level of statistical accuracy. Another problem with this method is that the shear rate varies across the system. In order to reach equilibrium quickly, an unrealistically high driving force is required. As shown by Thompson and Troian (1997), and discussed in section 5.3.1, the slip length is unaffected by shear rate up until some critical point. As such the driving force must be low enough such that the shear rate never exceeds this critical value. Due to the varying shear rate across the corrugated system, the driving force must be even lower to satisfy this condition. This leads to a requirement for much longer simulation times that are increasingly infeasible. Additionally, the curvature varies rapidly across the system which can mean there is not enough space for the flow field to equilibrate at a given curvature.

For these reasons, in order to study the effects of curvature on the amount of slip, a series of cylinders are simulated independently. Equilibrium MD simulations are performed in order to further exclude shear rate effects on the slip.

In order to have a comparable structure to the graphitic slit pores, the cylinders

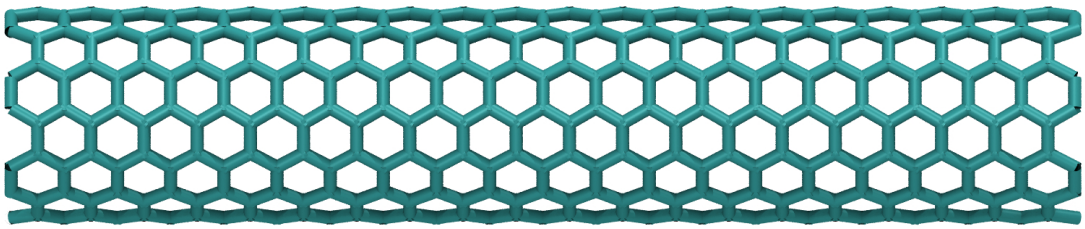


Figure 3.11: Armchair carbon nanotube.

chosen are carbon nanotubes. Each carbon nanotube has a different radius, and as such the curvature effect on slip can be studied. All of the carbon nanotubes studied here are of armchair type, see figure 3.11, as opposed to zigzag or chiral type.

3.5.1 Modelling solid walls

There are several ways to represent a solid surface in molecular simulations. Some methods mentioned by Koplik et al. (1989) are listed:

- Perfectly reflecting walls, i.e. with specular reflection, where the normal component of the velocity is reversed whilst the tangential component is maintained.
- Diffuse or "thermal" walls corresponding to a heat bath maintained at a fixed temperature, where upon collision with the walls the molecules re-enter with a new velocity chosen to correspond with the wall temperature.
- Reverse reflection, where the tangential component of the velocity is reversed upon collision with the wall.

The Steele 10-4-3 potential (Steele 1973) is often employed in the study of activated carbons to describe interactions between an adsorbing fluid and the walls of a slit pore. In this method the solid surface is dealt with implicitly rather than explicitly where it is made up of constrained particles. The potential, $U_{sf}(z)$, is

given by:

$$U_{sf}(z) = 2\pi\rho_s\epsilon_{sf}\sigma_{sf}^2\Delta\left[\frac{2}{5}\left(\frac{\sigma_{sf}}{z}\right)^{10} - \left(\frac{\sigma_{sf}}{z}\right)^{4} - \frac{\sigma_{sf}^4}{3\Delta(0.61\Delta + z)^3}\right] \tag{3.21}$$

where ρ_s is the number density of carbon atoms in a graphite layer, Δ is the spacing between layers and z is the distance between the fluid particle and the surface.

Pinto Da Costa et al. (2011) used this wall definition in conjunction with Reverse Monte Carlo (RMC) in order to predict the pore size distribution of porous engine deposits. In their investigation they found that the pore sizes of intake-valve deposits are circa 1 and 4 nm. One of the obvious disadvantages of the Steele potential is that it integrates an explicitly-defined surface into a smooth flat surface and there is no way to implement physical roughness in this model.

A more realistic approach is to represent the wall as a collection of particles fixed to lattice sites which interact with fluid atoms via a 12-6 Lennard-Jones potential; see equation 3.1. Here the solid atoms do not have their positions updated during the integration step and as such there is no momentum transfer from the fluid molecules.

In the MD algorithm, the mass of an atom is only considered when calculating its new position and velocity after an inter or intra molecular interaction, during the collision step. Hence, if the position and velocity of an atom are not updated after a collision then interactions with these atoms occur in a way analogous to an interaction with an atom of infinite mass. When an atom collides with another atom of infinite mass, there is no kinetic energy transfer, other than between internal energy modes, and the new momentum has a magnitude equal to the magnitude of the momentum before the collision. The proof of this is shown in the following derivation. Momentum normal to the wall is conserved since another wall exists on the opposing side.

Equation 3.22 shows how momentum is conserved in a one-dimensional elastic collision:

$$m_1 u_1 + m_2 u_2 = m_1 \nu_1 + m_2 \nu_2. \tag{3.22}$$

In equation 3.22, m_α, u_α, and ν_α are the mass, velocity before collision, and velocity after collision of atom α involved in the collision.

Equation 3.23 shows how the kinetic energy is conserved in the same case:

$$\frac{m_1 u_1^2}{2} + \frac{m_2 u_2^2}{2} = \frac{m_1 \nu_1^2}{2} + \frac{m_2 \nu_2^2}{2}. \tag{3.23}$$

Combining equations 3.22 and 3.23, the velocities after a collision are as follows:

$$\nu_1 = \frac{u_1 (m_1 - m_2) + 2 m_2 u_2}{m_1 + m_2} \tag{3.24}$$

$$\nu_2 = \frac{u_2 (m_2 - m_1) + 2 m_1 u_1}{m_1 + m_2}. \tag{3.25}$$

As $m_2 \to \infty$:

$$\lim_{m_2 \to \infty} \nu_1 = \frac{2 u_2 m_2 - u_1 m_2}{m_2} = 2 u_2 - u_1. \tag{3.26}$$

Since $u_2 = 0$:

$$\nu_1 = -u_1 \tag{3.27}$$

$$\nu_2 = -u_2 = 0. \tag{3.28}$$

Similarly in an inelastic collision, where the total kinetic energy is not conserved, the velocities after the collision are as follows:

$$\nu_1 = \frac{\alpha m_2 (u_2 - u_1) + m_1 u_1 + m_2 u_2}{m_1 + m_2} \tag{3.29}$$

$$\nu_2 = \frac{\alpha m_1 (u_1 - u_2) + m_1 u_1 + m_2 u_2}{m_1 + m_2} \tag{3.30}$$

where α is the ratio of the total kinetic energy after the collision to the total kinetic energy before the collision. As $m_2 \to \infty$ and as $u_2 = 0$, the velocities after the collision are as follows:

$$\lim_{m_2 \to \infty} \nu_1 = \frac{\alpha m_2 (u_2 - u_1) + m_2 u_2}{m_2} = \alpha (u_2 - u_1) + u_2 = -\alpha u_1 \tag{3.31}$$

$$\lim_{m_2 \to \infty} \nu_2 = \frac{m_2 u_2}{m_2} = u_2 = 0. \tag{3.32}$$

The wall atoms can instead be constrained to their lattice sites via a harmonic potential, similar to how bonds are handled; see equation 3.8. In so doing, momentum and energy transfer between the fluid and wall can take place and as such the wall can exhibit temperature. This can be useful in applications for which the fluid temperature should not be controlled directly. Instead, the temperature of the walls is fixed and the fluid temperature is controlled indirectly via heat transfer from the wall. This is more representative of realistic conditions and reduces the unphysical effects introduced by direct coupling of the fluid. One such common effect is the "flying ice cube" phenomenon which is described in section 4.3.6.

In these works the surface is "frozen" in place and wall particles are fixed at lattice sites, as described earlier. Although, having temperature control at the surfaces would be advantageous and it is suggested that this be a possible next step in further studies.

The solid atoms are arranged in a hexagonal grid in order to mimic graphitic structures, with carbon-carbon separations of 0.142 nm and non-bonded parameters taken from the OPLS-AA force field carbon in naphthalene. Atoms are not explicitly bonded together as there is no need for this considering they are "frozen" in place. It is possible to use flexible walls that have bond lengths and angles maintained with harmonic potentials. These have not been used here for the pore surfaces, so that the effects of curvature and separation can be seen with-

out having to account for pore "wriggling". The pistons described in the next section are defined in this way and match existing models for flexible graphitic sheets and carbon nanotubes, however this is not necessary and has no impact on the results.

The pore geometries are generated in MATLAB (MATLAB 2010) using bond lengths of 0.142 nm and angles between adjacent carbon atoms of 120°. In order to minimised computing requirements cylindrical pores are contained within parallelepiped simulation cells and the slit pores are in regular cubic cells. These periodic cells can be seen in figure 3.3 and described in section 3.2.3.

3.5.2 Pistons

In order to fill pores at constant pressure from liquid reservoirs, pistons are used. See section 4.3.5 for details on how they are used. The pistons are modelled as periodic flexible sheets of graphene with carbon-carbon bond lengths of 0.142 nm and angles between adjacent carbons of 120°. The bonds and angles are maintained harmonically using equations 3.8 and 3.9 respectively. The proper dihedral, keeping the atoms in plane with each other, is handled using equation 3.10. Bonds and angles parameters are taken from the OPLS-AA force field parameters for phenol and the dihedral parameters are from an aromatic ring. The non-bonded parameters for use in equation 3.1 are the same as for the pore atoms and are the parameters for carbon in fused naphthalene.

All bonded and non-bonded parameters, for all of the models used in this work, are summarised in tables A.2 and A.3.

Chapter 4

Adsorption in nanopores via molecular simulation

4.1 Introduction

Having chosen models for molecular simulation of transport in nanopores, the models must be validated against known properties that are important to fluid transport and adsorption.

In this chapter, properties such as surface tension, vapour pressure, vapour-liquid equilibrium, and density are calculated and compared to literature values in order to validate the choice of TIP4P water and OPLS-AA n-heptane and to quantify the basic discrepancies between the models and experimental data.

After this, the adsorption of water and n-heptane in CNTs and graphitic slit pores are studied at temperatures between 300-450 K and at atmospheric pressure. The goal is to investigate the effect pore size has on the final fluid density and the rate and mechanisms of pore filling.

Finally, the equilibrated geometries are used as the input to the slip calculations performed in chapter 5.

4.2 Objectives

The main objective of this chapter is to create filled pore geometries for use in slip calculation in chapter 5 whilst simultaneously investigating adsorption mechanisms with regards to varying confinement.

Initially, the TIP4P water model and the OPLS-AA n-heptane model are validated against experimental literature for macroscopic properties, such as the bulk fluid density, saturated vapour pressure, surface tension, and the liquid vapour coexistence curve.

Adsorption phenomena are then studied in carbon nanotubes and graphitic slit pores, including comparison of fill mechanisms between water and n-heptane.

Several questions are to be answered, such as: How does the final pore density depend on the confinement and arrangement of packed fluid? Does the wettability of the surface to the fluid affect this packing? How would adsorption differ between the molecular models and reality? How does adsorption and packing of fluid change between liquid and vapour phase reservoirs during the filling process?

These questions and more shall be answered in this chapter.

4.3 Methodology

Herein, rates of adsorption are calculated using MD for hydrocarbons under various starting conditions. Specifically, this study entails the effect of fluid-solid combinations on the rate of sorption, adsorption and desorption, and the final equilibrium amount of adsorbate adsorbed onto the surface of the adsorbent. All fluid adsorption occurring in this work is due to physisorption, i.e. due to weak van der Waals forces, as covalent bonding processes are difficult to simulate and are not expected to take place. The equilibrated systems resulting from these

simulations are used in chapter 5 for calculating slip lengths via none-equilibrium and equilibrium MD techniques. Fluid and solid interaction parameters, as well as detailed surface geometry descriptions, can be found in chapter 3.

4.3.1 Pore specification

The surface is always a graphitic type carbon surface, either in the form of a single-walled carbon nanotube or a channel geometry. The fluids simulated are n-heptane and water. The carbon nanotubes are of armchair type, see figure 3.11, and are of various lengths ranging from 10 nm to 30 nm nm depending on the cross-sectional area available for fluid adsorption. Longer CNTs are used where possible to maintain relatively similar pore volumes, for comparative purposes. In some cases it is infeasible to increase the length of the CNT to match the pore volume. The infeasibility arises due to the limited physical simulation box size imposed by the Particle mesh Ewald (PME) long range interaction calculation algorithm. Large simulation boxes are possible, however as the length of the box is increased the simulation time increases with the square of the length, in addition to any time increase due to more molecules being present.

The same methodology for pore length is applied to the channel geometries, although due to the extra periodicity in one of the dimensions an increase in the pore length is not required since there is already a much larger area available for fluid adsorption. The dimensions of pores used in these simulations, when fluid is either inside a slit or cylindrical pore, are listed in table 4.1. When fluid is on the outside of a cylindrical pore, the length is always 10.185 nm.

The periodic simulation box encasing each pore is a triclinic box where the angles between box vectors are either all 90° or one of which is 120°, where the cross section with the xy-plane is hexagonal, for slit and cylindrical pores respectively. The hexagonal box has a cross-sectional area 13% less than the cubic box whilst maintaining the same image distance.

Table 4.1: Pore dimensions for all graphitic pores investigated herein.

Pore type	Solid-solid separation* (nm)	Effective radius† (nm)	Length x width‡ (nm)	Effective pore volume (nm^3)
Cylindrical	0.81	0.235	30.700	5.33
Cylindrical	0.94	0.300	30.700	8.68
Cylindrical	1.07	0.365	30.700	12.85
Cylindrical	1.21	0.435	30.700	18.25
Cylindrical	1.34	0.500	30.700	24.11
Cylindrical	1.47	0.565	30.700	30.79
Cylindrical	1.61	0.635	30.700	38.89
Cylindrical	1.74	0.700	30.700	47.26
Cylindrical	1.87	0.765	30.700	56.44
Cylindrical	2.01	0.835	30.700	67.25
Cylindrical	2.41	1.035	30.700	103.32
Cylindrical	2.81	1.235	30.700	147.10
Cylindrical	2.94	1.300	30.700	163.00
Cylindrical	3.21	1.435	10.185	65.89
Cylindrical	3.61	1.635	10.185	85.54
Cylindrical	4.95	2.305	10.185	170.00
Cylindrical	6.02	2.840	10.185	258.08
Cylindrical	6.95	3.305	10.185	349.51
Cylindrical	8.02	3.840	10.185	471.82
Cylindrical	10.03	4.845	10.185	751.10
Cylindrical	20.05	9.855	10.185	3107.59
Slit	0.70	0.180	8.82 x 8.4875	26.95
Slit	0.80	0.230	8.82 x 8.4875	34.44
Slit	0.90	0.280	8.82 x 8.4875	41.92
Slit	1.00	0.330	8.82 x 8.4875	49.41
Slit	1.10	0.380	8.82 x 8.4875	56.89
Slit	1.20	0.430	8.82 x 8.4875	64.38
Slit	1.30	0.480	8.82 x 8.4875	71.87
Slit	1.40	0.530	8.82 x 8.4875	79.35
Slit	1.50	0.580	8.82 x 8.4875	86.84
Slit	1.60	0.630	8.82 x 8.4875	94.32
Slit	1.70	0.680	8.82 x 8.4875	101.81
Slit	1.80	0.730	8.82 x 8.4875	109.30
Slit	1.90	0.780	8.82 x 8.4875	116.78
Slit	2.00	0.830	8.82 x 8.4875	124.27
Slit	2.10	0.880	8.82 x 8.4875	131.75
Slit	2.20	0.930	8.82 x 8.4875	139.24
Slit	2.30	0.980	8.82 x 8.4875	146.73
Slit	2.40	1.030	8.82 x 8.4875	154.21
Slit	2.50	1.080	8.82 x 8.4875	161.70
Slit	2.60	1.130	8.82 x 8.4875	169.13
Slit	2.70	1.180	8.82 x 8.4875	176.67
Slit	2.80	1.230	8.82 x 8.4875	184.16

Slit	2.90	1.280	8.82 x 8.4875	191.64
Slit	3.00	1.330	8.82 x 8.4875	199.13
Slit	5.00	2.330	8.82 x 8.4875	348.85
Slit	6.00	2.830	8.82 x 8.4875	423.71
Slit	7.00	3.330	8.82 x 8.4875	498.57
Slit	8.00	3.830	8.82 x 8.4875	573.43
Slit	10.00	4.830	8.82 x 8.4875	723.15

* The solid-solid separation is the centre to centre distance between atoms on opposite sides of the pore.
† The effective radius is the surface to surface distance between atoms on opposite sides of the pore, approximately centre to centre minus σ_{sf}.
‡ Length is in the x-dimension whereas width is in the y-dimension and non-existent for cylindrical pores.

For simulations involving fluid on the outside of cylindrical pores all the pores are the same length. The minimum separation between adjacent periodic images of the same cylinder is 5 nm, since the box is triclinic, and the minimum pore length used is 10.185 nm, the total pore volume is always larger than 220.5 nm^3.

Gas and liquid adsorption are treated differently due to the large difference in the bulk fluid density. These cases are discussed in detail in sections 4.3.5 and 4.3.6. In both cases 5 nm of empty space is added normal to the pore surface, between periodic images, achieved by increasing the size of the periodic simulation cell. In this way there is at least a 5 nm gap between each adjacent pore to minimise the affect of periodicity normal to the pore surfaces. A single graphene layer barrier is added to both ends of the pore, preventing fluid from entering the vacuum region created between images. Any fluid molecules allowed outside of the pore during equilibration would interact across the solid pore boundary and influence the fluid inside the pore.

Large fluid reservoirs are then added adjacent to the two ends of the pore which are filled with fluid at its equilibrium density. The fluid is allowed to fill the pore, whilst the time for filling and final equilibrium density are measured.

Each reservoir is handled separately and as such independent pressure and com-

positions can be specified. However, in all cases the temperature is constant across the entire system.

4.3.2 Density calculation

A separate isothermal-isobaric ensemble, NPT, simulation is performed in order to calculate the fluid density at a given pressure and temperature. Pressure is controlled with the Parrinello-Rahman barostat and temperature with the v-rescale themostat, which are described in sections 3.2.10 and 3.2.9 respectively.

It is usually possible to predict the fluid phase, at a given pressure and temperature, with a specific model, from the model literature. However, since this is not always available for every fluid model or for specific fluid mixtures, the phase is determined before calculating the density rather than assuming the phase before simulating. The following methodology is used for all fluids, whether the phase transition point is known or not, in order to maintain consistency.

Initially, the vapour pressure is determined as a function of temperature. From this an initial estimate of the density is known and the actual density is then found. The vapour pressure is found by simulating a liquid film, aligned with the xy-plane, in the centre of a periodic box, where the box dimensions are $x = y = (1/4)\, z$. The film is in equilibrium with a surrounding vapour phase and the temperature is varied. The vapour pressure here is simply the z component of the pressure tensor, which is found using equation 3.19.

The specific procedure for producing the vapour pressure curve is as follows. A cubic box filled with 1000 fluid molecules, at a known liquid phase temperature and pressure, is equilibrated in an NPT simulation. This is preceded by a short canonical, NVT, simulation to prevent any unreasonably high forces causing the simulation box to expand uncontrollably during NPT. The geometry is then extended in the z-dimensions, resulting in a thin liquid film surrounded by vacuum

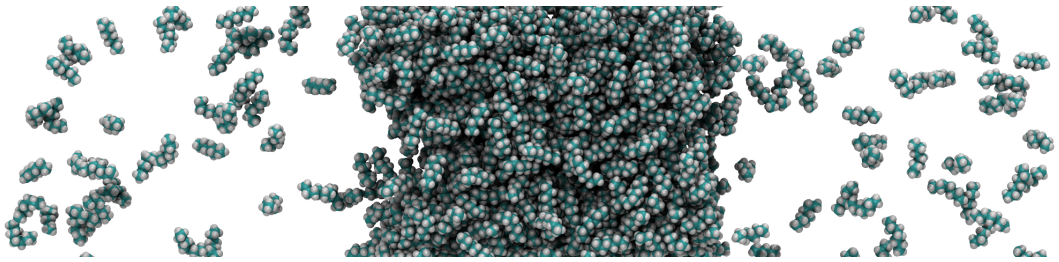


Figure 4.1: Orthographic (side on) view of an equilibrated film (approx. 6 nm wide) of n-heptane at 440 K used for determining the vapour pressure curve.

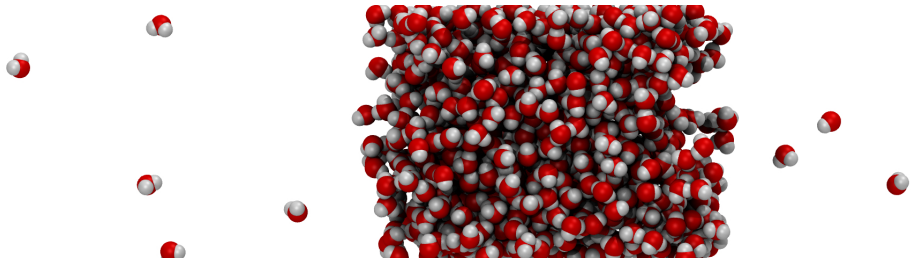


Figure 4.2: Orthographic (side on) view of an equilibrated film (approx. 3 nm wide) of water at 440 K used for determining the vapour pressure curve.

in one dimension (where vapour phase fluid will fill into during equilibration), and a long simulation is performed to find the entire vapour pressure curve. The long simulation consists of an initial 200 ps equilibration period at constant volume, where the temperature is gradually increased towards the target temperature, followed by 200 ps at constant temperature to ensure equilibrium is reached. The pressure is calculated from the virial, equation 3.19, from a final 2 ns period of simulation. The vapour pressure in this case is found from the component of the pressure tensor normal to the film surface. Subsequent data points are found by repeating the above process during the same long simulation, gradually increasing the temperature. Examples of two phase systems for n-heptane and water are shown in figures 4.1 and 4.2.

As described in section 3.2.2, due to the existence of a cut-off distance, a long range correction for dispersion forces is required. All residual forces beyond the cut-off distance are attractive forces and as such, without dispersion correction, the pressure is always underestimated. However, dispersion correction is only viable in situations where the fluid is homogeneous as the derivation of equation 3.7

requires the radial distribution function, $g(r)$, to be 1 beyond the cut-off. In the vapour pressure calculation the system is inherently non-homogeneous, due to the coexisting phases. In addition to this, all of the complex systems studied in these works are non-homogeneous in one way or another. Therefore, in all of these cases dispersion correction has not been used. This results in the problem that all the pressure calculations are underestimated, as explained. This issue must be addressed on a fluid by fluid basis, as the model parametrisation affects any workaround.

In the case of TIP4P water, the long-range electrostatic forces dominate the potential and as such the cut-off distance for dispersion forces can be increased, beyond the cut-off used during parametrisation, without significantly influencing the results. Here this distance can be safely increased such that the remaining long range dispersion forces are negligible. Additionally, the coulombic forces provide a higher contribution to the total interaction potential, such that the lack of long range van der Waals correction has a smaller impact on the vapour pressure than for n-heptane. The cut-off is set to the maximum value of half the smallest box vector, approximately 1.5 nm. This is generally not a desirable setting for normal simulations due to the increase in simulation time.

Due to the parametrisation of the OPLS-AA forcefield for alkanes being performed with set cut-offs, it is not appropriate to increase the cut-off for n-heptane. Additionally, the long range dispersion forces have a larger impact on the total interaction potential than for water. It is possible to solve the long-range van der Waals, dispersion, interactions via PME in a similar manner as for the charged interactions, see section 3.2.2. This has been implemented into a later version of GROMACS, version 5.0.0, than the one predominantly used herein. This version has been used only for the vapour pressure and VLE calculations, however it is not possible at the time of writing to use version 5.0.0 for the rest of these works due to some required features being unavailable.

The vapour pressure is required in order to find the vaporisation point at a pressure of 1 bar. This is then used for density calculations and subsequently generating adsorption isobars. Knowing the vapour pressure before finding the density reduces computing time and avoids numerical instabilities caused by initiating a simulation in a different phase to its equilibrium state.

Since the vapour pressure curve is found using PME, whilst the adsorption and slip calculations, see chapter 5, use cut-offs it is not appropriate to use this to find the phase transition point for n-heptane. These calculations have however been performed here. Additionally, the parameterisation of the OPLS-AA forcefield does not allow for PME, just as it does not for large cut-offs. So for n-heptane the experimental literature data for the boiling point has been used for determining the phase. It just so happens that the simulation and experimental value for the temperature at a vapour pressure of 1 bar are very similar, see figure 4.8. As such, this has little impact on the results, however this will affect adsorption and slip at higher pressures.

Once the phase is known, the density can be calculated at all relevant conditions. For liquid phase calculations fluid molecules are inserted randomly into a 5 nm cubic box until no more molecules can fit. A short NVT simulation is performed followed by a 2 ns NPT simulation.

For gas phase calculations 50 molecules are inserted randomly into a much larger box, matching a typical gas phase density. If the initial density is far from the equilibrium value then the box size will oscillate with a large amplitude. The correct density is still recovered on average, however this makes it difficult to extract a corresponding geometry for reservoir filling. As such, an iterative process is used whereby the new initial box size is chosen based on the previous steps' density. This iterative process is broken when the root mean square deviation of the density, averaged over the entire trajectory, is no more than 1% of the mean.

The resulting geometry is used to fill one of the reservoir adjacent to the pore

entrances. In the liquid case there is an extra step required before the pore can be allowed to fill from this reservoir. This is described in section 4.3.5.

When calculating the densities inside pores the choice of surface location will impact the results, since the pore volume will change. In this work the location of the surface is consistently defined as the point $\sigma_{sf}/2$ away from the centre of the innermost wall particles. This, along with other methods of choosing the surface location, is discussed in section 2.4.2.

4.3.3 Surface tension

The surface tension is calculated for every point along the saturated vapour pressure curve, using the same two-phase simulation as before. From the pressure tensor the interfacial tension can be calculated using the following equation:

$$\gamma = \int_{-\infty}^{\infty} \left[P_N(z) - P_T(z)\right] \mathrm{d}z = \int_{-\infty}^{\infty} \left[P_{zz}(z) - \frac{1}{2}\left(P_{xx}(z) + P_{yy}(z)\right)\right] \mathrm{d}z \qquad (4.1)$$

where $P_{\alpha\beta}$ is an element of the pressure tensor and P_N and P_T are pressures normal and tangential to the interface respectively. In the case described above, with two interfaces, equation 4.1 becomes:

$$\gamma = \frac{1}{2} L_z \left[P_{zz} - \frac{1}{2}\left(P_{xx} + P_{yy}\right)\right] \qquad (4.2)$$

where L_z is the length of the periodic simulation cell in the z direction. The pressure tensor, $P_{\alpha\beta}$, is described in equations 3.19, 5.13, and 5.14. In addition to calculating the surface tension in this way, Alejandre et al. (Alejandre et al. 1995) also calculated the normal and tangential pressures, which depend on z. In this way the surface tension is calculated again using equation 4.1, and gives

the same solution. However, by calculating the normal and tangential pressures one can establish whether the system has reached equilibrium, as $P_N(z)$ is constant and $P_N \equiv P_T$ away from the interfaces. In this work this is not calculated, instead the simulation time has been set such that there is no change in density distribution and that the probability of being at equilibrium is high. This becomes significant in multi-component systems where dissolution and outgassing processes can occur, which happen over longer time-scales.

4.3.4 Adsorption process

Each reservoirs is treated independently of the other reservoir. The only exception to this is when both reservoirs are in the gas phase. In this case, having the same composition and at the same pressure, only one reservoir is used spanning across the periodic boundaries and in contact with both pore entrances. This is to increase efficiency, as increasing the box size has an exponential (L^2) impact on computation time due to calculating long range interactions.

Since each of the two reservoirs can be specified independently, with the exception of temperature, it is possible to explore the effects of multiple different filling/draining mechanisms. For instance, initially the pore can be empty and fill simultaneously from the two adjacent reservoirs. The resulting equilibrated system can be used in slip calculations or used with two new reservoirs to explore adsorption against an existing pore fluid. The rate of this adsorption will differ depending on whether the new adsorbate is in both reservoirs or just one of the two, where the other contains pore fluid at the same conditions as the fluid in the pore. In the former case, pore fluid has to overcome surface tension in order to escape the pore, whereas in the latter case there is no need as there is a connected fluid pathway out of the pore.

In all cases, results are taken over a period of at least 2 ns for liquid phase simulations and a minimum of 10 ns for gas phase, however some of the smaller

pores can take up to 35 ns to fill from a gas phase reservoir. This depends on how easily the fluid can pack inside the pore. The smallest pore is not necessarily the slowest to fill to equilibrium. The resulting amount adsorbed is plotted against time and compared for slit and cylindrical pores of multiple sizes. Additionally the adsorption isobars are plotted.

4.3.5 Adsorption from a bulk liquid phase

Equilibrated fluid reservoirs are added to either side of the pore. First, the barricaded pore is placed into a periodic box. Infinitely large, single layered, graphene sheets are added either side of the pore, with a gap between the pore and sheet where fluid will be added. The length of this empty space is equal to the total pore volume divided by the cross sectional area of the empty space, plus a minimum distance of 10 nm. This way, once the fluid has entered the pore from this reservoir there will still be 5-10 nm between the pore and the graphene sheet. This is to maintain a continuous bulk region of fluid and prevent the formation of a pseudo-pore, such that any fluid layering at the piston surface does not influence the filling process or the fluid density and arrangement in the main pore at equilibrium.

An additional gap is added which is initially 5 nm between each graphene sheet across the periodic boundary. This is to minimise the influence of long range interactions in this dimension.

The space between the pore and the graphene sheet is then filled with liquid phase fluid by stacking the equilibrated fluid boxes from the NPT density simulations, as shown in figures 4.3 (a) and 4.4 (a).

Each graphene sheet then has a force applied to it corresponding to a set pressure, acting in the direction of the pore, such that it acts as a piston which compresses the reservoir fluid. Unlike the pore and barrier atoms, the piston is allowed to

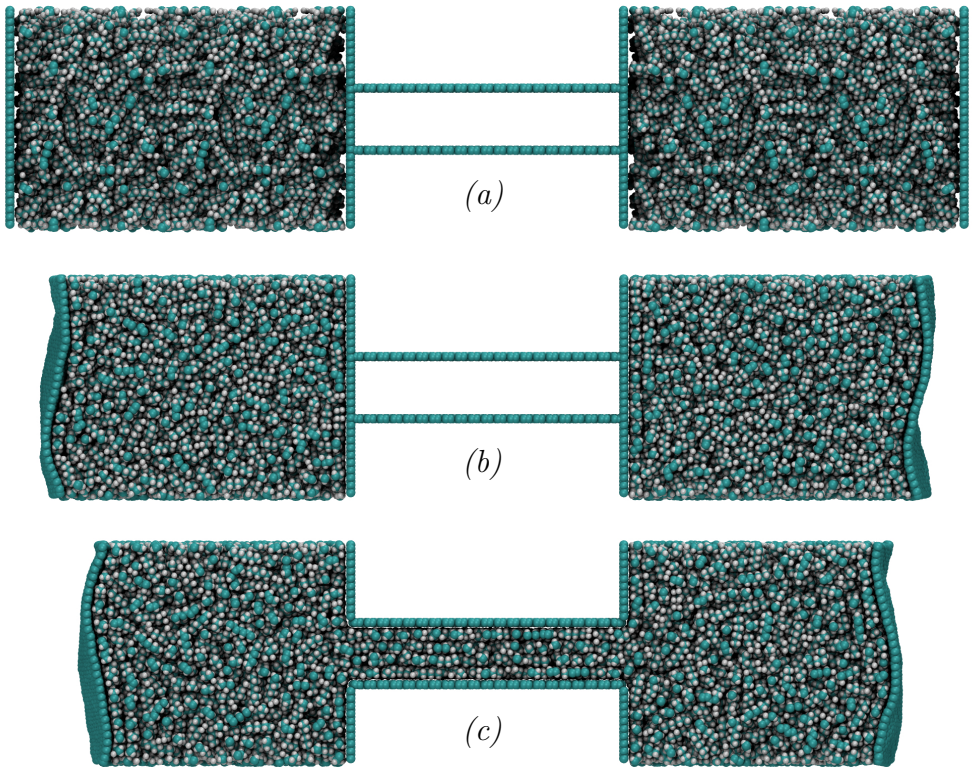


Figure 4.3: Orthographic (side on) view of a 2 nm slit pore attached to two reservoirs filled with n-heptane. (a) Before the reservoirs have been equilibrated, n-heptane has been added from an equilibrated system at the correct temperature and pressure. (b) After the reservoirs have equilibrated at 300 K and 1 bar. (c) After the barricade has been removed and the pore has completely filled. The fluid in the top image looks slightly different due to molecules having been made whole for the image creation. Molecules in the other two images have been left broken by the periodic boundaries.

move freely and contains bond length and angle constraints to match a realistic graphene surface. This definition of the piston is an arbitrary choice and has no a significant impact on the bulk fluid.

The reservoir is then allowed to equilibrate for 20 ps, this is relatively short since the fluid has already been equilibrated separately. This is shown in figure 4.3 (b) and 4.4 (b). Once the reservoir fluid has equilibrated under this compression at the specified pressure, the pore barrier is removed and the fluid is allowed to fill the pore, figure 4.3 (c) and 4.4 (c). During adsorption, the piston continues to maintain a constant bulk density and pressure.

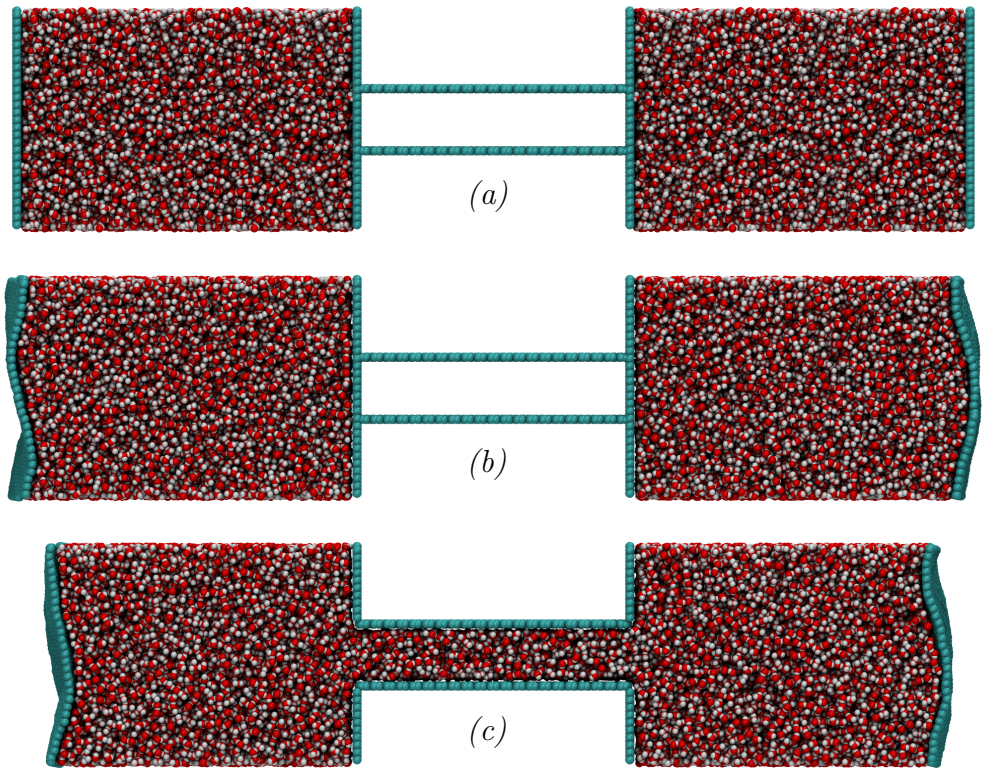


Figure 4.4: Orthographic (side on) view of a 2 nm slit pore attached to two reservoirs filled with water. (a) Before the reservoirs have been equilibrated, water has been added from an equilibrated system at the correct temperature and pressure. (b) After the reservoirs have equilibrated at 300 K and 1 bar. (c) After the barricade has been removed and the pore has completely filled. The fluid in the top image looks slightly different due to molecules having been made whole for the image creation. Molecules in the other two images have been left broken by the periodic boundaries.

4.3.6 Adsorption from a bulk gas phase

Pistons are not used to maintain the pressure for gas phases reservoirs. The reason for this is that due to the low fluid density the piston oscillates back and forth with large amplitude. This causes transient and inertial effects on the pore filling process, such that the pore fluid density never stops changing with time. An additional problem with this is that the simulation box needs to be several times larger, which results in excessive computing requirements as the computational cost of the PME algorithm increases with the square of the box length.

For a gas reservoir, fluid is added by stacking the equilibrated fluid boxes from the NPT density simulations adjacent to the barricaded pore entrance. In this



Figure 4.5: Orthographic (side on) view of a 2 nm slit pore adjacent to a single gas phase n-heptane reservoir spanning the periodic boundary. The pore is barricaded whilst the reservoir equilibrates. The reservoir is larger than the portion shown in this image.



Figure 4.6: Orthographic (side on) view of a 2 nm slit pore adjacent to a single gas phase water reservoir spanning the periodic boundary. The pore is barricaded whilst the reservoir equilibrates. The reservoir is larger than the portion shown in this image.

case the bulk density is kept constant during adsorption by adding/removing fluid molecules to/from the reservoir as molecules leave or enter the pore, maintaining a constant number density of molecules in the bulk fluid.

Before the barricade is removed the number of molecules in the gas phase reservoir is allowed to stabilise and the fluid equilibrate for 200 ps. Once the reservoir(s) has equilibrated, the barricade is removed and the pore is allowed to fill.

The gas phase reservoir, attached to a pore before the barricade has been removed, can be seen in figures 4.5 and 4.6.

During adsorption, at frequent and regular intervals the number of molecules remaining in the bulk is counted and if there is any discrepancy a molecule is either added or removed, maintaining a constant number of molecules and as such a constant density. If the density drops too low, i.e. a molecule enters the pore, then a new molecule is inserted at a random location in the reservoir. The interval chosen for this is 2 ps, as this is small enough that the molecule count is updated as soon as possible after a molecule enters or leaves the pore. This

generally results in the addition of roughly 1 molecule at a time. The interval is also larger than the relaxation time for temperature coupling (0.1 ps).

Since the reservoir density is so low, there are very few intermolecular interactions occurring in comparison to in a liquid phase simulation. This is expected as in the case of an ideal gas molecules are none interacting. Unfortunately this introduces numerical issues when temperature coupling. This issue will be discussed here.

Avoiding the flying ice cube

In a simple system one can think of most of the kinetic energy either being in vibrational modes or translational modes. Vibrational modes are high frequency oscillating motions, i.e. bond stretching and bond-angle bending, whereas translational modes are zero frequency motions such as overall movement of a molecule in a certain direction. Without intermolecular interactions, i.e. collisions, the translational energies are independent of time.

Most thermostatting methods maintain a constant temperature by employing a scaling of velocities, and thereby the kinetic energies, based on the deviation of the mean kinetic energy from the expected value for a given temperature. This introduces an instability where energy is drained from the high frequency modes to low frequency modes (Harvey et al. 1998). The overall effect is that the internal energy of a molecule goes to zero whilst the translational motion reaches a maximum. This violates the principle of equipartition, which states that energy is shared equally amongst all energetically accessible degrees of freedom of a system. It should be noted that this is a completely unphysical effect and is purely an artefact of the MD algorithms employed.

This phenomenon can be seen clearly when looking at a single diatomic molecule in vacuo with temperature coupling applied (Harvey et al. 1998). In this case the vibrational energy is severely damped after just 100 ps and is essentially zero by

300 ps. It is shown that as the ratio between vibrational and total kinetic energy decreases, the energy drain from vibrational to translational modes increases, leading to a runaway effect.

In liquid phase, or high density, systems the energy of these modes can couple back into the system through collisions. However, since the centre of mass translational energy has no way to couple back, there is an energy drain to this mode from the high frequency modes. Removing the centre of mass motion at regular intervals, by subtracting the overall velocity of the system from the velocities of all molecules in the system, is an effective method of preventing this so called "flying ice cube".

On the other hand, in gas phase systems few collisions take place to redistribute these energies and as such centre of mass motion removal does not prevent this issue. The removal of the centre of mass motion in this case can cause more detrimental effects than it fixes.

Further to this, when a solid surface is introduced the process is accelerated. Additionally, fluid in contact with the surface will have energy drained from all modes. The energy of fluid in contact with the surface is able to redistribute via collisions with the surface and via collisions between other fluid molecules in contact with the surface, since fluid is more densely packed at the surface than in the bulk. Additionally, translational motion is no longer a zero frequency motion due to constant surface interactions. This means that as the vibrational energy of the bulk fluid drains into translational energy, energy is also drained from the surface fluid to the bulk. This causes the fluid at the solid surface to freeze completely as it has zero energy in all modes, whereas the bulk fluid exhibits high translational energy and zero internal energy.

To prevent this effect from influencing the adsorption results and subsequently the slip results, a Langevin thermostat is used. Here Newton's equations of motion are altered to include a frictional term to relax the temperature, unlike other methods that use velocity scaling. In this way the motion of each molecule is

not dependent on the motion of other molecules, as such there is no build up of translational motion. More detail on the Langevin thermostat can be found in section 3.2.9.

In the liquid phase simulations this is not needed, as both fluid in the bulk and fluid at the solid surface collide enough to couple any drained energy back. When a pore is introduced it is no longer correct to remove the centre of mass motion, however due to friction between the pore entrance and the bulk and collisions between pore fluid and bulk fluid there is no build up of the centre of mass velocity. This would also affect the pistons in an undesirable manner.

4.4 Discussion

4.4.1 Density calculation

The saturated vapour pressure curves for the water and n-heptane are shown in figures 4.7 and 4.8. The region immediately left of the curve indicates liquid phase fluid whereas the region immediately right indicates gas phase fluid. The conditions applied here are always for either liquid or gas; no solidification processes have been observed.

Data from Lisal et al. (2001), Shen et al. (*NIST Standard Reference Simulation Website*) and Vega and De Miguel (2007), both using the TIP4P water model, are plotted alongside the results of this work for comparison purposes.

Similarly, data from Chen and Siepmann (1999) for OPLS-AA and TraPPe-EH n-heptane are plotted in figure 4.8 for comparison.

Using figures 4.7 and 4.8 the phase transition temperature at 1 bar is found to be 363.6 K and 367.0 K for TIP4P water and OPLS-AA n-heptane respectively. This is found by fitting a 3rd order polynomial to the data set and interpolating

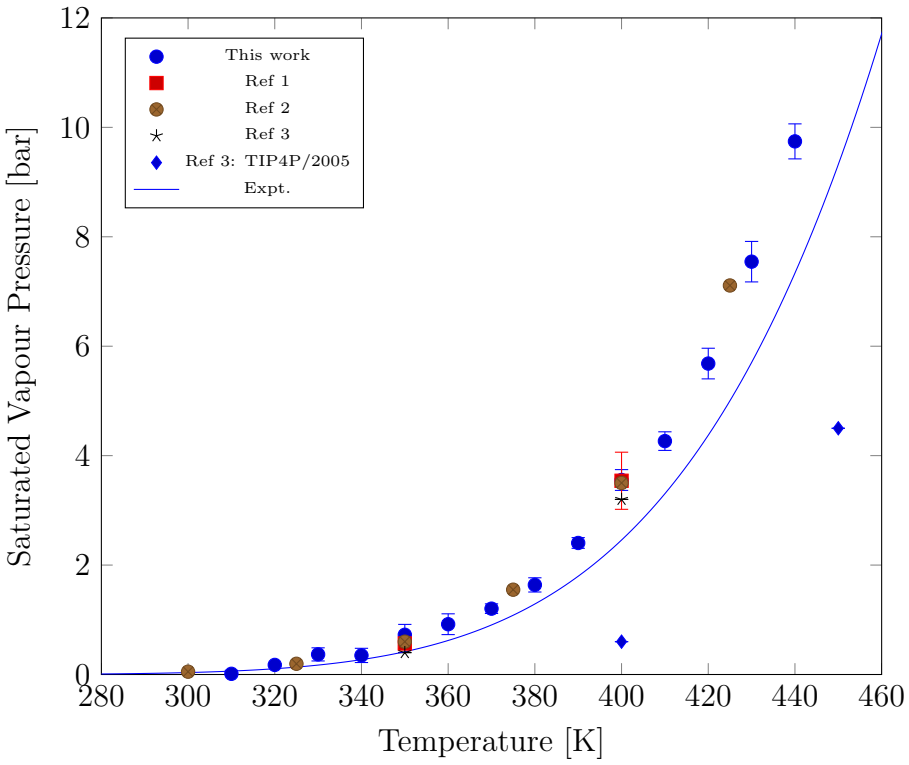


Figure 4.7: Saturated vapour pressure curve for TIP4P water. Ref 1: Lisal et al. (2001). Ref 2: Shen et al. (*NIST Standard Reference Simulation Website*). Ref 3: Vega and De Miguel (2007). Experiments: Wagner and Pruss (2002).

to 1 bar. This value is used later when equilibrating a fluid box for calculating density-temperature isobars. As explained earlier, in the case of n-heptane the experimental boiling point is used, which is 371 K at 1 bar.

For TIP4P water the vapour pressure is consistently over-estimated, which is in agreement with the results of Lisal et al. (2001) and Shen et al. (*NIST Standard Reference Simulation Website*) for TIP4P water. As the temperature increases the absolute deviation from the experimental results also increases, however the relative deviation remains constant at approximately 30 % beyond 370 K, with larger relative deviations below this temperature.

Unlike for water, the OPLS-AA n-heptane crosses the curve for the experimental results at a point between 350 and 360 K. Not only does the absolute deviation from the experimental results increase but also the relative deviations, reaching 50 % at 440 K. The vapour pressure matches well with the results of Chen and

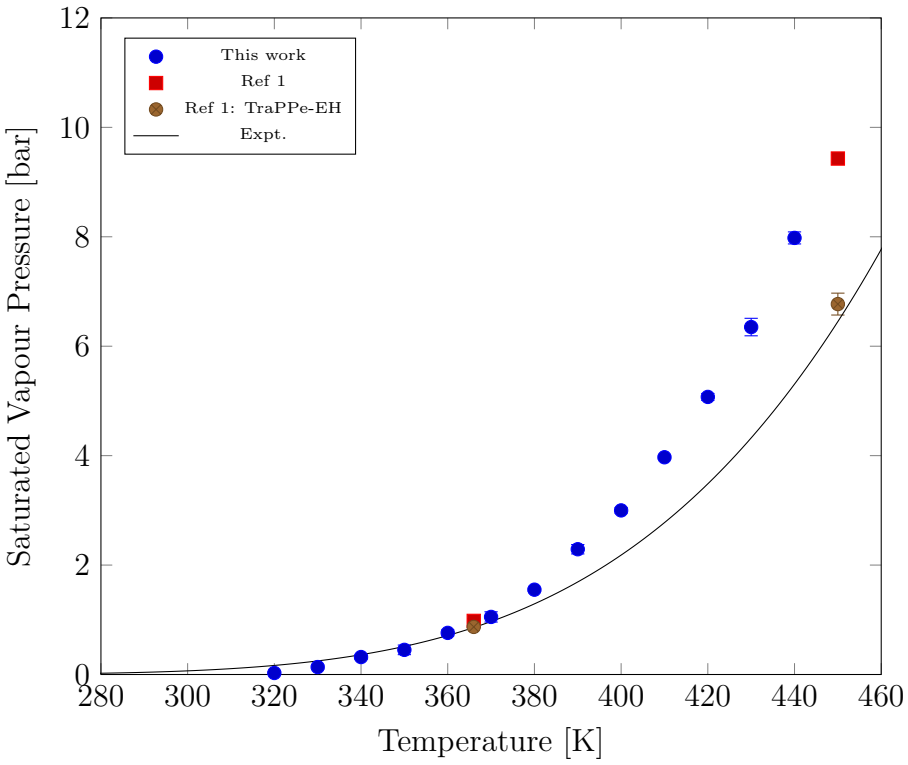


Figure 4.8: Saturated vapour pressure curve for OPLS-AA n-heptane. Ref 1: Chen and Siepmann (1999). Experiments: Span (2000).

Siepmann (1999) for OPLS-AA n-heptane, but the results for the TraPPe-EH forcefield for n-heptane is much closer to the experimental value at 450 K.

The density profiles across the fluid slab system for water and n-heptane are shown in figures 4.9 and 4.10. Here the increase in temperature causes a closing of the gap between the liquid and vapour phase densities. Although not shown, as the temperature approaches the critical point, the density becomes almost constant across the entire simulation box. Beyond the critical point there is no discernible liquid or vapour phases.

The liquid-vapour coexistence curves extracted from the mean liquid and vapour densities in figures 4.9 and 4.10 are shown in figures 4.11 and 4.12.

As in figure 4.11, data from Lisal et al. (2001) and Shen et al. (*NIST Standard Reference Simulation Website*) have been plotted, along with data from Vega and De Miguel (2007).

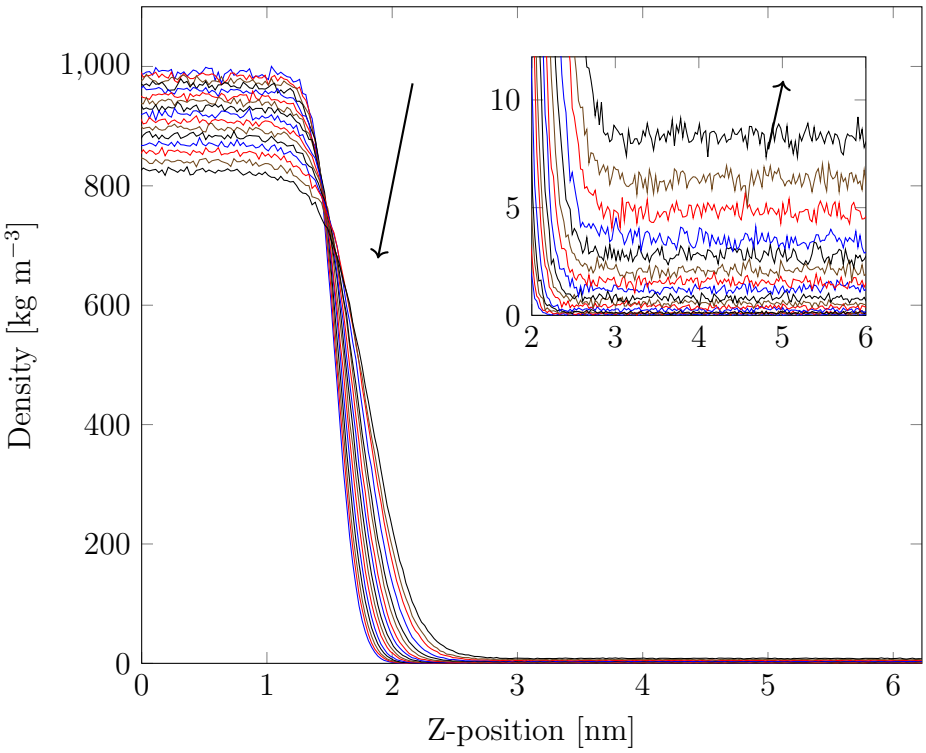


Figure 4.9: Density profile of saturated water along two phase system. Zero corresponds to the centre of the box. The arrows indicate the direction of increasing temperature, from 300 K to 450 K in increments of 10 K.

Similarly, data from (Chen and Siepmann 1999) for OPLS-AA and TraPPe-EH n-heptane are plotted in figure 4.12 for comparison.

For TIP4P water, the vapour phase density remains relatively unchanged until within approximately 50 K of the critical point, where there is an increasing rate of increase in the density. This also results in a wider peak in the density profile and a less sharp decline in the density at the liquid-vapour boundary. This can be seen also in figure 4.11.

In the case of the OPLS-AA n-heptane, the vapour phase density steadily increases from approximately 350 K up until it is within 50 K of the critical point. This can be seen clearly in figure 4.12.

For both TIP4P water and n-heptane the liquid-vapour coexistence curve matches the shape of the experimental data very well, however both fluids exhibit a critical point which is much less than the experimental critical point. The critical point

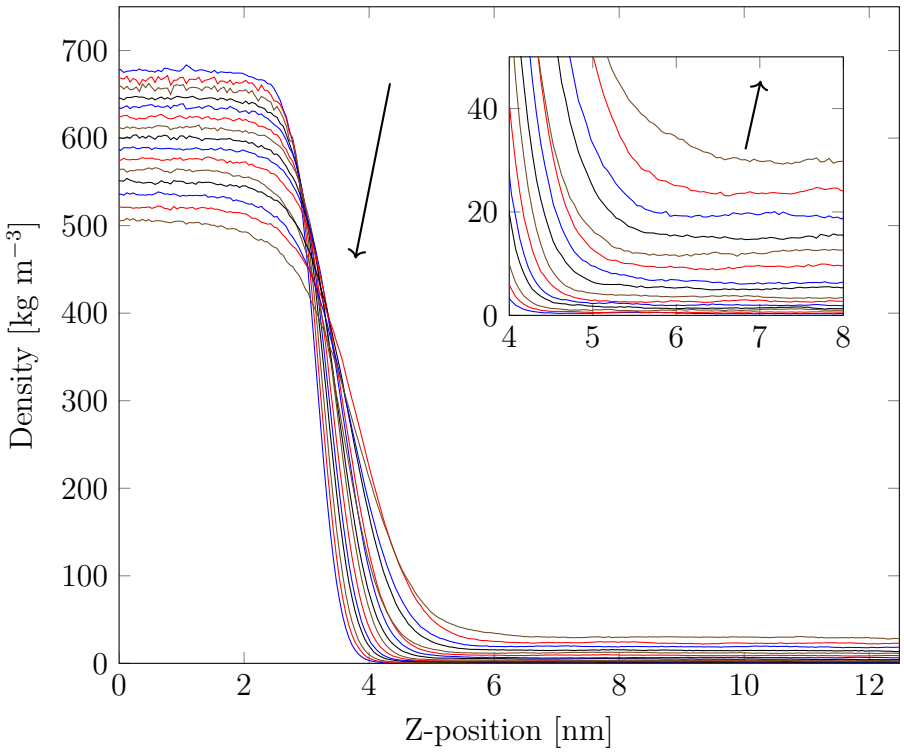


Figure 4.10: Density profile of saturated n-heptane along two phase system. Zero corresponds to the centre of the box. The arrows indicate the direction of increasing temperature, from 300 K to 440 K in increments of 10 K.

is underestimated by approximately 13 % for water and 7 % for n-heptane. When the simulation results are rescaled to match the experimental critical point, the simulation data overlaps with the experimental data closely. However, when the n-heptane data is rescaled to match the critical point, the liquid phase density is consistently overestimated by 2-7 %.

The n-heptane results presented here are not consistent with the work of Chen and Siepmann (1999) for either the OPLS-AA or the TraPPe-EH model, which match the experimental results better. Surprisingly, the gas phase density presented by Chen and Siepmann (1999) is lower than calculated in this work even though the vapour pressure is similar. This suggests that the long-range dispersion forces are over-accounted for in this work, when compared to the work of Chen and Siepmann (1999). Additionally, the difference in density between their results for OPLS-AA and TraPPe-EH n-heptane is small, even though the difference in vapour pressure is large, showing that the specifics of the model has an effect on

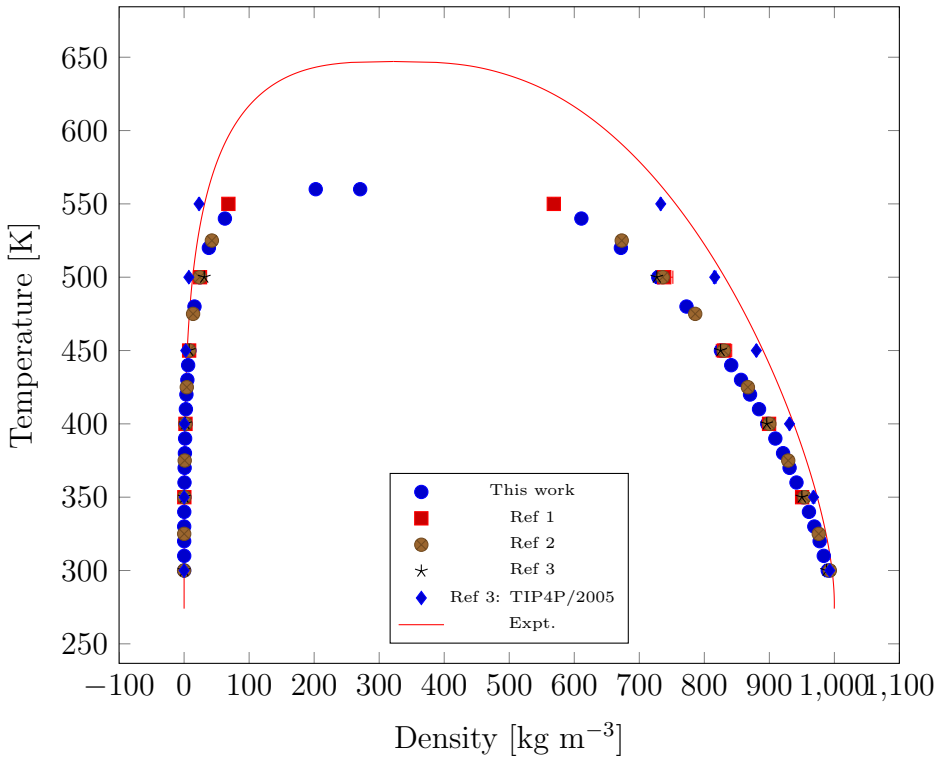


Figure 4.11: Liquid-vapour coexistence curve for TIP4P water. Ref 1: Lisal et al. (2001). Ref 2: Shen et al. (*NIST Standard Reference Simulation Website*). Ref 3: Vega and De Miguel (2007). Experiments: Wagner and Pruss (2002).

how vapour pressure and density are related. This also shows that a model that matches one property well will not necessarily work for other purposes.

The reason for the differences in the liquid-vapour coexistence curve is likely due to the difference in method used for calculating the surface tension. Chen and Siepmann (1999) performed Gibbs ensemble Monte Carlo simulations in order to calculate the phase equilibria. The method involves simulating two separate simulation boxes, each with a different fluid phase in. Unlike in this work, the long-range correction to the Lennard-Jones potentials are easily handled. Each simulation box contains only one phase and as such is homogeneous. Since it is homogeneous, and as the radial distribution function is 1 beyond the cut-off, the standard correction method for the long-range dispersion forces can be used. This correction is shown in section 3.2.2. However in this work the PME summation method is used (for liquid-vapour coexistence work only). As already discussed, the OPLS-AA forcefield is parametrised to be used with a set cut-off distance and

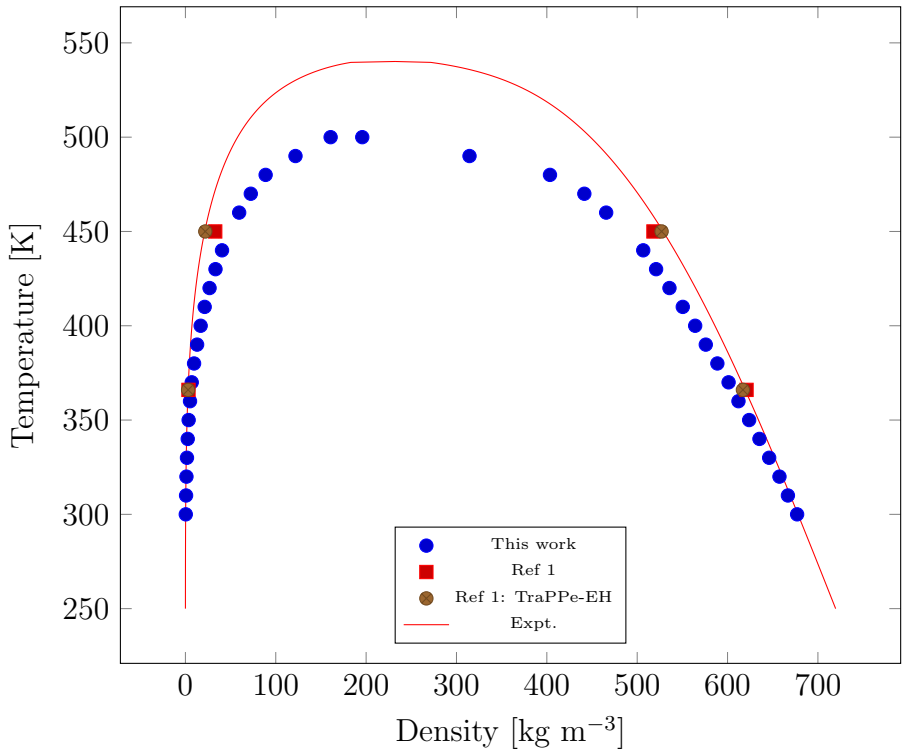


Figure 4.12: Liquid-vapour coexistence curve for OPLS-AA n-heptane. Ref 1: Chen and Siepmann (1999). Experiments: Span (2000).

the standard long-range dispersion correction. Due to this, the model is not as valid when this cut-off is changed or if another method of correcting for the long-range dispersion forces is used. In this work the long-range correction should not be used, since the adsorption simulations are non-homogeneous and the use of this would result in a higher pressure and increased surface tension. As a result, fluid would act strangely within the pore and the rate of filling would be completely different to that presented later in sections 4.3.5 and 4.3.6. Specifically, the rate of filling would be artificially slowed as it would be more difficult for fluid to break away from the bulk.

The results presented here show a lower liquid phase density than presented by Chen and Siepmann (1999), which suggests that the standard correction over corrects for the long-range dispersion forces, but that this over correction is accounted for in the parametrisation of the model. The adsorption and slip work presented later is performed with mainly temperatures between 300 and 400 K, over which range figure 4.12 shows acceptable agreement.

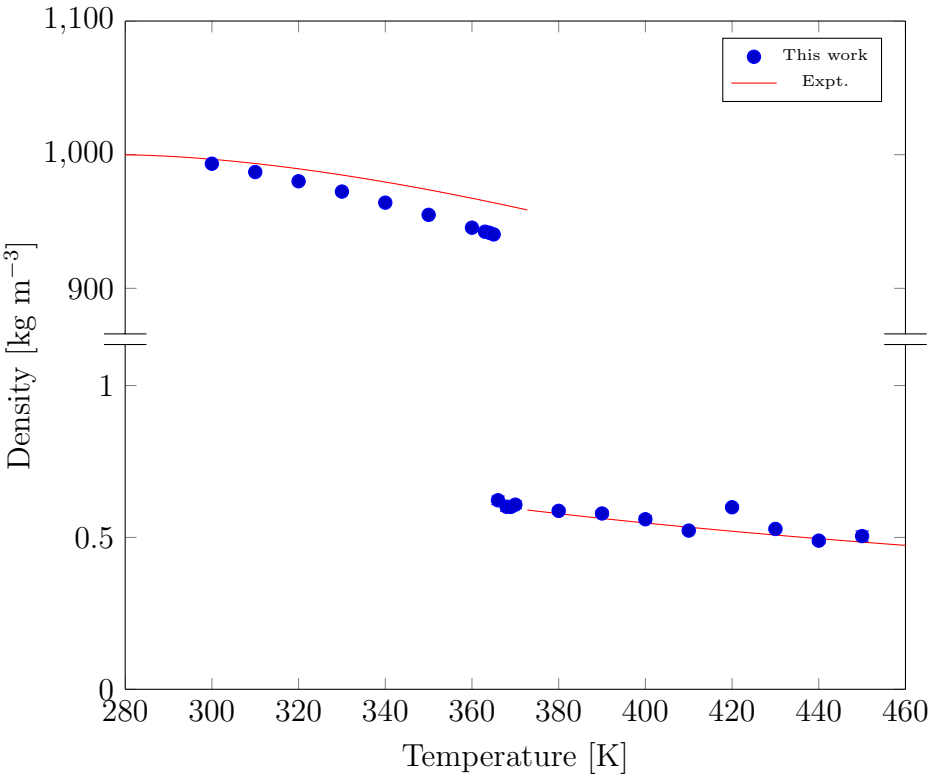


Figure 4.13: Density-temperature isobar for TIP4P water at 1 bar. Experiments: Wagner and Pruss (2002).

With the phase transition temperature known from figures 4.7 and 4.8, the density is calculated at 1 bar at points between 300 to 450 K using the method described in section 4.3.2. In these simulations the density is found from single phase simulations, including the standard long-range dispersion correction. The density-temperature isobar curves are shown in figure 4.13 and 4.14.

Figure 4.13 shows that there is good agreement between this work and the experimental data for TIP4P water. The maximum deviation from the experimental data is 3.5 % for the liquid phase at 365 K and 15.1 % for the vapour phase at 420 K. The second highest deviation in the vapour phase results is 4 % at 450 K. In general, the level of displacement from the experimental data is constant over the entire vapour phase. The average deviation over the entire range, excluding points with differing phases, is 2.7 %.

The liquid phase density exhibits an increasing deviation from the experimental data as the temperature approaches the phase transition temperature, or as the

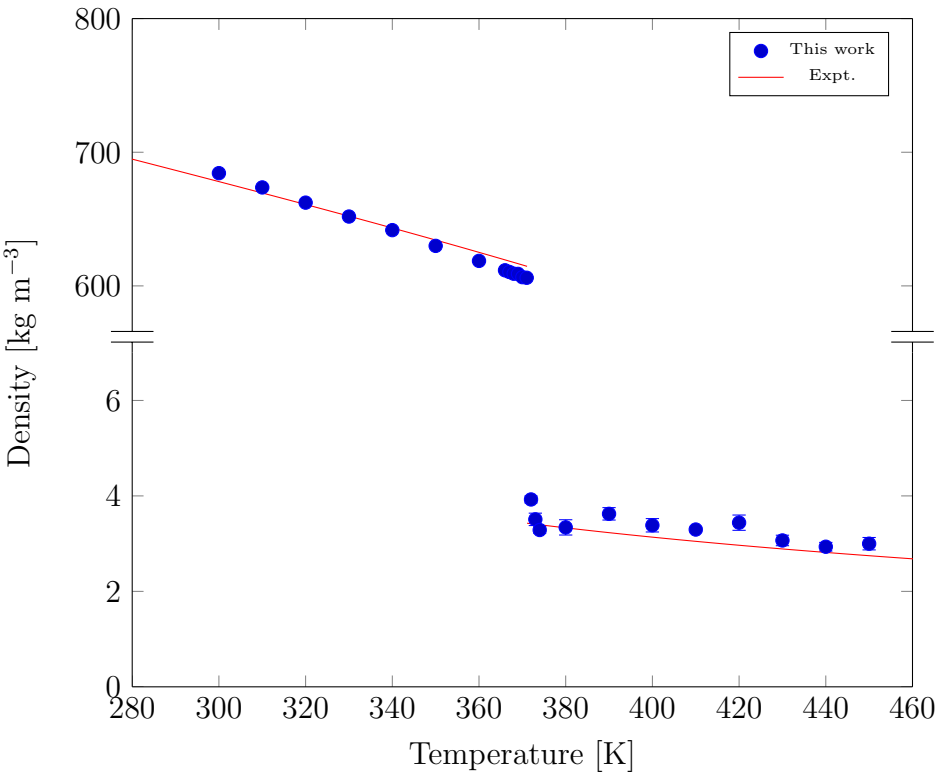


Figure 4.14: Density-temperature isobar for OPLS-AA n-heptane at 1 bar. Experiments: Span (2000).

temperature increases. This is consistent with the liquid-vapour coexistence data, which had a larger deviation from experimental results for higher temperatures in the liquid phase, but maintained a similar density for the vapour phase.

This is partially due to the inherently smaller change in density with temperature for vapour phase water until close to the critical point. Additionally, the density of TIP4P water depends fairly linearly on temperature in the liquid phase, whereas the experimental data is non-linear.

The n-heptane isobar, shown in figure 4.14, matches closer with the experimental data for liquid phase densities, including a similar linearity. The maximum liquid phase deviation from the experimental data is 1.5 % in this case. On the other hand, the vapour phase densities are systematically overestimated, with a maximum deviation of 16 % and an average deviation of 7.7 %. These results are reasonable, especially considering the OPLS-AA forcefield is parameterised for liquid phase simulations.

As explained earlier in this section, the phase transition point for n-heptane is taken to be the literature value when calculating the density. This is due to inconsistencies in the cut-offs between the isobar simulations and the vapour pressure simulations and is why the phase transition point in figure 4.14 matches exactly with the literature in this figure.

Near to the phase transition temperature, in the vapour phase fluid, the density sharply increases, which would not be expected since single phase simulations explore the metastable regions and therefore there should be a "jump" upon reaching the spinodal due to mechanical instability. This deviation is possibly a direct result of the chosen saturation temperature being an estimate (whether using the literature value or the value calculated earlier). This sharp increase in the density could also just be a statistical anomaly, considering the deviation from the experimental data is similar to that for 370 and 420 K.

The data from figures 4.7 and 4.8 is used for comparison with the adsorption isobars presented in sections 4.4.5 and 4.4.6.

4.4.2 Surface tension

Figures 4.15 and 4.16 show the surface tension as a function of temperature for TIP4P water and OPLS-AA n-heptane calculated from the same slab simulations used above.

For TIP4P water, the results are in line with those of Sides et al. (1999). However, the surface tensions calculated by Vega and De Miguel (2007) are consistently higher than those calculated here and the difference becomes more exaggerated at lower temperatures.

Vega and De Miguel (2007) performed the same calculations for TIP4P/2005 (Abascal and Vega 2005) and found that the surface tension and liquid-vapour coexistence data matched the experimental data extremely well. However, the vapour

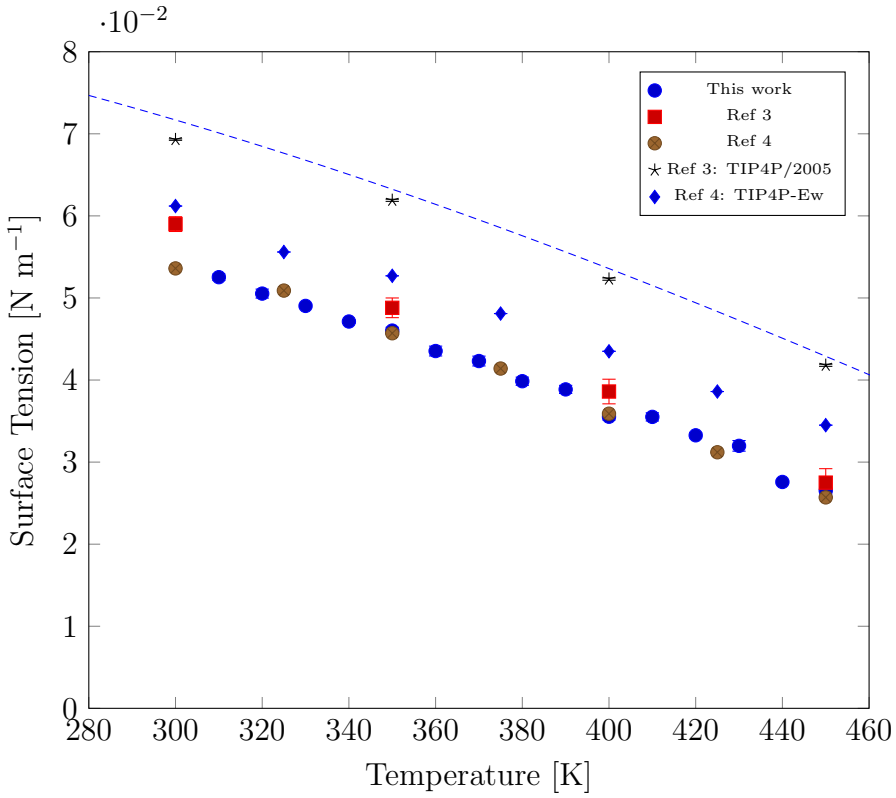


Figure 4.15: Surface tension for TIP4P water. The dashed line indicates experimental data. Ref 3: Vega and De Miguel (2007). Ref 4: Sides et al. (1999). Experiments: IAPWS (1994). The TIP4P/2005 and the TIP4P-Ew re-parameterisations presented in references 3 and 4 are for the purpose of comparison between models.

pressure data, shown in figure 4.7, provides some reason for scepticism for both the TIP4P/2005 and the TIP4P results. For TIP4P/2005, the vapour pressure is underestimated for 450 K and below and over estimated beyond 500 K. The vapour pressure is also negative for temperatures below 350 K. This suggests an issue with the method used, since a negative average pressure is not physical and suggests the system is under tension, specifically the vapour phase fluid has expanded beyond its equilibrium value. This is reflected in the vapour phase density, which has a negative deviation of 56.5 % from the experimental values at 400 K. However, the vapour phase density is still underestimated at 550 K, whereas the vapour pressure is 21.5 % overestimated, which adds to the confusion regarding their results. A separate, homogeneous, vapour phase simulation of the model at constant pressure would likely result in much higher densities than the ones presented.

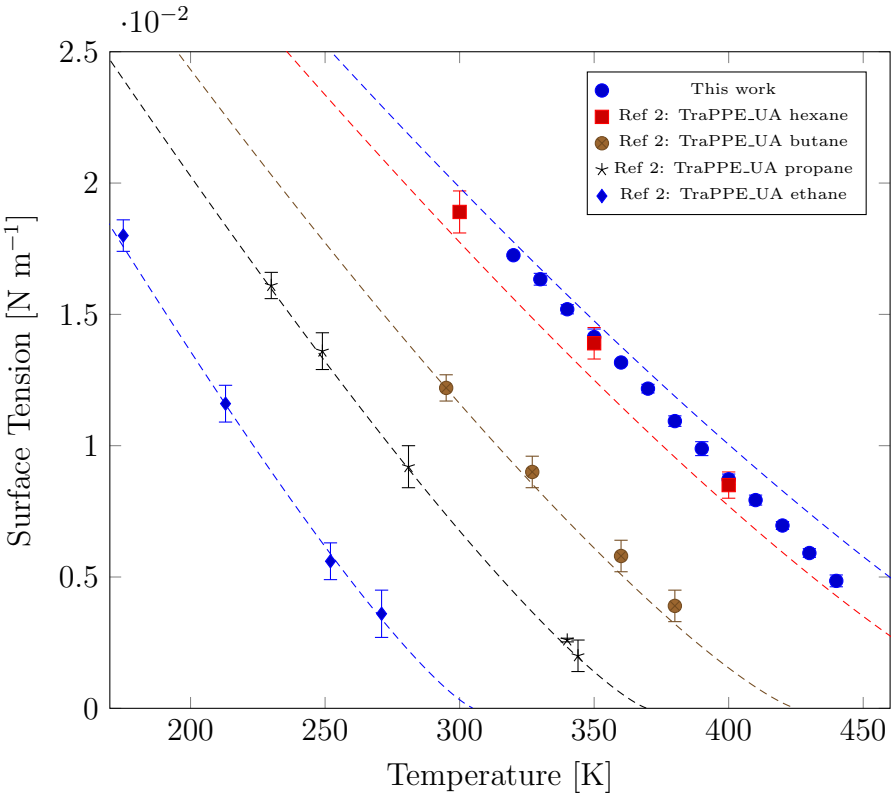


Figure 4.16: Surface tension for OPLS-AA n-heptane and other straight chain hydrocarbons for comparison. Dashed lines indicate experimental data. Ref 2: Mendoza et al. (2008). Experiments: heptane and hexane: Somayajulu (1988); butane: Calado et al. (1978), Coffin and Maass (1928); propane: Baidakov and Sulla (1985); ethane: Soares et al. (1986), Leadbetter et al. (1964), Katz et al. (1939).

The method they used was the same as presented here, except the calculation of the surface tension was performed, using 2×10^4 molecular configurations from the MD trajectory, with a separate Monte Carlo code using the test-area method. They used a similar number of molecules, however their simulation box had an aspect ratio 3:1 as opposed to 4:1. This difference should have little influence on the results. The major difference between the method used here and their method was that they used a 1.3 nm cut-off length, whereas this work uses a larger cut-off, equal to half the smallest box dimension (approx. 1.5 nm), in order to account as much as possible for the long range LJ interactions. This is the most likely reason for abnormalities in their work. It is unknown whether or not they used the standard correction which is only applicable for homogeneous fluids.

The same issue they had with TIP4P/2005 water may have occured when mod-

elling TIP4P water as well. This could be the reason for the deviation from both the results presented here and the results of Sides et al. (1999) for TIP4P water.

Li et al. (2013) calculated the interfacial tension of brine-CO_2 systems, with NaCl and $CaCL_2$ salts, as a function of pressure at 373 K. They found that with both SPC/E and TIP4P water, the interfacial tension was underestimated at relatively low pressures, less than 100 bar, whereas at higher pressures the opposite is observed. Although they did not perform simulations with pure water, this could suggest that current models for pure water do not always underestimate the surface tension over the entire pressure range. This, coupled with the surface tension results compared here, confirms that there is still a long way to go in creating a model that accurately exhibits the properties of water over all conditions.

Although limited literature exists which calculates the surface tension of n-heptane using the OPLS-AA forcefield, the deviation from experimental results is consistent with other organic liquids simulated using the TraPPE_UA forcefield. Here the surface tension is within 3% to 25% in the temperature range 320-440 K, with an average deviation of 15%. Zubillaga et al. (2013) calculated the surface tension of 61 organic liquids, at standard conditions, and found that the majority of results are within 25% of the experimental value. The mean deviation was 14% with a maximum deviation of 68% for pyrimidine and a minimum deviation of less than 1% for fluorobenzene and methoxybenzene.

Zubillaga et al. (2013) recognised that when calculating the surface tension using a slab geometry, such as used here, the standard long-range dispersion corrections cannot be included, due to the inhomogeneity of the system. Their approach was to use the Ewald sum method to calculate the long-range behaviour of dispersion interactions (López-Lemus and Alejandre 2002).

There are additional ways to account for the lack of long-range dispersion interactions when calculating the surface tension. One such way is to apply a long-range correction based on the density profile of a the system (Ghoufi et al. 2008).

4.4.3 Liquid adsorption against a vacuum

The simplest case to investigate is that of liquid adsorbing against a vacuum. Here, initially the pore is completely empty and both reservoirs contain liquid phase fluid. Fluid fills the pore from both ends and the amount of adsorbed fluid vs time is recorded.

Water in slit pores and nanotubes

The process of water filling a slit pore using this method is shown in figure 4.17. Initially the fluid equilibrates with a barrier in place of the pore entrance, after which the barrier is removed and fluid fills the pore. In the case of water, since the carbon nanotube is hydrophobic, the fluid fills the pore in a plug like flow fashion. There is no development of curvature induced by the presence of the solid surface and the fluid is able to fill the pore with little hindrance and without enhancement from high attractive forces with the surface which pulls the fluid in.

Figures 4.18 to 4.20 show the mechanisms of filling slit and cylindrical pores from liquid phase water reservoirs at 300 K, as well as filling around the outside of cylindrical nanotubes. For fluid inside cylindrical pores the length of the pores are either 10.185 nm or 30.7 nm, depending on the pore diameter. All pores with a diameter of 3 nm or less are longer, to account for decreasing pore volume. Due to this, the rate of increase in density with time is not directly comparable between pores, however the final density is. In order to make comparisons between the rates of pore filling the pore density is multiplied by the pore length. The rates reported are then the rates of change in the amount of fluid per cross sectional area of the pores. These rates allow for rough approximations of the time to fill pores of any length, assuming the filling mechanism is independent of the pore length.

Full page sized graphs can be found in Appendix C.

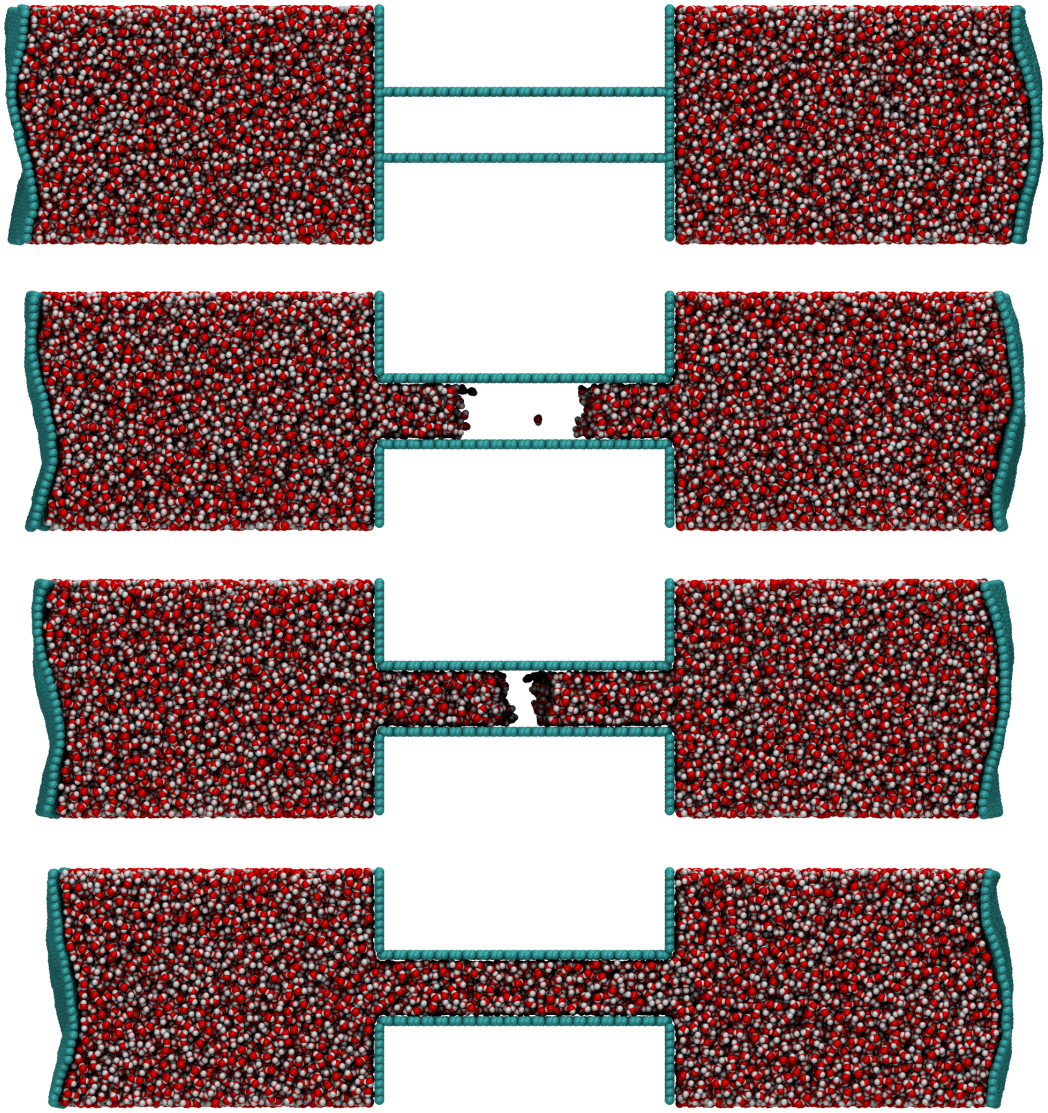


Figure 4.17: Orthographic (side on) view of liquid water at 300 K filling a 2.01 nm slit pore after 0, 100, 150, and 1,980 ps.

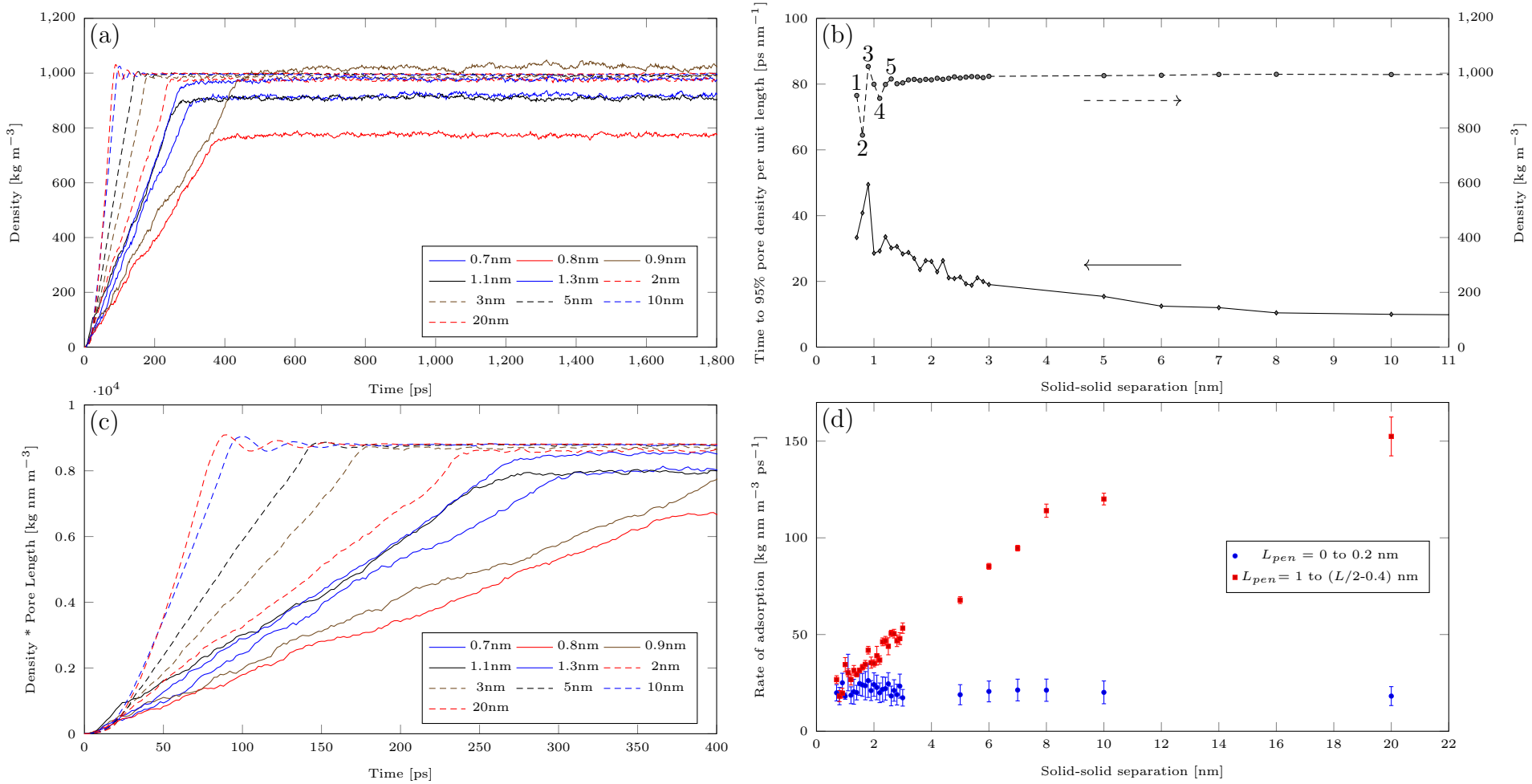


Figure 4.18: Liquid water at 300 K filling various slit pores. a) Pore density against time. b) Comparison between pore fill time and the mean density calculated over the final 500 ps of (a). The labels correspond to the density extremes in the smallest pores. The matching pore geometries are shown in figure 4.25. c) Pore density * pore length against time, for use in calculating initial fill rate of pore. d) Initial and secondary rates of adsorption, extracted from (c). The lengths stated in (d) are the equivalent pore penetration lengths, given that the fluid were to enter the pore in a plug fashion at the same local density as the final pore density.

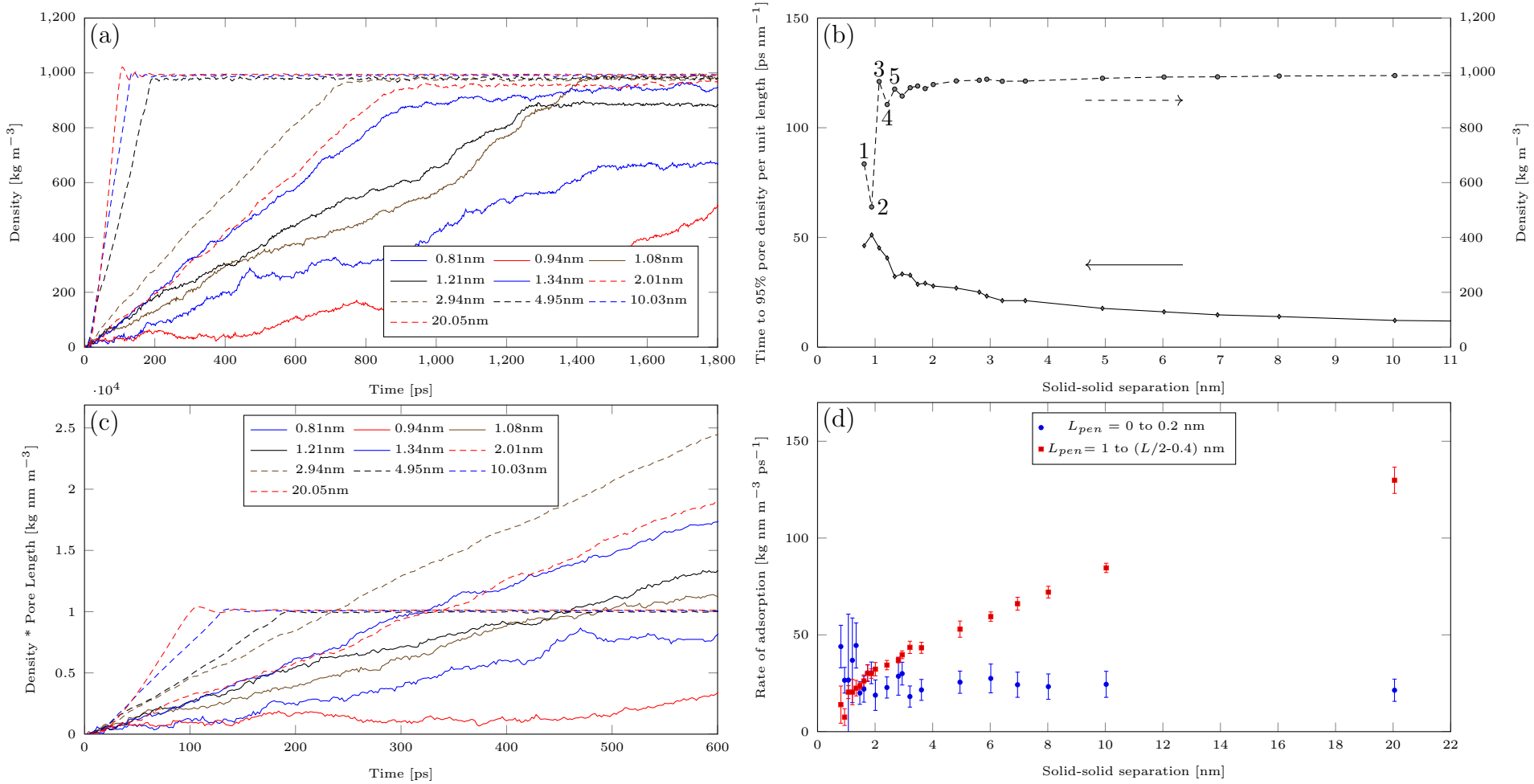


Figure 4.19: Liquid water at 300 K filling various cylindrical pores. a) Pore density against time. b) Comparison between pore fill time and the mean density calculated over the final 500 ps of (a). The labels correspond to the density extremes in the smallest pores. The matching pore geometries are shown in figure 4.25. c) Pore density * pore length against time, for use in calculating initial fill rate of pore. d) Initial and secondary rates of adsorption, extracted from (c). The lengths stated in (d) are the equivalent pore penetration lengths, given that the fluid were to enter the pore in a plug fashion at the same local density as the final pore density.

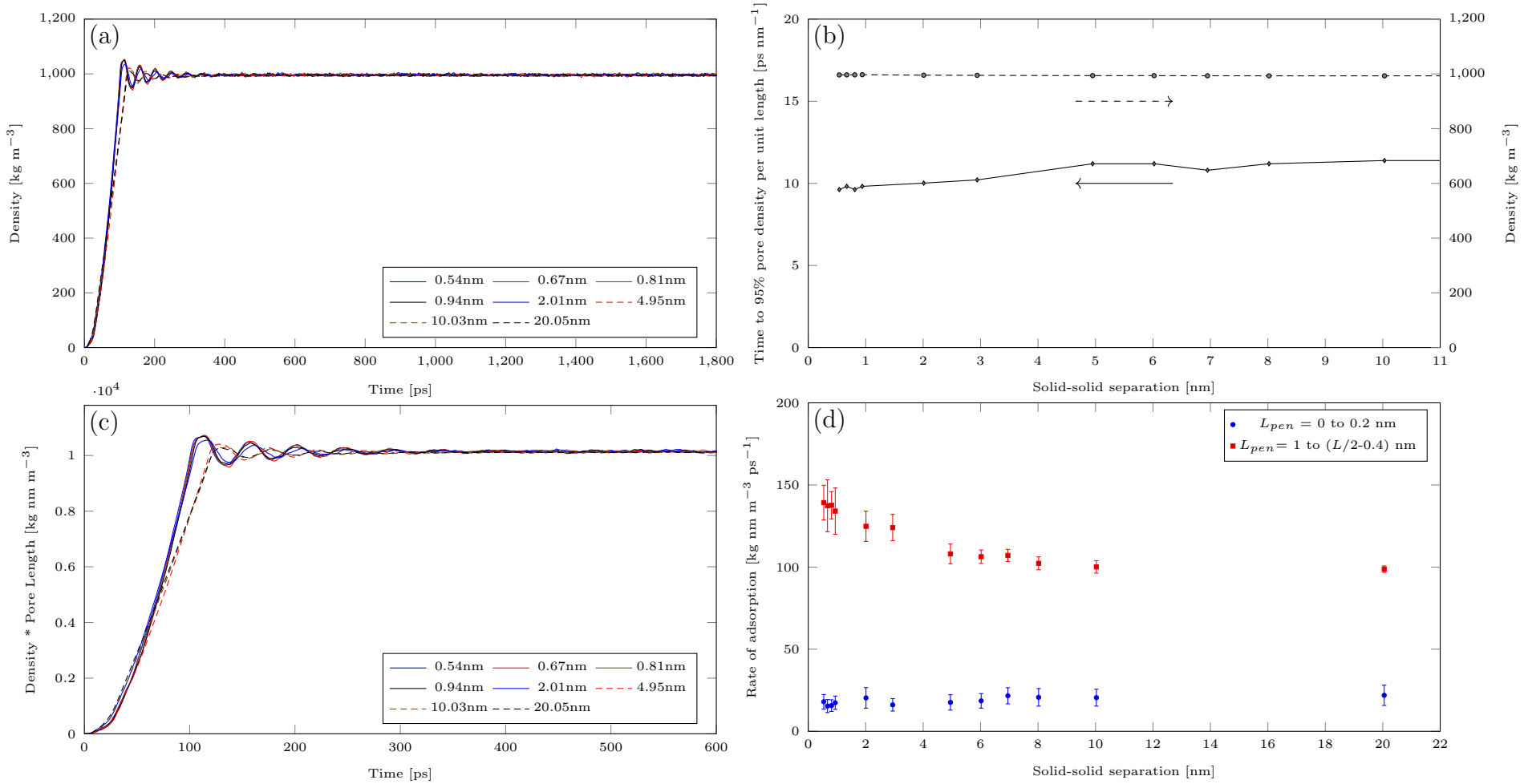


Figure 4.20: Liquid water at 300 K filling the outside of various cylindrical pores. a) Pore density against time. b) Comparison between pore fill time and the mean density calculated over the final 500 ps of (a). The labels correspond to the density extremes in the smallest pores. The matching pore geometries are shown in figure 4.25. c) Pore density * pore length against time, for use in calculating initial fill rate of pore. d) Initial and secondary rates of adsorption, extracted from (c). The lengths stated in (d) are the equivalent pore penetration lengths, given that the fluid were to enter the pore in a plug fashion at the same local density as the final pore density.

In sub-figure (c) of figures 4.18, 4.19, and 4.20 the density is multiplied by the length of the pore in order for comparison to be made between the rate of filling in each pore. This multiplication is required as some pores are different lengths and as such the change in density with time is not a comparable quantity. see table 4.1 for the specifications of each pore.

In sub-figure (d) in figures 4.18, 4.19, and 4.20 the rate of adsorption is plotted. This is calculated from the gradients of sub-figure (c).

Figure 4.21 is included here for completeness and contrast with the 400 K results presented in figure 4.63.

The linear relationship between pore fluid density and time for all pore sizes and shapes, seen in figure 4.18 (a) and (c), suggests that the filling mechanism is the same for liquid water in all pores. There is however a visible lag initially in the larger pores, in the first 20-30 ps once the pore has been made accessible.

There are several possibilities for the presence of this lag region. The first is that there is a relaxation period after the barrier is removed where the water has to break its initial surface, extending beyond the entrance of the pore, in order to form a new interface with the internal pore structure. The problem with this is that one would expect a bulging in the centre of the pore if this was the case however, as seen in figure 4.24, the fluid surface is flat in the 10 nm pore during this period. Only after the fluid is 2 nm into the pore does it begin to bulge out, indicated that the driving force behind the pore filling process is by majority the piston. The 0.7 and 3 nm slit pores are shown in figures 4.22 and 4.23 for comparison with the larger 10 nm pore. Another possibility is that there is an initial expansion of the liquid, due to it already being compressed by the piston, during a delay period whilst the effects of the piston compression reaches the fluid front and forces it into the pore. This is indicated by the gradual bulging of the surface seen in figure 4.24. This would be confirmed by a sudden reduction in the reservoir density at the time of barrier removal. A further reason is that there is

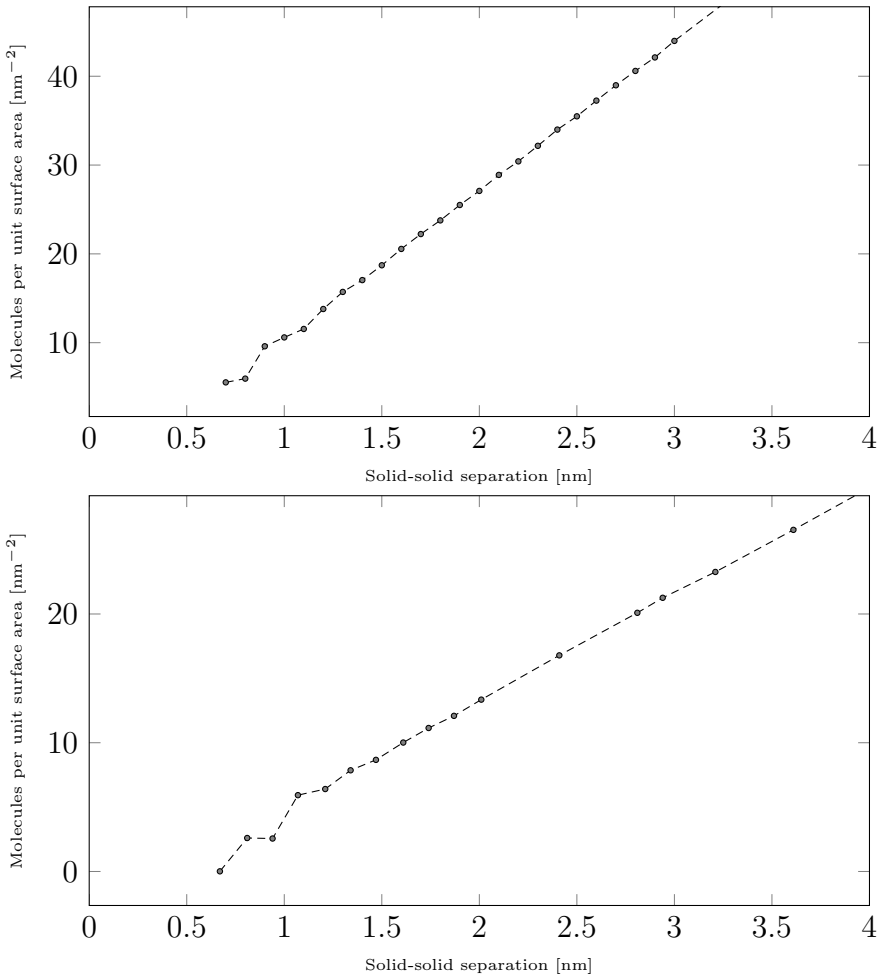
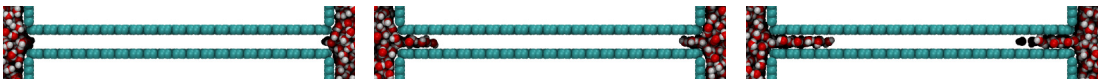


Figure 4.21: Average molecules of water within slit (top) and cylindrical (bottom) pores, after equilibration, at 300 K (liquid).

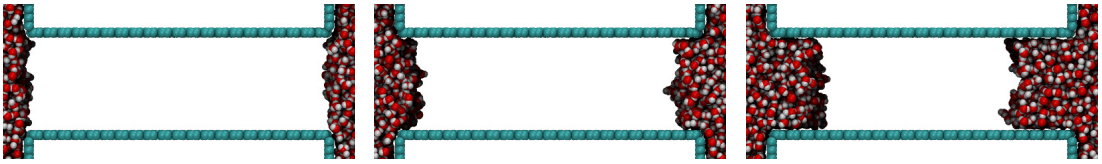
a region which the fluid has to pass before being counted as within the pore for density calculation purposes. The initial fluid front location is slightly away from the pore entrance due to the non-zero size of the barrier atoms that are initially in place. This leads to a slow initial rate due to only a few atoms counting as within the pore for density calculation purposes whilst the entire fluid front has not yet entered the pore space. If this was the case then the initial and secondary rates of filling should be proportional as the same distance is traversed before the pore is entered.

The two rates are shown in figure 4.18 (d), measured over two ranges. The lengths stated in this figure are the equivalent pore penetration lengths, L_{pen}, given that the fluid were to enter the pore in a plug fashion at the same local density as



4 ps, 1.4 % full *24 ps, 7.8 % full* *60 ps, 28.0 % full*

Figure 4.22: Snapshots of liquid water at 300 K filling a 0.7 nm slit pore.



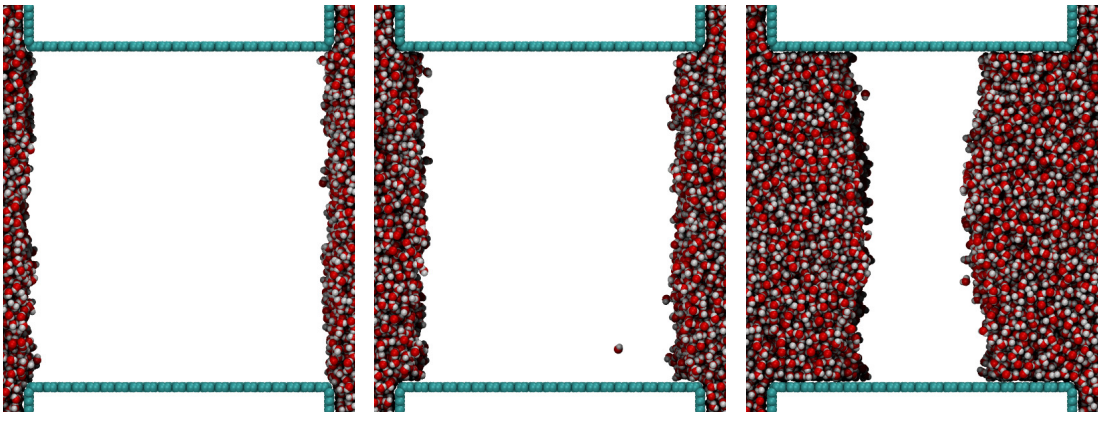
4 ps, 0.3 % full *24 ps, 11.7 % full* *60 ps, 41.1 % full*

Figure 4.23: Snapshots of liquid water at 300 K filling a 3 nm slit pore.

the final pore density. The conversion between this length and the instantaneous pore density, ρ_x, is as follows:

$$\rho_x = \rho_{mean} \frac{2L_{pen}}{L} \tag{4.3}$$

where ρ_{mean} is the final mean pore density and L is the total pore length. For liquid water inside slit pores the values of the penetration length are equivalent to 0-4.5 % and 22.7-90.7 % filled pores always, since the length of the slit pores is constant.



4 ps, 0.25 % full *24 ps, 12.0 % full* *60 ps, 64.7 % full*

Figure 4.24: Snapshots of liquid water at 300 K filling a 10 nm slit pore.

For water, the initial rate is independent of the pore size and seemingly independent of the level of packing within the pore, indicated by the final pore density shown in figure 4.18 (b). In slit pores smaller than 0.9 nm the initial rate is similar to the secondary rate.

The rate of filling of the pore has a strong dependence on the pore size for slit and cylindrical pores, with an increasing rate of filling up to a maximum value. The time to reach 95 % of the final pore density also reflects closely the secondary rate, as expected since the rate of filling does not change with time up until the pore has filled.

One would expect that the slit pores that fill to the higher fluid densities, the peaks in figure 4.18 (b), would take longer to fill and the lower fluid density pores, the troughs, would be quicker. However, the 0.8 nm pore, which is in a trough, takes almost as long to fill as the 0.9 nm pore, which is at a peak. The secondary rate measured is actually lower than that for the 0.9 nm pore, which suggests it would take even longer to fill. The reason it does not is that the final density in the 0.8 nm pore is much lower than the 0.9 nm pore. The other unusual point is that the 1 nm pore exhibits a larger fill rate than both the 0.9 and 1.1 nm pores, which are at a peak and trough in the density respectively.

These two points suggest that the slit pores that exhibit a peak or a trough in the density fill slower than the pores of similar sizes that do not. This is easy to understand when looking at figures 4.25 (2) and (3) which show the fluid arrangement for the 0.9 and 1.1 nm channels. In (3) the fluid is compacted into a quasi-solid arrangement for there to be two fluid layers. Any decrease in the pore size would result in a loosely packed single fluid layer. This is a high density system and fluid takes longer to find its place and attain an efficient packing. In (4) the fluid is almost as spread out as it can be for two layers and any further increase in the pore size would cause a tightly packed three layer system to form. The fluid here has no problem filling the space it has been provided with, however

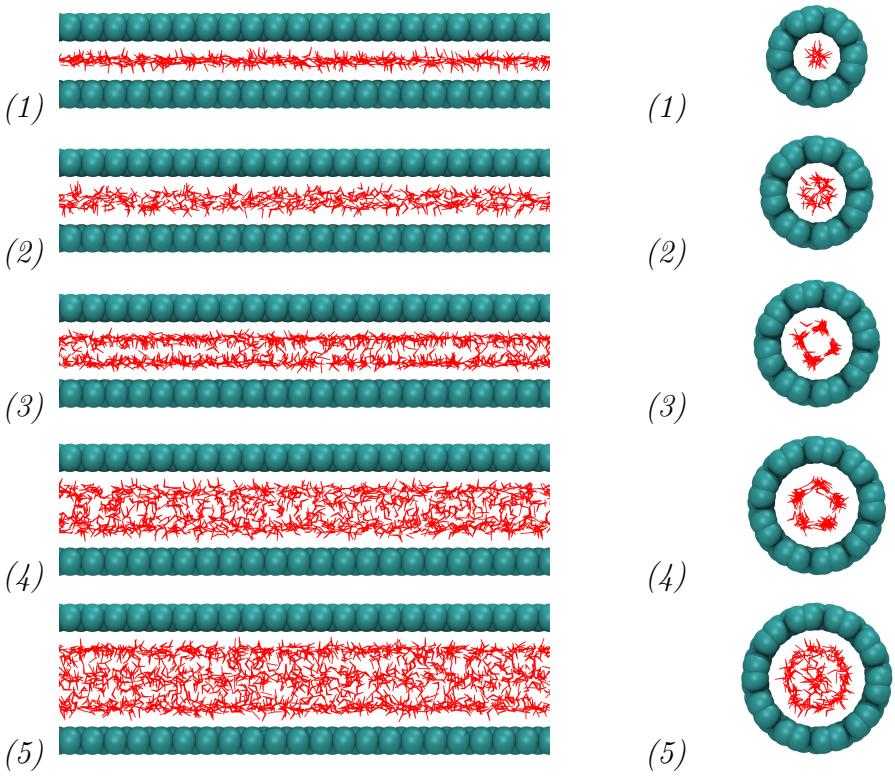


Figure 4.25: Orthographic (end on) views of slit (left) and cylindrical (right) pores filled with water. The carbon surface atoms are shown as spheres of radius σ_{ss} whilst the water is shown in skeletal form as bonds only. The depth of each pore has been cut to 8 nm for image comparison purposes. The numbering corresponds to the labelled points in figures 4.18 and 4.19 and capture significant fluid phases present in the smallest pores. Left: 1) 0.7 nm, 2) 0.8 nm, 3) 0.9 nm, 4) 1.1 nm, 5) 1.3 nm. Right: 1) 0.81 nm, 2) 0.94 nm, 3) 1.08 nm, 4) 1.21 nm, 5) 1.34 nm.

the fluid density is now lower than what it would be in the bulk. This means that the fluid wants to be more compacted, however it is pulled apart due to the presence of the walls. Since the fluid density in the pore is less than that of the bulk, the fluid is no longer arranged in its optimal configuration, preventing the fluid from being pulled/pushed into the pore as quickly as it would otherwise be. Also likely, is that the change in density between the bulk and the pore entrance results in a less steep pressure gradient and as such the fluid is not pushed in as fast as it would otherwise be. The pressure gradient is also less steep in the cases of higher fluid packing. It would seem then that the fluid in-between the peaks and troughs of the density profile, fluid of a closer density and fluid arrangement as the bulk as is the case in the 1 nm pore, flows through the pore more freely

when filling a vacuum.

These results are consistent with the work of Striolo et al. (2003). In their study of 0.6 to 2 nm slit pores, they noted that pores filled by a capillary-condensation-like mechanism. The authors observed oscillations in the solvation force profile as a function of the wall-to-wall separation. This indicates that there are repulsive and attractive peaks of the force which correspond to separations in which confined water molecules can or cannot establish well defined layers, stabilised by intralayer hydrogen bonds.

In the 400 K case discussed in section 4.4.4, the fluid is not attracted to the wall at all, which would suggest that the wall is not pulling the fluid apart here. However, the higher temperature of the fluid could mean that it is able to quickly break free from the pull of the wall atoms. It is questionable whether in a real system, where temperature coupling is imposed by the solid surface and not "magically" applied to the gas molecules, the same would occur. It is also possibly that in the liquid case the physical presence of the wall alone causes the fluid to arrange in a way such that the hydrogen bonds no longer align nicely and the fluid is more spread out due to that, rather than being pulled apart. However, this would mean that the 1 nm pore should take longer to fill, since the hydrogen bonds would become even less aligned. In reality, it is more likely that the temperature is low enough that there is some notable attraction to the wall.

The density profiles for the 0.9 and 1.1 nm slit pores are shown at the bottom of figure 4.26. As can be seen, between the centre of the pore and the wall, there is a single large peak. In the 1.1 nm case there is a relatively small peak close the the wall and then what looks to be a smaller peak within σ_{sf} of the first, before a sharp trough (only half of the profile is shown as it is symmetrical). The second, smaller, peak is due to the enforced arrangement of the fluid by the layer of fluid in contact with the opposing wall.

The density of the fluid flowing along the pore, before the two fronts have met,

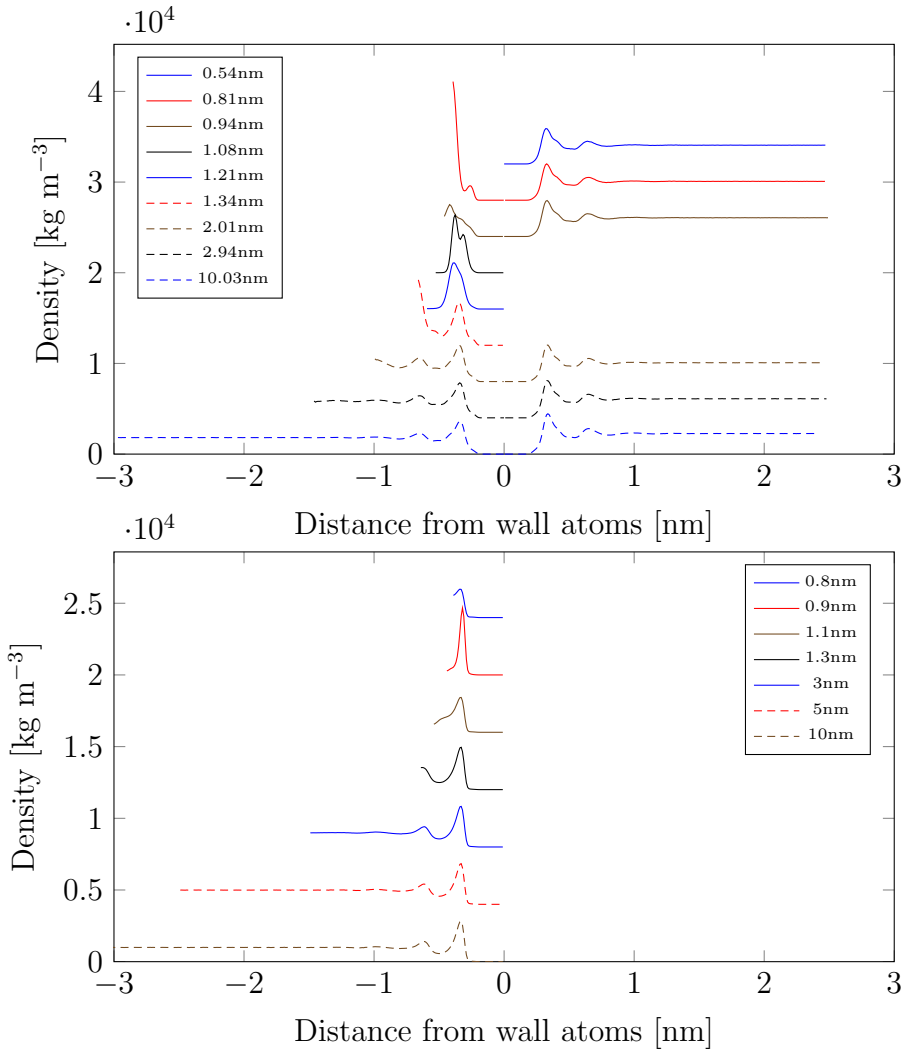


Figure 4.26: Density profiles of water, at 300 K, (top) inside and outside cylindrical pores and (bottom) inside slit pores. Calculated from a separate 5 ns simulation after the reservoirs have been removed and the pore made periodic.

is relatively unchanged from the bulk fluid. This is evident in the lack of any oscillations or further increase in the fluid density once the two fronts impact with one another. Oscillations only begin to occur for the larger pores and are likely due to the shock of the impact between the two fronts. Not long after the appearance of density oscillations, the relationship between pore size and rate of filling is unchanged. At this point the rate of filling of the pore has reached a maximum and is no longer a function of the pore size.

The time to fill reported in figure 4.18 does not account for any impact oscillations in the density and is measured up to the first point where the density becomes 95

% of the final mean density. For slit pores larger than 5 nm, where oscillations are present, the oscillations are dampened out by roughly 200 ps, approximately 120 ps after the fluid boundaries have met. Given this, it would seem that pores 3 nm and larger are the quickest to converge to equilibrium, even though figure 4.18 (b) suggests that 6 nm and above are quicker still.

Other than already already discussed, there is minimal difference between the filling mechanism for liquid water in slit pores of differing sizes even when different final densities are reached.

As seen in figures 4.27 and 4.28, the mean density of the fluid in the reservoirs quickly converges before the barrier is removed. Once the barrier is removed there is, on average, a small decrease in the mean density by approximately 0.5 % before it quickly recovers over 20 ps, which is less than the general total time for pore filling (roughly 100 - 350 ps). This change in the density is similar in magnitude to the small variations in the density over the entire range and as such likely has little effect on the results. This is however an indication that the initial lag observed and discussed earlier is caused by this, since the time-scales are similar.

For water inside cylindrical pores, the initial rate of filling is constant within reasonable uncertainty, as seen in figure 4.19. The initial and secondary rates become similar when the solid-solid separation is less than 2 nm. However, at this separation the statistical accuracy becomes much smaller than for the same separation in the slit shaped pores. The fill rates for both the slit and cylindrical pores asymptote towards a similar value, between 150 and 200 kg nm m^{-3} ps^{-1}.

This is unexpected for both the slit pores and cylindrical pores. The Navier-Stokes equations, when solved for continuum scale flow in channels and cylindrical pipes, predict that the mean fluid velocity is proportional to $(D_{ss}^2/C + bD_{ss})$, where D_{ss} is the solid-solid separation (height of channel or diameter of cylindrical pipe), b is the slip length and C is either 6 or 8 depending on if a channel or cylindrical

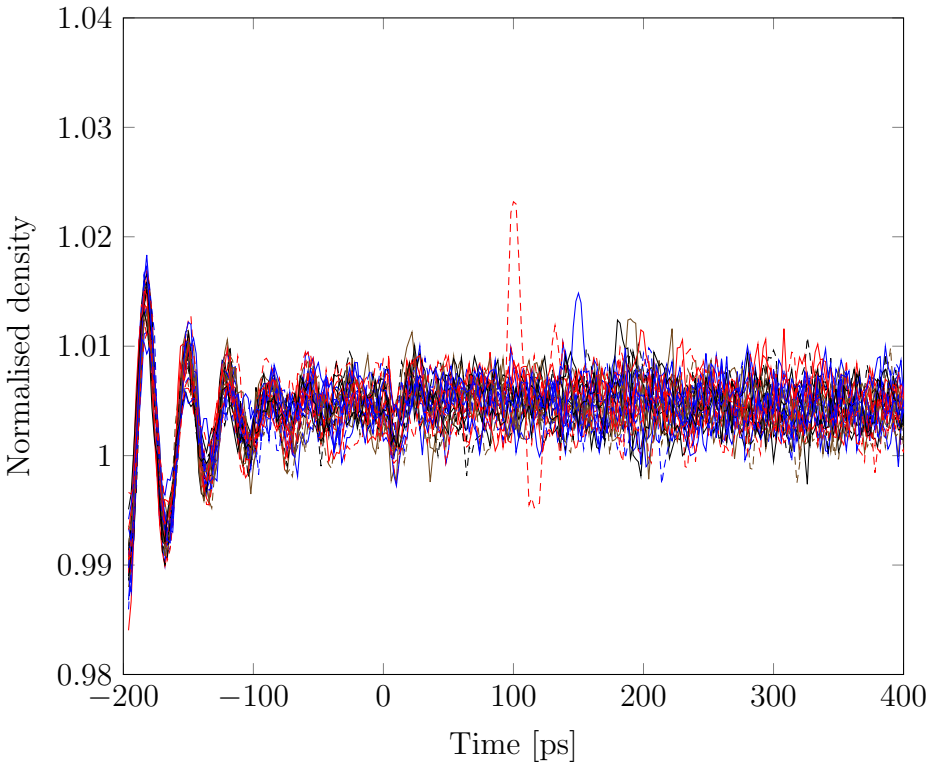


Figure 4.27: Mean water reservoir density over pore filling process for 0.7-10 nm slit pores. $t = 0$ ps is the point at which the barrier is removed. Densities have been normalised by the equilibrium bulk density.

pipe. See equations 5.2 and 5.3. Hence, the relationship between fill rate and the solid-solid separation should be proportional to D_{ss}^2 or D_{ss} if $b >> D_{ss}/C$ and given a constant slip length. The velocity of the fluid front is also well below the speed of sound and as such choking should not be occurring.

The rates presented here, if accurate, suggest a changing slip length. The slip length would have to decay exponentially with respect to the separation in order to cause the relationship seen in figures 4.18 (d) and 4.19 (d). This is unlikely to be the case as the single phase slip length, presented in chapter 5, is constant for all separations for liquid water in slit pores. A likely reason for the capping of the rate of filling seen here is that the length of the pores are simply not long enough for the fill rate to reach its maximum value for the larger pores. It is expected that a faster rate of filling would be achieved given that the pore was much longer and that an appropriate and accurate method of maintaining the reservoir pressures are used to match the longer pores. As such, the fill rates presented here

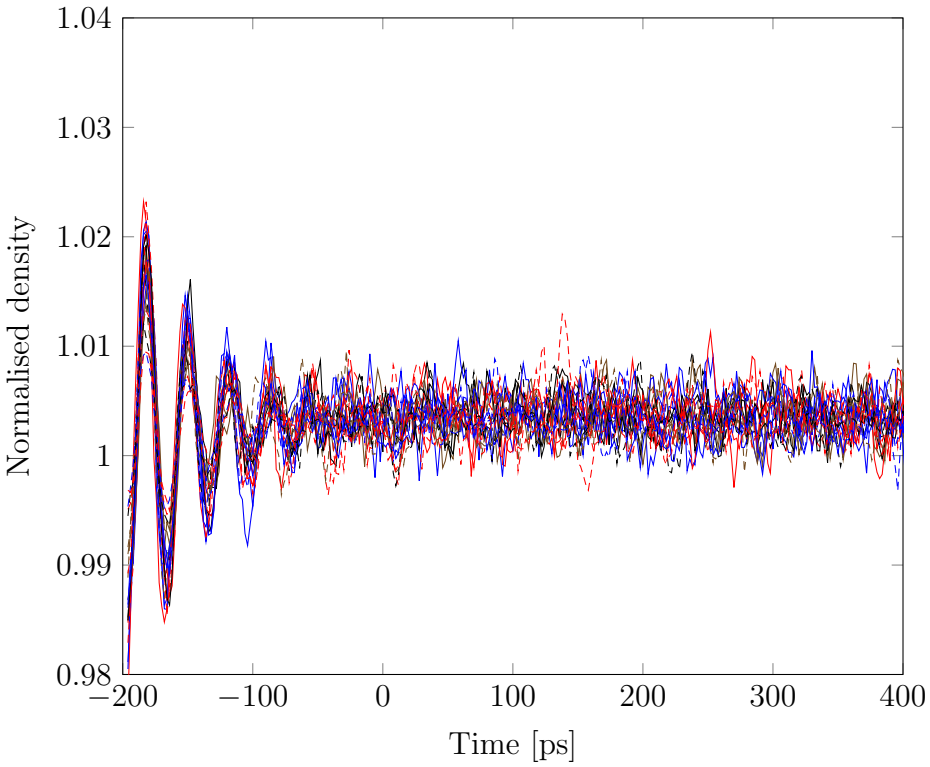


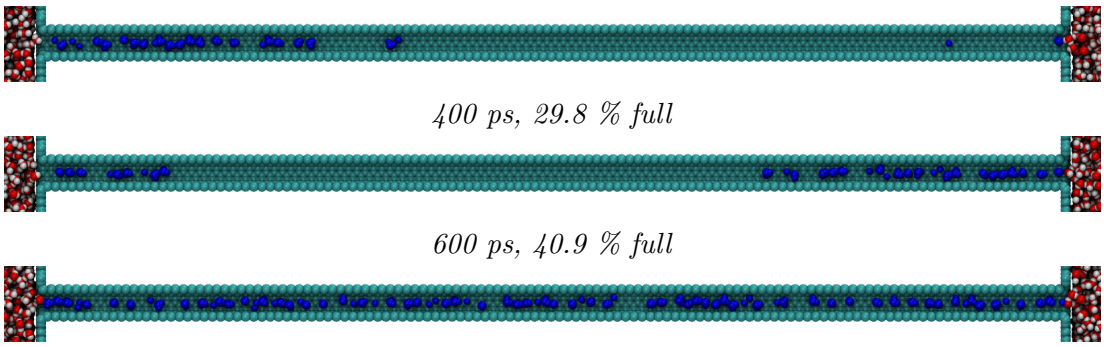
Figure 4.28: Mean water reservoir density over pore filling process for 0.81-10.03 nm cylindrical pores. $t = 0$ ps is the point at which the barrier is removed. Densities have been normalised by the equilibrium bulk density.

should be taken to be the initial fill rates due to inertial effects. This is confirmed somewhat in figures 4.18 (c) and 4.19 (c) for the 20 nm pores. Here there is a slight curvature seen, such that that the fill rate is not yet constant. This is easier to see for the slit pore as the pore density in the 20 nm pore crosses that of 10 nm pore. The results for cylindrical pore sizes 3 nm or less show this linear relationship that is expected due to a large slip length since the pores are long enough in these cases. It is also possible that the Poiseuille flow approximation is incorrect here and that concept of slip length loses its meaning. What is being seen here could be a plug-flow with a slip at the wall which is commensurate with this plug-flow.

Water filling the pore space created between a set of adjacent cylindrical pores, on the other hand, asymptotes towards a much lower value of approximately 100 kg nm m^{-3} ps^{-1}, however the fill rate for the smallest pores is constant at a value just short of 150 kg nm m^{-3} ps^{-1}. Unlike for fluid filling the inside of cylindrical pores,

the nanotubes here are all the same length, 10.185 nm. Additionally, the ratio of fluid flow area to total area (including solid boundary) decays exponentially as the solid-solid separation is increased as opposed to increasing in the case of slit and cylindrical pores. This increases logarithmically for slit and cylindrical pores. The area available to fluid flow is approximately linear with respect to D_{ss} in the outside fluid cases for the sizes studied here, given that the minimum separation between solid surfaces in adjacent cylinders is set constant at 5 nm. This is similar to the slit pore cases which is exactly linear with respect to D_{ss}, however for cylindrical pores the area is proportional to D_{ss}^2. This suggests that the ratio between the fluid flow area and the solid surface area, perpendicular to the direction of fluid flow, is responsible for the capped fluid fill rate, instead of the insufficient pore length. In this case the solid barrier surrounding the pore is limiting the rate at which fluid can enter the pore. Since figures 4.27 and 4.28 show a reasonably constant reservoir density, equal to the bulk fluid density, the reservoir specification is correct and is unlikely responsible for this phenomena. This points towards the conclusion that the solid surface surrounding the pore presents resistance for fluid entry in the initial stages of pore filling yet has little effect on the macro-scale. This could suggest that in nano-pores the geometry of the surface surrounding the pore entrance influences the fluid flow rate in the pore in a way that is not predicted by Navier-Stokes.

The piston in some of the pores begins to bulge in the centre during filling, suggesting fluid is entering the pore faster than it can be replaced by adjacent fluid and as such the piston motion is limited by the fluid between it and the solid barrier surface. This suggests that the reservoir is simply not large enough to avoid the effects of the pseudo-pore formation even though there is a large continuous density region between the piston and the solid surface. A larger reservoir would not exhibit this phenomena and thus this limited reservoir size could be the reason for the limited fill rate of the pore. Contrary to this, most pores do not exhibit this bulging and this is not seen at all in the cylindrical

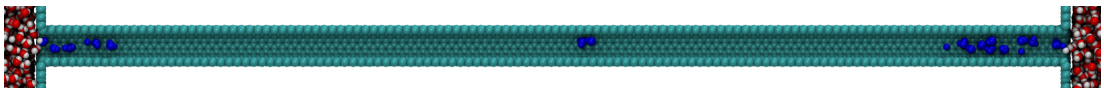


400 ps, 29.8 % full

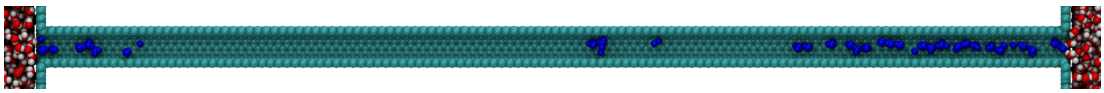
600 ps, 40.9 % full

1800 ps, 100.0 % full

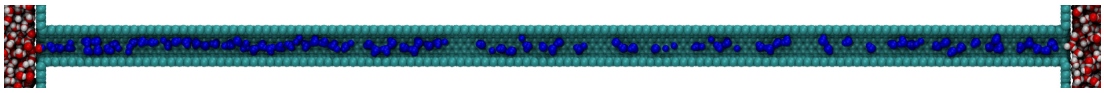
Figure 4.29: Snapshots of liquid water at 300 K filling a 0.81 nm cylindrical pore, coloured based on proximity to solid surface: 0-0.6 nm: blue; 0.6-1 nm: green; 1-1.4 nm: yellow; 1.4+ nm: as reservoir fluid.



400 ps, 7.6 % full



600 ps, 22.3 % full



1800 ps, 100.0 % full

Figure 4.30: Snapshots of liquid water at 300 K filling a 0.94 nm cylindrical pore, coloured based on proximity to solid surface: 0-0.6 nm: blue; 0.6-1 nm: green; 1-1.4 nm: yellow; 1.4+ nm: as reservoir fluid.

pores, although the reason for this could be that the shape of the pore limits the amount of possible distortion in the graphene sheet composing the piston. The flow could still be being restricted by this however, even without visible distortion in the piston. More work is required in order to confirm the reason for the capped flow rates observed here, although some possible explanations have been given above.

Unlike in the slit pores, where all pores exhibited the same plug filling mechanism, the fluid in the smallest cylindrical pores fill in a sliqhtly different manner to the larger pores. As seen in figure 4.29 (a), fluid enters the pore at a different time

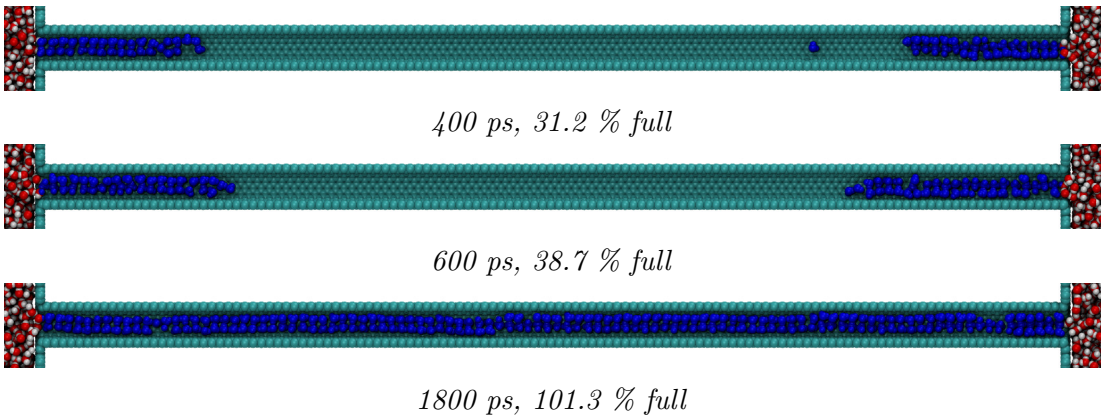


Figure 4.31: Snapshots of liquid water at 300 K filling a 1.08 nm cylindrical pore, coloured based on proximity to solid surface: 0-0.6 nm: blue; 0.6-1 nm: green; 1-1.4 nm: yellow; 1.4+ nm: as reservoir fluid.

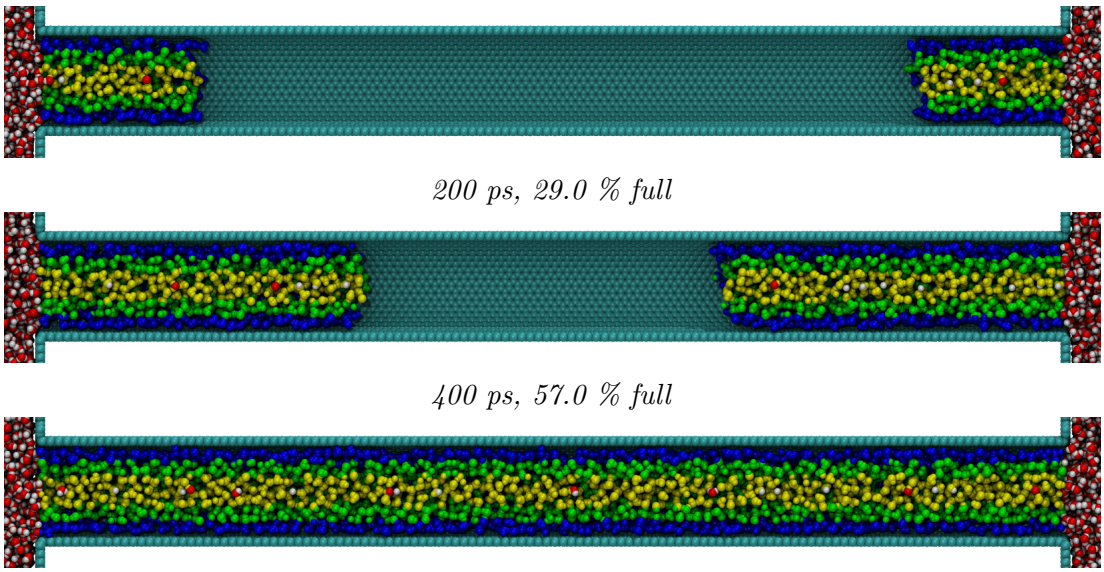
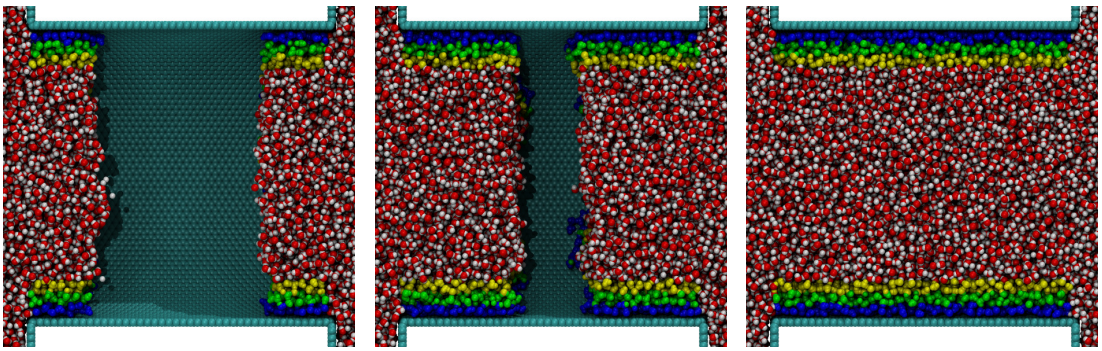


Figure 4.32: Snapshots of liquid water at 300 K filling a 2.94 nm cylindrical pore, coloured based on proximity to solid surface: 0-0.6 nm: blue; 0.6-1 nm: green; 1-1.4 nm: yellow; 1.4+ nm: as reservoir fluid.

from each end, even though the reservoir specification is the same. There is also a significant lag period before any fluid enters the pore.

Figure 4.29 (a) shows fluid entering from the left hand side of the pore whilst figure 4.29 (b) shows fluid at both ends. Here the water has entered from the left and continued to travel along the pore all the way to the right hand side. In the mean time fluid has stopped entering the pore from the left and as such there



60 ps, 42.1 % full *92 ps, 68.3 % full* *120 ps, 91.5 % full*

Figure 4.33: Snapshots of liquid water at 300 K filling a 10.03 nm cylindrical pore, coloured based on proximity to solid surface: 0-0.6 nm: blue; 0.6-1 nm: green; 1-1.4 nm: yellow; 1.4+ nm: as reservoir fluid.

is a gap. Fluid molecules then enter at random times and in random numbers and travel through the pore at a rate much faster than the rate of fluid entering into the pore. This suggests that given there was only a single reservoir, fluid would quickly make its way along and out the other side of the pore before more fluid could enter. This is an exclusive phenomena for single file flow in hydrophobic cylindrical pores. The fluid goes from having several degrees of freedom for translational motion to just one, resulting in molecules exploding into and along the pore like a bullet along the barrel of a gun. This occurs to a lesser degree in the 0.94 nm pore (figure 4.30), where there is still only a single fluid layer present, however the fluid has more space to align itself favourably with the adjacent fluid molecules and retain hydrogen bonding.

This behaviour has completely disappeared in the 1.08 nm and larger pores where the fluid enters in a similar plug like manner as in the case of slit pores. As seen in figures 4.31, 4.32, and 4.33, the fluid now fills in a a plug like fashion, similar to the slit pore cases. Here however, no pronounced curvature is seen at the pore fluid front, possibly indicating decreased friction at the solid fluid interface.

For very small pores there is an energy barrier to enter the nanotube. This can be understood as water has to break hydrogen bonds to enter and lose entropy (as the pore induces a linear ordering). The free energy, A, increases with both

an increase in the internal energy, U, and with a decrease in the entropy, S, as follows: $A = U - TS$. Because of this, the fluid will not enter naturally, but only after a fluctuation large enough to overcome this barrier. The barrier decreases as pores becoming larger, so this is only seen in especially tiny pores.

The 1.08 nm pore is only slightly larger than the 0.94 nm pore, however the 1.08 nm pore is the first pore to exhibit more than 1 fluid layer, as seen in figures 4.25 (2) and 4.26. As such, there is a sudden change in the pore filling mechanism observed. Figure 4.25 (3) shows the neat alignment of fluid molecules in the 1.08 nm pore, allowing for strong hydrogen bonding to occur and preventing individual molecules from breaking free of the plug. This is in contrast to sub-figure (2), where there is no clear arrangement in the fluid molecules even at equilibrium.

The rate of adsorption in the 0.81 nm cylindrical pore is $13.96\,\mathrm{kg\,nm\,m^{-3}\,ps^{-1}}$, which corresponds to a flow rate of 40.41 molecules per nanosecond from each end of the pore. This is over an order of magnitude larger than the flow rate presented by Kalra et al. (2003) (5.8). However, that value is for water transport from a pure water reservoir into a salt reservoir by osmosis. The pressure driven flow against a vacuum presented here will be much faster than this due to the lack of resistance to flow and limited backward hopping of water molecules. Kalra et al. (2003) also found that for single file osmotic water flow there is an almost perfect slip boundary condition in CNTs and concluded that flow is mainly limited by particle entry and exit events and independent of the channel length up to at least several nanometers.

n-Heptane in slit pores and nanotubes

The process of n-heptane filling a 2 nm slit pore is shown in figure 4.34. Initially the fluid equilibrates with a barrier in place of the pore entrance, after which the barrier is removed and fluid fills the pore.

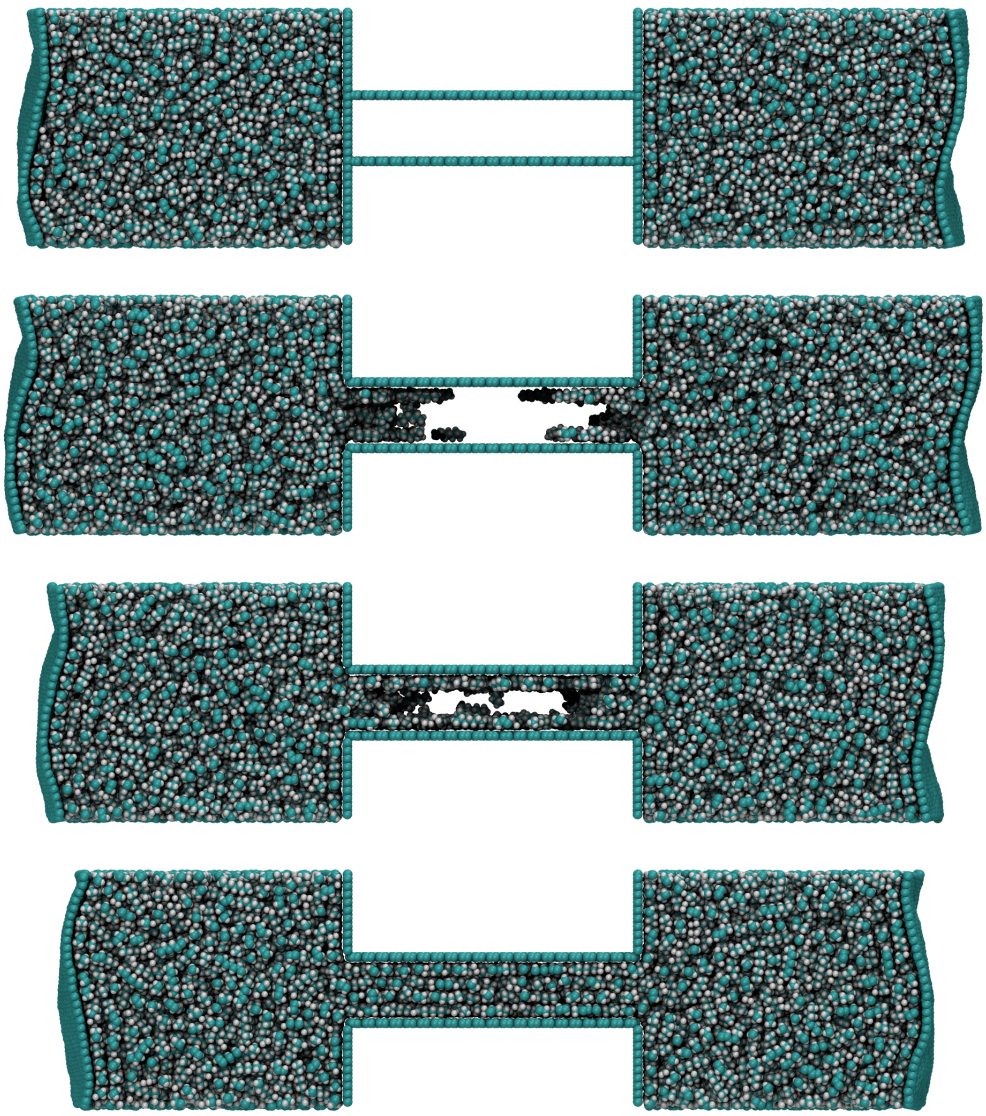


Figure 4.34: Orthographic (side on) view of liquid n-heptane at 300 K filling a 2 nm slit pore after 0, 10, 34, and 1,980 ps.

Unlike water, which has a single linear filling mechanism, n-heptane has several different filling regimes that are dependent on the size of the pore. It is difficult to predict the filling rate, even though there appears to be only two possible filling mechanisms the rates at which filling occur seem almost random.

The 2 nm slit pore imaged here exhibits three stages of filling: A surface adsorption phase, a bulk plug stage, and a slow diffusion phase to fill the remaining central vacuum. The larger slit pores do not exhibit this third stage of filling and instead act similar to water once the wall adsorption phase has occurred. The key difference being the rate at which the plug surface extends into the pore.

As in the case of water, figures 4.35 to 4.39 show the mechanisms of filling slit and cylindrical pores from liquid phase n-heptane reservoirs at 300 K, as well as filling around the outside of cylindrical nanotubes. Again, two pore lengths are used for the cylindrical pores; the full specification of each pore is shown in table 4.1.

Full page sized graphs can be found in Appendix C.

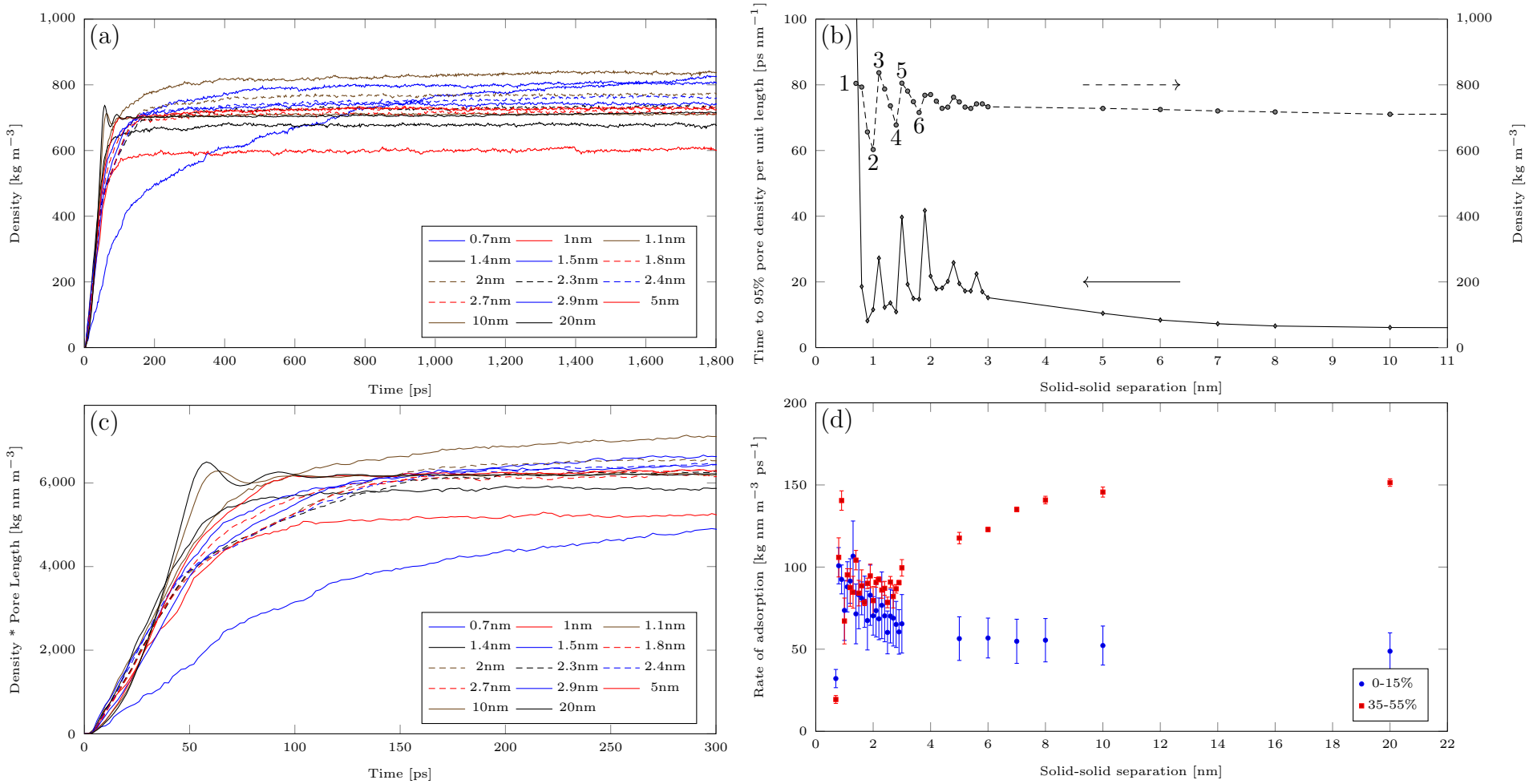


Figure 4.35: Liquid n-heptane at 300 K filling various slit pores. a) Pore density against time. b) Comparison between pore fill time and the mean density calculated over the final 500 ps of (a). The labels correspond to the density extremes in the smallest pores. The matching pore geometries are shown in figure 4.45. c) Pore density * pore length against time, for use in calculating initial fill rate of pore. d) Initial and secondary rates of adsorption, extracted from (c). The lengths stated in (d) are the equivalent pore penetration lengths, given that the fluid were to enter the pore in a plug fashion at the same local density as the final pore density.

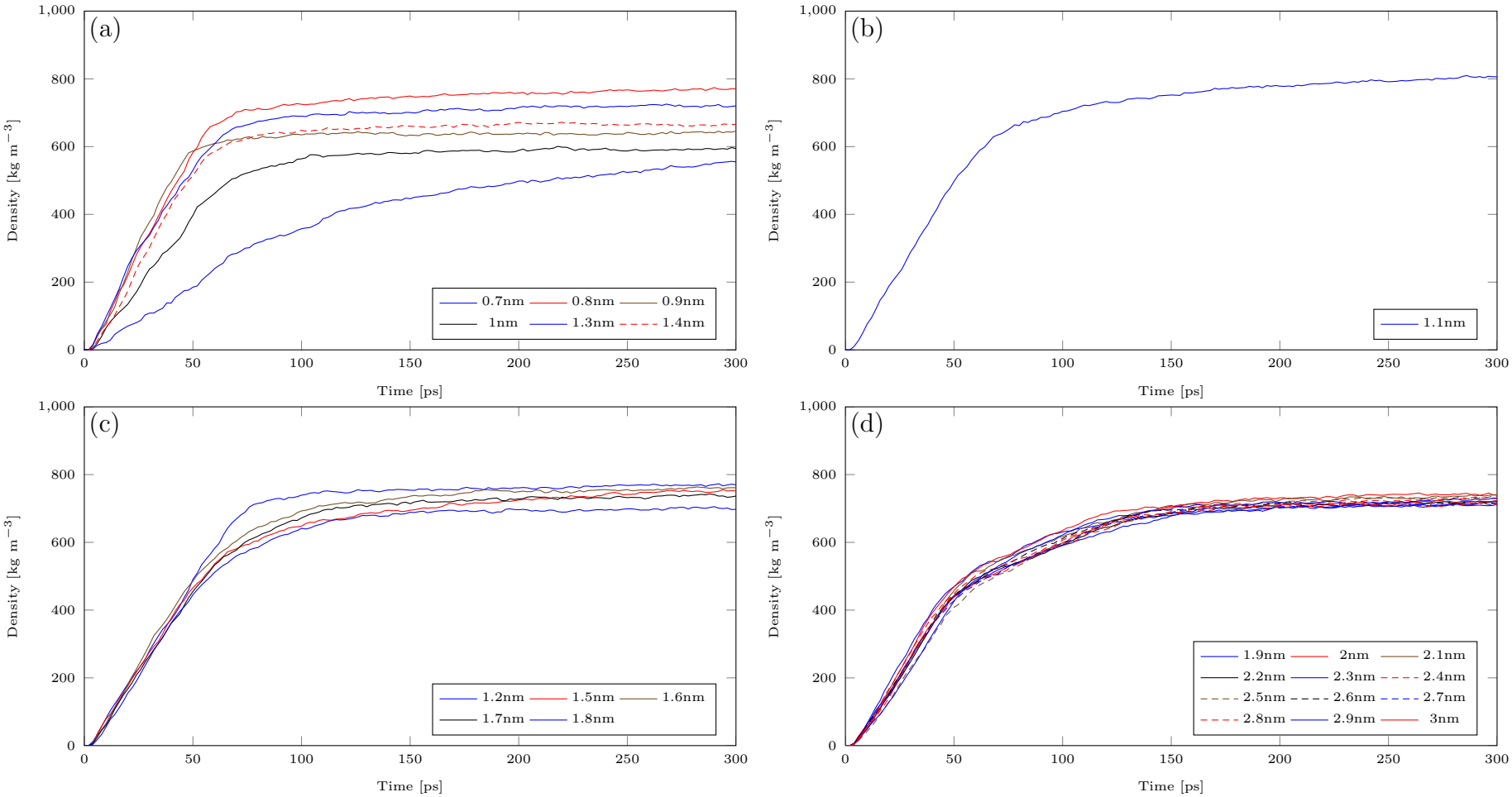


Figure 4.36: As in figure 4.35 (a), separated into groups, based on the shape of the data.

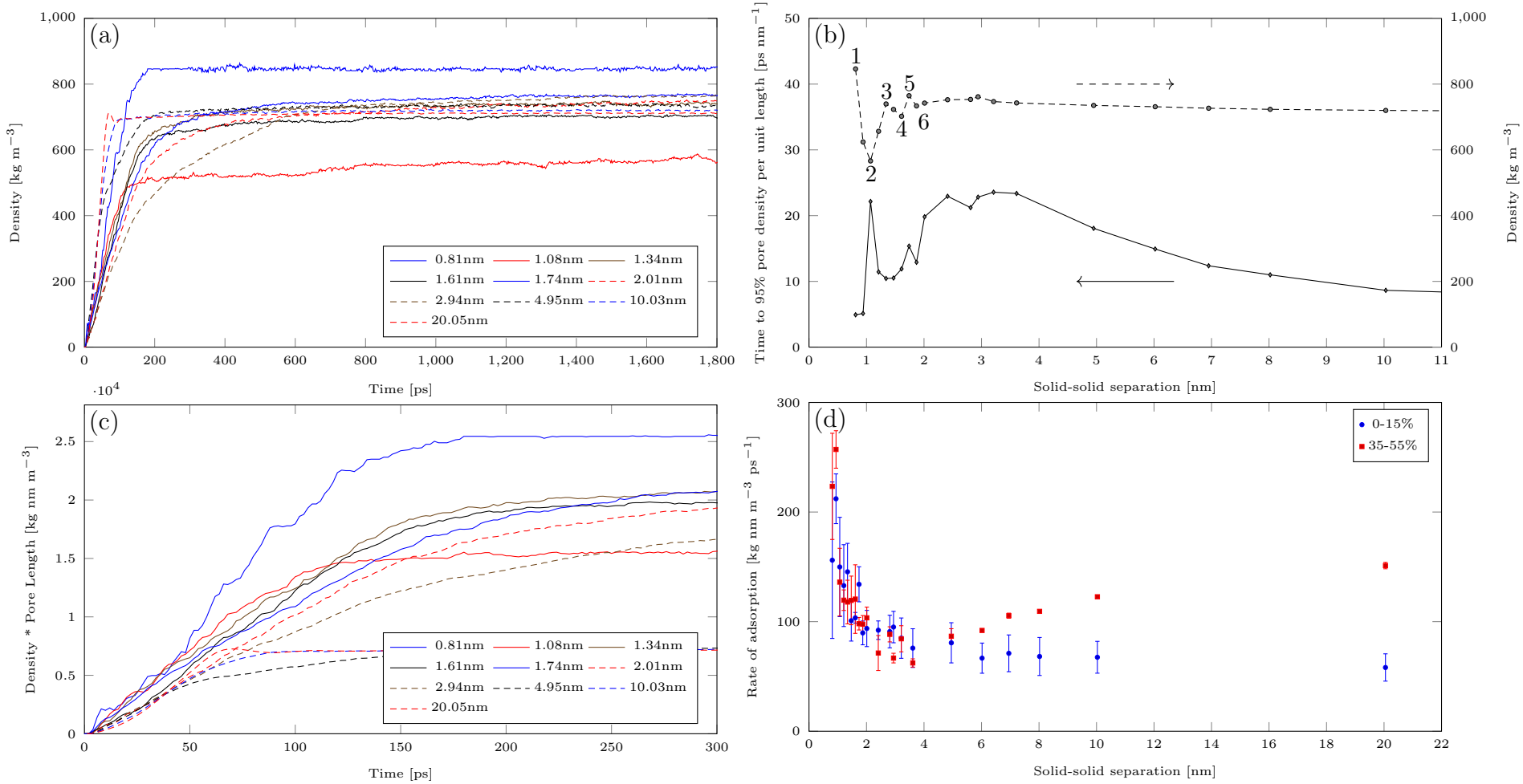


Figure 4.37: Liquid n-heptane at 300 K filling various cylindrical pores. a) Pore density against time. b) Comparison between pore fill time and the mean density calculated over the final 500 ps of (a). The labels correspond to the density extremes in the smallest pores. The matching pore geometries are shown in figure 4.45. c) Pore density * pore length against time, for use in calculating initial fill rate of pore. d) Initial and secondary rates of adsorption, extracted from (c). The lengths stated in (d) are the equivalent pore penetration lengths, given that the fluid were to enter the pore in a plug fashion at the same local density as the final pore density.

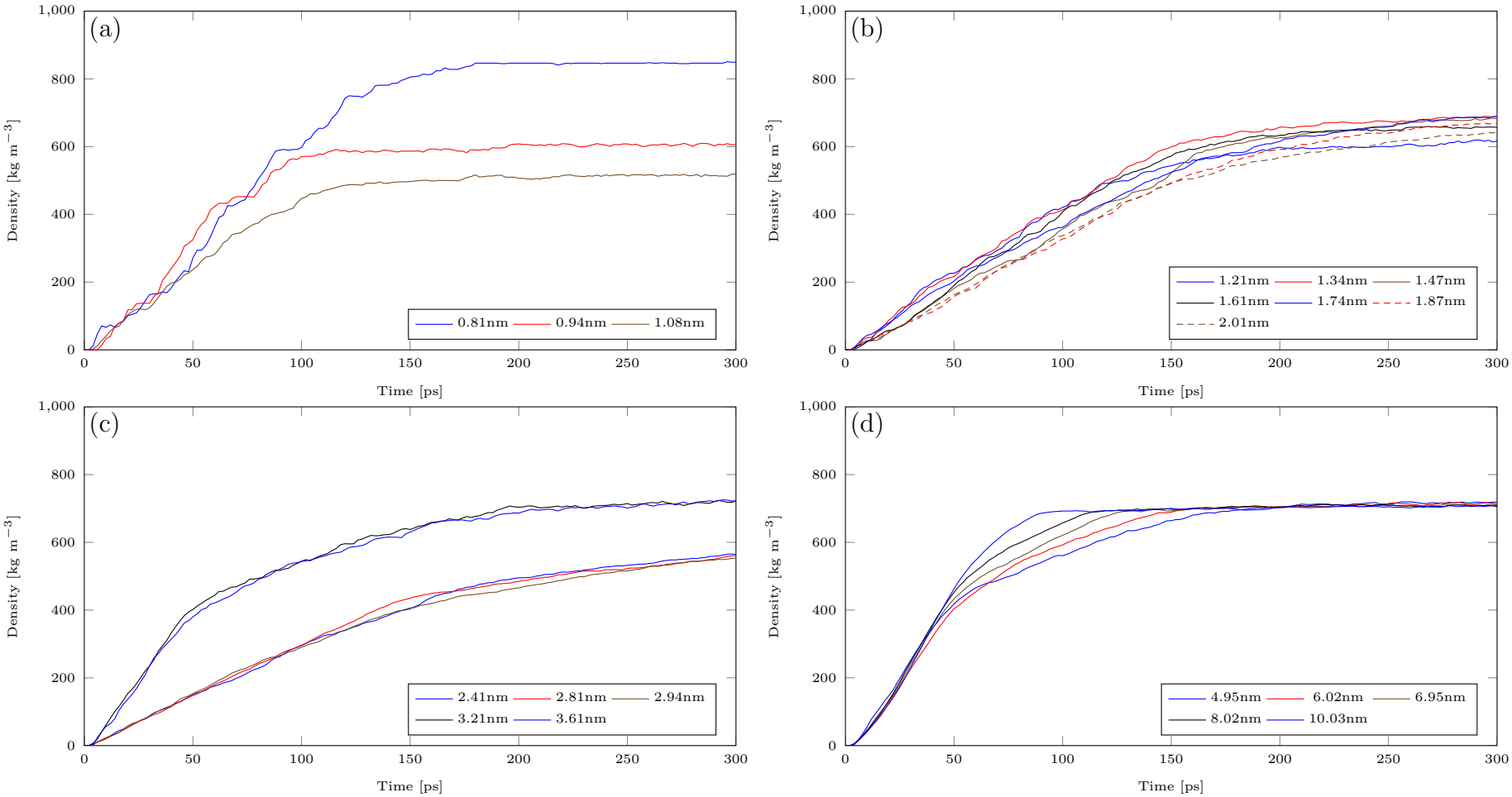


Figure 4.38: As in figure 4.35 (a), separated into groups, based on the shape of the data.

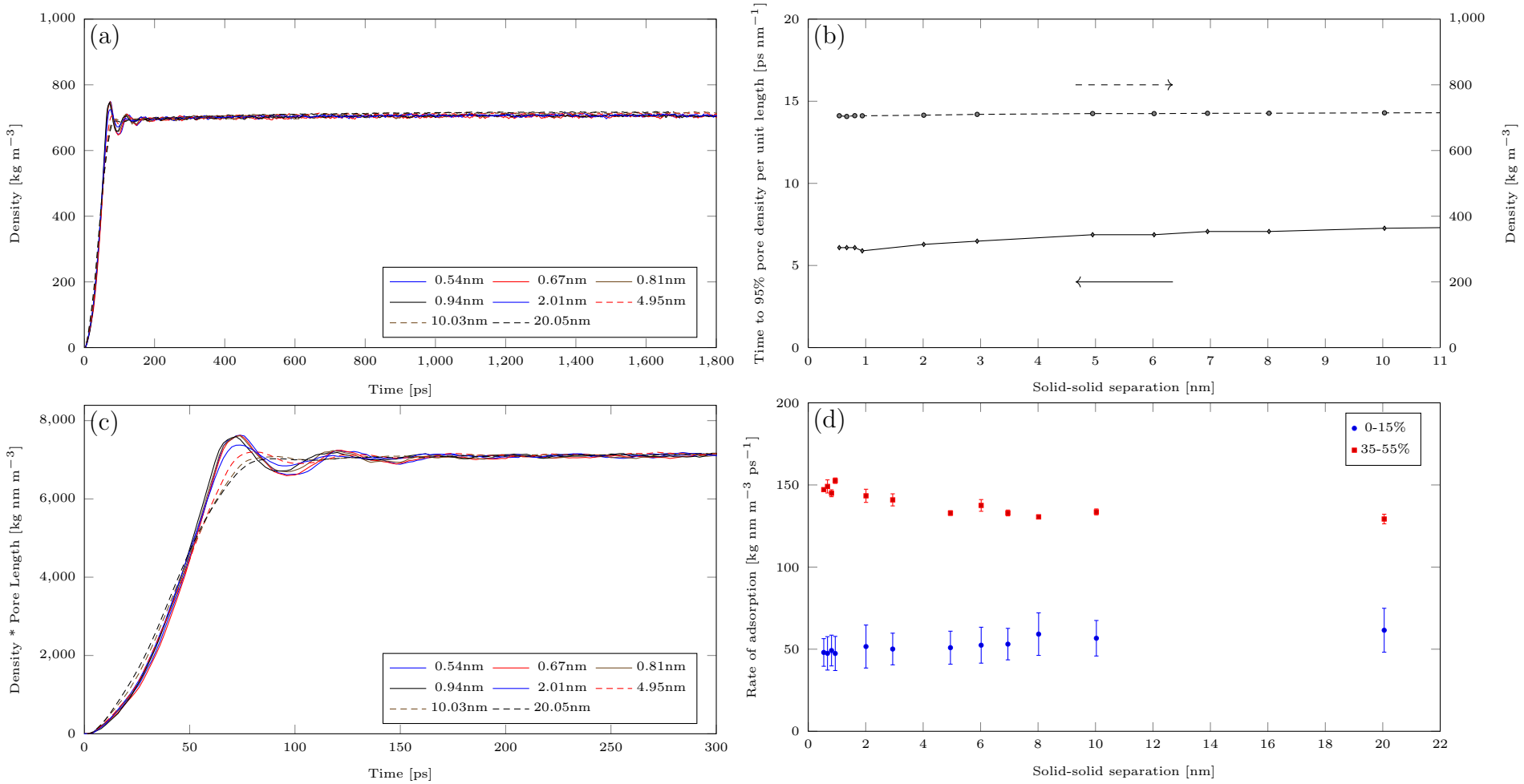


Figure 4.39: Liquid n-heptane at 300 K filling the outside of various cylindrical pores. a) Pore density against time. b) Comparison between pore fill time and the mean density calculated over the final 500 ps of (a). The labels correspond to the density extremes in the smallest pores. The matching pore geometries are shown in figure 4.45. c) Pore density * pore length against time, for use in calculating initial fill rate of pore. d) Initial and secondary rates of adsorption, extracted from (c). The lengths stated in (d) are the equivalent pore penetration lengths, given that the fluid were to enter the pore in a plug fashion at the same local density as the final pore density.

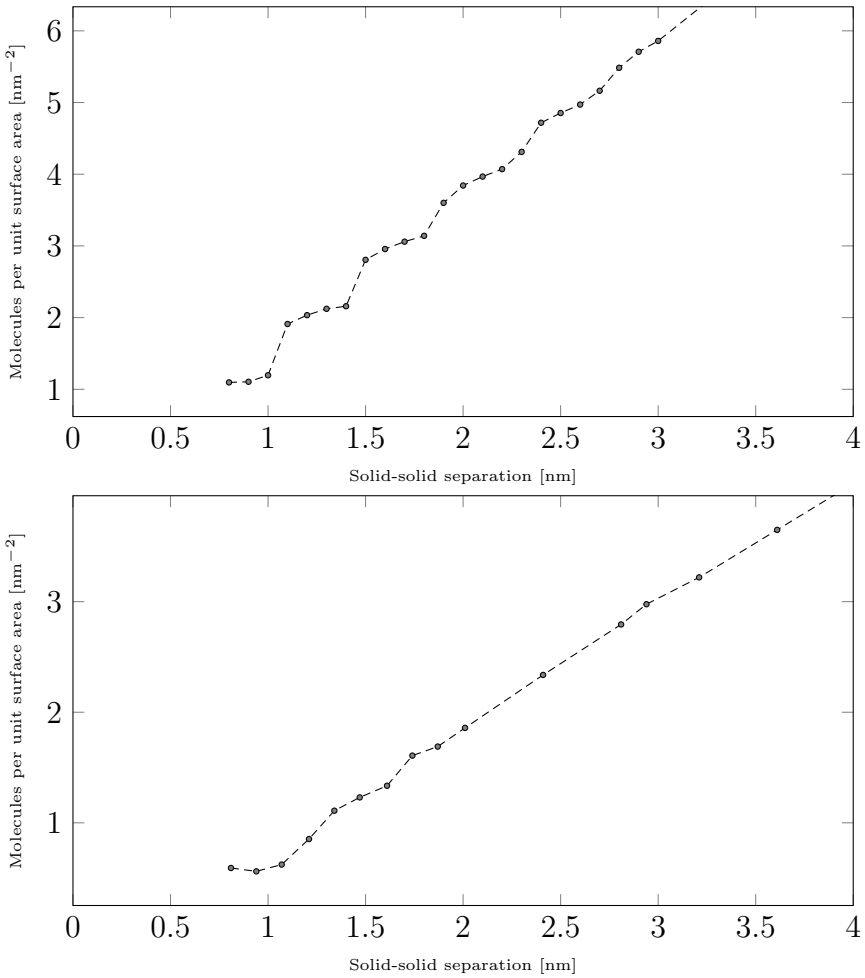


Figure 4.40: Average molecules of n-heptane within slit (top) and cylindrical (bottom) pores, after equilibration, at 300 K (liquid).

The amount of n-Heptane adsorbed from a liquid phase reservoir inside various slit and cylindrical pores is shown in figures 4.35 and 4.37. Figure 4.39 shows the amount of liquid phase n-heptane adsorbed on the outside of cylindrical pores.

As before, sub-figure (c) is created by multiplying the density by the pore length of each pore and sub-figure (d) is the rate of adsorption, calculated from the gradient of sub-figure (c).

In figure 4.36 the plots for density vs time for n-heptane in slit pores has been separated based on the shape of the graph. From this figure it is easier to see the different filling regimes present during the adsorption process.

Figure 4.40 is included here for completeness and contrast with the 400 K results

presented in figure 4.72.

Based on figure 4.36, a selection of slit pores are imaged over time in figures 4.41 to 4.44.

The larger slit pores, such as the 10 nm pore imaged fill in a simple manner in comparison to the smaller pores.

The fluid enters the pore in both the central bulk region of the pore and at the walls of the pore. The walls fill much quicker than the bulk region, however the bulk flow dominates due to the much larger volume of fluid. Once the two fronts meet, the pore has filled entirely and there is no further adsorption due to diffusion or another mechanism. Finally, the pore fluid density oscillates due to the impact of the two fronts and the sudden effect on the motion of the pistons. These steps can be seen in figure 4.44.

The smaller pores, 0.7-3 nm, exhibit a range of different behaviours dependent on the pore size and how full the pore already is. Excluding the smallest pore, 0.7 nm, which exhibits it's own unique filling mechanism due to the single file nature of the fluid in pores of that size, the data can be split by eye into four subsets shown in figure 4.36. Even given this, there are only two fill regimes in effect here, pull dominated and push dominated, although some pores display traits of both depending on how full the pore already is.

Generally, pores smaller than, and including, 1.4 nm fill via a pull dominated fill mechanism. In these pores the fluid density is linear up until the point at which the pore has filled entirely. Hence figure 4.36 (a) shows little change in the fill rate early on, unlike seen for the 10 nm pore. Here the surface area to pore size ratio is high and the majority of fluid in the pore is in contact with a surface, given that at most there are two fluid layers in the pore at these sizes. This possibly suggests that in general the fluid adjacent to the wall is unaffected by the reservoir pressure and surface adsorption occurs independent of any bulk

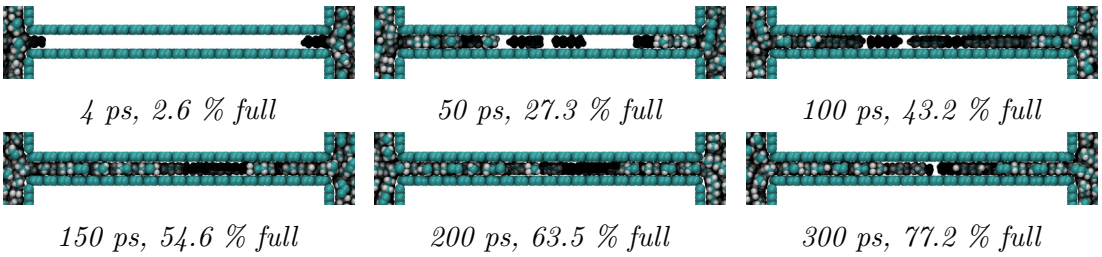


Figure 4.41: Snapshots of liquid n-heptane at 300 K filling a 0.7 nm slit pore.

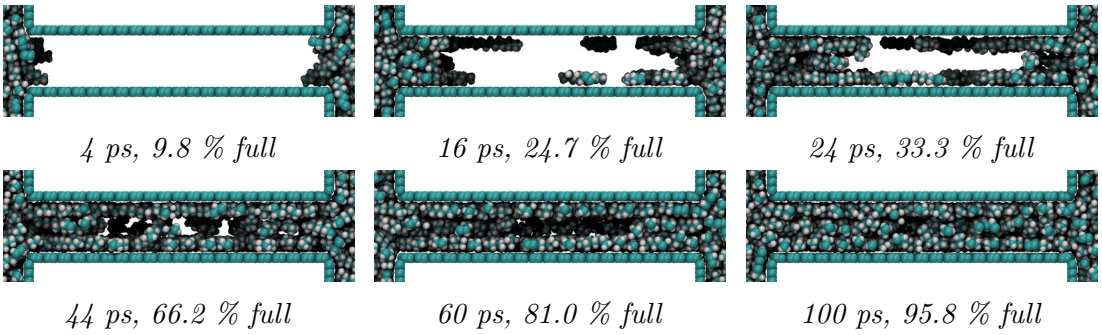


Figure 4.42: Snapshots of liquid n-heptane at 300 K filling a 1.8 nm slit pore.

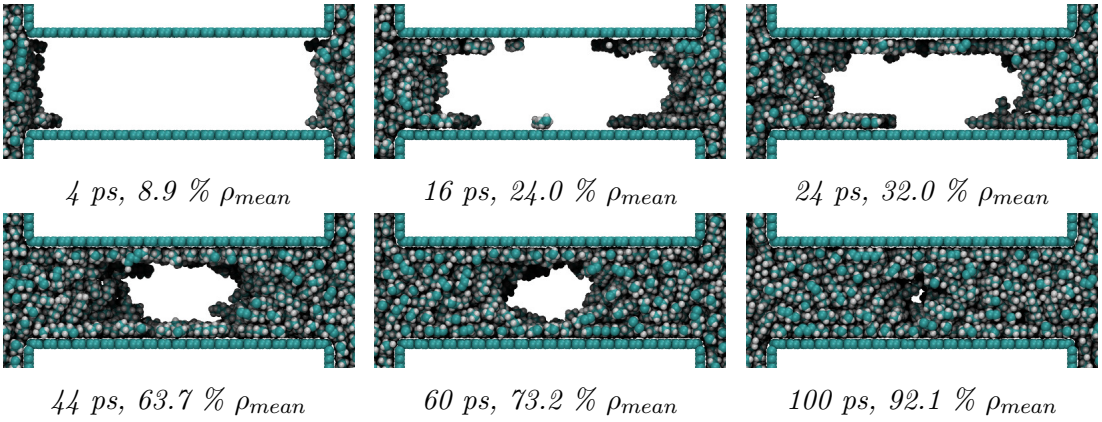


Figure 4.43: Snapshots of liquid n-heptane at 300 K filling a 3 nm slit pore.

driving force. The filling process here is unaffected by the level of packing in the pore, however the rate of filling is higher for looser packed pores. One exception to this is the 1.1 nm pore.

The 1.1 nm pore fills in a similar manner to the other pores, however there is an almost asymptotic behaviour beginning once the density has reached approximately 65 % of its final value. As can be seen in figures 4.45 (3) and 4.36 (b), this pore is the first to exhibit two fluid layers. This change in fluid phase to a highly

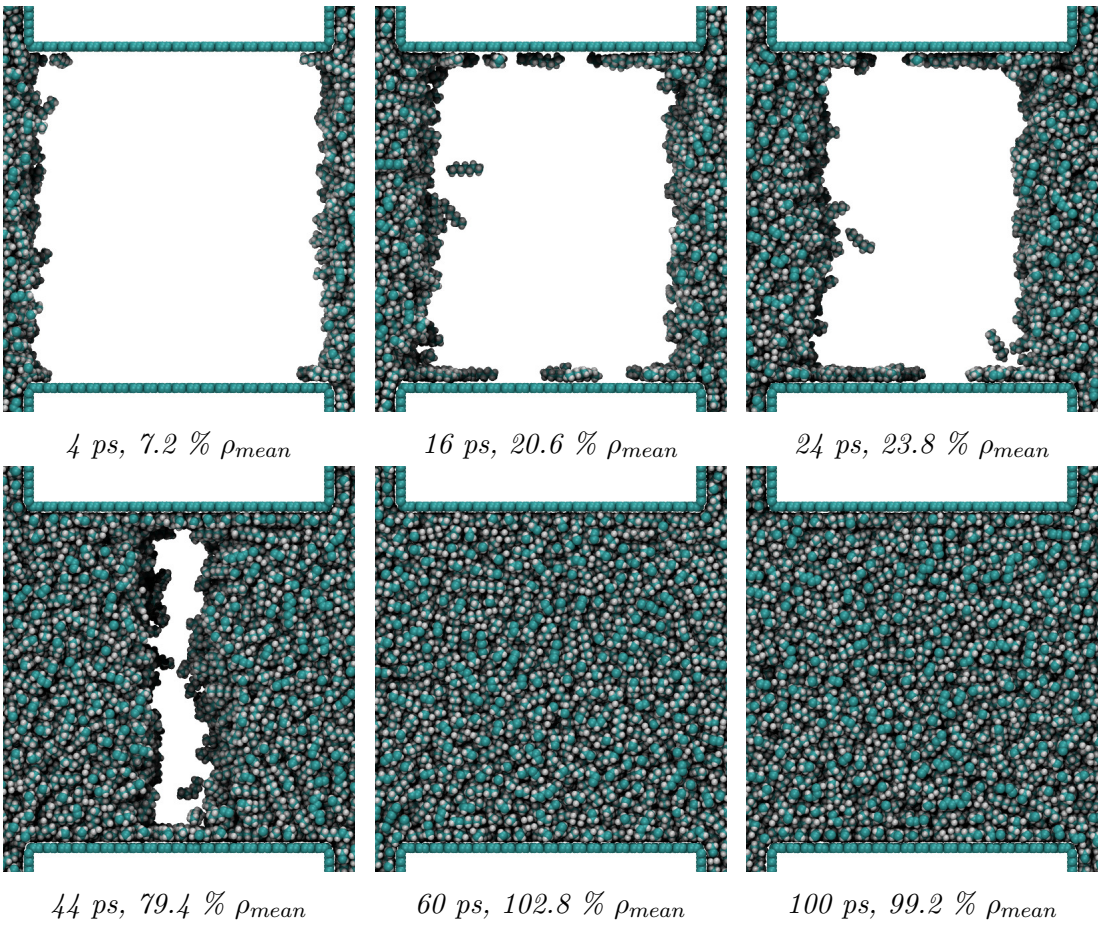


Figure 4.44: Snapshots of liquid n-heptane at 300 K filling a 10 nm slit pore.

packed system results in the increased difficulty for fluid to fill gaps in the system. It is possible that the fluid in the smaller pores would exhibit this asymptotic behaviour if the pores were longer, hence these pores have been categorised as all being in the pull dominated transport regime. This would match with the behaviour expected from spontaneous imbibition, due to fluid-solid attraction, as described by the Lucas-Washburn equation (Washburn 1921):

$$L = \sqrt{\frac{\gamma H t \cos\theta}{3\mu}} \tag{4.4}$$

where H is the height of the channel and L is the distance into the pore that a fluid with dynamic viscosity μ, surface tension γ, and contact angle θ has penetrated after elapsed time t. This states that the fluid will penetrate the pore at a rate

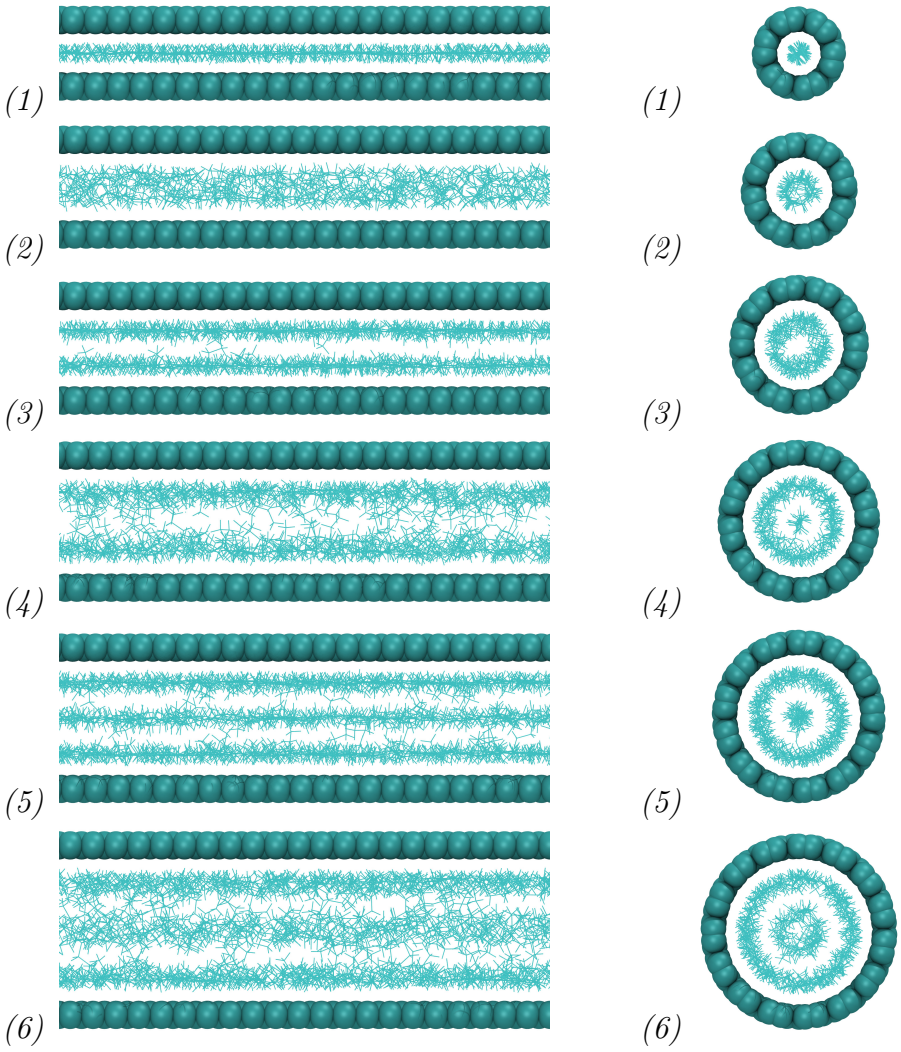


Figure 4.45: Orthographic (end on) views of slit (left) and cylindrical (right) pores filled with n-heptane. The carbon surface atoms are shown as spheres of radius σ_{ss} whilst the n-heptane is shown in skeletal form as bonds only. The depth of each pore has been cut to 8 nm for image comparison purposes. The numbering corresponds to the labelled points in figures 4.35 and 4.37 and capture significant fluid phases present in the smallest pores. Left: 1) 0.7 nm, 2) 1 nm, 3) 1.1 nm, 4) 1.4 nm, 5) 1.5 nm, 6) 1.8 nm. Right: 1) 0.81 nm, 2) 1.08 nm, 3) 1.34 nm, 4) 1.61 nm, 5) 1.74 nm, 6) 2.01 nm.

proportional to $\sqrt{t}$.

The cylindrical solution to the Lucas-Washburn equation similarly states that the fluid will penetrate the pore at a rate proportional to $\sqrt{t}$ as follows:

$$L = \sqrt{\frac{\gamma D t \cos\theta}{4\mu}} \tag{4.5}$$

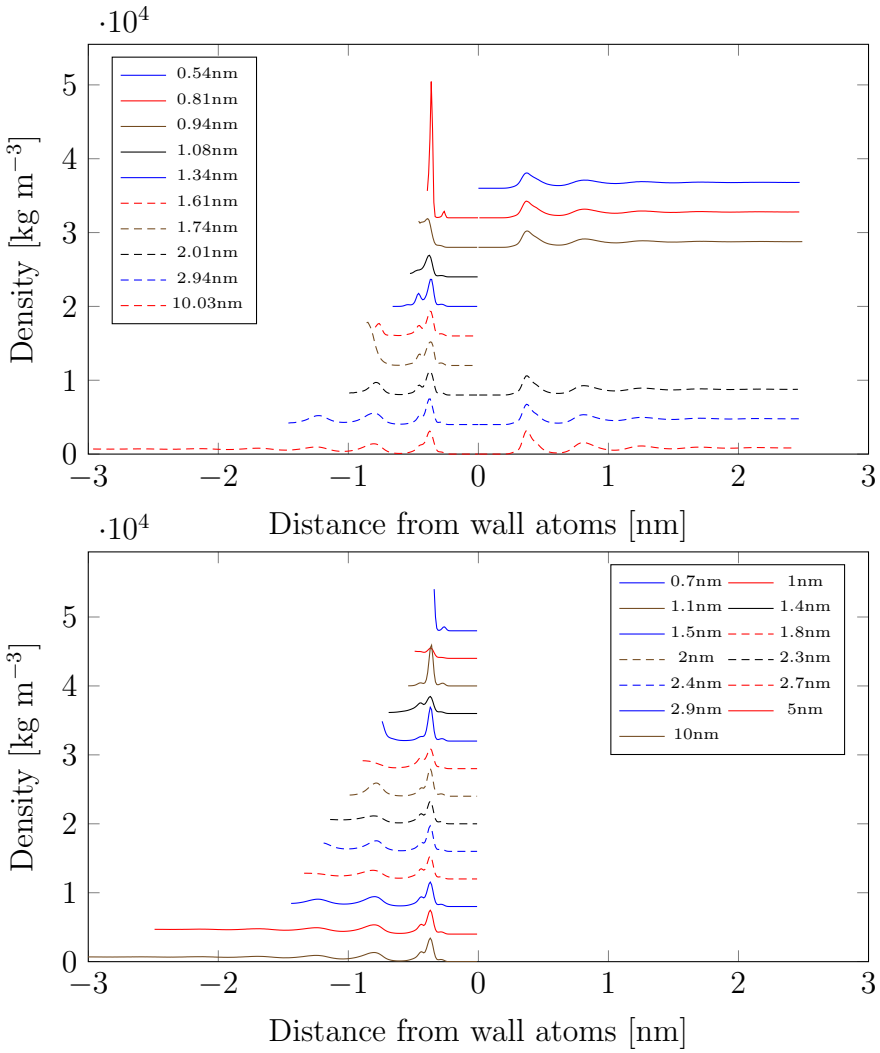


Figure 4.46: Density profiles of n-heptane, at 300 K, (top) inside and outside cylindrical pores and (bottom) inside slit pores. Calculated from a separate 5 ns simulation after the reservoirs have been removed and the pore made periodic.

where D is the diameter of the cylindrical pore.

Longer pores have not been studied here as the main function of these pores is to be used to calculate slip lengths in the following chapter and an increase in the pore length would increase computation time to unreasonable levels. This is especially true considering the increase in reservoir size to compensate for a longer pore and the scaling of computation time with simulation box length due to PME.

Figure 4.47 shows a comparison between the density in the pore and the reservoir density. It is clear here that there is little change in the reservoir density after

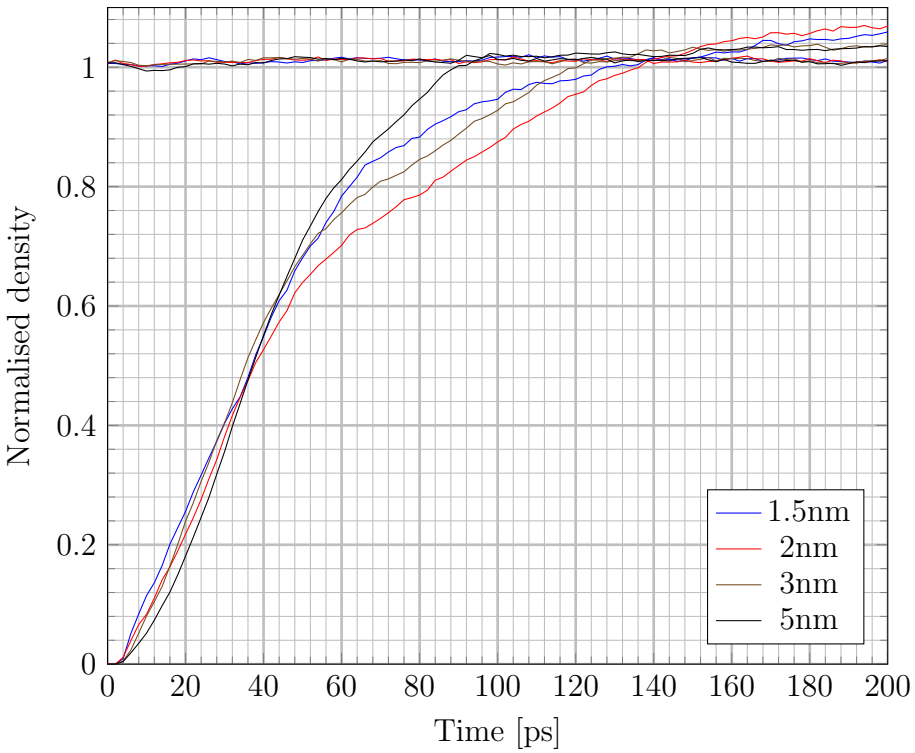


Figure 4.47: Comparison between the n-heptane reservoir density and the pore density for a selection of slit pores. $t = 0$ ps is the point at which the barrier is removed and the density has been normalised by the equilibrium bulk density.

the barrier is removed. The bulk density continues to remain constant during the entire process and remains within 2 % of the equilibrium density.

In figure 4.48 the fluctuations in the reservoir density can be seen much clearer. The mean density of the fluid in the reservoirs converges at a much slower rate than that of water once the barrier is removed. Even so, the reservoirs have completely recovered by $t = 0$ ps, when the barrier is removed.

There is a small drop in the reservoir density once the barrier is removed that is in line with what was saw for water. The dip is approximately 2 %, which is larger than in the case of water. Here the n-heptane enters the pore faster due to the additional pulling force caused by the strong fluid-solid interactions. This initial expansion into the pore causes a larger dip in the density of the reservoir, however this has recovered by approximately 20 ps in most cases. This re-equilibration of the reservoir occurs well before any change in the filling rates are observed in figures 4.35 and 4.37 and as such likely have little impact on the data.

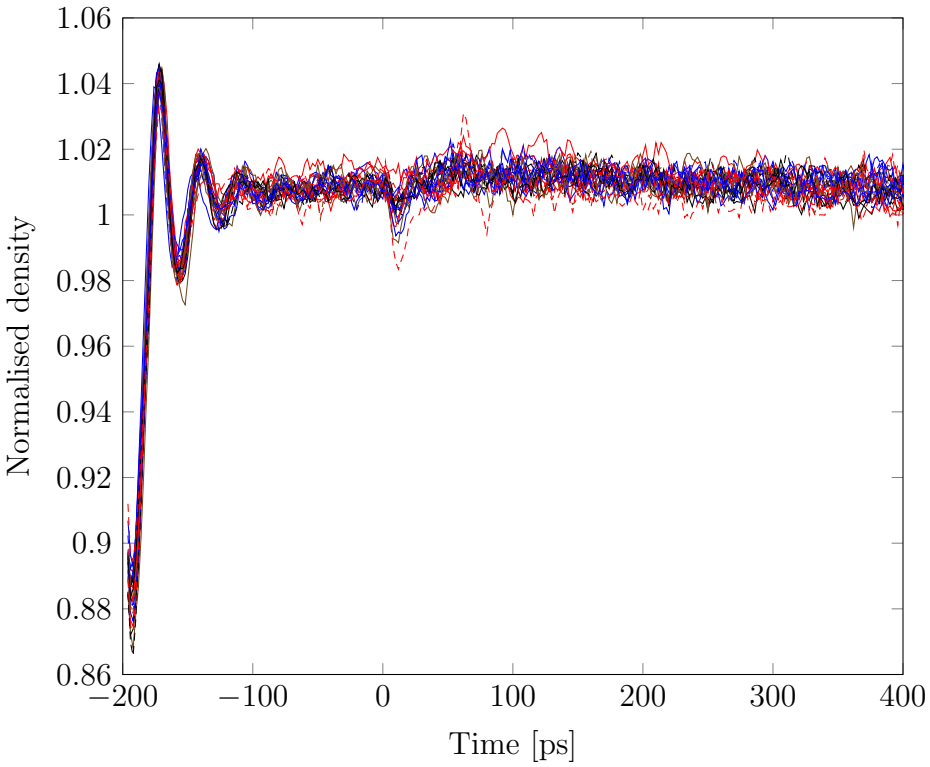


Figure 4.48: Mean n-heptane reservoir density over pore filling process for 0.7-10 nm slit pores. $t = 0$ ps is the point at which the barrier is removed. Densities have been normalised by the equilibrium bulk density.

As seen in figures 4.41 to 4.44, the change in the filling mechanism observed in some pores after approximately 44 ps matches with the point at which the pore surface is almost entirely covered with fluid. This fluid is now stationary, forming a new pseudo-surface which subsequent fluid layers fill against. This new pseudo-surface contributes to the change in the rate of fluid entry to the pore.

For pores that have 3 fluid layers at equilibrium, 1.5-1.8 nm, the filling continues from this point on as if the pore is only large enough for a single fluid layer. The fluid in the centre of the pore now acts as if it is in confined within a thinner pore with a rougher solid n-heptane surface. From this point the graph shown in figure 4.36 (c) looks similar to that of the smaller pores, where the transport of fluid is pull dominated, and again the filling process looks similar to that of spontaneous imbibition and the Lucas-Washburn equation. This makes sense as the pore is now effectively two layers thinner than it initially was.

The pores in the 1.9-2.3 nm range have 4 fluid layers, 2.4-2.7 nm pores have 5 layers, whilst the 3 nm pore has 6 layers. All of which undergo the same transition in fluid transport mechanism once the first fluid layer is filled, however this time the fill rate is constant up until the pore is filled. This is likely due to the limited length of the pore, however the larger pores in this set would likely continue to fill from the reservoir pressure driving force after the transition, since there are still 4 layers unfilled in the case of the 3 nm pore.

It is unknown, based on this data, whether this transition would take place if the pores were made to be much longer. If it it were the case that this transition still takes place, it could be possible that another transition point would occur after the second fluid layer has filled and so on. This would suggest that any n-heptane pore lacking a clear central bulk fluid region, given it is long enough, will eventually fill under spontaneous imbibition only and will not need an external pressure to fill. However, this has not been investigated here and is a possible continuation of this work.

Such a case would mean that if one wanted to force n-heptane, or any wetting fluid, into pores smaller than 3 nm the filling process would be limited by the rate of spontaneous imbibition. In an analogous manner, any non-wetting fluid, such as water, would not have this limit and has potential for quicker fill rates even though wetting fluid prefers to enter the pore. These transitions do not occur for water since no molecules fill against the solid hydrophobic surface ahead of the bulk fluid front.

The largest pores, including the 10 nm pore described earlier, are in a push dominated regime, but are cut off early due to the pore not being long enough. It is again unknown how the rate of pore filling would change if the pore length was increased, however it is expected that fluid would flow uninhibited under a reservoir pressure driving force due to a clear continuous bulk fluid region in the centre of the pore.

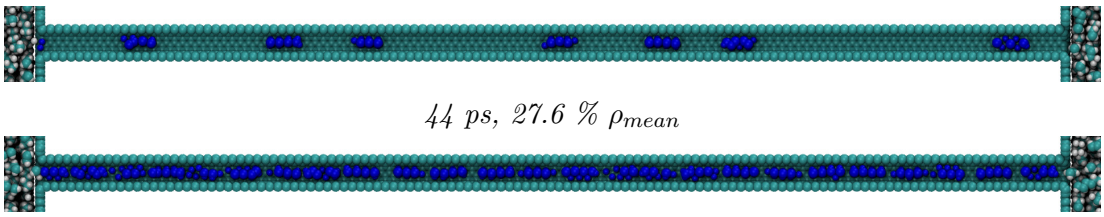
Given the values of γ and μ at 300 K for OPLS-AA n-heptane and assuming a contact angle of 0, equation 4.4 matches closely with the results presented here, for pores up to 3 nm, after the pore surface has filled with a single fluid layer and the bulk fluid has begun entering the pore. As described earlier, the effective penetration length can be found from the pore density using equation 4.3. Whilst making this comparison, H is taken to be the solid-solid separation minus $3\sigma_{sf}$ to account for the size of wall atoms and the first fluid layer on either side of the pore.

Haneveld et al. (2008) performed experiments on nanochannels ranging in height between 5 and 50 nm. The authors introduced de-ionized water into the channels and tracked the position of the meniscus as a function of time. They found that the filling kinetics are described by equation 4.4 with the addition of a correction factor, C, as follows:

$$L = \sqrt{\frac{1}{C}\frac{\gamma H t \cos\theta}{3\mu}}. \tag{4.6}$$

Handbook values for γ and μ along with a value of $\cos\theta$, determined by macroscopic contact angle measurements, were used to find the correction factor as a function of H. They found that the value of C increased from 1.902 for 47 nm channels up to 2.5 for 5 nm channels. They presented several hypothesises for this relationship, one of which is that the slower than expected filling could be caused by solidified fluid layers at the channel walls. Evidence for this is seen as the value of C becomes 1 for all channel sizes if an effective channel height of $H - 2\sigma_{ff}$ is used in place of H.

This is in line with what is observed in this work for n-heptane, where the fluid fills the walls of the pore initially and forms a new pseudo-surface for the bulk n-heptane to imbibe against. However, in this work it is not possible to see more than the first fluid layer solidifying as the pore is not long enough to make this



44 ps, 27.6 % ρ_{mean}

150 ps, 95.3 % ρ_{mean}

Figure 4.49: Snapshots of liquid n-heptane at 300 K filling a 0.81 nm cylindrical pore, coloured based on proximity to solid surface: 0-0.6 nm: blue; 0.6-1 nm: green; 1-1.4 nm: yellow; 1.4+ nm: as reservoir fluid.

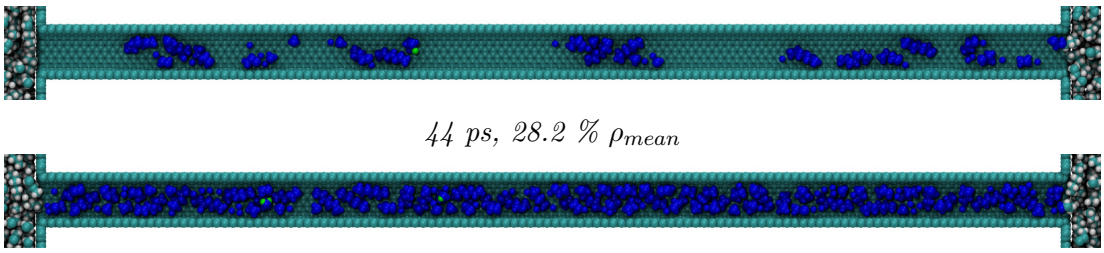
observation. Additionally, in this work, the effects of spontaneous imbibition cannot be observed entirely due to the additional pressure driving force that is present.

The cylindrical pores exhibit similar filling behaviour to the slit pores for n-heptane. The change in pore density for each pore is shown in figure 4.37 (a). In figure 4.38 these density evolutions are separated based on the filling mechanism, as observed from the shape of the graphs in figure 4.37 (a).

The striking result observable in figure 4.37 (d) is that the fill rate changes discretely with the solid-solid separation, unlike in the slit pore case or any case for water. These discrete steps in the rate correspond exactly with the number of fluid layers in the pore.

The rate also reaches a minimum point, which is the critical pore size above which fluid entry is push dominated and below which spontaneous imbibition occurs as if there is no pressure driving force.

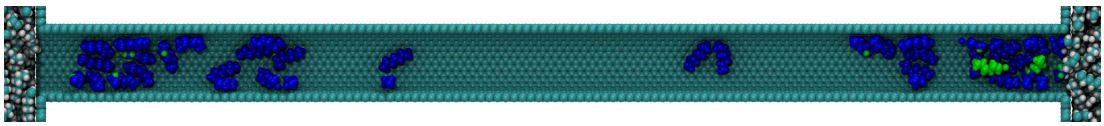
In all cylindrical cases n-heptane fills the surface of the pore first whilst the bulk fluid in the centre of the channel remains relatively stationary until the entire surface has filled. Once the surface is filled entirely, the bulk fluid enters the pore whilst fluid simultaneously diffuses out from the surface and into the centre of the pore at a distance away from the bulk fluid front. This condensation in the central of the pore can be seen in figures 4.51, 4.52, and 4.53 for the 2.01 nm,



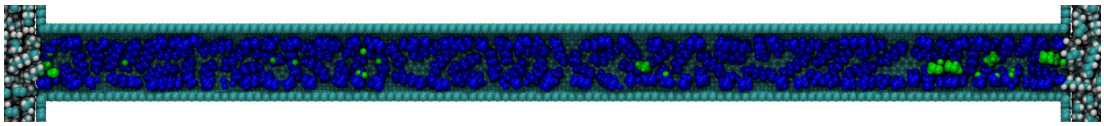
44 ps, 28.2 % ρ_{mean}

150 ps, 81.5 % ρ_{mean}

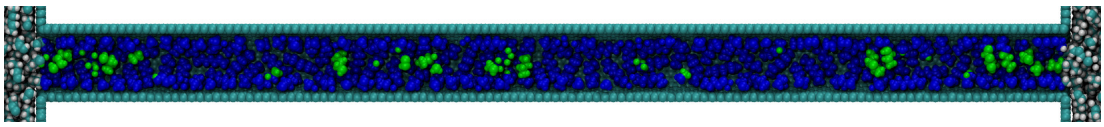
Figure 4.50: Snapshots of liquid n-heptane at 300 K filling a 1.34 nm cylindrical pore, coloured based on proximity to solid surface: 0-0.6 nm: blue; 0.6-1 nm: green; 1-1.4 nm: yellow; 1.4+ nm: as reservoir fluid.



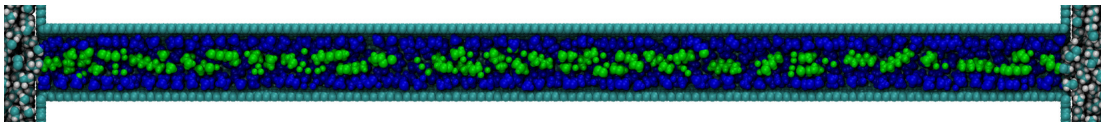
44 ps, 19.6 % ρ_{mean}



150 ps, 67.0 % ρ_{mean}



200 ps, 76.8 % ρ_{mean}



600 ps, 95.1 % ρ_{mean}

Figure 4.51: Snapshots of liquid n-heptane at 300 K filling a 2.01 nm cylindrical pore, coloured based on proximity to solid surface: 0-0.6 nm: blue; 0.6-1 nm: green; 1-1.4 nm: yellow; 1.4+ nm: as reservoir fluid.

2.81 nm, and 2.94 nm pores respectively. Figures 4.54 and 4.55 show the pore filling for the 3.61 nm and 10.03 nm cylindrical pores. In these cases the pores studied are not long enough to show this condensation of fluid in the centre of the pore away from the fluid fronts.

Unlike in the slit case for n-heptane and unlike the same pore in the case of water, the 0.81 nm pore, imaged in figure 4.49, fills at a faster rate than any other pore. The single file nature of the fluid molecules in this pore is not a detriment to

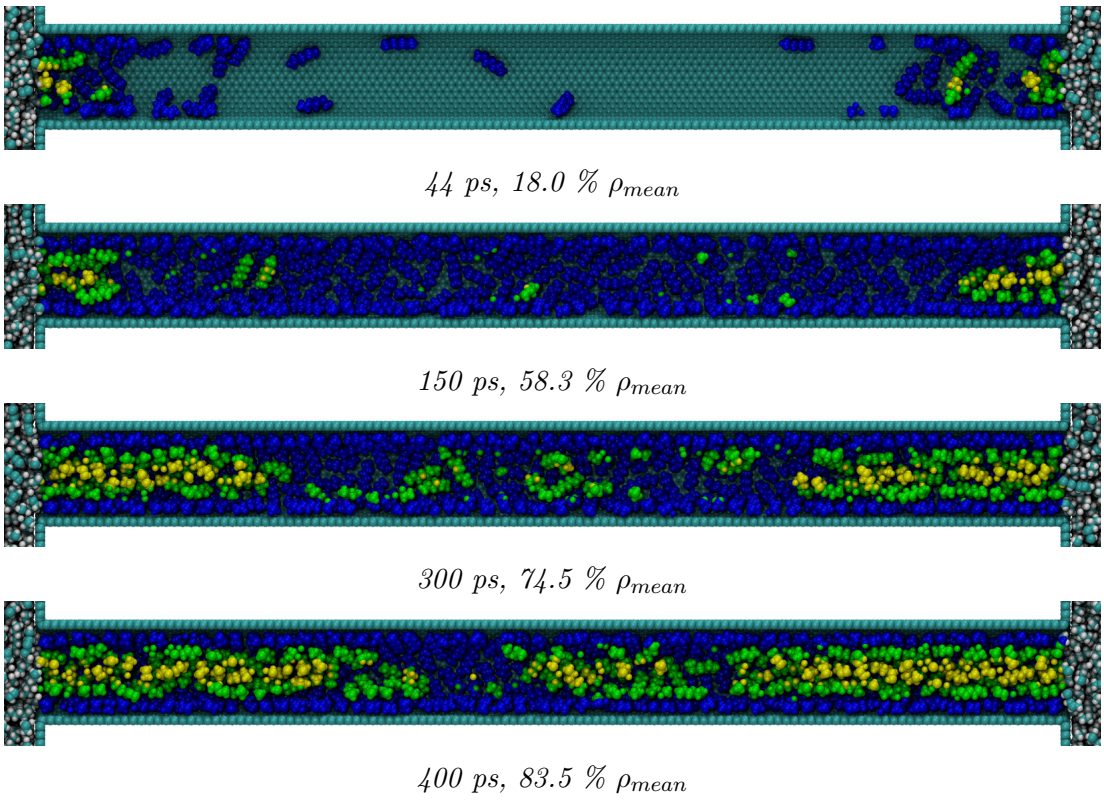


Figure 4.52: Snapshots of liquid n-heptane at 300 K filling a 2.81 nm cylindrical pore, coloured based on proximity to solid surface: 0-0.6 nm: blue; 0.6-1 nm: green; 1-1.4 nm: yellow; 1.4+ nm: as reservoir fluid.

the filling process for n-heptane due to the attraction between the n-heptane molecules and the solid surface. Fluid is pulled into the pore, and since there are very few structural arrangements available to the fluid the pore fills rapidly. The fluid already enters the pore in its optimal orientation due to its long chain structure. For the slit pore, this high attraction between the fluid and the surface has the opposite affect since there are many possible arrangements of the fluid molecules in the pore and as such the time taken to reach an optimal arrangement is increased. n-Heptane molecules can enter the slit pore in any orientation and must diffuse around one another in order to maximise the fluid surface area in contact with the solid surface.

The 0.94 nm, 1.08 nm, 1.21 nm, and 1.34 nm pores fill in a similar manner to the 0.81 nm pore, as n-heptane molecules in the pore are always in contact with the solid surface of the pore. The equilibrium layering of n-heptane in

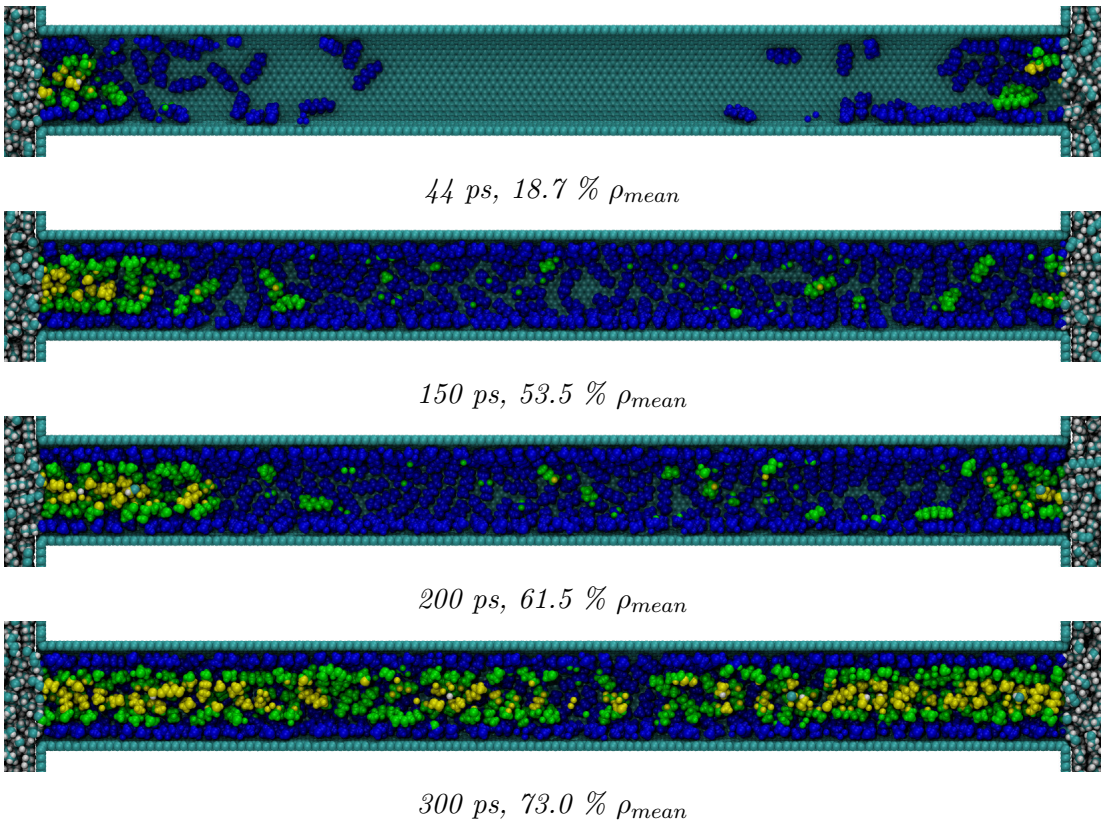


Figure 4.53: Snapshots of liquid n-heptane at 300 K filling a 2.94 nm cylindrical pore, coloured based on proximity to solid surface: 0-0.6 nm: blue; 0.6-1 nm: green; 1-1.4 nm: yellow; 1.4+ nm: as reservoir fluid.

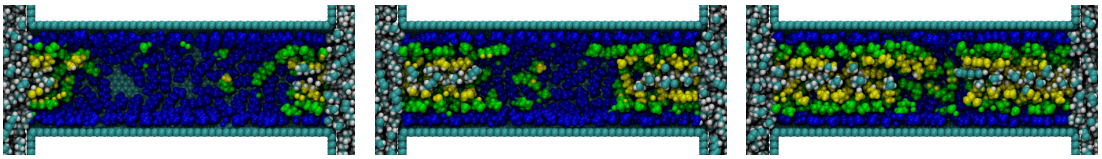
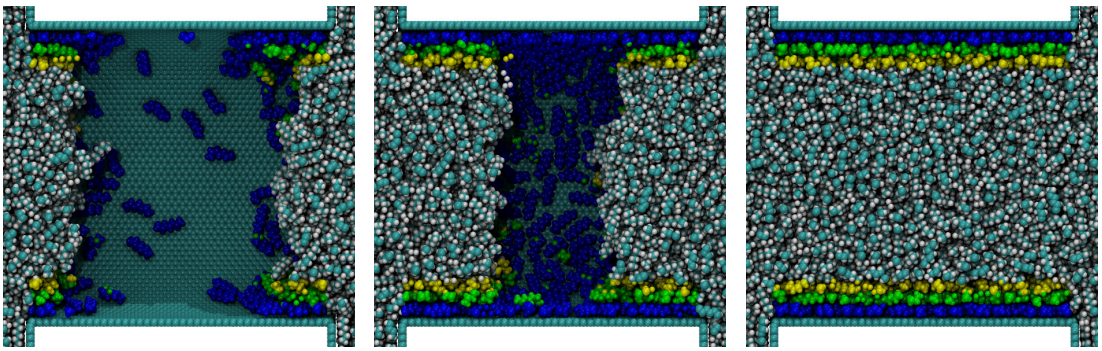


Figure 4.54: Snapshots of liquid n-heptane at 300 K filling a 3.61 nm cylindrical pore, coloured based on proximity to solid surface: 0-0.6 nm: blue; 0.6-1 nm: green; 1-1.4 nm: yellow; 1.4+ nm: as reservoir fluid.

the 1.08 and 1.34 nm pores can be seen in figure 4.45 and the filling process is imaged in figure 4.50. However, the rate of filling is slower since n-heptane is now able to position itself in non-ideal orientations. The fluid in all of these pores fills randomly all along the pore, although the n-heptane molecules will tend to nucleate around one another.

The rate of pore filling decreases until it is at its lowest in the 1.61 nm pore.



24 ps, 25.4 % ρ_{mean} *44 ps, 58.3 % ρ_{mean}* *150 ps, 97.0 % ρ_{mean}*

Figure 4.55: Snapshots of liquid n-heptane at 300 K filling a 10.03 nm cylindrical pore, coloured based on proximity to solid surface: 0-0.6 nm: blue; 0.6-1 nm: green; 1-1.4 nm: yellow; 1.4+ nm: as reservoir fluid.

This is the first pore to exhibit a central fluid layer not in contact with the solid surface. Here fluid fills the pore walls first before having to fill the central layer. n-Heptane molecules must either diffuse along the centre of the new pseudo-surface consisting of the n-heptane in the first fluid layer, or diffuse out of the first fluid layer into the central layer. In the former case the new pseudo-surface is much rougher than the smooth carbon surface of the pore and as such fluid diffuses much slower than in the single file case discussed above. In the latter case, the molecules do not always diffuse entirely into the central layer and most of the time instead remain partially in contact with the solid surface, creating an obstacle for central diffusing molecules and further increasing the time taken to fill the pore entirely.

As can be seen in figures 4.38 (c) and (d), the larger pores exhibit a change in the rate of filling once the pore surface has been filled. Just as for n-heptane in the slit pores the rate is constant up until this transition point, after which the relationship between the density and time becomes less linear. Again, this is comparable to the Lucas-Washburn equation for a cylindrical pore, equation 4.5, where D is the solid-solid separation minus $3\sigma_{sf}$ to account for the solidified n-heptane layer at the surface which reduces the effective radius of the pore.

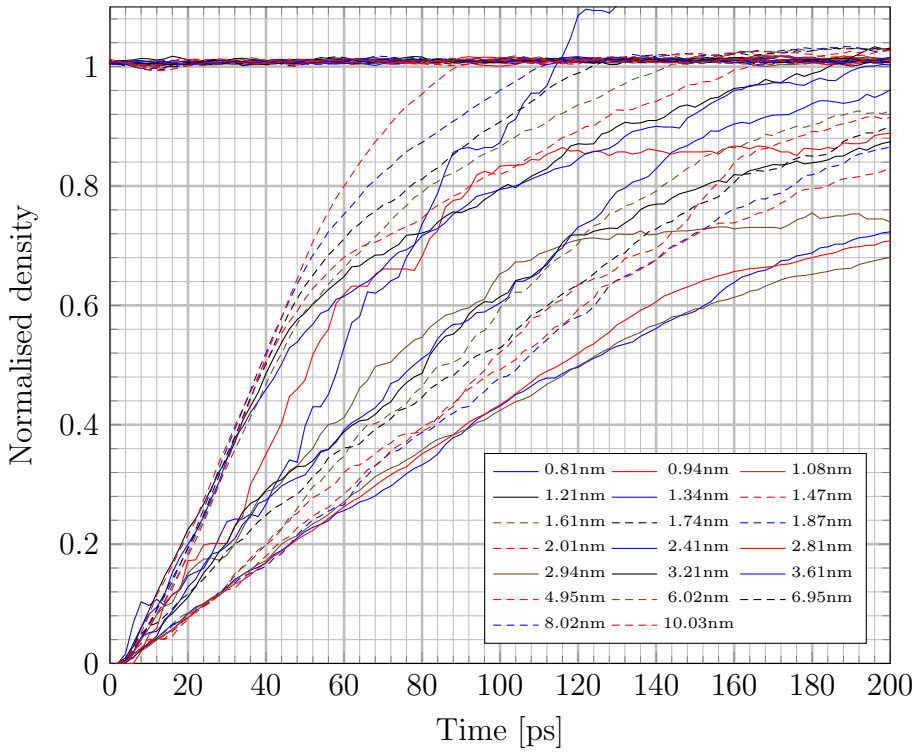


Figure 4.56: N-heptane reservoir and pore densities for a selection of cylindrical pores. $t = 0$ ps is the point at which the barrier is removed. Reservoir and pore densities have been normalised by the equilibrium bulk density.

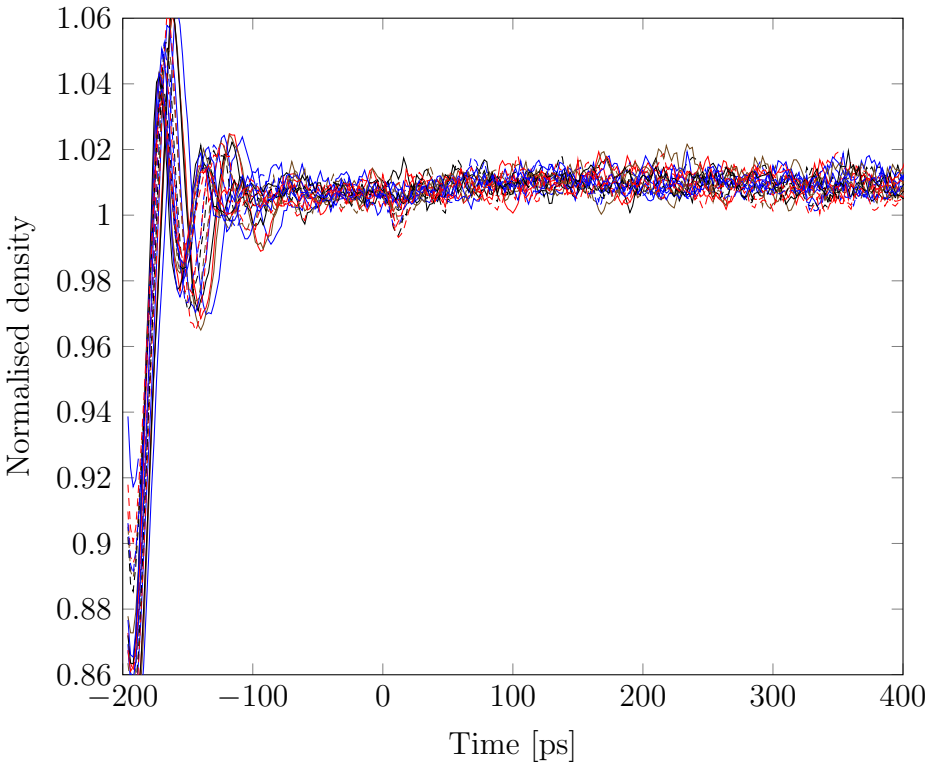


Figure 4.57: Mean n-heptane reservoir density over pore filling process for 0.81-10.03 nm cylindrical pores. $t = 0$ ps is the point at which the barrier is removed. Densities have been normalised by the equilibrium bulk density.

Figure 4.56 shows the comparison between the pore fluid and reservoir densities. This confirms that the change in rate is in fact due to the filled surface area of the pore and not due to the reservoir density oscillations. Figure 4.57 also shows that the reservoir has equilibrated before the pore barricade is removed and that the subsequent oscillations in the reservoir density have subsided by circa. 20 ps.

4.4.4 Gas adsorption against a vacuum

Following on from the case of liquid adsorption against a vacuum, the same results have been generated for pore filling from gas phase reservoirs. Fluid is able to enter the pore from both ends. Here the reservoir pressure is maintained at 1 bar by the addition and removal of molecules to the reservoir every 2 ps, correcting for any discrepancies. The temperature is maintained with a Langevin thermostat, as described in section 3.2.9, at 400 K for both water and n-heptane.

Water in slit pores and nanotubes

Figure 4.58 shows the slit pore with a periodic vapour phase water reservoir attached before removal of the barricade and after the system has fully equilibrated. The reservoir has been cropped for visual purposes and is several times larger than imaged here.

Results for rates of adsorption of gas phase water inside various slit and cylindrical pores are shown in figures 4.59 and 4.60. Figure 4.61 shows the amount of gas phase water adsorbed on the outside of cylindrical pores.

As seen in figure 4.58, due to the hydrophobic nature of the graphitic pore surface, vapour phase water fills the pore to the same density as in the bulk and there is no noticeable layering occurring at the walls in this case. These pore fill in the Knudsen self diffusion regime, this is where fluid molecules collide much more frequently with the pore walls than with other fluid molecules due to the mean free

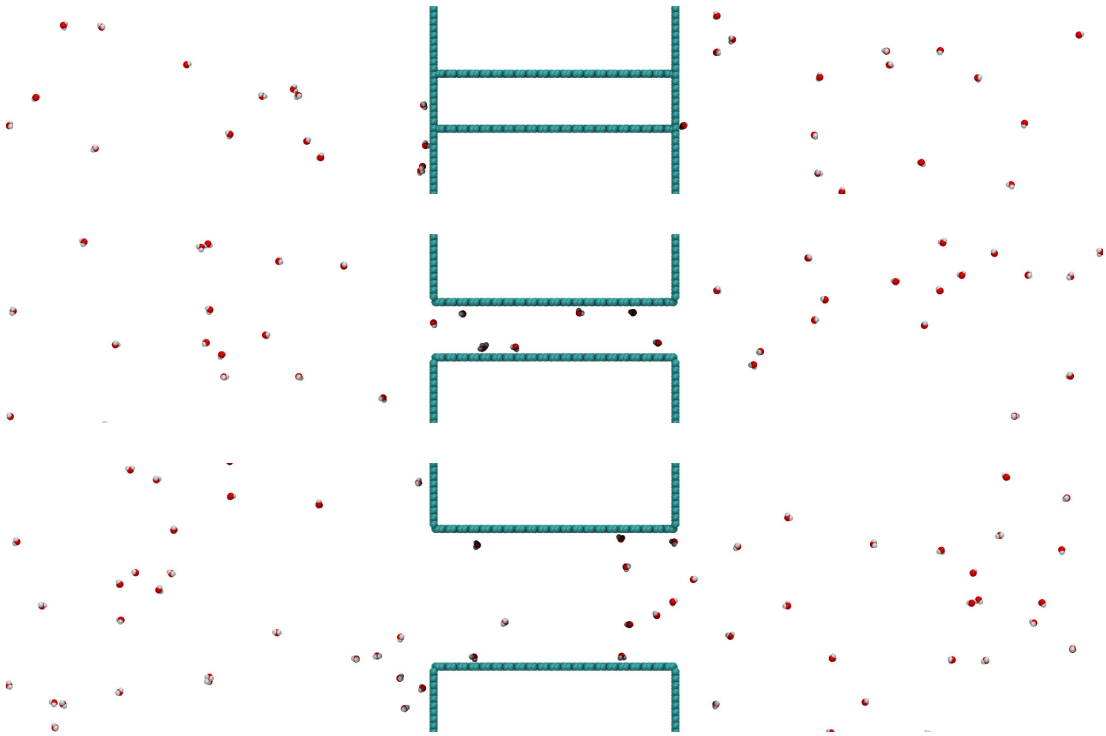


Figure 4.58: Orthographic (side on) view of vapour phase water at 400 K filling a 2 nm slit pore after 0 and 4,800 ps. The final image is of the same fluid filling a 5 nm slit pore, after 4,800 ps.

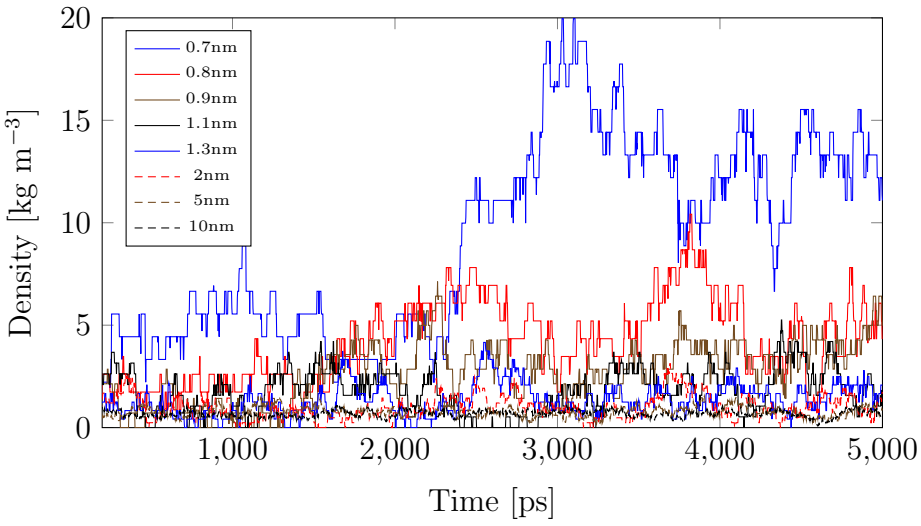


Figure 4.59: Pore density against time for water at 400 K (gas) filling various slit pores.

path being comparable to or smaller than the length scale of the system, i.e. the pore diameter or height. Here it is expected that the penetration distance into the pore is linear with time. However, due to the the short length of the pores they fill to an equilibrium value almost instantly other than in the smallest pores, as seen

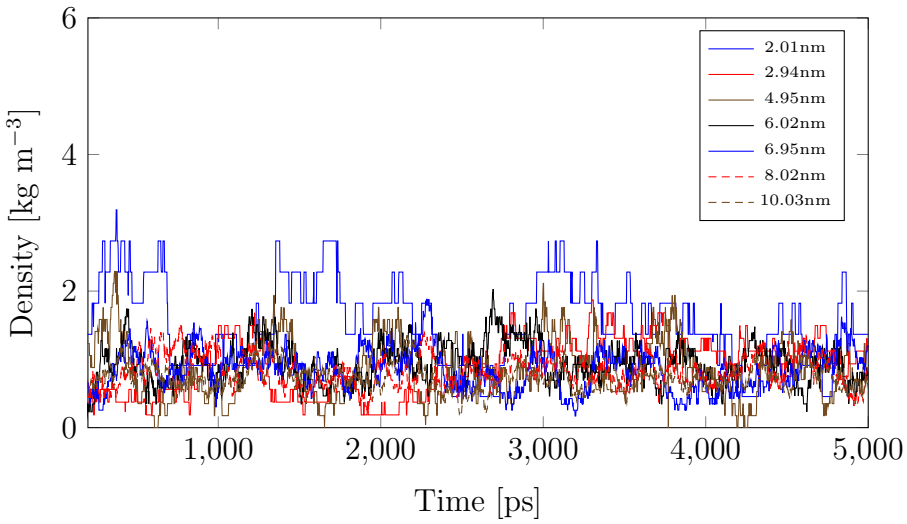


Figure 4.60: Pore density against time for water at 400 K (gas) filling various cylindrical pores.

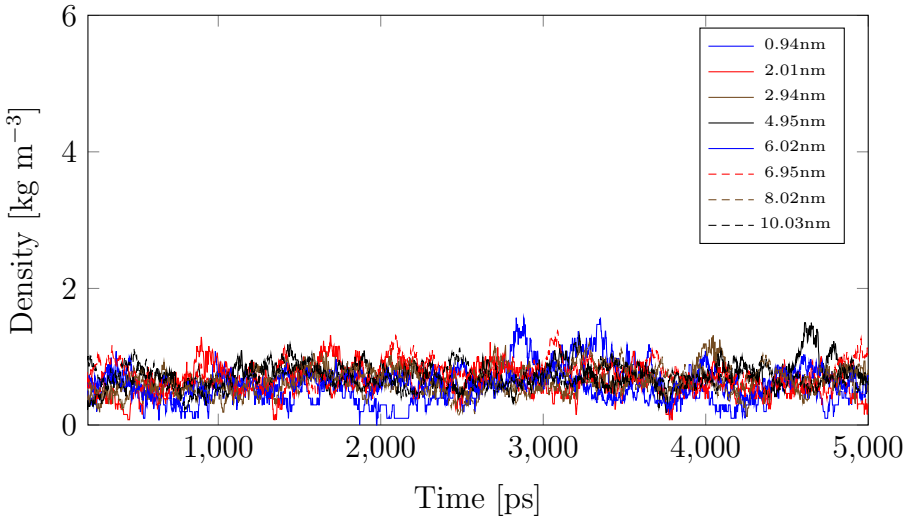


Figure 4.61: Pore density against time for water at 400 K (gas) filling the outside of various cylindrical pores.

in figures 4.59, 4.60, and 4.61. In the smallest pores, the time to fill to equilibrium can take up to 3 ns, however the statistical accuracy is not high enough to obtain any meaningful conclusion based on the rate of filling. It is also not possible to make any quantitative comparisons with Knudsen diffusion as the pores fill simultaneously from both ends. The huge difference in the fill rate between the larger and smaller pores suggests that the limiting factor in the smaller pores is the probability of entering the pore. Unlike n-heptane, discussed later, the fluid is not attracted to the solid surface in and around the pore entrance. As such,

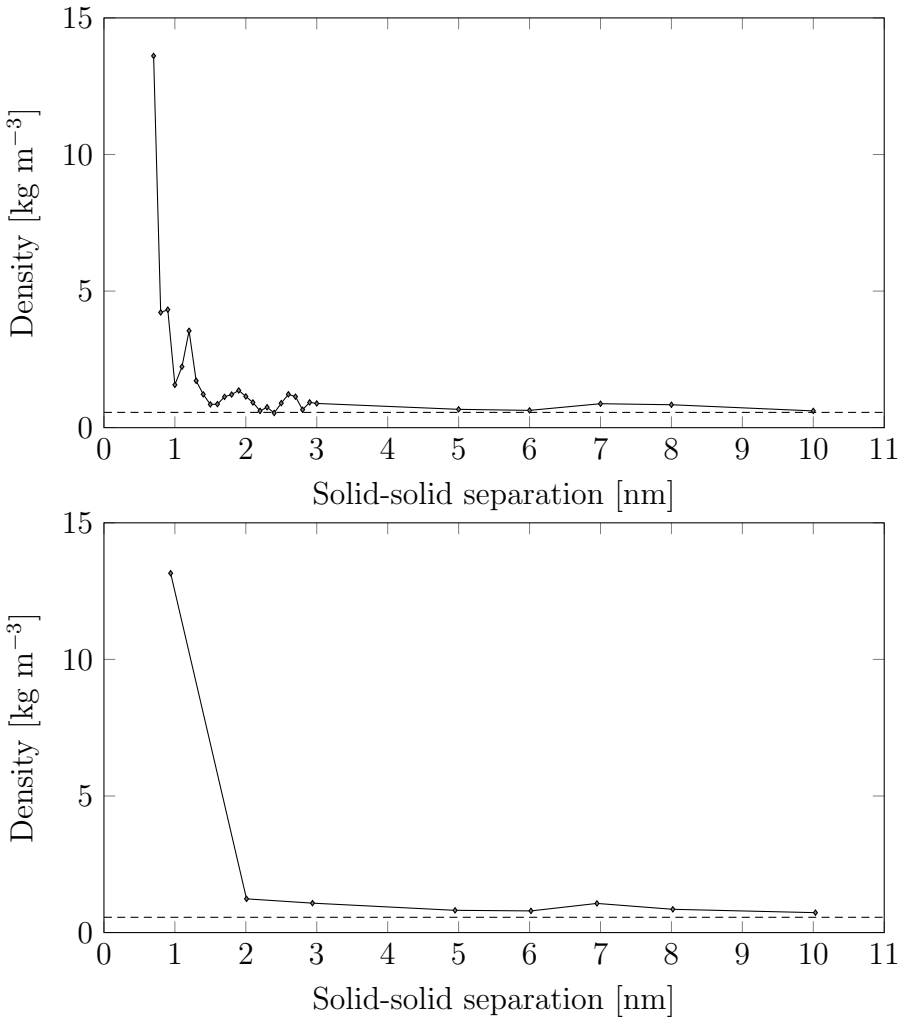


Figure 4.62: Average density of water within slit (top) and cylindrical (bottom) pores, after equilibration, at 400 K (gas). The dashed line is the bulk fluid density.

the fluid relies on the probability that a water molecule directly enters the pore from the bulk fluid reservoir. In the case of a hydrophilic surface, the fluid would be attracted to the surface of the pore and the surrounding solid barrier. In this case the molecules have more opportunity to enter the pore as the density around the pore entrance is much higher than the bulk.

Figures 4.62 and 4.63 show the final densities within the slit and cylindrical pores for each size simulated. The minimum equilibrium pore density is always greater than or equal to the bulk density. For 3 nm and larger pores the pore density is independent of the pore size for the slit pores. Below 3nm there is an increasing trend in the density. The water molecules spend a larger amount of time in

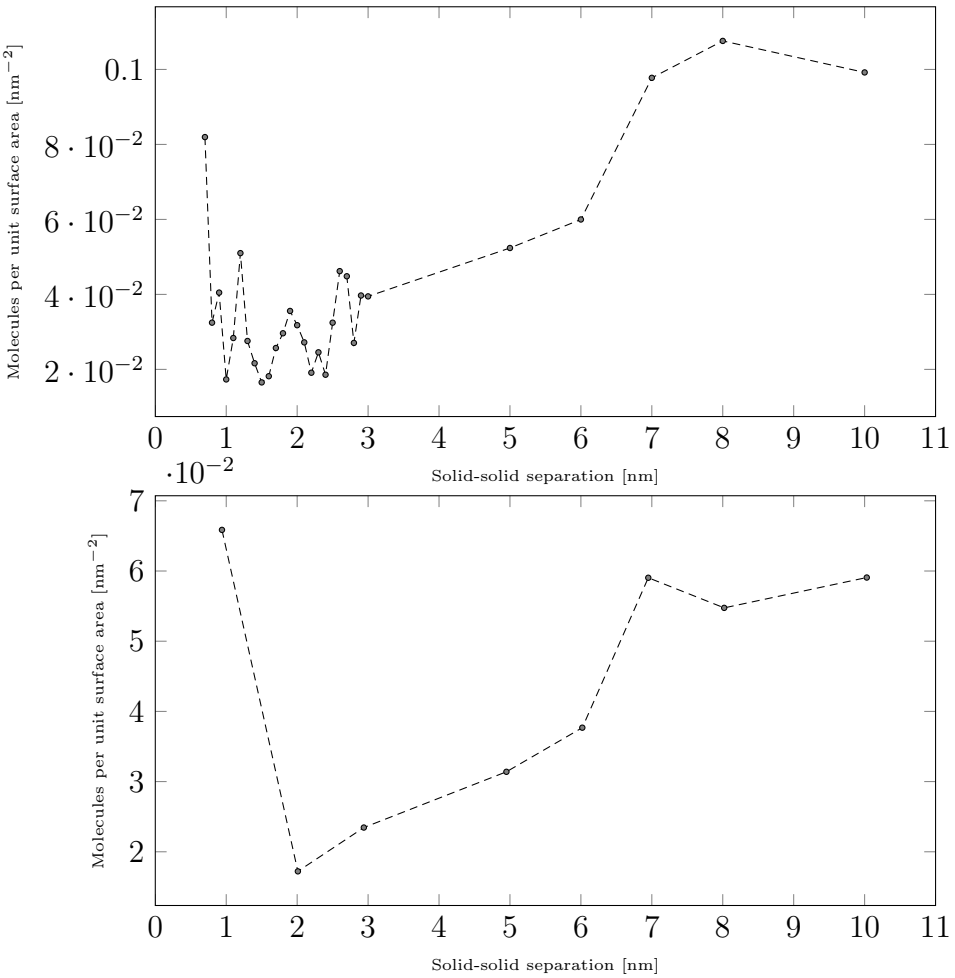


Figure 4.63: Average molecules of water within slit (top) and cylindrical (bottom) pores per unit surface area, after equilibration, at 400 K (gas).

close proximity to the pore surface than in the centre of the pores, as seen in figure 4.64, due to the non-negligible attractive force between fluid molecules and the surface. Unlike for liquid phase water, the temperature here is high enough such that any attraction between the surface and the water molecules is overcome by the kinetic energy of the molecules. The increased time spent at the surface coupled with the decreased ratio between pore volume to surface area accounts for this increase in the density with decreased separation. This does not however explain the non-uniform approach. There is not enough data for the cylindrical pores to make any detailed conclusions, however there is still a general increase in the fluid densities in the smallest pores.

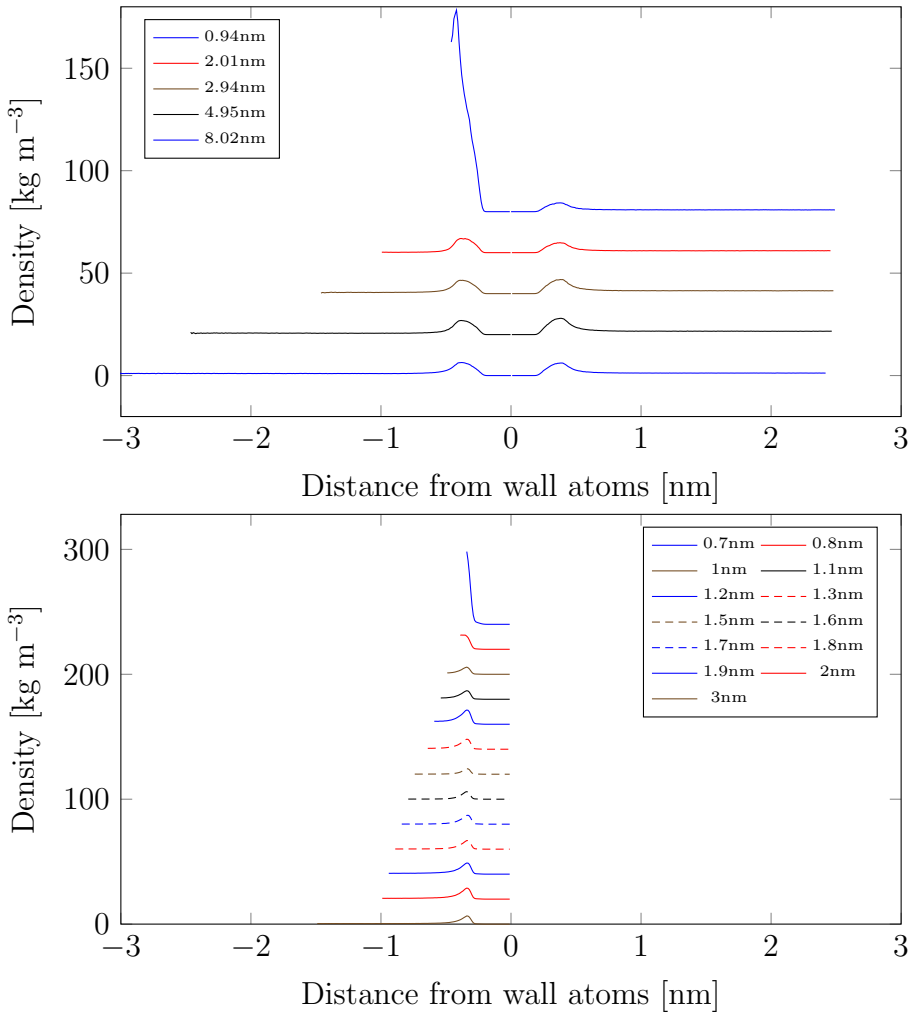


Figure 4.64: Density profiles of water, at 400 K, (top) inside and outside cylindrical pores and (bottom) inside slit pores. Calculated from a separate 5 ns simulation after the reservoirs have been removed and the pore made periodic.

n-Heptane in slit pores and nanotubes

Figures 4.65 and 4.66 show the 2 nm and 5 nm slit pores with a periodic vapour phase n-heptane reservoir attached before and after removal of the barricade and during equilibration. The reservoir has been cropped for visual purposes and is several times larger than imaged here. Unlike in the case of water adsorbing in the same pores, here n-heptane is highly attracted to the carbon pore surface atoms. Here n-heptane inside the pore exists in two phases, a high density solidified phase in direct contact with the pore surface and a vapour phase similar to the bulk fluid density. Fluid initially fills the pore surface directly, before vapour phase n-heptane molecules are seen consistently in the centre of the pore.

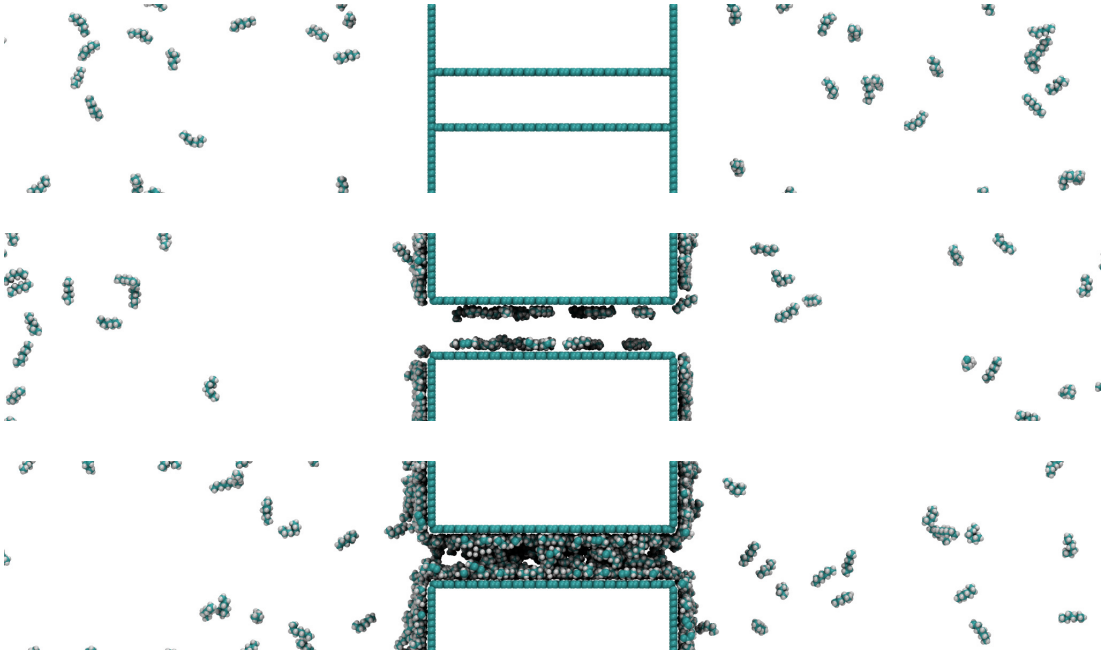


Figure 4.65: Orthographic (side on) view of vapour phase n-heptane at 400 K filling a 2 nm slit pore after 0, 4,000, and 34,800 ps.

Results for rates of adsorption of gas phase n-heptane inside various slit and cylindrical pores are shown in figures 4.67 and 4.68. Figure 4.69 shows the amount of gas phase n-heptane adsorbed on the outside of cylindrical pores. Since there are two fluid phases inside the pore the amount of molecules per unit surface area has been plotted vs time, rather than the density. The change in the amount of adsorbed molecules with time is similar for all pore sizes and there is a general

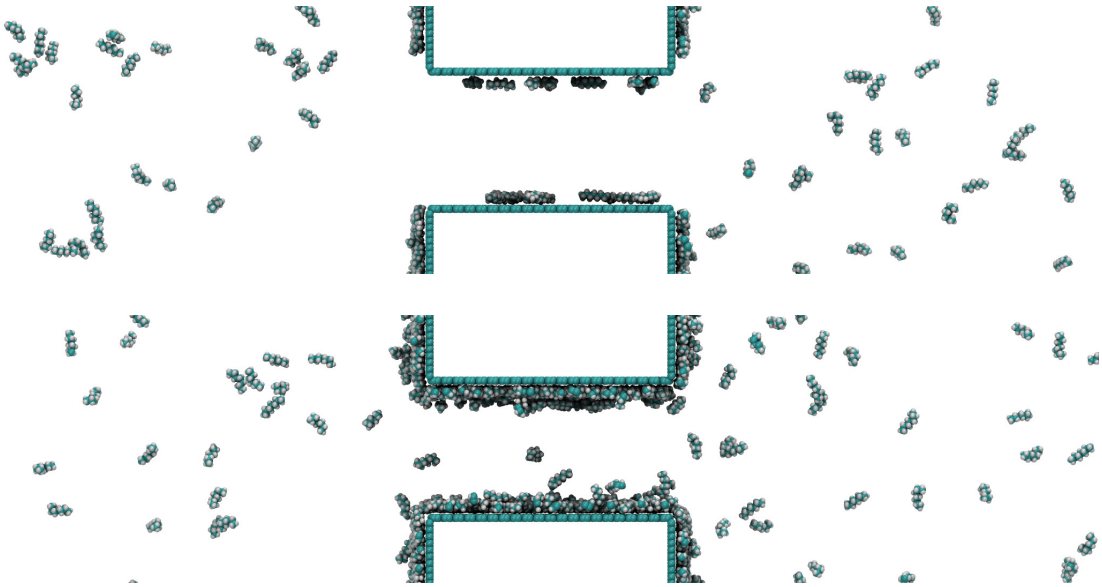


Figure 4.66: Orthographic (side on) view of vapour phase n-heptane at 400 K filling a 5 nm slit pore after 1,420 and 19,800 ps.

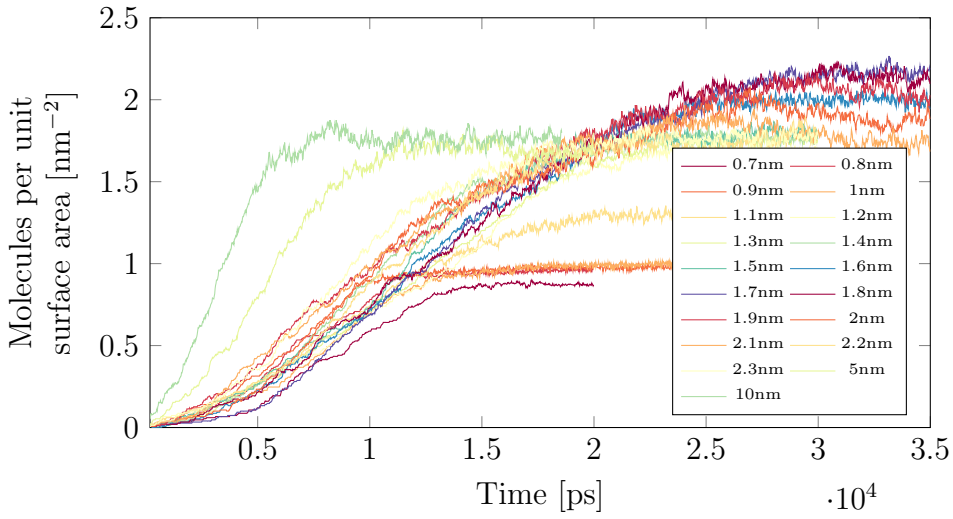


Figure 4.67: Pore density against time for n-heptane at 400 K (gas) filling various slit pores.

increase in the rate of filling with pore size in the slit pores, although the final number of molecules varies with pore size in the smallest pores.

In the cylindrical pores, n-heptane enters the 0.94 nm pore at a faster rate than the 2.01 and 2.94 nm pores, whilst otherwise the rate increases with the pore size. The 0.94 nm pore exhibits a single fluid layer, as in the case of liquid n-heptane in figure 4.45. For liquid n-heptane the 2.01 nm pore exhibits 4 clear fluid layers. This is unlike the vapour case, where there is only a single high density layer and

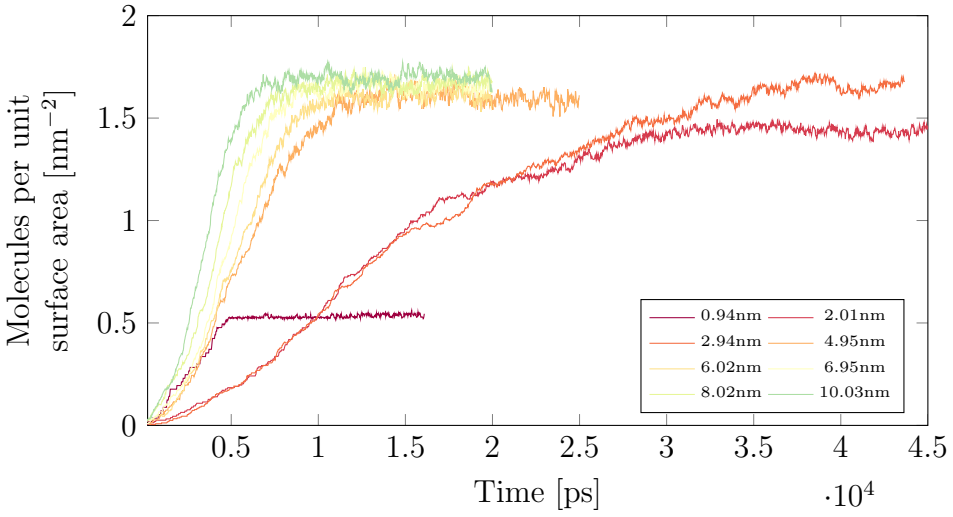


Figure 4.68: Pore density against time for n-heptane at 400 K (gas) filling various cylindrical pores.

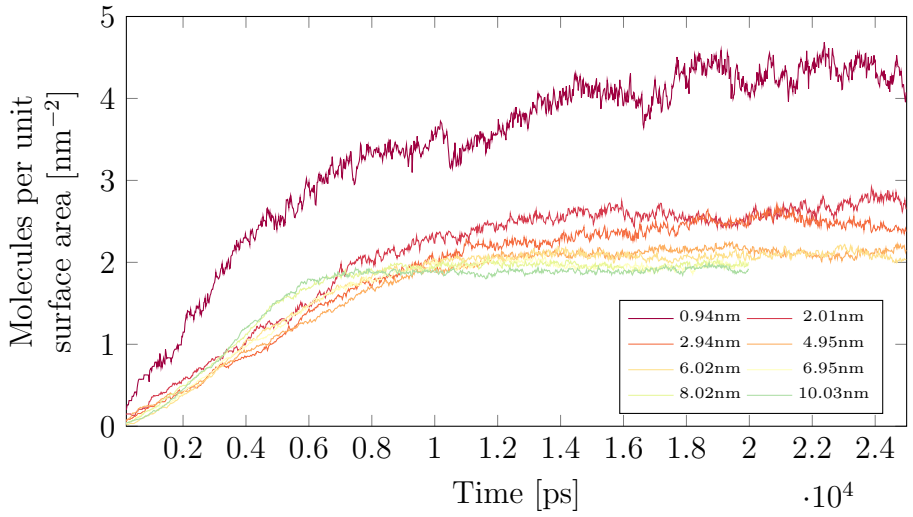


Figure 4.69: Pore density against time for n-heptane at 400 K (gas) filling the outside of various cylindrical pores.

the central region is large enough to allow for a vapour phase. This is confirmed in figure 4.70. Hence, the 0.94 nm case has a higher driving force for fluid to enter the pore, since each fluid molecule is in contact with more of the surface.

The size of the fluid layer at the surface matches that of the liquid case, as seen when comparing figures 4.70 and 4.46. Whilst the first fluid layer at 400 K in the 10.03 nm pore is 56 % of the density as in the 300 K case, the 0.94 nm pore is approximately the same for both the 300 K and 400 K cases. The ratio

between the first fluid layer density in the case of 400 K n-heptane and the case of 300 K n-heptane is fairly constant for pores larger than 3 nm. In pores smaller than this, the density approaches that of in the liquid case. This shows that the temperature and the phase has less influence on the final pore density, between 300 K and 400 K, in the smallest cylindrical pores and only the time in which the pore takes to fill increases with temperature. There is more data for comparison between the 300 K and 400 K cases for the slit pores. Here the same observations are made, with the 0.7 nm slit pore exhibiting a first fluid layer density 91% of that of the 300 K fluid in the 400 K case. In pores larger than 3 nm the ratio is constant at approximately 57 %, roughly the same as for the cylindrical case. However, fluid in the 1.1, 1.5, 2, and 2.4 nm slit pores exhibits a first fluid layer density less than 56 %: 36, 37, 49, and 55 % respectively. These pores correspond to the highly packed fluid cases, as shown in figure 4.45.

Figure 4.71 shows the final densities in the slit and cylindrical pores along with the time taken to reach 95 % of the final density. This final density is inversely proportional to the solid-solid separation, as the n-heptane only fills in a single fluid layer at the surfaces. For both the slit pores and cylindrical pores the density exponentially decreases with the solid-solid separation, as the surface area to volume ratio decreases. Figure 4.72 shows the final number of molecules in each pore per unit surface area. This is a better comparison to make than the final density, as the fluid mainly exists in the first fluid layer at the solid surface. Any increase in the solid-solid separation changes the density mainly since the vapour phase in the centre of the pore increases. The number of molecules in the slit pore remains constant in pores larger than 3 nm. This is also the case for the cylindrical pores, however the number of molecules does still increase with the increased solid-solid separation since the surface area is proportional to the pore diameter. Although the increase in molecules with separation is much greater in the pores smaller than 3 nm. In the slit pore case, clear constant regions can be seen. These plateaus are at 0.8-1 nm, 1.3-1.5 nm, 1.7-1.8 nm, 2.1-2.3 nm,

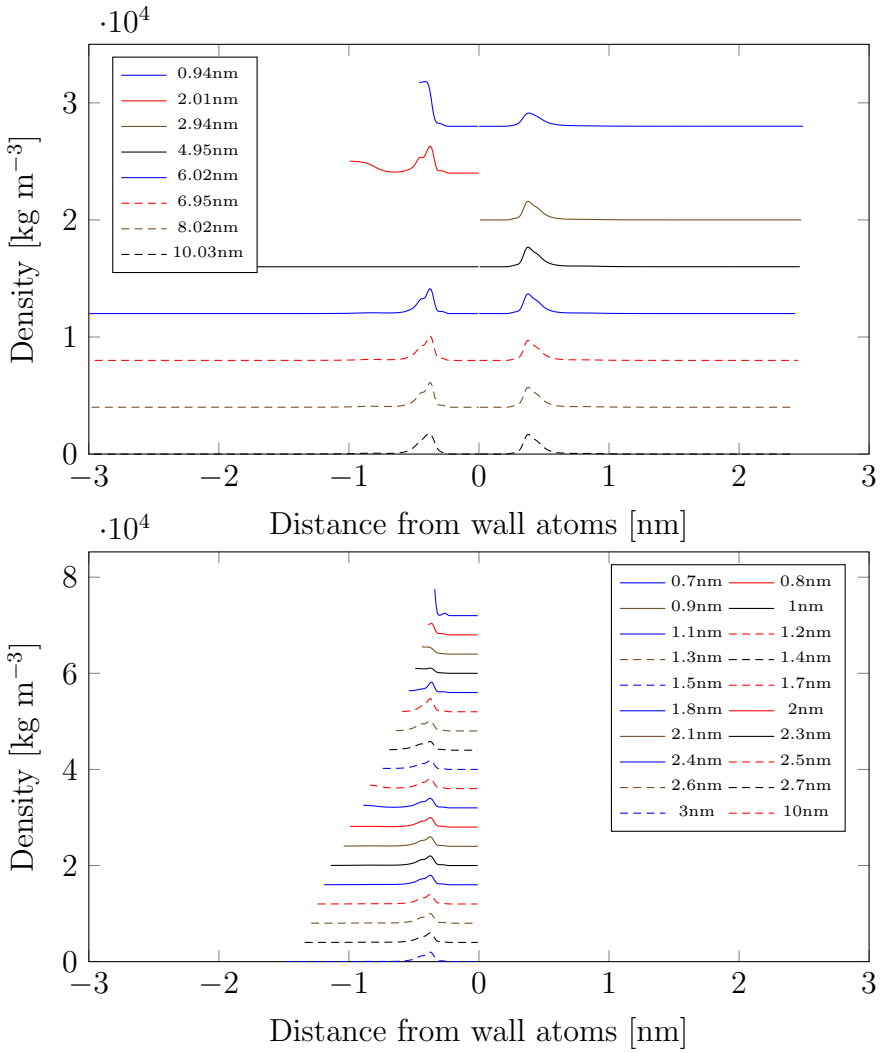


Figure 4.70: Density profiles of n-heptane, at 400 K, (top) inside and outside cylindrical pores and (bottom) inside slit pores. Calculated from a separate 5 ns simulation after the reservoirs have been removed and the pore made periodic.

and 2.4-2.7 nm and approximately correspond to the number of layers present in the pore in the liquid case, where 2.4-2.7 nm slit pores correspond to 6 fluid layers. However, for the 2.1-2.3 and 2.4-2.7 nm pores the density profile does not look dissimilar from the larger pores in figure 4.70 and no slit pore looks to have more than 2 obvious fluid layers at most. This suggests that although only 1-2 discernible fluid layers are present in figure 4.70, the actual amount of fluid in the pore is still based on the fluid layers present for liquid phase simulations.

The 0.7 nm pore filling process is shown in figure 4.73. Here the fluid enters the pore as individual molecules and fills out the pore randomly from within. The

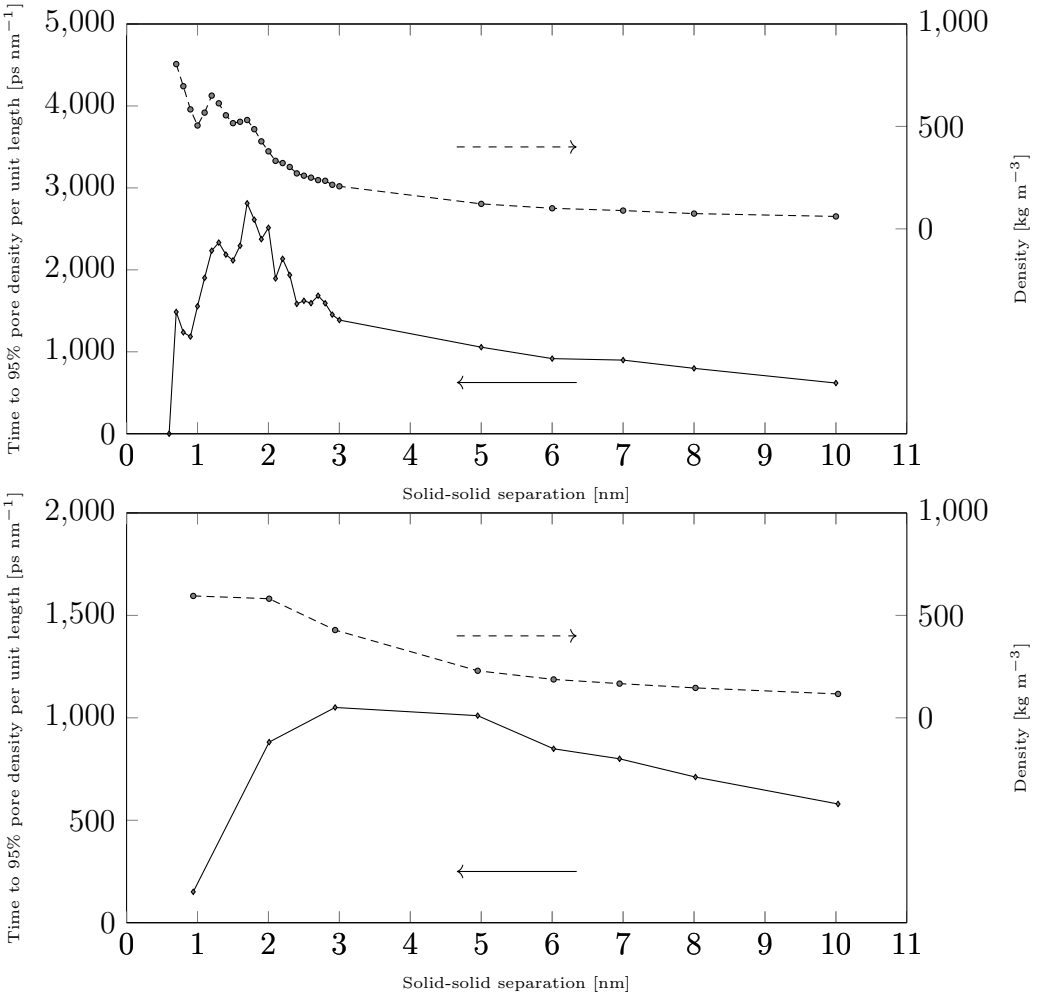


Figure 4.71: Average density and time taken to reach 95 % full for n-heptane within slit (top) and cylindrical (bottom) pores, after equilibration, at 400 K (gas).

peak in figure 4.72 for the slit pores corresponds to the 1.8 nm and 1.7 nm pores. The process of the 1.8 nm pore filling is shown in figure 4.74. Individual molecules are unable to interact with both surfaces simultaneously here. The pore surfaces fill first, forming a new 1.1 nm pseudo pore, with approximately 0.7 nm of free space in the centre between the surfaces of fluid molecules. Fluid continuing to enter into this space is able to form contacts with molecules on either side of the pore space, in contact with the pore walls. The increased force acting on each molecule, due to contact with multiple surfaces, keeps the fluid in a compact arrangement, allowing more fluid to enter the pore space. The fluid in the centre of the channel now acts similarly to liquid phase n-heptane as in the 300 K case.

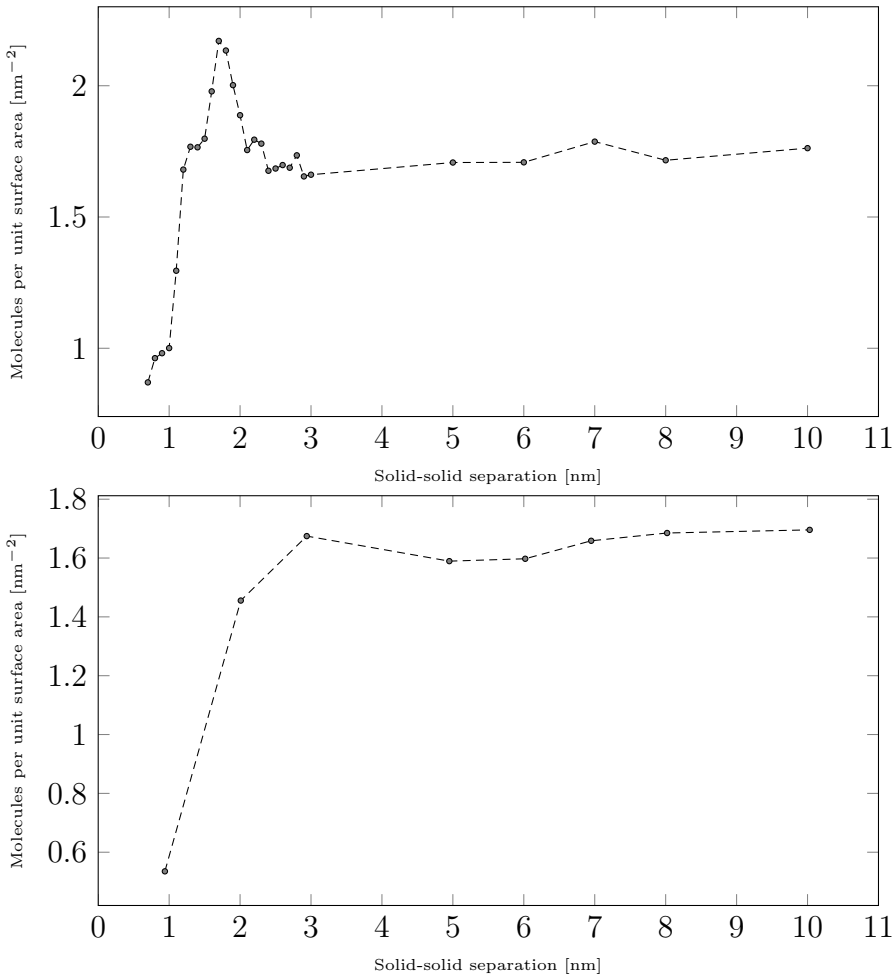


Figure 4.72: Average molecules of n-heptane within slit (top) and cylindrical (bottom) pores, after equilibration, at 400 K (gas).

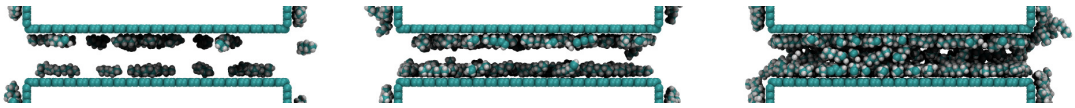
The 2 nm pore shown in figure 4.75 is at a point between the 1.7-1.8 nm peak and the 2.1-3 nm plateau. The fluid here in the centre of the channel is still in contact with the two primary fluid layers, however the molecules are stretched further across the pore and as such aren't as constrained as in the 1.7-1.8 nm cases. For pores 3 nm and larger there is no possibility of fluid being held in place by opposite primary fluid layers and no a central vapour phase can be seen in figure 4.76. Finally, in the 10 nm pore the extreme case can be seen, whereby only a single fluid layer is in contact with the surface and the rest of the fluid is in the vapour phase with a matching fluid density to the bulk, in figure 4.77.

Figures 4.78 to 4.81 show n-heptane at 400 K filling cylindrical pores. Here the fluid filling the pores looks similar to the liquid n-heptane case before the bulk



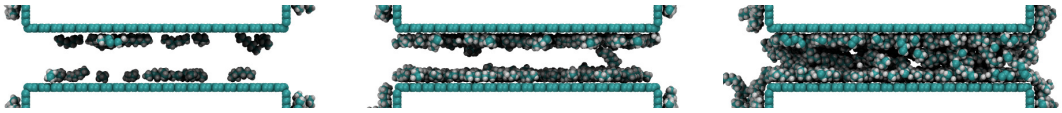
4,000 *ps, 8.4 %* ρ_{mean} 10,000 *ps, 68.6 %* ρ_{mean} 15,000 *ps, 99.1 %* ρ_{mean}

Figure 4.73: Snapshots of liquid n-heptane at 400 K filling a 0.7 nm slit pore.



4,000 *ps, 8.1 %* ρ_{mean} 10,000 *ps, 34.4 %* ρ_{mean} 20,000 *ps, 81.0 %* ρ_{mean}

Figure 4.74: Snapshots of liquid n-heptane at 400 K filling a 1.8 nm slit pore.



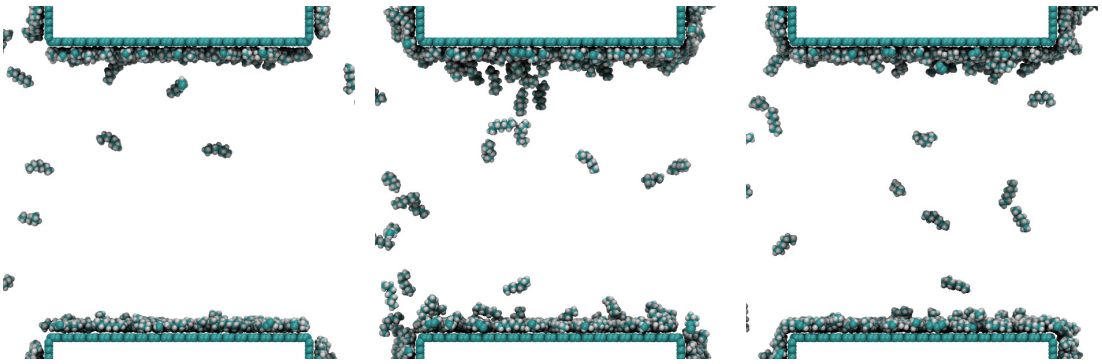
4,000 *ps, 8.1 %* ρ_{mean} 10,000 *ps, 48.7 %* ρ_{mean} 30,000 *ps, 104.9 %* ρ_{mean}

Figure 4.75: Snapshots of liquid n-heptane at 400 K filling a 2 nm slit pore.



4,000 *ps, 22.5 %* ρ_{mean} 10,000 *ps, 76.5 %* ρ_{mean} 15,000 *ps, 99.2 %* ρ_{mean}

Figure 4.76: Snapshots of liquid n-heptane at 400 K filling a 3 nm slit pore.

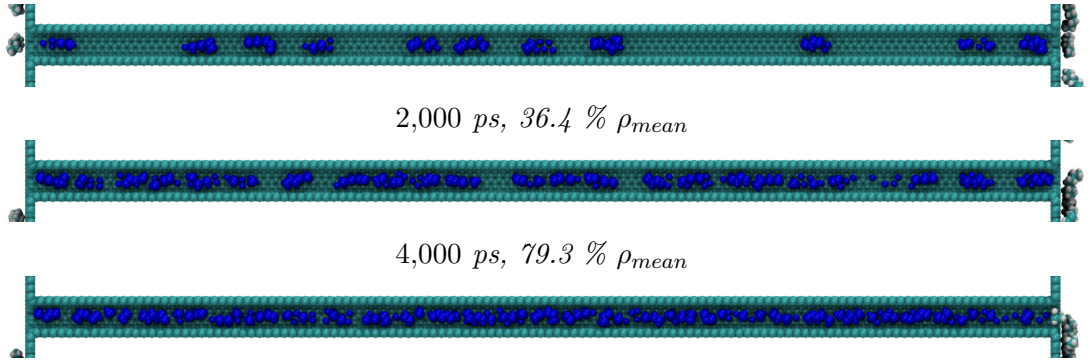


4,000 *ps, 66.2 %* ρ_{mean} 10,000 *ps, 98.0 %* ρ_{mean} 15,000 *ps, 97.3 %* ρ_{mean}

Figure 4.77: Snapshots of liquid n-heptane at 400 K filling a 10 nm slit pore.

fluid has begun to enter. The walls fill randomly first, with some areas filling faster than others from nucleation due to existing n-heptane molecules in the vicinity. Once the walls have filled completely, additional fluid that reaches the

primary fluid layer is able to break free and re-enter the centre of the pore as a vapour phase. There is a slightly increased density within one molecular diameter of the first fluid layer in all pores due to molecules spending an increased amount of time adjacent to the first fluid layer due to the attraction of the surface.

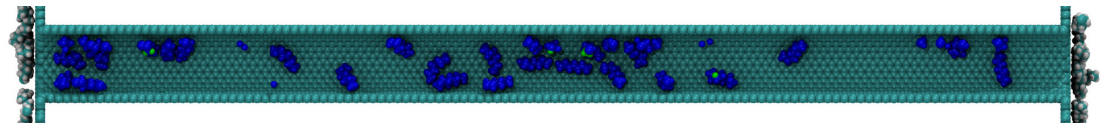


2,000 *ps, 36.4 %* ρ_{mean}

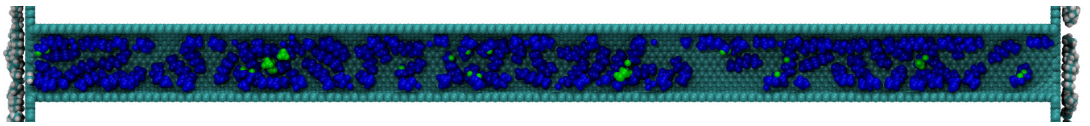
4,000 *ps, 79.3 %* ρ_{mean}

5,000 *ps, 98.4 %* ρ_{mean}

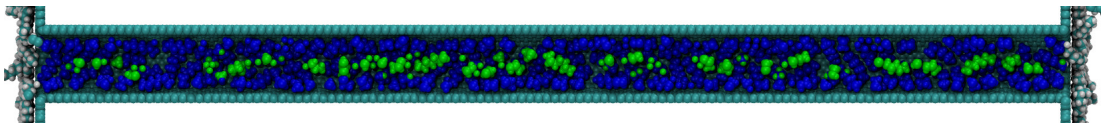
Figure 4.78: Snapshots of liquid n-heptane at 400 K filling a 0.94 nm cylindrical pore, coloured based on proximity to solid surface: 0-0.6 nm: blue; 0.6-1 nm: green; 1-1.4 nm: yellow; 1.4+ nm: as reservoir fluid.



8,000 *ps, 25.3 %* ρ_{mean}



15,000 *ps, 65.7 %* ρ_{mean}



40,000 *ps, 97.9 %* ρ_{mean}

Figure 4.79: Snapshots of liquid n-heptane at 400 K filling a 2.01 nm cylindrical pore, coloured based on proximity to solid surface: 0-0.6 nm: blue; 0.6-1 nm: green; 1-1.4 nm: yellow; 1.4+ nm: as reservoir fluid.

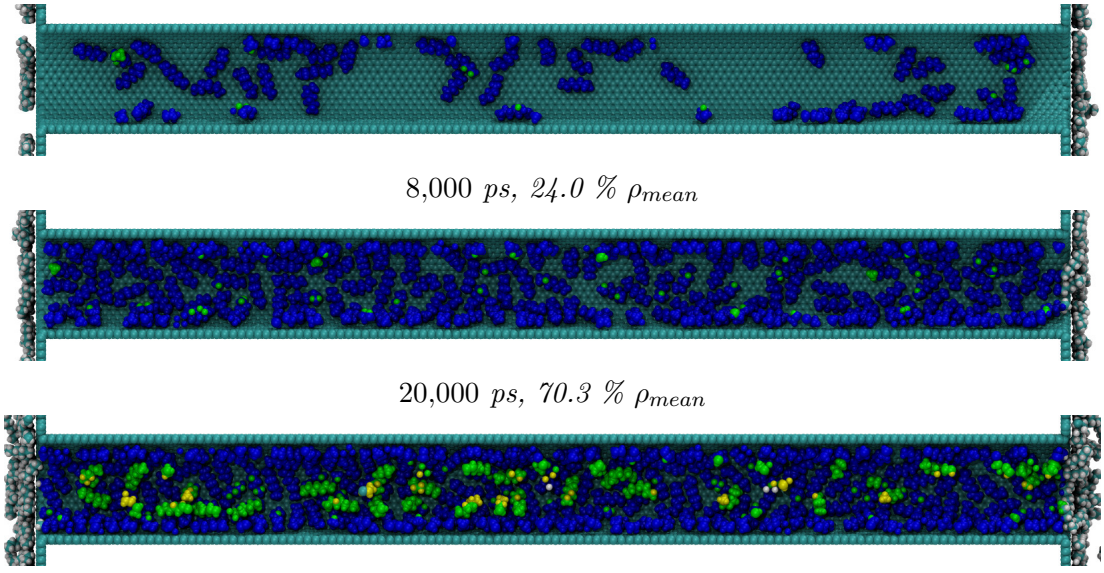


Figure 4.80: Snapshots of liquid n-heptane at 400 K filling a 2.94 nm cylindrical pore, coloured based on proximity to solid surface: 0-0.6 nm: blue; 0.6-1 nm: green; 1-1.4 nm: yellow; 1.4+ nm: as reservoir fluid.

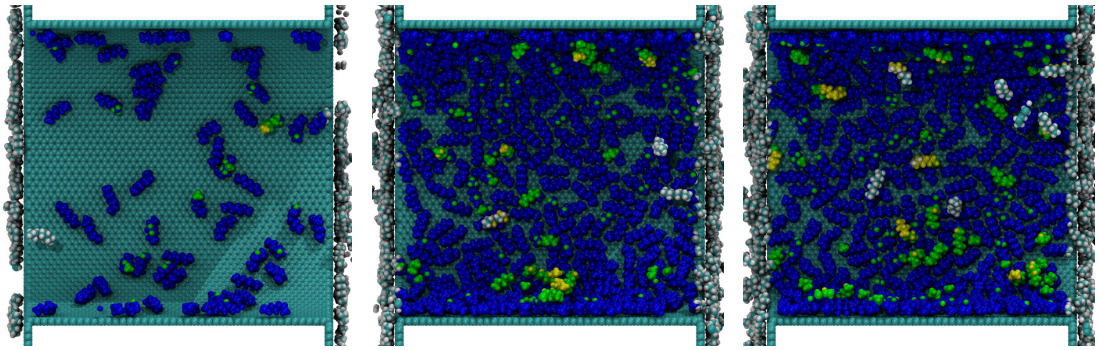


Figure 4.81: Snapshots of liquid n-heptane at 400 K filling a 10.03 nm cylindrical pore, coloured based on proximity to solid surface: 0-0.6 nm: blue; 0.6-1 nm: green; 1-1.4 nm: yellow; 1.4+ nm: as reservoir fluid.

4.4.5 Water isobars

Here, the same procedure is used as for liquid and gas adsorption. In each subsequent simulation the fluid temperature is decreased at a constant pressure of 1 bar and the resulting pore fluid density is recorded. The temperature has been varied between 300 - 400 K and the resulting adsorption isobars are presented in figure 4.82 for the 1 nm and 5 nm slit pores and the 0.94 nm and 4.95 nm (approximated as 1 nm and 5 nm in this discussion) cylindrical pores. The 400 K simulations presented earlier show that the pore fluid density is always larger than the bulk density, with the 5 nm pore having a similar density to the bulk and the 1 nm pore being 2.8 times the bulk density in the slit pore and 23.5 times larger in the cylindrical pore. Here all simulations above the boiling point resulting in a pore density higher than the bulk density. The data here is scattered as the error is larger due to condensation in the pore which cause an increase in the density, however there is an average decrease in the density with temperature, much greater than the decrease in the bulk. The same can be seen for the cylindrical pore, however here the drop in density with temperature is much easier to see. There is a stronger attraction between the fluid and the pore. This, coupled with the small cross-sectional area available for the motion of water molecules, causes a larger general density at 400 K (1.08 rescaled). The heavy confinement of the water molecules in the 0.81 nm pore only allows for major translational motion in one-dimension. As the temperature increases, this motion back and forth along the pore is increasingly rapid, allowing for less molecules to enter the pore and a decline in the density with respect to temperature more rapid than in the bulk. In the 5 nm slit and cylindrical pores the density is still higher than the bulk density, and is still seen to drop quicker with temperature than the bulk, however unlike in the 1 nm pores the density is similar in both the slit and cylindrical pores.

The 300 K simulations presented earlier show that, with the exception of the

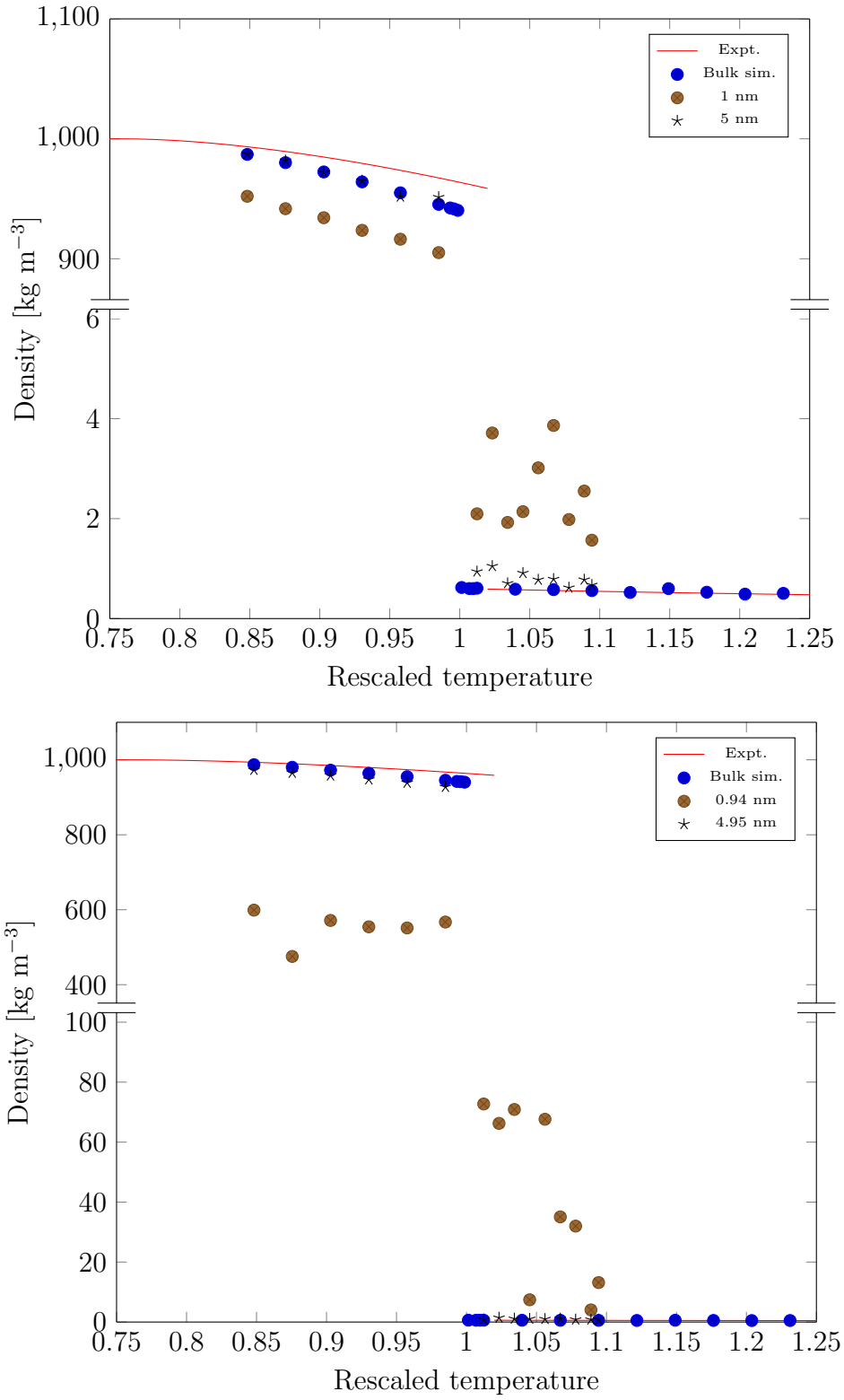


Figure 4.82: Adsorption isobars of TIP4P water at 1 bar inside slit (top) and cylindrical (bottom) pores. The temperature is rescaled by the bulk fluid boiling point (365.5 K).

immediate point after a pore is large enough to exhibit an additional fluid layer, the pore fluid density is generally less than the bulk density. In the 5 nm slit

and cylindrical pores it is 98.8 % and 97.7 % of the bulk density, whilst in the 1 nm pore it is 95.5 % and 54.5 %. Here this difference is maintained between the bubble point and 300 K. The overall density is much lower in the 1 nm pore than in the 5 nm pore for both the slit and cylindrical pores, more-so in the cylindrical case due to the much lower cross-sectional area and higher surface area to volume ratio allowing for more surface layering. As discussed earlier, the surface layering affect allows for both increased and decreased fluid density depending on the commensurability of the pore with respect to the optimal layer widths.

A key point to note here is that the densities presented in figure 4.82 are directly affected by the volume used to determine this density. Specifically, the choice of surface location will impact this result. As discussed in sections 2.4.2 and 4.3.2, the surface location in this work is chosen to be the point $\sigma_{sf}/2$ away from the centre of the innermost wall particles.

The largest realistic volume would be obtained if the surface location was specified to be the centre of the innermost solid atoms, whereas arguably the smallest volume would result from a surface location approximately σ_{sf} away from the solid centres. Given this knowledge, the pore densities presented in figure 4.82 could be out by $\pm\sigma_{sf}/H$, corresponding to approximately $\pm 34\%$ and $\pm 6.8\%$ in the 1 and 5 nm slit pores respectively. In the cylindrical pores the density could be between $\left(D-\sigma_{sf}\right)^2/D^2$ and $\left(D+\sigma_{sf}\right)^2/D^2$, corresponding to approximately -59% and $+84\%$ in the 1 nm pore and -13% and $+14\%$ in the 5 nm pore. Clearly here the larger the pore is, the smaller the overall impact of the choice of surface location.

Another key observation to make is that the phase change in confinement matches with that of the bulk. This is an artefact of performing the simulations with decreasing temperature steps (filling branch of isobar). If the temperature were to be increased incrementally then the phase change in confinement would shift (to the right in this case), as seen in adsorption isotherms by Striolo et al. (2005a), Müller

and Gubbins (1998), Liu and Monson (2005) (to name a few).

4.4.6 n-Heptane isobars

The same simulations are performed for n-heptane and the resulting adsorption isobars are presented in figure 4.83.

Unlike for water, the change in pore density with temperature for both the slit and cylindrical pores is different from the change seen for the bulk density. For the 1 nm case the density is constant with the decreasing temperature, suggesting that the maximum density is reached for every temperature and is independent of the temperature. The attraction between the solid surface and the fluid molecules holding the fluid in place is greatly enhanced in these cases due to multiple contacting surfaces. This attraction is too strong to be broken by an increase in molecular thermal energy. The 1 nm cylindrical pore even crosses the bulk fluid density before the boiling point, however this is possibly an artefact of the choice of surface location chosen for calculating the pore density, as a surface closer to the centre of the solid surface atoms would result in a lower calculated density. The surface location choice will also affect the relationship between the pore density and pore diameter shown in figure 4.71. See the previous discussion for water for details on the impact of the surface location choice, along with sections 2.4.2 and 4.3.2.

The gas phase reservoir also fills the pore to a density independent of temperature, however the value of the density is lower than when filling from a liquid reservoir. This suggests that even though there is a maximum density that is attained independently of the reservoir temperature it does still depend on the phase of the reservoir attached. This is likely due to the vastly reduced rate of fluid entering into the pore balancing the residence time of fluid inside the pore, suggesting fluid is able to detach from the pore surface and leave the pore and is in a constant equilibrium with fluid entering.

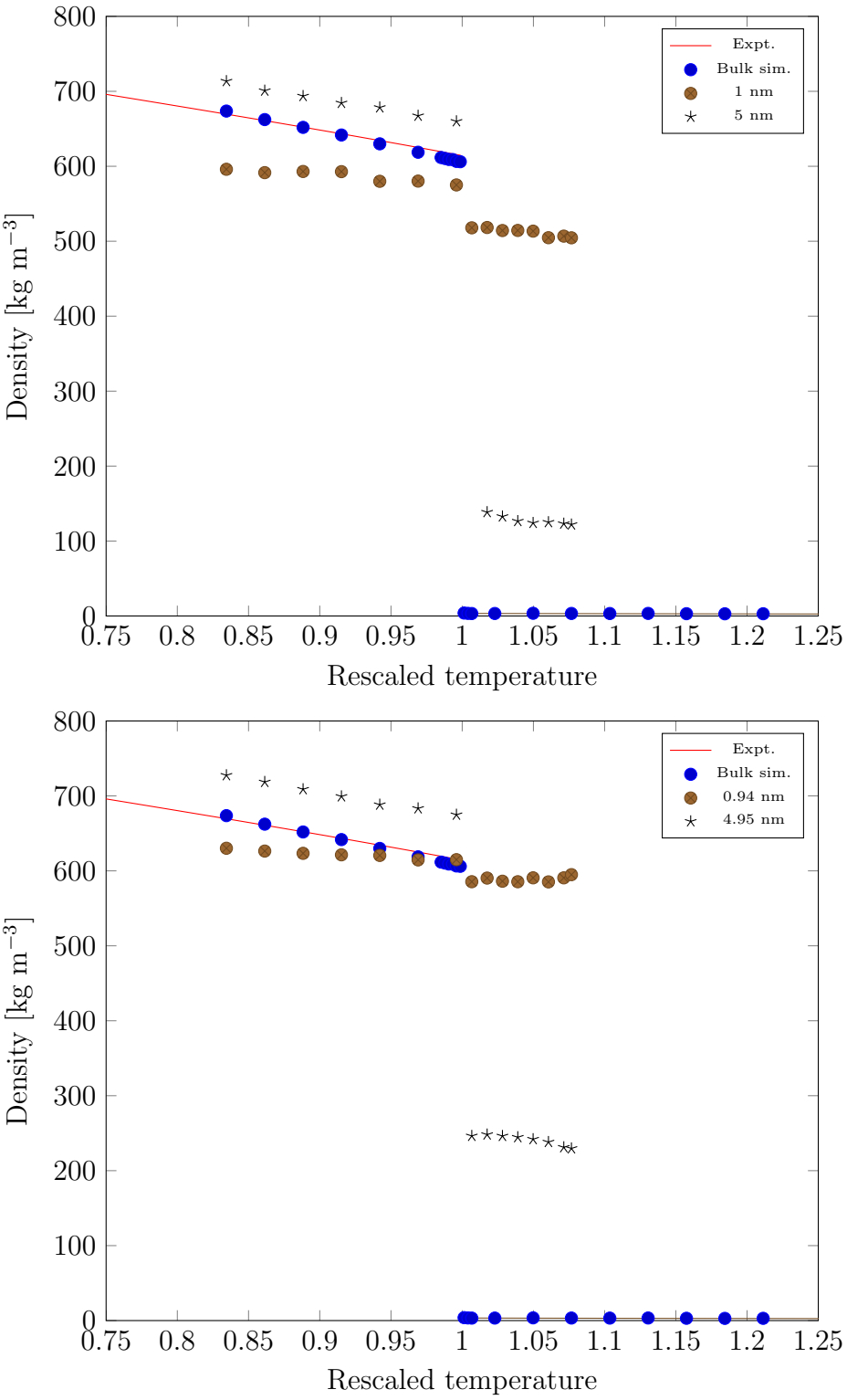


Figure 4.83: Adsorption isobars of n-heptane at 1 bar inside slit (top) and cylindrical (bottom) pores. The temperature is rescaled by the bulk fluid boiling point (371.5 K).

The 5 nm pore also exhibits a relationship between pore density and temperature that is not in line with the change in the bulk density, however to a lesser degree

than the 1 nm pores. Here the fluid molecules are only in contact with a single solid surface and as such there is lower energy barrier to overcome to break free of the surface. Vapour phase n-heptane from the centre of the pore also collides with fluid molecules in contact with the surface which may disturb them and also pull them away from the surface.

As discussed for water, if the hysteresis of these systems was investigated, by increasing the temperature and using the output of one simulation as the input of the next, the expected result is that the point of phase change would increase beyond the bulk fluid boiling point, to a greater degree in the smaller pores. This is the expected scenario as the pore fluid will have a different phase transition point as the bulk fluid due to increased intermolecular interactions and an elevated pressure due to confinement. This would be analogous to the adsorption isotherm results presented by Striolo et al. (2004) and Striolo et al. (2005b), in which the width of hysteresis loops were found to decrease with decreasing pore size.

4.5 Conclusions

Here the TIP4P and OPLS-AA models for water and n-heptane have been validated against experimental data and alternative models for the bulk density at 300-400 K, the saturated vapour pressure, the surface tension, and the liquid-vapour coexistence curves. The phase transition temperature at 1 bar has also been calculated for validation of the models. Additionally, density-temperature isobars are calculated.

In this work the phase transition temperature is found to have good agreement with the literature, being out by -2.6 % and -1.3 % for TIP4P water and OPLS-AA n-heptane respectively.

The saturated vapour pressure curve is overestimated with TIP4P by approximately 30 % over the entire range of temperatures simulated here. For OPLS-AA

n-heptane the curve does not follow the same trend as the experimental data, as it crosses the experimental data at approximately atmospheric conditions. The TraPPe-EH model shows a much better agreement and should be the model of choice for higher pressure, higher temperature, simulations. However, the OPLS-AA model is good for use in simulations at atmospheric pressure.

Both the TIP4P water model and the OPLS-AA n-heptane model underestimated the critical point by approximately 13 % and 7 % respectively. However, upon rescaling the shape of the liquid-vapour coexistence curves match well with the experimental values.

The curves for the OPLS-AA model of n-heptane generated here are inconsitent with literature data for the same fluid model. With reference to the work of Chen and Siepmann (1999), these results are out by -2.1% and -6.1% in the liquid phase and 72% and 52% in the gas phase. This is likely a result of the long-range dispersion forces being over-accounted for in the method of surface tension calculation used here. Gibbs ensemble Monte Carlo simulations would better suit the calculation of the surface tension and the VLE curves, however this has not been used here as the adsorption and slip processes require dynamic systems and as such any surface tension calculated would not match with what was really happening in the MD simulations. Use of a PME summation for the long-range dispersion forces is one way to avoid these issues, but would require a n-heptane model that has been parametrised with this in mind, rather than the OPLS-AA model which is parametrised with specific cut-offs.

The surface tension for water was consistently underestimated by the TIP4P model. However, most water models have trouble reproducing surface tensions due to the complexity of water. OPLS-AA n-heptane is shown to have very good agreement with the experimental surface tension, however there is few to no literature data available for the surface tension of OPLS-AA n-heptane for comparison.

The bulk density-temperature isobars match well with experimental data for both liquid and vapour phase systems. However, the rate of change of density with temperature for liquid phase systems was not captured entirely by the TIP4P water model.

After confirming the applicability of the water and n-heptane models for both vapour and liquid phase systems, the adsorption in carbon nanotubes and graphitic slit pores is studied. The rate and mechanisms of adsorption in slit and cylindrical pores of varying separation and radii is studied and discussed.

Water is found to enter all pores in a plug like manner due to the hydrophobic nature of the surface. However, in the larger pores, some curvature in the fluid front is seen indicating that the walls still restrict the motion of fluid, even if to only a small degree. This plug flow results in a constant fill rate up until the pore is filled entirely. There is however an initial lag region for all pores that occurs for both water and n-heptane and is likely due to a short re-equilibration period of the reservoirs after the pore barrier is removed.

The final density in the pore is shown to be highly dependent on the level of packing of fluid, since under extreme confinement all fluid exists in discrete layers. As such the fluid density varies drastically over only small relative changes in the pore sizes due to sudden phase changes. The rate of filling is shown to be slower for cases with high or low extremes in the density. In general the largest pores fill quickest and there is little deviation from a $1/R$ relationship between fill time and radius, other than a small amount for the density extremes. In the smallest cylindrical pore, where a single fluid layer exists under extreme confinement which reduces the number of translational kinetic modes, the fill mechanism is very different. Water molecules entering this pore separate from the bulk fluid and are shot along the pore until coming in to contact with the opposite fluid surface. This is unique to this pore due to the single file nature and extreme confinement that prevents hydrogen bonding.

As discussed in section 3.3 the viscosity of water is underestimated by the TIP4P model in the lower temperature range. The fill rates presented here are then expected to be overestimates due to the enhanced mobility of the fluid.

Unlike water, n-heptane was found to fill the same pores under a combination of push and pull mechanisms. The largest pores are still the fastest to fill, however there is a large variation in the time for filling in the smallest pores, depending on the ratio of the number of layers to pore area. In general, the pore fills at a constant rate until the pore surface has been covered entirely. At this point any fluid in contact with the solid surface has effectively frozen and forms a new pseudo pore surface for the remaining fluid to fill against. The new surface is rougher than the original and fluid filling the pore now does so at a reduced rate, comparable to what would be predicted for an effectively smaller pore. If the remaining pore space allows for a clear, continuous density, bulk fluid region then the pore will continue to fill under the pressure driving force imposed by the reservoirs at constant pressure. However, if no continuous region exists then the pore fills entirely under the pulling force of the solid surface. In this case the rate of fluid entry matches that of the Lucas-Washburn equation for spontaneous imbibition.

There exists a critical pore size for n-heptane in CNTs, above which filling occurs via a push dominated mechanism and below which it occurs via a pull dominated mechanism. Further, it is observed that, for n-heptane in the pores studied here, fluid is able to condense out from the wall away from the fluid front.

As discussed in section 3.4 the viscosity of n-heptane is overestimated whilst the self-diffusion coefficient is underestimated by the OPLS-AA model of n-heptane for all temperatures studied here. Both of these factors result in an retarded mobility of the fluid with respect to experiments. Hence, rates of adsorption reported here are expected to be consistently lower than in reality. Since the water results are expected to be overestimates, whilst the n-heptane results are

underestimates, the actual difference in fill rates between the two fluids will be larger than presented here.

For both water and n-heptane, a maximum fill rate is achieved that is contrary to predictions based on Navier-Stokes equations which show that the fill rate should increase linearly with the square of the pore size when the amount of slip is large. This is possibly related to entrance effects caused by the surrounding solid barricade or it could be due to the limited pore lengths studied here. There may be a further increase in the rate if the pore is sufficiently long, however pores here are stunted in the interest of reduced computational costs.

For vapour phase water the final pore density is similar to the bulk density and pores fill almost instantly, other than in the smallest pores where the reduced size prevents some modes of transport, effectively increasing the density.

Heptane at 400 K acts in a very different manner to water in CNTs and graphitic pores. Fluid fills to a single fluid layer at the pore surfaces whilst the central region of the pore fills with fluid at its equilibrium bulk density. The density in the fluid layer adjacent to the wall is similar to the liquid phase case, where the n-heptane molecules have effectively frozen against the surface. As the pore size is reduced, a third fluid layer is observed as molecules are held in place by the frozen first fluid layers in contact with the solid surface. The time for these pores to fill to equilibrium can be O(100) times longer than for the liquid cases due to fluid diffusing along the surface and from the central region at a slower rate due to the low reservoir density.

Graphene is oil-wetting and water-nonwetting. The contact angle of water on graphene is typically 95-100° (Taherian et al. 2013). For water, hydrophobicity of the surface dominates, hence the filling mechanisms depend on an external force. For n-heptane, the surface is strongly lipofilic and a surface layer is always present. The fill mechanism is dominated by surface diffusion and the bulk filling is a slower process.

Finally, density-temperature isobars are generated for water and n-heptane within 1 nm and 5 nm slit and cylindrical pores. For water, the 5 nm pore exhibited a density-temperature relationship in-line with that of the bulk, with a slight increase in the vapour phase densities. The 1 nm pores filled to much lower liquid densities and much higher vapour phase densities than the bulk. In the cylindrical case there appears to be a second phase transition point at which the vapour phase pore density drops towards the bulk value.

For n-heptane, both the 1 nm and 5 nm pores exhibit a density much higher than the bulk for vapour phase reservoirs and there is no secondary transition point observed in the temperature range studied. In the pores the vapour phase densities reduce at a steeper rate than the bulk, indicating that the increased kinetic energy of the fluid molecules allows for fluid to break free from the surface.

An improvement to these works would be to use PME summation for long-range dispersion forces, in addition to electrostatic forces, and a fluid model that has been parametrised to match.

In these works the temperature has been coupled directly to the fluid molecules. By coupling the temperature to the solid pore molecules the rate and mechanisms of adsorption may change. This could be introduced by artificially bonding solid molecules to lattice sites at the solid surface and controlling the temperature via bond oscillations. This could also be introduced by allowing the solid surface to move freely, in the same way as the piston has been defined. This would require a large number of individual simulations though as the random motion of the pore will affect adsorption.

Further investigation into hysteresis effects on isobars within CNTs and graphitic slit pores should also be performed. For a pore that is already filled with liquid phase fluid, gradually reducing the temperature of the fluid will likely result in a phase transition point that is higher than the bulk transition point. This is of importance for adsorption in engine deposits, as the engine temperature is

initially cold during start-up.

The equilibrated filled geometries that are generated here are now used in the following chapter for calculation of the slip length as a function of curvature.

Chapter 5

Calculation of slip lengths and friction coefficients via molecular simulation

5.1 Introduction

When studying nano-porous media, conventional computational fluid dynamics (CFD) and Lattice Boltzmann (LB) (Yang et al. 2013; Yang and Boek 2013; Boek and Venturoli 2010) methods may not be suitable to predict flow and transport properties in their current conditions. The reason is that these techniques make the assumption of a no-slip boundary condition at fluid-solid interfaces, which is not necessarily the case when pore sizes become comparable to molecular diameters. If slip is not taken into account, then the mean velocity in the channel can be underestimated drastically. Quantifying the amount of slip in a channel of given curvature and solid-fluid combination is a challenge that requires explicit molecular scale simulation techniques such as Molecular Dynamics (MD).

It can be fairly straightforward to simulate and understand flow in a straight chan-

nel or cylindrical pore using MD simulations alone. Even so, there are challenges involved in modelling fluid flow and slip in nanopores, especially with regards to water. Some of these have been highlighted by Kannam et al. (2017), along with an outline of some ways to resolve these. See the reference or section 2.4.2 for details. However, in reality in most porous materials the geometry can be complex and non-trivial. Unfortunately, the slip in a complicated geometry, with many twists and turns and even roughness at the atomic scale, is not the same as that for a straight channel. It turns out that the slip length changes with the curvature of the solid-fluid interface in both the direction of flow and the perpendicular direction (Falk et al. 2010).

This chapter will focus on quantifying slip in graphitic geometries as well as focusing on the effect of surface curvature on the friction coefficient, and therefore the slip length. If we are able to determine the slip length and the relationship this has with surface curvature, we can upscale our systems from the molecular scale to the continuum scale. This can be implemented via a slip parameter in a nanoscale Lattice Boltzmann model for complex geometries and long time simulations. This allows for an accurate estimation of flow rates. At larger scales simulations can be easily performed on large complex geometries that are inaccessible to molecular simulations. From these, parameters such as permeability can be extracted for further upscaling. In addition to engine deposits, this is of particular use to hydrocarbon recovery from tight pore spaces, such as gas shales and tight rocks. More information on how the slip length is implemented into a Lattice Boltzmann model can be found in chapter 6.

The work presented in this chapter is an extension of Ross and Boek (2016).

5.2 Objectives

As part of achieving one of the key objectives of this thesis, the calculation of the slip length, there are several questions that should be addressed. The first of which is whether the slip length depends on the surface geometry, or whether it is independent as concluded by Chen et al. (2014). If the slip length is dependent on geometry then how important is the confinement and curvature in this regard. Additionally, is there a level of confinement/curvature, beyond which the amount of friction is independent of geometry?

Since the EMD method of Bocquet and Barrat (2013) is used, it is also important to confirm that the slip length calculated from EMD simulations matches with those from NEMD.

An attempt will be made to answer all of these questions in this chapter.

5.3 Methodology

The equilibrated fluid-filled pores generated in chapter 4 are removed from their respective reservoirs and made periodic, such that the pore is continuous in the z-dimension. An example of the geometry before this procedure takes place is shown in figure 5.1. This process involves selecting only the pore and all fluid molecules that are at least partially inside the pore and resizing the periodic box. Any overlapping molecules are removed, to prevent numerical instabilities. This process works well for small molecules such as water, but an extra step is needed for n-heptane. Since n-heptane is a long molecule more overlapping occurs, which results in a low density at the periodic boundary. This dissipates after a few time-steps, however it results in a low density across the entire pore and bubbles of vacuum can form. The barriers which were previously obstructing fluid access to the exterior of the pore are also removed.

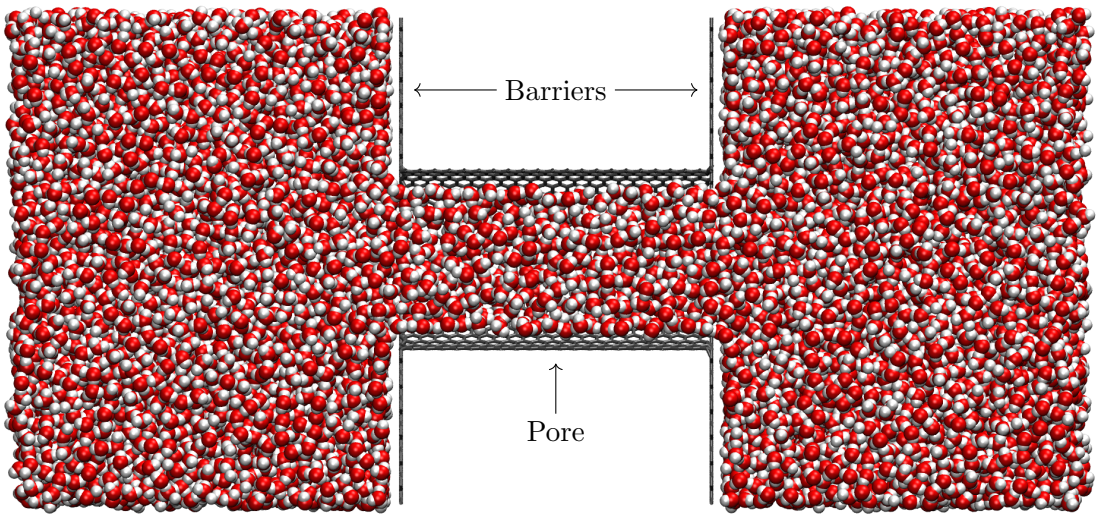


Figure 5.1: Cross section of equilibrated system of water inside a carbon nanotube, before removal of the reservoirs.

The reduced density at the periodic boundary in the z-dimension can be clearly seen in figure 5.2 along with the density after several time steps.

Due to the spreading out of the fluid, it is difficult to add back any molecules that are missing. To counter this, the system is first simulated at a much lower temperature such that the fluid freezes and large vacuum bubbles form. It is then easier to insert enough additional fluid molecules into the system to match the equilibrium pore density found in chapter 4. The temperature is then set back to normal and the fluid is allowed to equilibrate.

A sample set of equilibrated pores are shown in figure 5.3. The advantage of using this method is that the fluid maintains its structure in proximity of the solid surface, as opposed to being structured in an unrealistic way, which may occur if the entire pore fluid is replaced.

The equilibration method affects the number of fluid molecules present and thus the calculated friction coefficient and slip length. It is for that reason that the filled pores produced in chapter 4 are used here, as pores have been filled from reservoirs at the stated conditions rather than filled directly based on a known value of the bulk density. As shown in chapter 4 the pore density is not equal to the bulk density and can be vastly different when the bulk conditions correspond

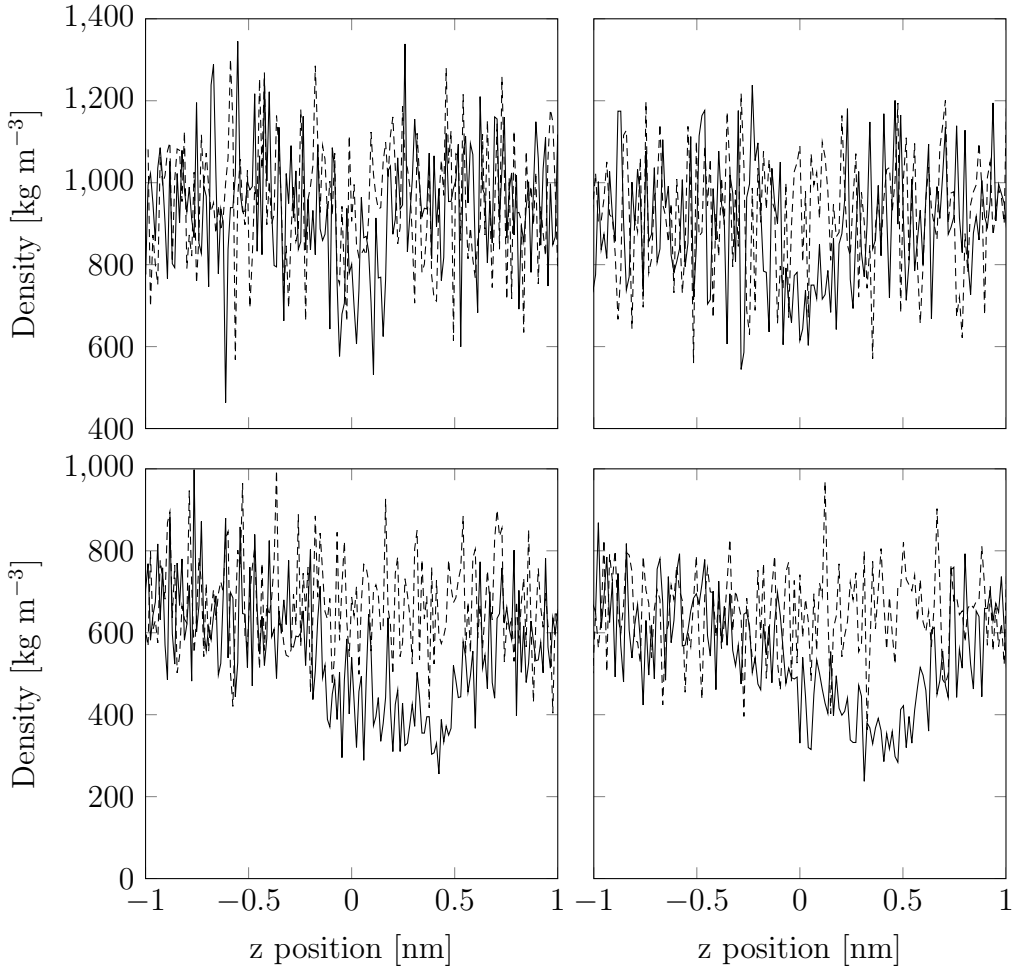


Figure 5.2: Density profile along the length of the pore initially (solid) and after several time steps once filled back up to equilibrium value (dashed) for water (top) and n-heptane (bottom) in 10 nm slit (left) and cylindrical (right) pores. The z-position has been shifted, such that zero is the location of the end of the pore prior to removal of the reservoirs and addition of periodicity.

to a gas phase.

With the resulting geometry, friction coefficients and slip lengths are calculated using an equilibrium MD (EMD) method and verified where possible with a non-equilibrium MD method.

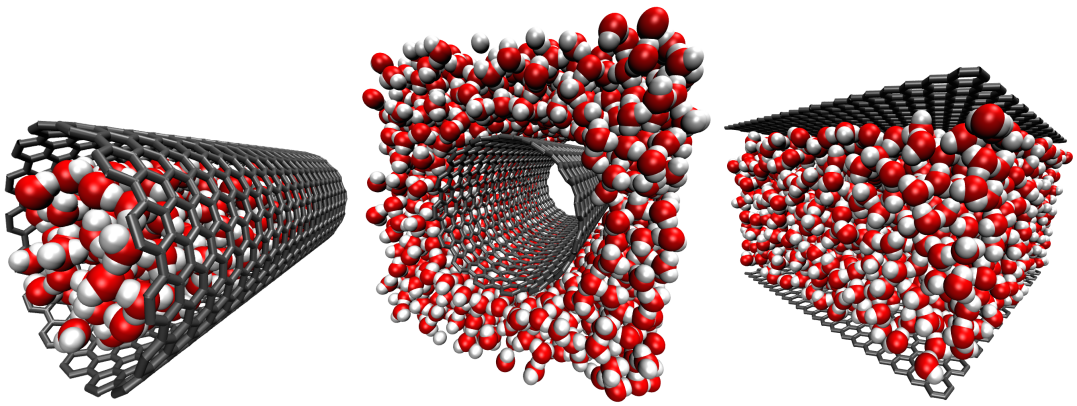


Figure 5.3: Example of geometries studied here. From left to right: Fluid inside carbon nanotube. Fluid outside of carbon nanotube. Fluid inside graphitic slit pore.

5.3.1 Non-equilibrium slip calculation

A simple approach for calculating the slip length is to apply a driving force to fluid molecules in a pore that has been filled at a realistic density. This driving force is applied via updating atom velocities each time-step to reflect some acceleration. The result, after a long equilibration period, is some overall flow through the pore.

Here a relatively low acceleration, in comparison to the point at which divergence from shear independent slip occurs (Thompson and Troian 1997), of 0.0001 nm ps^{-2} is used in order to avoid high shear rate effects. The dependence of the slip length on shear rate is discussed later in this section. System snapshots are output every 1 ps and results are extracted by averaging over the final 35 ns (35,000 snapshots) of a 40 ns simulation for each acceleration and geometry. These NEMD simulations are repeated 5 times and the average slip length is taken. Two methods of extracting the slip length from the resulting data are discussed here, however only the latter case is used.

Slip length from velocity profile

The amount of slip at a surface is defined by the Navier slip length, b. The steady-state velocity profile can be extracted via binning and ensemble averaging over many time-steps. Finally, using the wall velocity, u_{wall}, and the shear rate at the wall, $\mathrm{d}u/\mathrm{d}x|_{wall}$, the slip length can be found:

$$b = \frac{u_{wall}}{\mathrm{d}u/\mathrm{d}x|_{wall}}. \tag{5.1}$$

Slip length from mean velocity

The graphitic surfaces used in this work are atomistically smooth. As such, the slip length is high, especially in the case of water which is repelled by the hydrophobic surface. In this case, the velocity profile is difficult to measure directly due to it being virtually flat. As such, equations 5.2 and 5.3 are used to calculate the slip length from NEMD trajectories for the slit and cylindrical cases respectively:

$$b = \frac{2\mu u_m}{\rho g_z H} - \frac{H}{6} \tag{5.2}$$

$$b = \frac{2\mu u_m}{\rho g_z R} - \frac{R}{4} \tag{5.3}$$

where u_m is the mean fluid velocity in the direction of flow, μ is the shear viscosity, ρ is the fluid density, g_z is the applied acceleration, R is the cylinder radius, and H is the height of the channel.

This requires the assumption that the viscosity and density are constant across the entire pore and that the viscosity in the pore is the same as in bulk. The density is certainly not constant across the pore and so the average density has been used instead. It is difficult to measure the viscosity under extreme confinement.

However, the larger scale Lattice Boltzmann method, for which these results shall be incorporated into, only currently accepts a single value of the viscosity, independent of the confinement. Therefore, in order to maintain consistency between the mean fluid velocities measured from MD and LBM, the same constant viscosity should be used in all cases.

Equations 5.2 and 5.3 are derived via the integration of the Navier-Stokes solutions for unidirectional, laminar, flow in slit and cylindrical geometries, equations 5.4 and 5.5 respectively.

$$u_z = \frac{\rho g_z}{2\mu}\left(Hx - x^2 + bH\right) \tag{5.4}$$

$$u_z = \frac{\rho g_z}{4\mu}\left(R^2 - r^2 + 2bR\right) \tag{5.5}$$

The detailed derivation of equations 5.2 and 5.3 is given in Appendix A.

Mean velocity

Following on from equations 5.4 and 5.5, it is possible to derive the slip length as a function of the mean velocity. In order to obtain the mean velocity the following two equations are use:

$$u_m = \frac{1}{H}\int_0^H u_z \mathrm{d}x \tag{5.6}$$

$$u_m = \frac{2}{R^2}\int_0^R u_z r \mathrm{d}r. \tag{5.7}$$

Combining equations 5.6 and 5.7 with 5.4 and 5.5 results in:

$$u_m = \frac{\rho g_z}{2\mu}\left(\frac{H^2}{6} + bH\right) \tag{5.8}$$

$$u_m = \frac{\rho g_z}{2\mu}\left(\frac{R^2}{4} + bR\right). \tag{5.9}$$

It is then trivial to rearrange for the slip length, resulting in equations 5.2 and 5.3.

Shear rate effects on slip

Typically forces in excess of O(10) times gravity are required for computational feasibility. With lower forces comes longer equilibration times as well as times for result analysis. Depending on the system, the slip length can vary with shear rate at these unrealistically high driving forces (Thompson and Troian 1997). As such, special care should be taken in order to make sure that the transport is still reasonable and reflective of realistic conditions.

As shown in equations 5.4 and 5.5 the shear rate at the wall scales proportionally with the driving force and is independent of the slip length.

Problems with the non-equilibrium method

The NEMD method used here has its weak points. For instance, the time required for equilibration is large, in that steady-state must be achieved before the mean velocity can be extracted. This time is dependent on the size of the driving force and can be in excess of 10s of ns.

Similarly the time over which to average results is long. Ideally, each data point should be made up of 5-10 repeated simulations in order to ensure sufficient statistical accuracy. Given that roughly 10-20 data points are necessary in order to ensure the correct functional relationship between slip and geometry has been found, up to 200 simulations would be required. This makes this method increasingly impractical, as even a single simulation is time consuming, with even slightly more realistic driving forces. For this reason, the more computationally efficient equilibrium method has been used in addition to this method.

5.3.2 Equilibrium slip calculation

An alternative approach for quantifying and calculating the amount of slip in a given geometry, used herein, was proposed by Bocquet and Barrat (Bocquet and Barrat 2007). The method involves calculating the friction coefficient from equilibrium MD (EMD) simulations and then relating this back to a slip-length. The advantage of this is that equilibration times are significantly reduced as compared to non-equilibrium simulations. This is also particularly useful as the friction coefficient can be calculated for any flow direction from the same data set. The friction coefficient, λ, is calculated using the following Green-Kubo type relation:

$$\lambda = \frac{1}{Ak_BT}\int_0^\infty \mathrm{d}t\langle F\left(t\right)F\left(0\right)\rangle_{equ} \tag{5.10}$$

where A is the total surface area, k_B is the Boltzmann constant, T is temperature and $F(t)$ is the sum of the tangential forces applied by the fluid on the solid surface. $\langle F(t)F(0)\rangle_{equ}$ is the autocorrelation function averaged over equilibrium configurations. The slip length is recovered from the friction coefficient using the following relation:

$$b = \frac{\mu}{\lambda}. \tag{5.11}$$

In equation 5.11, μ is the shear viscosity, which can be found from a single-phase fluid simulation using a similar Green-Kubo type expression as used for the friction coefficient (Zwanzig 1965). Details of the viscosity calculation can be found later in this section.

Here, the same geometry is used as in the case of the non-equilibrium method. The fluid has no driving force applied and instead is allowed to freely interact with the solid surface. The systems are re-equilibrated at 300 K and at constant volume

for 200 ps before a final 1 ns results run. During this time the full trajectories are written every time-step. The sum of the interaction forces between the solid surface atoms and the fluid is recovered from the trajectories and is autocorrelated for use in equation 5.10.

Viscosity calculation

There are several methods of calculating the shear viscosity, including by both equilibrium and non-equilibrium means. Hess (2002) describes and compares four methods, two equilibrium and two non-equilibrium methods. The first method involves the pressure fluctuations; in this the viscosity is calculated by integrating the Green-Kubo-correlation-function formula:

$$\mu = \frac{V}{k_B T} \int_0^\infty \langle P_{\alpha\beta}(t_0)\, P_{\alpha\beta}(t_0 + t) \rangle \, \mathrm{d}t \tag{5.12}$$

where μ, V, k_B, T are the viscosity, volume, Boltzmann constant and temperature respectively. $P_{\alpha\beta}$ is an off-diagonal element of the pressure tensor, i.e. $\alpha \neq \beta$ such as xy, xz and yz, given by:

$$P_{\alpha\beta} = \frac{1}{V} \left(\sum_i m_i v_{i\alpha} v_{i\beta} + \sum_i \sum_{j>i} r_{ij\alpha} f_{ij\beta} \right) \tag{5.13}$$

where $r_{ij\alpha}$ is the α component of the separation between particles i and j. $f_{ij\beta}$ is the β component of the force between the two particles, where $\boldsymbol{f}$ is given by:

$$\boldsymbol{f} = -\frac{\partial U}{\partial \boldsymbol{r_{ij}}} = -\frac{\partial U}{\partial r_{ij}} \frac{r_{ij}}{\boldsymbol{r_{ij}}} \tag{5.14}$$

U is the potential between particles. The integrand in equation 5.12 is known as the stress autocorrelation (SAC) function.

The second equilibrium method Hess (2002) describes uses the transverse-current correlation functions for plane waves. In this method the viscosity is determined from the autocorrelation of the amplitude of plane waves in the simulation box. Considering an incompressible liquid with the following initial velocity due to a plane wave in one direction:

$$\boldsymbol{u}\left(\boldsymbol{r},0\right)=u_0\cos\left(kz\right)\hat{i}+0\hat{j}+0\hat{k}. \tag{5.15}$$

Solving Navier-Stokes equation and incorporating a relaxation time as a phenomenological correction for the short time correlation function not being a pure exponential (the solution without such correction displays an exponential decay with a time constant inversely proportional to the viscosity), the following equation is found:

$$u_x(z,t)=u_0e^{-\beta}\left(\cosh\left(\Omega\beta\right)+\frac{1}{\Omega}\sinh\left(\Omega\beta\right)\right)\cos\left(kz\right) \tag{5.16}$$

where

$$\beta=\frac{t}{2\tau_m} \tag{5.17}$$

and τ_m is the relaxation time and

$$\Omega=\sqrt{1-4\tau_m\frac{\mu}{\rho}k^2}. \tag{5.18}$$

The velocity is found by fitting the transverse-current correlation functions for different $\boldsymbol{k}$-vectors to equation 5.16. The shear viscosity depends on the magnitude of k and so the macroscopic viscosity is found by extrapolating to $\boldsymbol{k}=0$. The viscosity can be approximate in third order by:

$$\mu(k) = \mu(0)(1 - ak^2) + O(k^4). \tag{5.19}$$

A study by Payal et al. (2012) demonstrates the difficulty of recovering the correct viscosity with different fluid models using an equilibrium MD simulation. In their study the shear viscosity is calculated using the Green-Kubo formalism. They find that even moving from an all-atom (AA) force field to a united-atom (UA) forcefield results in a less accurate result for the viscosity, up to a 30% underestimate for UA compared to a 10% overestimate for AA. Another issue they highlight is that in the conventional equilibrium MD approach, where one trajectory is sampled at equilibrium, it is likely that a reasonable amount of configuration space has not been sampled as the system may be 'stuck' in a metastable configuration. Their solution is to assume that a spread over all accessible phase space, with appropriate Boltzmann weight, can be covered by averaging over a set of independent trajectories at equilibrium. This results in a faster convergence of viscosity versus a single trajectory approach with improved accuracy.

5.4 Discussion

5.4.1 Water at 300 K

Figure 5.4 shows the friction coefficient as a function of the radius for liquid water, at 300 K, inside and outside of a CNT. The central points are the base case for fluid confined between two slabs of graphene, where the radius plotted is half the separation. As expected, the friction coefficient, and consequently the slip length, is independent of the separation between flat slabs whilst a clear functional relationship exists between the friction coefficient and the surface curvature.

The base case is the case of zero curvature, effectively infinite radius. The curva-

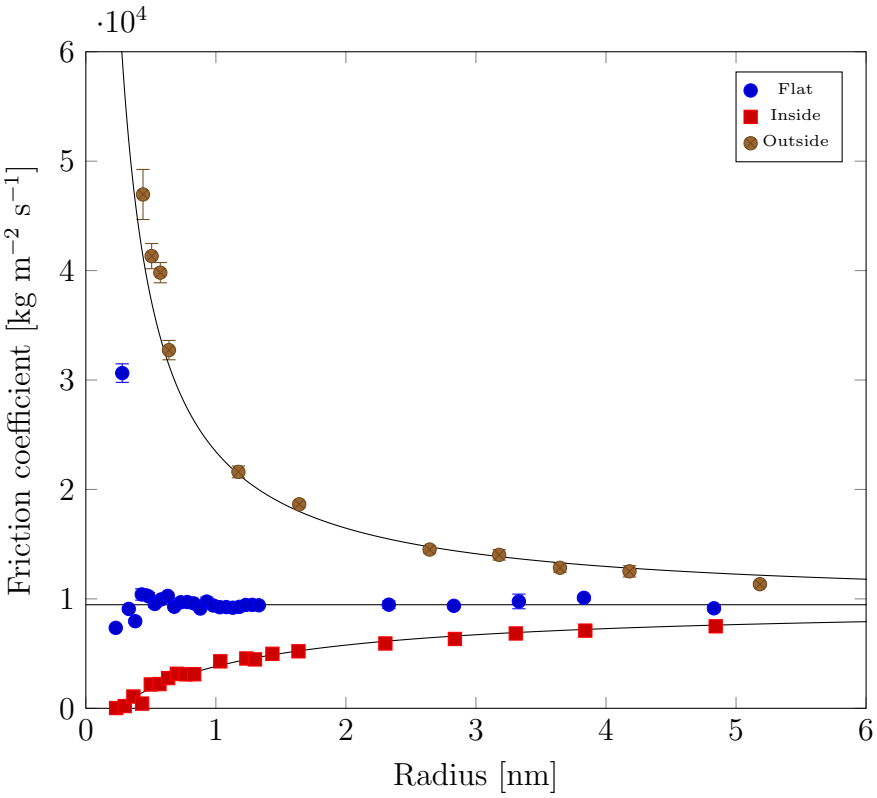


Figure 5.4: Friction coefficient calculated using equation 5.10, for water at 300 K, inside and outside of a carbon nanotube. The central dataset is for water between two flat surfaces. The lines of fit shown are used to find the constants in equations 5.22.

ture, κ, is related to the radius, R,as follows:

$$\begin{aligned} \text{Fluid inside} : \kappa &= \frac{1}{R} \\ \text{Fluid outside} : \kappa &= -\frac{1}{R}. \end{aligned} \tag{5.20}$$

The data in figure 5.4 is fitted to functions chosen based on the assumption that the friction coefficient for fluid on the outside or inside of cylindrical pores takes the following form:

$$y = \frac{C_1}{R + C_2} + C_3 \tag{5.21}$$

where C_1, C_2, and C_3 are constants and C_2 is assumed to be zero for fluid against a convex surface, i.e. for cases of negative curvature. The solid lines in figure 5.4

are the fits to data using the subsequently derived relationships:

$$\begin{aligned} \kappa < 0 &: \lambda = A\kappa + \lambda_{flat} \\ \kappa = 0 &: \lambda = \lambda_{flat} \\ \kappa > 0 &: \lambda = \lambda_{flat}\left(\frac{1-\kappa R_m}{1+\kappa B}\right) \end{aligned} \tag{5.22}$$

where A and B are fitting parameters, λ_{flat} is the friction coefficient for the base case, and R_m is the radius at which fluid inside the cylinder experiences a minimum friction coefficient. In all cases studied here fluid enters the pore space from a reservoir at 1 bar, without any additional driving forces. As such, the effect of decreasing the cylinder radius to molecule size ratio below the point at which no fluid will naturally enter the pore has not been studied. The cylindrical pore sizes studied here are limited to discrete radii, due to the molecular structure of the solid surface and the chemical bonds present with constrained lengths. Further work could include investigating the effect of increasing the size of the adsorbate molecules within a pore in order to see whether the friction coefficient increases with an increasing ratio above the maximum studied here.

λ_{flat} is found from the base case and is used as a constraint whilst fitting for the positive and negative curvature cases. Although it is possible to estimate R_m from the size of the fluid molecules, this has been left as an open constant for the fit. The values for the fitting parameters in equation 5.22 are as follows:

$$\begin{aligned} \lambda_{flat} &= (9460 \pm 60)\,\mathrm{kg\,m^{-2}\,s^{-1}} \\ R_m &= (0.233 \pm 0.033)\,\mathrm{nm} \\ A &= (14\,000 \pm 600)\,\mathrm{kg\,m^{-2}\,s^{-1}\,nm} \\ B &= (0.896 \pm 0.095)\,\mathrm{nm}. \end{aligned} \tag{5.23}$$

A clear result here is that the type of curvature, whether concave or convex, impacts the amount of friction experienced by the fluid at the solid surface.

Fluid on the inside of a CNT experiences a decreasing amount of friction for a decreasing radius. Whilst fluid on the outside experiences a larger amount of friction as the radius is decreased. These results are consistent with the work of Falk et al. (2010).

A key result here is that, once the friction against a flat surface is known, there are only two unknown parameters, A and B, that need to be determined. It is likely that these parameters are a function of the solid material along with the fluid structure and properties. This relationship is not investigated here however is an important next step, as reducing the number of simulations required to determine the friction coefficient, and as such the slip length, would reduce computational costs.

Figure 5.5 shows the conversion to the slip length from the friction coefficient, using equation 5.11, and the comparison to the value calculated using the same filled geometries in non-equilibrium MD simulations. Although the viscosity value is used for conversion from the friction coefficient to the slip length here, it has also been used during calculation of the slip length in NEMD. The slip length calculated from the NEMD trajectories is not directly proportional to the viscosity and as such the value selected will have some impact on the comparison if the viscosity used is incorrect. However, for large mean velocities (as measured here) the second terms in equations 5.2 and 5.3 have a small impact on the slip length and as such the value of the viscosity used here makes little difference on the comparison between methods. Only the magnitude of the slip length will change whilst the relative sizes between the two methods remains comparable.

There is very good agreement here between the NEMD results and the EMD results, confirming that this EMD method is an appropriate method for atomistically smooth and symmetrical surfaces such as those studied here.

Small oscillations in the friction coefficient for the slab geometries can be seen for separations less than 2 nm. This is a result of the changes in the density

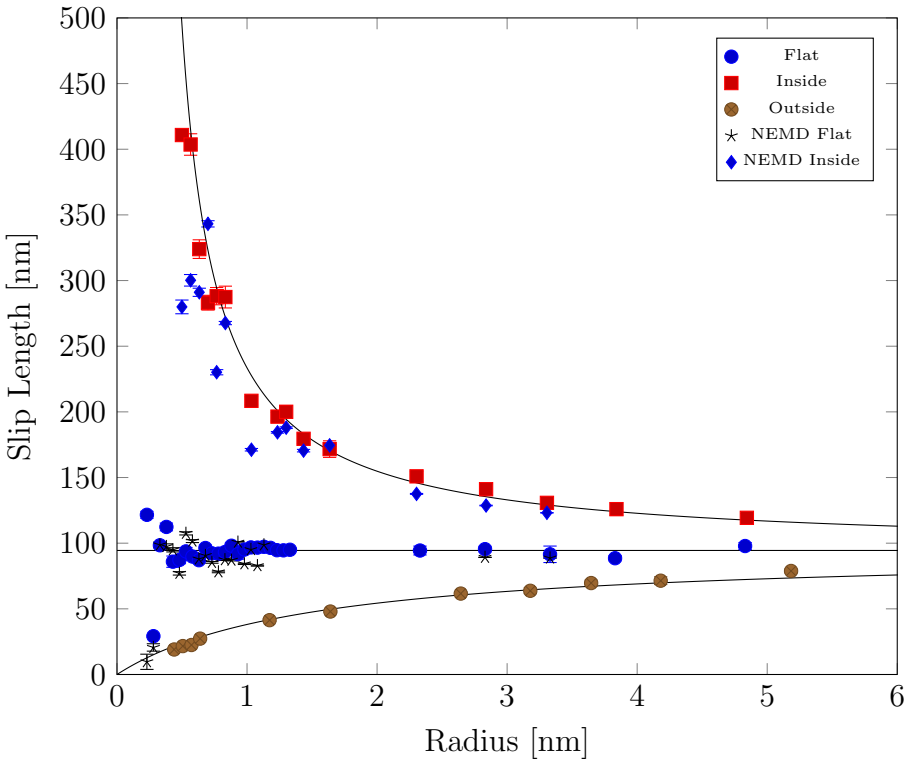


Figure 5.5: Comparison between EMD and NEMD slip lengths, for water at 300 K, calculated using equation 5.11 and equations 5.2 and 5.3 respectively. The lines are the fits from the EMD method and are equivalent to those in figure 5.4. NEMD results only exist for the inside and flat cases as there is no simple analytical solution to the Navier-Stokes equation for the outside case.

within the pores as the level of confinement is varied, caused by the discrete fluid layering that occurs under extreme confinement. The effect of confinement on the pore density and layering are discussed in chapter 4. The pores with higher filled-fluid densities exhibit larger friction coefficients due to an increased number of molecules in proximity to the surface atoms, resulting in a larger total force.

The same density variations are present for fluid inside cylindrical pores, however the impact on the friction coefficient here is much smaller than in the slab cases due to the already decreasing friction coefficient. The affect can be seen somewhat in figure 5.5 however it is difficult to conclude that the distribution of data is cased by this or just statistical noise. The statistical accuracy is also questionable down at this radius, as the number of molecules is significantly reduced in comparison to the slab geometry. This can be countered by increasing the pore length, however the length of the pore is already at its maximum feasible value.

The slip length is O(100) nm here which results in an enhancement to the mean flow rate of approximately 20-200 times that in the 10 nm and 1 nm straight pores respectively. This is even higher in the cylindrical geometries due to the larger slip lengths, reaching in excess of 2000 times the expected value in the smallest pores given no slip.

5.4.2 n-Heptane at 300 K

Figure 5.6 shows the friction coefficients, calculated for liquid n-heptane at 300 K. The general trend of the data matches that of liquid water, however large oscillations in the friction coefficient can be seen in the slab geometry case. This is due to the much more variable density in n-heptane filled pores and the difference in the scale. An obvious observation is that the friction coefficient is an order of magnitude larger in this case (as expected due to the very large fluid-solid interactions). The points of increased friction correspond to the pores with the higher fluid densities. This is a key result that is possibly only visible due to the use of a realistic method of equilibration. If the pore is filled directly using fluid at its bulk density, rather than filling naturally from a reservoir, then these oscillations in the average pore density would not be present. This cements the importance of using a realistic method of equilibration.

The constants found from the fits to equation 5.22 are as follows:

$$\begin{aligned} \lambda_{flat} &= (51.200 \pm 0.400)\,\mathrm{kg\,m^{-2}\,s^{-1}} \\ R_m &= (0.298 \pm 0.036)\,\mathrm{nm} \\ A &= (38.200 \pm 3.900)\,\mathrm{kg\,m^{-2}\,s^{-1}\,nm} \\ B &= (0.236 \pm 0.103)\,\mathrm{nm}. \end{aligned} \tag{5.24}$$

Here λ_{flat} is more than five times larger than for liquid water, again due to the increased surface attraction. R_m is also 28 % larger than for water, as would be

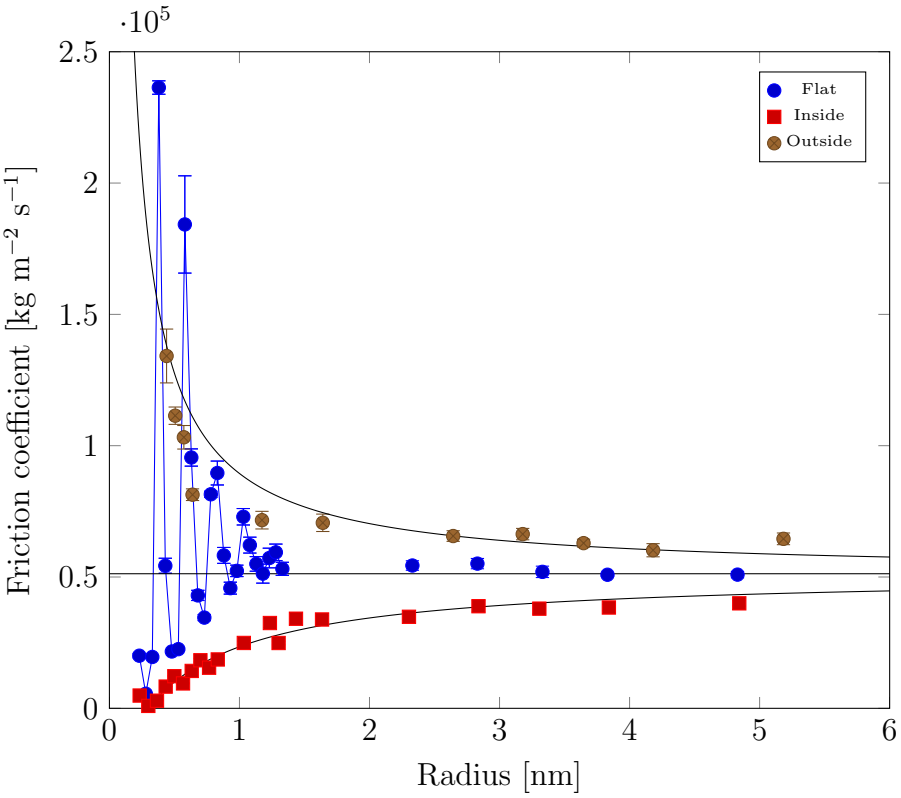


Figure 5.6: Friction coefficient calculated using equation 5.10, for n-heptane at 300 K, inside and outside of a carbon nanotube. The central dataset is for water between two flat surfaces. The lines of fit shown are used to find the constants in equations 5.22.

expected since n-heptane is a wider molecule, even though it has an easier time entering the pore. The values of the constants A and B are also different here than for water, with A 270 % larger and B 74 % smaller for n-heptane. This confirms that the parameters A and B are a function of the fluid in addition to likely being a function of the surface material.

Again, the friction coefficients are converted to slip lengths for comparison with NEMD in figure 5.7. As before there is good agreement with the NEMD results.

The slip length here is O(10) nm, whilst liquid water exhibits slip lengths of O(100) nm due to the hydrophobic nature of the CNTs and graphitic geometries. Although the slip length is much smaller for n-heptane, it is still non-negligible and results in an enhanced flow rate of approximately 3-21 times for 10 and 1 nm pores respectively. In the smallest cylindrical pores this is still in excess of 200

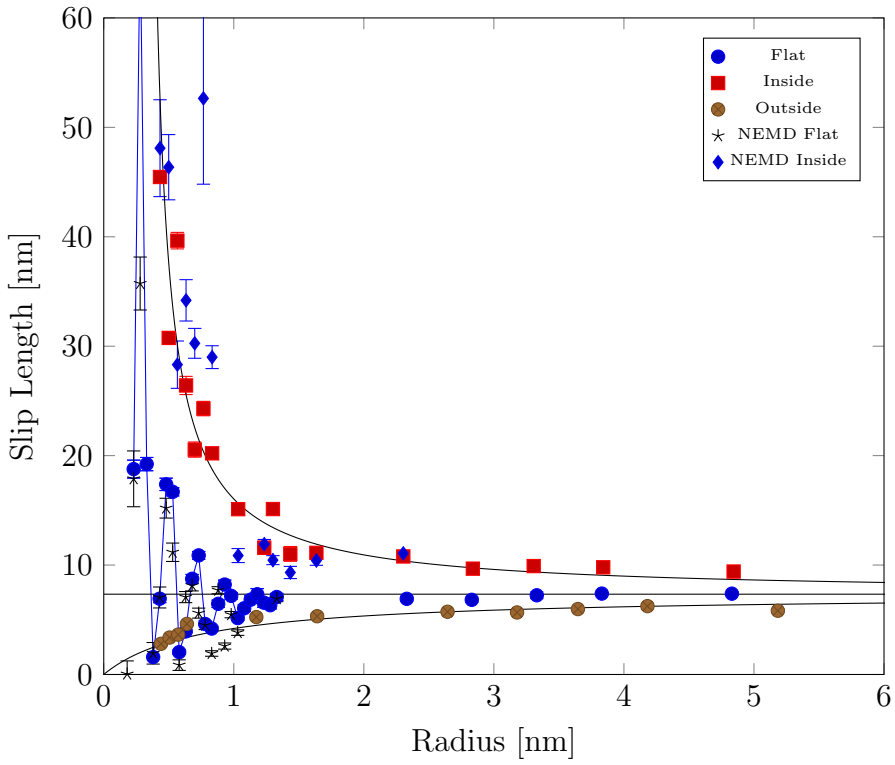


Figure 5.7: Comparison between EMD and NEMD slip lengths, for n-heptane at 300 K, calculated using equation 5.11 and equations 5.2 and 5.3 respectively. The lines are the fits from the EMD method and are equivalent to those in figure 5.4. NEMD results only exist for the inside and flat cases as there is no simple analytical solution to the Navier-Stokes equation for the outside case.

times the expected no-slip value. This iterates the point that slip is important even for fluids that are highly attracted to the pore surface in the case of smooth pores. This is consistent with simulations by Ho et al. (2011) where liquid water exhibited slip even on hydrophilic surfaces. This reference is discussed in section 2.4.2.

More importantly, detailed molecular simulation gives insight on the actual physics, which is different from the continuum model, which presents a smooth increase in the velocity from the wall inwards.

Klein and Kumacheva (1998) observed this same abrupt liquid-solid transition relationship in surface force balance experiments using cyclohexane, octamethyl-cyclotetrasiloxane, and toluene confined between smooth mica surfaces. They were able to probe in detail the transition between liquid-like and solid-like be-

haviour whilst reducing the separation between confining surfaces. The authors noted that this sharp transition is reversible and occurs as a function of confinement alone. The number of monolayers, below which the behaviour is observed, depends on the fluid but was typically six in their experiments, corresponding to approximately 5 nm separation.

Subsequently, the authors investigate shear and frictional behaviour of these solidified films (Kumacheva and Klein 1998), again using surface force balance experiments. Like in this work, they showed that their friction coefficient does vary with the number of monolayers between the confining surfaces, generally with larger friction coefficients being measured when less monolayers are present. The yield shear stress, corresponding to an effective friction coefficient, also increased with increasing normal pressure before transitions in the number of layers occurs. This matches qualitatively well with what is seen in figure 5.6.

5.4.3 Water at 400 K

Calculations are performed for vapour phase water at 400 K, although the results are much less accurate due to the low fluid density and the difficulty in selecting a single viscosity to represent the entire fluid volume when the density varies drastically across the pore. Figure 5.8 shows that the data is much more scattered for the friction coefficient for vapour phase water. This is presumably due to the poor statistics derived from performing a single simulation with fewer molecules than for the liquid case. In general the friction coefficient is much smaller than for the liquid case, inherently due to the reduced fluid density in the pore coupled with the lower solid-fluid interaction strength.

The friction coefficients are converted to slip lengths, using a literature value the viscosity of bulk vapour phase water (IAPWS 1997), in figure 5.9. Here the base case slip length is O(1000) nm.

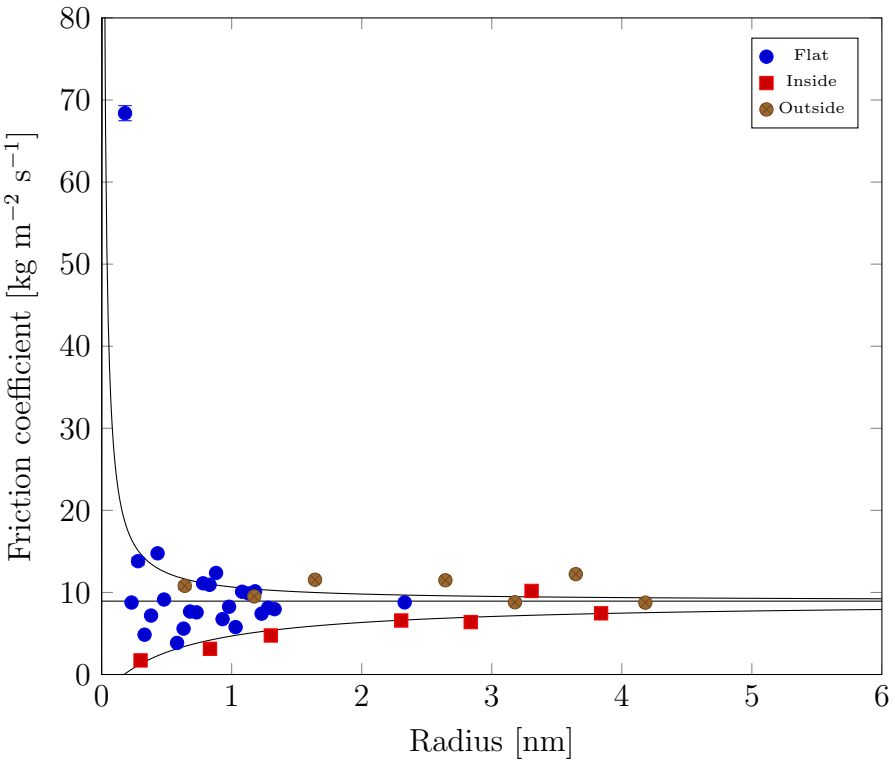


Figure 5.8: Friction coefficient calculated using equation 5.10, for water at 400 K, inside and outside of a carbon nanotube. The central dataset is for n-heptane between two flat surfaces. The lines of fit shown are used to find the constants in equation 5.22.

Due to the small number of fluid atoms in the pore and the inherent disadvantages of the NEMD method for slip calculation, the error in the slip length is similar to the scale of the plot. As such the slip lengths from NEMD have not been plotted for comparison, although the average values were of the same order of magnitude to those calculated from the friction coefficient.

The parameters found from the fit to equation 5.22 are as follows:

$$\begin{aligned} \lambda_{flat} &= (8.94 \pm 0.50)\,\mathrm{kg\,m^{-2}\,s^{-1}} \\ R_m &= (0.174 \pm 0.187)\,\mathrm{nm} \\ A &= (1.73 \pm 0.83)\,\mathrm{kg\,m^{-2}\,s^{-1}\,nm} \\ B &= (0.575 \pm 0.440)\,\mathrm{nm}. \end{aligned} \tag{5.25}$$

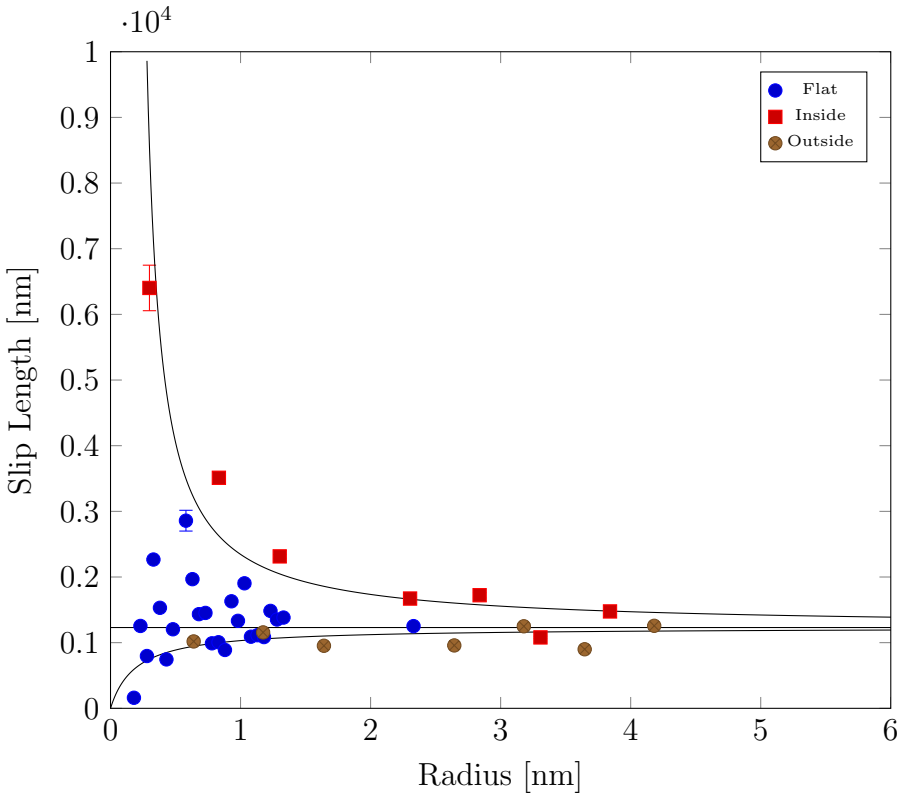


Figure 5.9: EMD slip lengths, for water at 400 K, calculated using equation 5.11. The lines are the fits from the EMD method and are equivalent to those in figure 5.4.

5.4.4 n-Heptane at 400 K

Calculations are performed for vapour phase n-heptane at 400 K. Here figure 5.10 takes a similar form to the liquid phase n-heptane case, due to the strong layering at the surface which is fairly independent of the equilibrium bulk fluid phase. However, a key observation is that for fluid against a convex surface there is no longer an asymptotic behaviour at low radii. In fact the relationship now is linear between the friction coefficient and the radius of curvature. This is presumed to be a consequence of the monolayer adsorption, which allows molecules to break free from the surface given the relatively weak fluid-solid interaction. In contrast, the fluid inside cylindrical and slit pores is unable to break from the solid surface even at these conditions. Increasing oscillations in the friction coefficient with decreasing radii is still seen in the vapour case, however to a much lesser degree.

The friction coefficients are converted to slip lengths, using a literature value the

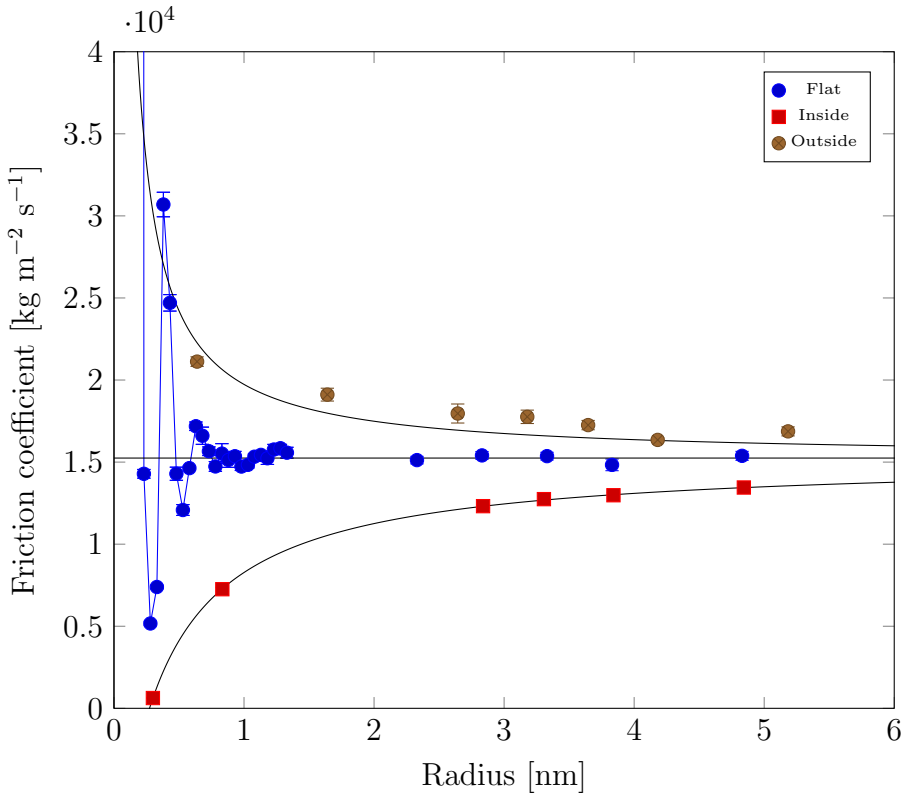


Figure 5.10: Friction coefficient calculated using equation 5.10, for n-heptane at 400 K, inside and outside of a carbon nanotube. The central dataset is for n-heptane between two flat surfaces. The lines of fit shown are used to find the constants in equation 5.22.

viscosity of bulk vapour phase n-heptane, in figure 5.11. Here the slip length is O(1) nm. This is the opposite result as that found for water, in which the slip length was much larger for vapour phase fluid in comparison to liquid phase. Here the fluid layering at the surface, and as such the forces contributing to the friction coefficient, is similar to that of the liquid phase fluid due to the high solid-fluid attraction. The true viscosity of the fluid in contact with the surface is in fact much higher than the fluid in the centre of the pore, the former taking values close to those of the liquid state viscosity, leading to much smaller slip lengths. In practice however, the bulk fluid (gas) viscosity would be used for flow calculations and as such this choice of viscosity used in the conversion is the relevant one.

As is the case with water, so is the case for n-heptane, whereby the errors for the NEMD slip results are too large for inclusion here. Again, the average magnitude was found to be of the same order as for the results found using EMD and the

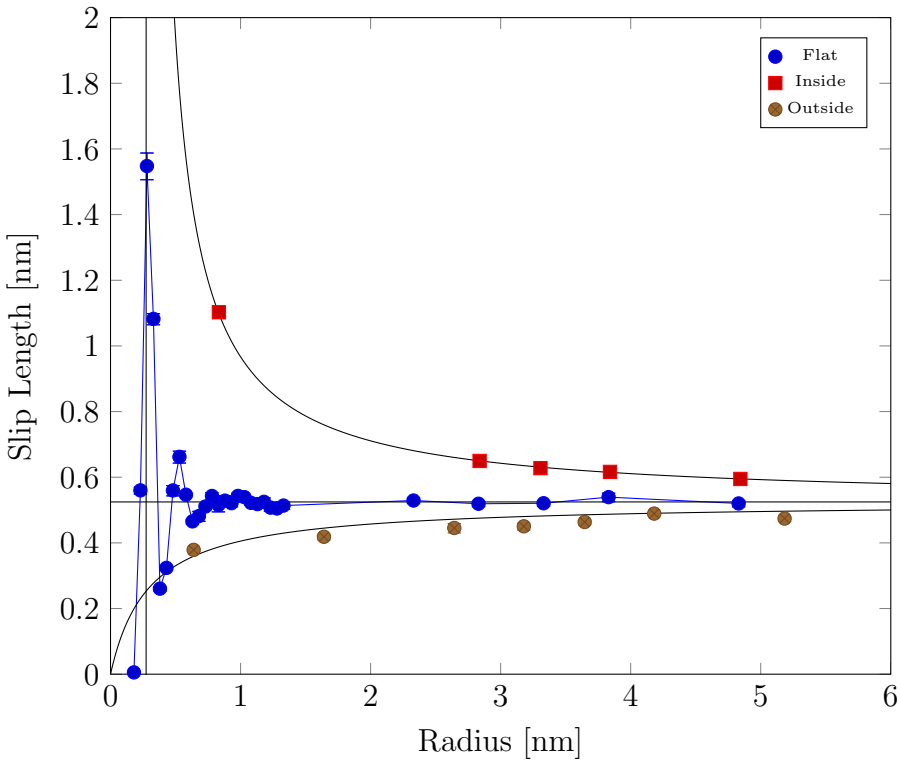


Figure 5.11: EMD slip lengths, for n-heptane at 400 K, calculated using equation 5.11. The lines are the fits from the EMD method and are equivalent to those in figure 5.4.

friction coefficient method.

The parameters found from the fit to equation 5.22 are as follows:

$$\begin{aligned} \lambda_{flat} &= (15.200 \pm 0.100)\,\mathrm{kg\,m^{-2}\,s^{-1}} \\ R_m &= (0.273 \pm 0.002)\,\mathrm{nm} \\ A &= (4.490 \pm 0.560)\,\mathrm{kg\,m^{-2}\,s^{-1}\,nm} \\ B &= (0.339 \pm 0.005)\,\mathrm{nm}. \end{aligned} \tag{5.26}$$

5.5 Conclusions

Equilibrium MD and non-equilibrium MD simulations are performed in order to calculate friction coefficients and slip lengths against flat surfaces and surfaces of both concave and convex curvature and under increasing levels of confinement.

The EMD method presented by Bocquet and Barrat (2013) and used here is proven to be an effective method of calculating friction of both liquid water and n-heptane against graphitic surfaces and within carbon nanotubes. The calculated friction coefficients are converted to slip lengths via the bulk fluid viscosity and compared to NEMD and match extremely well for liquids. For vapour phase fluids, NEMD slip lengths are difficult to obtain due to the low statistical accuracy and the requirement of unrealistically large driving forces for flow. This iterates the importance of the EMD method of calculating the slip length when computational costs are an issue. Even when computational costs are not an issue, it is still challenging to simulate at realistic driving forces with reasonable statistical accuracy.

Here it has been shown that the average slip length is independent of separation for flat surfaces. However, when there is strong solid-fluid attraction, the fluid layering and confinement cause increasingly large deviations from the average that are dependent on the pore density. There is also a clear functional relationship between the slip length and curvature that differs depending on whether the surface is concave or convex. Functions are proposed here which depend on two currently unknown parameters over the entire slip range of radii. The slip length has been shown to increase with decreasing radii for both water and n-heptane inside CNTs whilst it decreases for fluid on the outside of the same CNTs. The slip length is also much larger for vapour phase water in the same geometries as liquid phase water, whilst for n-heptane the opposite is observed due to the large solid-fluid attractive forces. It has also been shown here that the method of filling the pore is important for gaining accurate insight into the fluid arrangement in the pore and as such calculate accurate slip lengths. By filling from an equilibrated reservoir of fluid the pore naturally fills to the correct density and proper layering is observed. This is unlike what would be expected based on simply adding fluid to a periodic pore at its known bulk density.

The results presented here confer a clear geometry and curvature dependence

of the slip length and friction coefficient, unlike those presented by Chen et al. (2014), who concluded that the the slip length was independent of shape or confinement. These results are not necessarily conflicting, as the systems studied are very different. In their work Chen et al. (2014) used a solid surface with an atomic number density equal to that of the fluid, this leads to a surface which is approximately 30 times less dense than in the present work. This difference in surface could have a significant impact on the results, as the likely reason for the deviation in the amount of slip seen between flat and curved surfaces is the smoothing of the surface energy landscape experienced by the fluid in proximity to the surface with increasing concave curvature and the roughening exhibited with increasing convex curvature. This is discussed in detail by Falk et al. (2010). In addition to this, the smallest radius of curvature tested is approximately 3.5 nm for flow external to a cylinder and 16 nm for internal flow. For internal flow, concave curvature, the radius is already much larger than curvatures studied in this work for which deviations occur between the slip length and the radius. However, for flow externally, 3.5 nm is within the range at which curvature should have an impact on the slip length. The lack of a change seen in their work is likely due to the differences between the surface density and the fluid model. It is unknown for sure where the critical curvature, at which curvature dependence arrises, would be for less dense surfaces. However, it is suspected that it would be smaller or non-existent due to the inability to reach such small cylinders with such a low solid density. The critical radius of curvature would also shift depending on the wettability of the surface and structure of the fluid, as seen in the work of Falk et al. (2012). Another difference between this study and theirs is that they use a solid surface which can hold a temperature, unlike the unmoving surface in this work, which may result in a change in the mechanism of slip.

The trends in the friction coefficients and the liquid-solid transitions presented here are also qualitatively comparable with the results of other works, including Reiter et al. (1994), Gao et al. (1997), Klein and Kumacheva (1998), Kumacheva

and Klein (1998), Cummings et al. (2010), and Docherty and Cummings (2010).

In conclusion, the EMD method provides accurate data that can now be implemented as part of a slip boundary condition into larger scale Lattice Boltzmann simulations. In order to accurately capture the oscillations in the friction coefficient for highly wetting fluids, a more complex fitting function is required such that a continuous function is passed to larger scale simulation methods.

Chapter 6

Lattice Boltzmann implementation of slip parameter

6.1 Introduction

Lattice Boltzmann method (LBM) can be regarded as a kinetic approach for high performance Computational fluid dynamics (CFD). The main difference between conventional CFD methods and LBM is that the former are performed by solving conservation equations of the macroscopic properties and therefore involve numerically solving the Navier-Stokes equations, which contain complex partial differential equations. In contrast, LBM involves modelling a fluid element as a system composed of virtual particles that are allowed to move only on a discrete lattice mesh. The Fundamental idea of LBM is to use a simplified kinetic model which incorporates the underlying physics of microscopic phenomena such that the macroscopic averaged properties honour the desired macroscopic equations, avoiding the need for directly solving complex equations (Chen and Doolen 1998).

The lattice Boltzmann method evolved from lattice gas cellular automata (LGCA) in the late 1980s. It was first introduced by McNamara and Zanetti (1988) in order to overcome the initial drawbacks of LGCA, specifically intrinsic noise, non-

Galilean invariance, an unphysical velocity dependent pressure and large numerical viscosities (Perumal and Dass 2015). Unlike LGCA, which models particles discretely at lattice sites, lattice Boltzmann methods use a density distribution to represent virtual fluid particles. Boolean operation is removed from here by neglecting particle correlations and introducing averaged distribution functions. Macroscopic variables can then be obtained by evaluating hydrodynamic moments of the particle distribution function (He and Doolen 1997). The lattice Boltzmann method has been further improved since its initial conception, undergoing multiple evolutionary steps. A simple linearised collision operator based on the Bhatnagar-Gross-Krook (BGK) (Bhatnagar et al. 1954) model was introduced by Koelman (1991) and Chen et al. (1991) independently, allowing for the recovery of the macroscopic Navier-Stokes equations from the local equilibrium distribution function. Furthermore, Lallemand and Luo (2000) showed that, with a multi-relaxation-time model, high Reynolds numbers could be achieved with high accuracy results and numerical stability.

LBM has attracted numerous researchers due to it being an ideal candidate for parallel computing, hence enhancing the efficiency in terms of computation time, while still maintaining its high accuracy. Another appealing aspect of LBM is its ability to simulate fluid flows with complex physics and geometries. Owing to these, LBM has found applications in many industries and engineering fields.

6.1.1 Lattice gas cellular automata (LGCA)

Lattice gas cellular automaton (LGCA) models are the precursor to LBM and were first introduced by Hardy et al. (1973). A cellular automaton is an algorithmic entity containing a collection of cells on a grid or lattice point of specific shape that evolves through a number of discrete time-steps and interacts with its identical neighbours according to a set of rules based on the neighbouring cells states, where each cell is in one of a finite number of states.

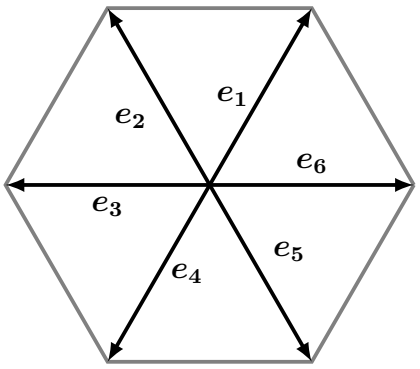


Figure 6.1: The two-dimensional FHP model and its unit velocity vectors (adapted from Sukop and Thorne (2013)).

In 1986, Frisch, Hasslacher, and Pomeau proposed the first lattice gas model that could properly simulate the two-dimensional incompressible Navier-Stokes equation. The model, commonly referred to as the FHP model, which is named after its pioneers, takes the form of a regular lattice with hexagonal symmetry (Frisch et al. 1986).

Each lattice is surrounded by six neighbours, as in figure 6.1, such that the lattice points are spaced at a distance of 1 lattice unit (lu) and the motion of particles between lattice points occur at 1 lu ts^{-1}, where ts is a single time-step. Each lattice site hosts up to six particles of equal mass and the particles can only move along one of the six directions defined by the discrete displacements. At each time-step, the evolution of a lattice gas model proceeds in two steps. The first one being the streaming, or propagation, step in which the particles hop to the nearest neighbouring site by the corresponding discrete vector. The second step is collision step in which the particles collide and scatter according to collision rules, such that the microscopic scale collisions honour mass and momentum conservation. In the case of a lattice gas, the conservation of momentum reduces to conservation of the vector sum of the velocities since all particles have the same mass.

The fundamental computational advantage of the LGCA approach to fluid dynamics are that it allows for exact computing, hence giving round-off freedom due

to its underlying pure Boolean nature, making it possible to conduct simulations with virtually unlimited parallelism (Succi 2001).

However, some drawbacks exist due to the discretisation of the lattice. The main one is that the lattice gas dynamics are intrinsically noisy hence giving a fair amount of statistical fluctuations (Qian and Orszag 1993). LGCA also shows a numerical weakness in that it is controlled by the maximum number of collisions per unit time that the automaton is able to support, hence limiting it to be computable only for low Reynolds numbers (Succi 2001).

Although rarely used today, LGCA was an important stepping stone in the development of the lattice Boltzmann models that are becoming increasingly popular due to their advantages over traditional CFD.

6.1.2 Boltzmann equation

The key difference between LBM and LGCA is that operations are no longer Boolean. Instead of lattice nodes representing six particles each able to move in one of six directions, they now represent a collection of many virtual particles. Now vectors represent a density distribution of particles, based on the probability of a single particle being ejected in that direction after a collision step.

Consider a fluid that is composed of N particles with certain velocities and colliding elastically. In principle, by employing classical mechanics and by knowing each molecule's position, $\boldsymbol{x}$, and momentum, $\boldsymbol{p}$, at a given time, the future states of the particles can be predicted with high precision.

The distribution function of such system can be described by $f^{(N)}\left(\boldsymbol{x}^N, \boldsymbol{p}^N, t\right)$. However, the change of such system with time would produce a set of functions containing 6N variables, making the computation not feasible when dealing with real gases, for instance, where approximately 10^{23} (N) particles are involved in

just 1 mole of gas. However, most often only low order distribution functions ($N = 1, 2$) are of interest.

In the derivation of the Boltzmann equation, it is assumed that interactions with other molecules only occur for a very small fraction of time compared to their lifetime, such that only binary interactions are important.

The distribution $f^{(1)}(\boldsymbol{x}, \boldsymbol{p}, t)$ is called the single particle distribution function, showing the probability of finding a molecule with a particular position and momenta. The choice of molecule does not matter as it is not possible to distinguish between molecules under investigation; the information of the remaining $N - 1$ molecules can remain undetermined.

Given that initially at time t the molecules are at positions $\boldsymbol{x}$ and have momenta $\boldsymbol{p}$, upon introducing an external force, $\boldsymbol{F}$, to the fluid molecules and in the case where there are no collisions occurring, new positions and momenta can be found. The new positions and momenta of molecules at time $t + \mathrm{d}t$ are $\boldsymbol{x} + \mathrm{d}\boldsymbol{x} = \boldsymbol{x} + (\boldsymbol{p}/m)\mathrm{d}t$ and $\boldsymbol{p} + \mathrm{d}\boldsymbol{p} = \boldsymbol{p} + \boldsymbol{F}\mathrm{d}t$, respectively. Therefore, at time $t + \mathrm{d}t$, the streaming process can be described as:

$$f^{(1)}(\boldsymbol{x} + \mathrm{d}\boldsymbol{x}, \boldsymbol{p} + \mathrm{d}\boldsymbol{p}, t + \mathrm{d}t)\mathrm{d}\boldsymbol{x}\mathrm{d}\boldsymbol{p} = f^{(1)}(\boldsymbol{x}, \boldsymbol{p}, t)\mathrm{d}\boldsymbol{x}\mathrm{d}\boldsymbol{p}. \tag{6.1}$$

However, due to collisions, there are molecules that start at $\boldsymbol{x}$ that do not arrive at $x + \mathrm{d}\boldsymbol{x}$ and those that start somewhere other than $\boldsymbol{x}$ but arrive at $x + \mathrm{d}\boldsymbol{x}$. $\boldsymbol{\Gamma}^{(-)}\mathrm{d}\boldsymbol{x}\mathrm{d}\boldsymbol{p}\mathrm{d}t$ is used to represent the former situation and $\boldsymbol{\Gamma}^{(+)}\mathrm{d}\boldsymbol{x}\mathrm{d}\boldsymbol{p}\mathrm{d}t$ to represent the latter. This results in the change of equation 6.1 into:

$$f^{(1)}(\boldsymbol{x}+\mathrm{d}\boldsymbol{x}, \boldsymbol{p}+\mathrm{d}\boldsymbol{p}, t+\mathrm{d}t)\mathrm{d}\boldsymbol{x}\mathrm{d}\boldsymbol{p} = f^{(1)}(\boldsymbol{x}, \boldsymbol{p}, t)\mathrm{d}\boldsymbol{x}\mathrm{d}\boldsymbol{p} + \left[\boldsymbol{\Gamma}^{(+)} - \boldsymbol{\Gamma}^{(-)}\right]\mathrm{d}\boldsymbol{x}\mathrm{d}\boldsymbol{p}\mathrm{d}t. \tag{6.2}$$

Expanding the LHS of equation 6.2 using Taylor series expansion results in the Boltzmann equation:

$$\boldsymbol{v} \cdot \nabla_x f^{(1)} + \boldsymbol{F} \cdot \nabla_p f^{(1)} + \frac{\partial f^{(1)}}{\partial t} = \boldsymbol{\Gamma}^{(+)} - \boldsymbol{\Gamma}^{(-)}. \tag{6.3}$$

This equation was derived by Boltzmann in 1872, however it took more than 50 years before an approximate solution was found. In lattice Boltzmann methods the equation is solved approximately by limiting the particles positions to lattice sites and similarly using discretised time-steps.

6.1.3 Model

The first lattice Boltzmann method was introduced by McNamara and Zanetti (1988) in an effort to eliminate statistical noise in LGCA simulations, by replacing the Boolean particle occupation variables, n_i, with a discretised single distribution function $f_1 = \langle n_i \rangle$. The kinetic form used in LBM is the same as for LGCA, therefore maintaining the advantages of locality in the kinetic approach, making it useful for implementation in complicated boundary conditions and multiphase interfaces modelling (Chen and Doolen 1998).

There are several choices of underlying lattice for LBM, commonly referred to in DαQβ-notation, where α and β denote the dimensionality of the lattice and the number of discrete velocities within the momentum discretisation, respectively. Among the commonly used lattices are D2Q9 and D3Q19. For the purpose of simplicity only the 2D, D2Q9, model will be described here, although the D3Q19 lattice used in this study follows an analogous procedure. In this model, the variations of momenta are reduced to 9 directions which includes a rest state, 3 magnitudes and a single particle mass (Sukop and Thorne 2013).

In figure 6.2, $\boldsymbol{e}_a$ represents the 9 velocity directions, where a is the direction index

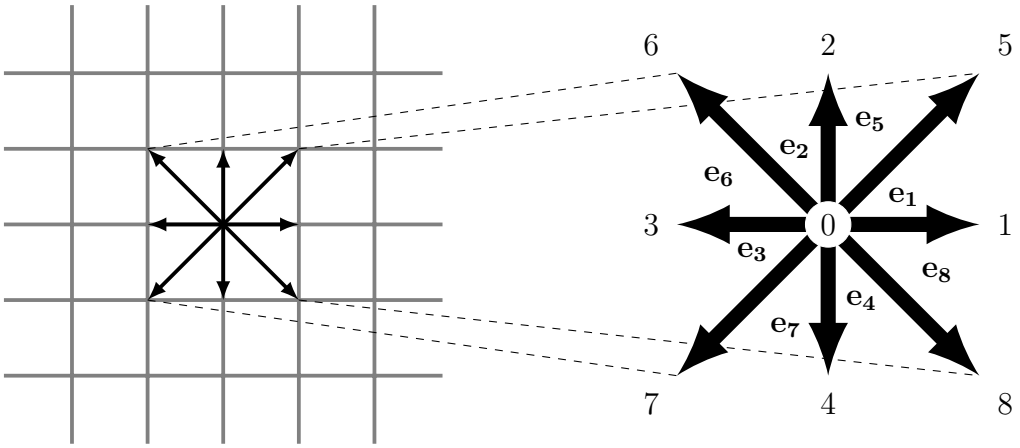


Figure 6.2: The D2Q9 model lattice (adapted from Sukop and Thorne (2013)).

and $a = 0$ signifies a particle is at rest. These velocities are as follows:

$$\boldsymbol{e}_0 = (0, 0) \tag{6.4}$$

$$\boldsymbol{e}_{1,2} = (\pm 1, 0) \text{ at } 1 \text{ lu ts}^{-1} \tag{6.5}$$

$$\boldsymbol{e}_{3,4} = (0, \pm 1) \text{ at } 1 \text{ lu ts}^{-1} \tag{6.6}$$

$$\boldsymbol{e}_{5,6,7,8} = (\pm 1, \pm 1) \text{ at } \sqrt{2} \text{ lu ts}^{-1} \tag{6.7}$$

Where the lattice unit (lu) and time-steps (ts) are the measure of length and time unit respectively.

The distribution function has 9 discrete bins and represents a probability of occurrence which can be considered to be the direction-specific fluid densities. Hydrostatic properties can be recovered using the Chapman-Enskog procedure, which shows that in the limit of long-wavelength and low-frequency the lattice Boltzmann equation reproduces exactly the Navier-Stokes equation. The macroscopic density is thus as follows:

$$\rho = \sum_{0}^{8} f_a. \tag{6.8}$$

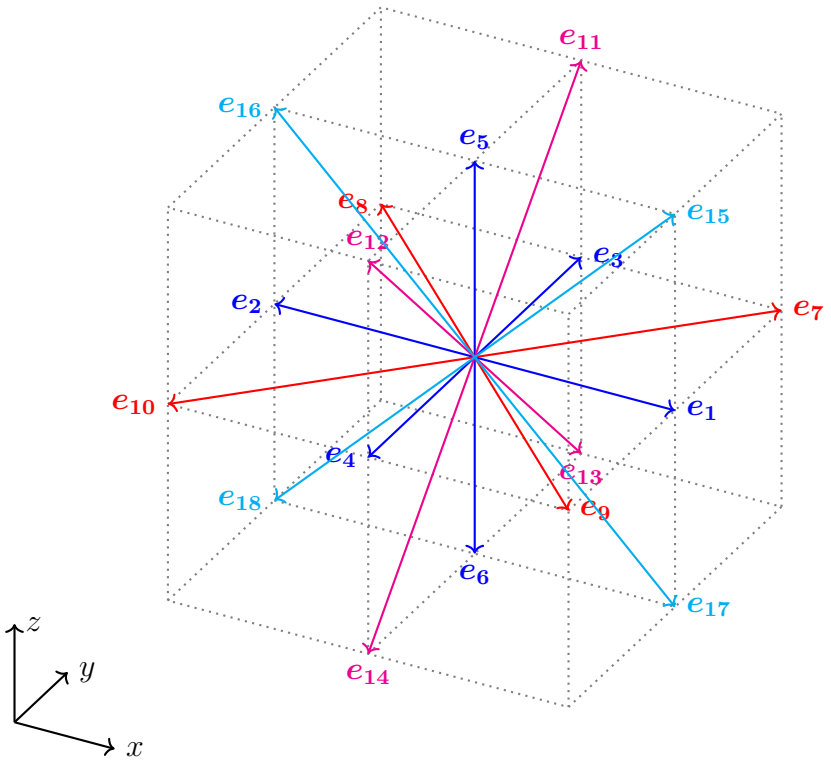


Figure 6.3: The D3Q19 model lattice.

The macroscopic velocity, $\boldsymbol{u}$, is obtained by taking the average of the microscopic velocities, $\boldsymbol{e}_a$, whilst accounting for the directional densities f_a, or distribution function, as follows:

$$\boldsymbol{u} = \frac{1}{\rho} \sum_{0}^{8} f_a \boldsymbol{e}_a. \tag{6.9}$$

As mentioned above, the lattice grid used in these works is the D3Q19 lattice, which allows for fluid transport in 3-dimensions as opposed to 2. The grid, along with the relevant distributions, is shown in figure 6.3.

Single relaxation time lattice BGK (LBGK)

In order to solve for the distribution function, and thus the macroscopic properties of the system, the Boltzmann equation is discretised with the BGK approximation (Bhatnagar et al. 1954) to become the discretised Boltzmann equation:

$$f_a\left(\boldsymbol{x}+\boldsymbol{e}_a\Delta t, t+\Delta t\right) = f_a\left(\boldsymbol{x}, t\right) - \frac{f_a(\boldsymbol{x},t) - f_a^{eq}(\boldsymbol{x},t)}{\tau} + \boldsymbol{F} \tag{6.10}$$

where $f_a\left(\boldsymbol{x}, t\right)$ and $\left(f_a(\boldsymbol{x},t) - f_a^{eq}(\boldsymbol{x},t)\right)/\tau$ are the streaming and collision parts respectively. f_a^{eq} is the equilibrium distribution, towards which the distribution function is relaxed with the relaxations time, τ, and $\boldsymbol{F}$ is a driving force term. The kinematic viscosity, ν, is related to τ as follows:

$$\nu = \frac{1}{3}(\tau - \frac{1}{2}). \tag{6.11}$$

The local equilibrium distribution function, f^{eq}, is as follows:

$$f_a^{eq}(\boldsymbol{x}) = w_a\rho(\boldsymbol{x})\left[1 + 3\frac{\boldsymbol{e}_a\cdot\boldsymbol{u}}{c^2} + \frac{9}{2}\frac{(\boldsymbol{e}_a\cdot\boldsymbol{u})^2}{c^4} - \frac{3}{2}\frac{\boldsymbol{u}^2}{c^2}\right] \tag{6.12}$$

where w denotes the weight of the particles and c is the basic speed on the lattice which takes the value of 1 lu ts^{-1}. The weights are 4/9 for $a = 0$, 1/9 for $a = 1, 2, 3, 4$, and 1/36 for $a = 5, 6, 7, 8$.

Equation 6.10 holds true for lattice points within the fluid domain, but not for the domain-boundaries, such as for periodic boundaries, velocity boundaries, solid boundaries, etc. These are discussed in section 6.1.4. Due to this reason, numerical implementation of the two streaming and collision steps are treated separately (Cercignani 1969).

Figure 6.4 shows the streaming step in D2Q9 model where distribution functions are translated to the neighbouring sites according to their discrete velocity direction. In the collision step, which is illustrated in figure 6.5, the distribution functions redistribute according to local relaxation Maxwellian rule, while still maintaining the invariance of local mass and momentum.

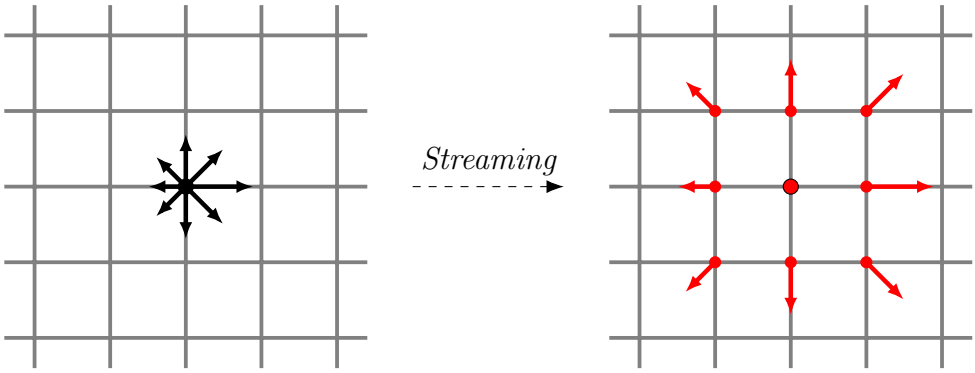


Figure 6.4: The streaming process on a D2Q9 lattice (adapted from Cercignani (1969)).

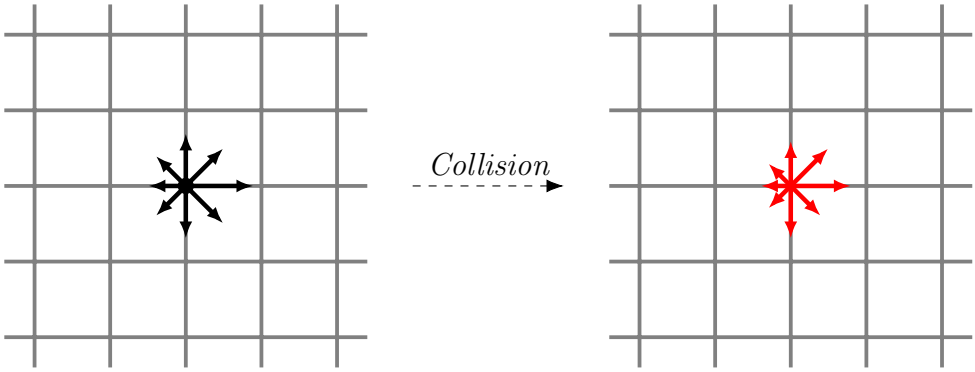


Figure 6.5: The collision process on a D2Q9 lattice (adapted from Cercignani (1969)).

Multiple relaxation time model (MRT)

The lattice Boltzmann method has shown great promise for simulating multiphase flows. However, the BGK collision operator has been shown to have problems with numerical stability as the relaxation time is decreased (McCracken and Abraham 2005). Additionally, the single relaxation time model requires a fixed Prandtl number and fixed ratio between the kinematic and bulk viscosities. Boundary conditions are also sensitive to viscosity and can cause a viscosity-dependant slip velocity. Here the multiple relaxation time (MRT) model, which requires only a small increase in computation time, is used in place of the BGK collision operator, overcoming these defects. With this change, equation 6.10 becomes:

$$f_a\left(\boldsymbol{x}+\boldsymbol{e}_a\Delta t, t+\Delta t\right) = f_a\left(\boldsymbol{x}, t\right) + \boldsymbol{S}\left[f_a^{eq}(\boldsymbol{x}, t) - f_a(\boldsymbol{x}, t)\right] + \boldsymbol{F} \tag{6.13}$$

where $\boldsymbol{S}$ is an a by a diagonal matrix of relaxation times (Lallemand and Luo 2000). This can then be simplified and solved in a new moment space, as follows:

$$f_a\left(\boldsymbol{x}+\boldsymbol{e}_a\Delta t, t+\Delta t\right) = f_a\left(\boldsymbol{x},t\right) + \boldsymbol{M^{-1}SM}\left[f_a^{eq}(\boldsymbol{x},t) - f_a(\boldsymbol{x},t)\right] + \boldsymbol{F} \quad (6.14)$$

where M is a linear mapping into moment space and M^{-1} is its inverse. For a D2Q9 lattice, M is:

$$M = \begin{pmatrix} 1 & 1 & 1 & 1 & 1 & 1 & 1 & 1 & 1 \\ -4 & -1 & -1 & -1 & -1 & 2 & 2 & 2 & 2 \\ 4 & -2 & -2 & -2 & -2 & 1 & 1 & 1 & 1 \\ 0 & 1 & 0 & -1 & 0 & 1 & -1 & -1 & 1 \\ 0 & -2 & 0 & 2 & 0 & 1 & -1 & -1 & 1 \\ 0 & 0 & 1 & 0 & -1 & 1 & 1 & -1 & -1 \\ 0 & 0 & -2 & 0 & 2 & 1 & 1 & -1 & -1 \\ 0 & 1 & -1 & 1 & -1 & 0 & 0 & 0 & 0 \\ 0 & 0 & 0 & 0 & 0 & 1 & -1 & 1 & -1 \end{pmatrix}. \quad (6.15)$$

In the BGK scheme, the forcing term is incorporated directly into the distribution functions. However, Guo et al. (2002) found that this caused deviation from the Navier-Stokes equations upon using the Chapman-Enskog procedure. They proposed a force term that is in powers of particle velocity which is much more accurate for large body-forces:

$$F_a = \left(1-\frac{1}{2\tau}\right)\omega_a\left[\frac{\boldsymbol{e_a}-\boldsymbol{u}}{3} + \frac{\mathbf{e_a}\cdot\mathbf{u}}{9}\mathbf{e_a}\right]\cdot\mathbf{g} \quad (6.16)$$

where $\mathbf{g}$ is the body-force and $\mathbf{u}$ is the fluid velocity, obtained from the distribution function as follows:

$$\rho \mathbf{u} = \sum_a \mathbf{e_a} f_a + \frac{\rho \mathbf{g}}{2}. \tag{6.17}$$

This force term is then implemented into equation 6.14 as follows Guo and Zheng (2008):

$$f_a\left(\mathbf{x} + \mathbf{e}_a \Delta t, t + \Delta t\right) = f_a\left(\mathbf{x}, t\right) + \mathbf{M^{-1}} \left[\mathbf{SM}\left(f_a^{eq}(\mathbf{x}, t) - f_a(\mathbf{x}, t)\right) + \left(\mathbf{I} - \frac{1}{2}\mathbf{S}\right)\mathbf{MF} \right] \tag{6.18}$$

where $\mathbf{I}$ is the unity matrix. Equation 6.18 is separated into the streaming and collision terms during implementation, as each term is affected independently at boundaries.

6.1.4 Boundary conditions

There are many boundary conditions that have been implemented for LBM, such as periodic, bounce-back, constant pressure, constant velocity, constant concentration, constant flux, zero diffusive flux etc. In the following section only periodic and bounce-back boundaries shall be discussed as they are the most important boundary conditions for flow in porous media. More detailed discussion of boundary conditions can be found by Sukop and Thorne (2013) and Succi (2001).

For both periodic and solid boundaries, implementation occurs via modifying the streaming term in equation 6.18. As previously discussed, the streaming step occurs after the collision step and involves shifting distribution functions in the direction of their vector by a single lattice, either 1 lu, $\sqrt{2}$ lu, or $\sqrt{3}$ lu depending on the direction in a cubic lattice. As such, in both cases, only the destination and/or direction of the translated distribution function is changed.

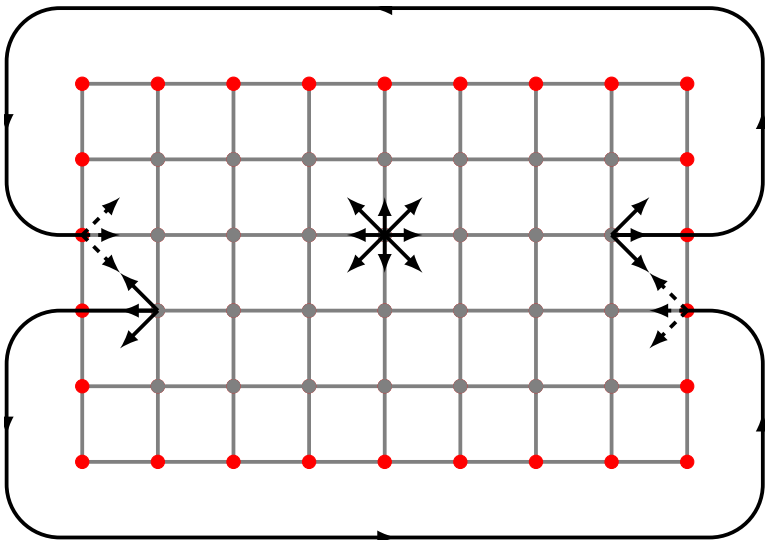


Figure 6.6: The movement of particles in periodic boundaries (adapted from Succi (2001)).

6.1.5 Periodic boundaries

Periodic boundary conditions are the simplest to implement and are typically intended to simulate flows where surfaces effects play a negligible role. This boundary condition is analogous to the PBC described in section 3.2.3, however in this case it is much easier to implement due to the discrete lattice.

Figure 6.6 illustrates the periodic boundary conditions. The periodicity is imposed by specifying that the population leaving from the far right column, **W**, enters the far left column, **E**, upon streaming and vise versa, when the population leaves from the left it enters at the right. The same goes for the top most, **N**, and bottom most, **S**, columns.

$$f_{in,\mathbf{W}} = f_{out,\mathbf{E}} \tag{6.19}$$

$$f_{in,\mathbf{E}} = f_{out,\mathbf{W}} \tag{6.20}$$

$$f_{in,\mathbf{N}} = f_{out,\mathbf{S}} \tag{6.21}$$

$$f_{in,\mathbf{S}} = f_{out,\mathbf{N}} \tag{6.22}$$

6.1.6 Bounce-back boundaries

At solid interfaces, distributions are not streamed into solid lattice nodes for obvious reasons. The question then arises of what to do with these distributions, and the missing distributions that would have otherwise originated from those nodes, in order to preserve conservation laws. The most simple solution relies on the specification of a no-slip boundary condition. This is used in physical situations where the fluid velocity is zero at a given solid surface, such as in macroscopic pores or pipes where the Knudsen number is small.

In addition, solid surfaces in LBM are forced to align with the grid, for example the north/south walls in a 2D rectangular channel. This requirement means that a true representation of a curved surface is difficult to implement. In these cases, a curved surface is approximated by cubic voxels, meaning that upon close inspection each curved surface, or any surface not in line with the lattice, will look like a jagged "staircase" rather than a continuous line or surface. Even at high resolutions the true surface area cannot be resolved. This causes difficulty when slip boundary conditions are required, however under the traditional no-slip method this has little impact on the implementation.

In order achieve the no-slip velocity, a bounce back boundary condition is employed. In this, when a particle distribution moves to a wall node, it collides with the wall and bounces back to its origin node with the same magnitude of the velocity but with the direction reversed. Bounce-back boundaries have the advantage of simplicity but it turns out they only have first order numerical accuracy.

The implementations of the no-slip boundary conditions can be divided into two types: on-grid and mid-grid. The computation of the on-grid situation is simpler since the population entering a boundary node is just reversed upon the completion step. Second order accuracy can be obtained for bounce-back bound-

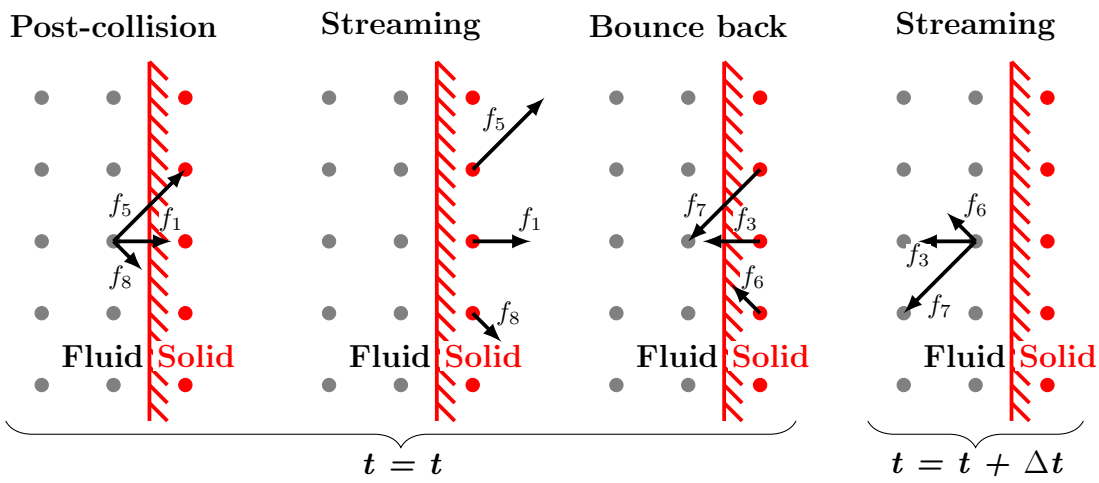


Figure 6.7: The process of mid-plane bounce back movement in D2Q9 model (adapted from Sukop and Thorne (2013)).

aries by shifting the boundary to a position half way between lattice sites; this is the mid-grid boundary. Figure 6.7 shows the process of bounce back occurring over two time-steps. As seen, the densities are stored in the solid nodes and are re-introduced into the fluid nodes in the following time-step.

The purpose of these works involve implementation of a slip length into LBM. Having calculated the slip length as a function of channel/pore dimensions and surface curvature in chapter 5, the remaining step is to modify the lattice Boltzmann model in order to allow for non-zero velocities at solid surfaces. This is not possibly using bounce-back boundaries directly and alternatives are discussed in section 6.4.

6.2 Literature review

In these works, the objective is to use LBM to model flow in nano-scale complex geometries. The procedure chosen here is to implement a slip boundary condition into LBM. The final model should allow for slip lengths to be specified as functions of curvature and surface structure, based on MD simulations presented in chapter 5. Here, the first step is taken towards this, in that slip boundary con-

ditions are implemented for basic geometries and are validated against analytical solutions for channel and pipe flow. The viscosity and other fluid properties required by LBM can also be calculated from MD.

There has been a plethora of other works intent on implementing a slip boundary condition into LBM, with varying success rates and some having few applications beyond the specific systems used for validation.

The simplest method for incorporating slip into LBM is via a specular boundary condition. In this, instead of non-head-on distributions being bounced back to their origin node with a reversed vector, they are moved on to the next fluid node in the direction of the distribution vector parallel to the solid surface. The component of the distribution perpendicular to the solid surface is then reflected, such that the direction is now away from the surface but not completely like in the bounce-back condition. This is analogous to light reflecting off a mirror and is arguably more representative of how a particle colliding with a perfectly smooth surface would act. However, in reality solid surfaces have varying levels of molecular roughness that prevent perfect reflection, along with interference and collisions by and with other particles in contact with the surface at a higher density than the bulk due to intermolecular attraction. Hence, specular reflection alone is not often a useful boundary condition and often leads to system crashes or non-physical large velocities, from personal experience, due to the lack of friction in systems of straight channels. For variable levels of slip, a mixture of specular and bounce back boundaries can be used, whereby the ratio is tuned to reach a matching slip length. This ratio can be referred to as the slip coefficient, C_s, and is always between 0 and 1, with 1 being the case of a specular reflection dominated boundary. The unknown distributions at a fluid node adjacent to a solid node are then:

$$f_a = (1 - C_s) f_{bb} + C_s f_{spec} \tag{6.23}$$

where f_{bb} and f_{spec} are the distribution contributions from bounce-back and specular conditions respectively. The issue then is choosing a value of the slip coefficient which results in the correct slip length. Ideally the slip coefficient should behave as a material property, just as the Navier slip length does, in situations where the systems smallest dimension is larger than O(10) nm (see chapter 5.

This method has been employed by Ahmed and Hecht (2009), Švec and Skoček (2013), Lim et al. (2002), Succi (2002), and Guo et al. (2006) to name but a few. Both Ahmed and Hecht (2009) and Švec and Skoček (2013) presented approximate relations between the slip coefficient and the Navier slip length.

Ahmed and Hecht (2009) studied this boundary condition, implemented as part of a single-relaxation-time LBM, in Pouseuille flow and in linear shear flow, along with patterned walls with varying amounts of slip. They found that the slip length resulting from a constant slip coefficient is independent of shear rate and density, and proportional to the BGK relaxation time. This is an important result as the Navier slip length is known to be a material property and as such does not change with the shear rate. They also find it to be independent of channel width in straight channels, however they did not simulate cylindrical geometries. The independence of the slip length with respect to the density is a negative aspect in terms of how the slip length changes with density in reality. However it can be a positive aspect in the respect that it allows for specifying a local density dependent slip parameter without having to account for any existing density dependence in the model. They found that the slip length varied linearly with the relaxation time, and thus linearly with the fluid viscosity. They fit their numerical data to a power law relationship between the slip length and the slip coefficient of the form $b \propto 1/\left(C_s^{-\alpha} - 1\right)$ and found that an exponent of 1 and a pre-factor of 1/3 fit best, therefore:

$$C_s = \frac{3b}{a\tau + 3b} \tag{6.24}$$

where a is the lattice constant.

Švec and Skoček (2013) performed a parametric study containing 500 individual simulations for each of four different values of the slip coefficient, $C_s = \{0.1, 0.5, 0.9, 0.98\}$. They argue that the relationship presented by Ahmed and Hecht (2009) is incorrect and apply the following correction, given the lattice constant is 1:

$$C_s = \frac{2b}{2(\tau + b) - 1}. \tag{6.25}$$

This imposes the condition that for any non-zero slip coefficient the slip length will approach zero as the kinematic viscosity of the fluid approaches zero and therefore as the relaxation time approaches 0.5. This is unlike the relationship of Ahmed and Hecht (2009), where as $\tau \to 0.5$: $b \to C_s/(6(1 - C_s))$.

In order to calculate the shear rate tensor, $\dot{\gamma}_{ij}(x,t)$, at a fluid node adjacent to a solid boundary for use in calculating the Navier slip length from LBM data, the following equation can be used (Švec and Skoček 2013):

$$\dot{\gamma}_{ij}(x,t) \approx \frac{2}{2\tau(x, t - \Delta t)} \sum^{\alpha} e_{i\alpha} e_{j\alpha} f_{\alpha}^{neq}(x,t) \tag{6.26}$$

where $f_{\alpha}^{neq}(x,t)$ is the non-equilibrium part of the particle distribution:

$$f_{\alpha}^{neq}(x,t) = f_{\alpha}(x,t) - f_{\alpha}^{eq}(\mathbf{u}, \rho). \tag{6.27}$$

Equation 6.26 results in a shear rate at a location 0.5 lu away from the solid surface due to the mid-grid boundary and hence this should be accounted for when calculating the slip length. Švec and Skoček (2013) presented a method to obtain a better approximation of the shear rate tensor at the solid surface, $\dot{\gamma}_{ij,0}$, using the shear rate at both the first, $\dot{\gamma}_{ij,1}$, and second, $\dot{\gamma}_{ij,2}$, fluid nodes adjacent

to the solid boundary. Since $\dot{\gamma}_{ij,1}$ can be expressed as the average of $\dot{\gamma}_{ij,0}$ and $\dot{\gamma}_{ij,2}$, $\dot{\gamma}_{ij,0}$ can be found using the following relation:

$$\dot{\gamma}_{ij,0} = 2\dot{\gamma}_{ij,1} - \dot{\gamma}_{ij,2} \tag{6.28}$$

where $\dot{\gamma}_{ij,1}$ is computed by equation 6.26 and $\dot{\gamma}_{ij,2} = u_2 - u_1$.

Guo et al. (2006) studied the effect that confinement has on the relaxation time for microgas flows. The authors define an effective viscosity, related to the shear viscosity in the bulk fluid via a wall effect that is a function of the Knudsen number. Since the relaxation time is a linear function of the viscosity, it is a function of the Knudsen number and as such it is a function of the channel width. The approximate relation between the bounded relaxation time, $\tau*$, and the Knudsen number, Kn, is approximated as follows:

$$\tau* = \tau \left[\frac{2}{\pi} \arctan\left(\sqrt{2} Kn^{-3/4} \right) \right]. \tag{6.29}$$

The issue with specifying the relaxation time as a function of the Knudsen number is that the channel height must be known and specified. This can be difficult to do in complex geometries where the height can vary along a channel and where non-parallel surfaces can exist. Guo et al. (2006) additionally implemented a slip boundary condition similar to equation 6.23, however instead of a bounce-back term, a term involving the equilibrium distribution function is used in an analogous manner. This is the discrete version of Maxwell's diffuse boundary condition and has a clearer physical significance than equation 6.23, although both equations involve a fitting parameter and as such both can be used to model the same slip length.

Lim et al. (2002) compare a purely specular boundary condition with an extrapolation scheme, whereby the streaming velocity at the wall is found by a

second-order polynomial extrapolation whilst setting the normal velocity to zero. The unknown distributions at the wall are then approximated by their equilibrium functions. Both methods were able to capture slip at the walls, however the authors preferred the heuristic specular boundary condition, due to the extrapolation scheme's pure mathematical premise.

Chen et al. (2015) use LBM, with a no-slip boundary condition, to simulate fluid flow in complex porous structures, reconstructed from scanning electron microscopy (SEM) images of shale samples, in order to extract the intrinsic permeability. A correction factor, which relates the apparent permeability to the intrinsic permeability, is calculated by comparing the permeability calculated from LBM with locally varying relaxation times to that calculated from LBM with a global constant relaxation time. For the apparent permeability calculations the authors used a relaxation time that varies locally based on the ratio of the pore size to a reference pore size with reference relaxation time.

Although this method allows for accurate calculation of a correction factor, it lacks in realism with respect to a non-zero fluid velocity at solid boundaries. The effects of a slip surface have been incorporated via an effective local viscosity, that includes both an actual viscosity change and a slip contribution, such that the resulting mean velocity in each pore matches that of a fluid exhibiting slip, whilst the velocity profile is that of a non-slipping fluid. This is useful in terms of simplicity and for predicting permeability based on an effective viscosity, however it does not necessarily have a physical meaning. In addition, the assumption made is that the apparent viscosity is a linear function of the pore size alone and as such this assumes that the actual slip length, that this is effectively accounting for, is constant everywhere in the sample. This assumption appears to result in a correct correction factor for this specific fluid and pore surface material, however as shown in chapter 5 the slip length is no longer constant with pore size below some critical solid-solid separation and this relationship is dependent also on the level of curvature below this critical value. This critical value has been

shown to be fluid dependent in chapter 5 whilst the slip length itself depends on the material properties of the surface, which may not necessarily be the same throughout the porous structure.

Zhang et al. (2014) performed lattice Boltzmann simulations of shale gas, methane, transport in organic nano-pores. For high Knudsen numbers they introduced a correction to the relaxation time in a similar manner to Chen et al. (2015), however simulations were limited in this case to individual cylindrical pores of varying diameter. In addition, they have included a slip boundary condition at the surface in order to directly model the non-zero fluid velocity boundary. This is implemented via the specular/bounce-back combination boundary condition represented in equation 6.23.

Hecht and Harting (2010) implemented a on-site velocity boundary condition, whereby the equilibrium distributions at a boundary node is set explicitly in order to match a given velocity. The non-equilibrium components of the unknown distributions, those exiting from the boundary node into the fluid, are calculated by assuming that the bounce-back rule is still correct for the distribution normal to the surface. however, in the case of a flat boundary one of the main planes of the lattice, this leaves two missing equations for the system to be fully defined for the D3Q19 lattice. For that reason bounce-back has also been assumed for the non-equilibrium part for all unknown distributions. This introduces four new equations which leaves the system of equations overdetermined. To counter this, a transverse momentum correction is needed for distributions propagating in the directions tangential to the surface. These values vanish in equilibrium but are non-zero if velocity gradients are present. The equilibrium distributions are simply calculated based on the set velocity and equation 6.12.

The benefit of this method is that the velocity can be specified in any direction at the boundary, including directions not aligned with the computational lattice. Although this specification option is not necessarily useful for a slip boundary

condition, it does mean that this method can be used for a large range of applications where a velocity boundary would be required. The method described by the authors is also easily adaptable to specify a pressure boundary condition by only specifying 2 components of the velocity and allowing the 3rd to be calculated based on the chosen pressure.

The authors recognised the use of this method for a no-slip boundary condition in the special case where the on-site velocity is set to zero. However, they do not discuss the use of this method to specify an explicit slip velocity at a solid boundary and thus enable a slip boundary condition.

6.3 Objectives

The main objective of this chapter is to validate and compare both the specular reflection plus bounce-back combination boundary condition and the on-site velocity boundary condition in order to choose one for progressing to simulations of complex geometries.

The proposed models are tested in straight, cylindrical, and off-grid straight channels, in two dimensions and compared to analytical solutions as a first validation step. The effect of surface corrugation/pixelation on the velocity profile and slip length is also investigated in order to choose the most appropriate model. The suitability of conversion to full three-dimensional simulations of complex geometries is also considered.

Both models inherently allow for slip lengths to be specified as functions of curvature and surface structure, such that the functional relationships between slip and curvature presented in chapter 5 can eventually be included.

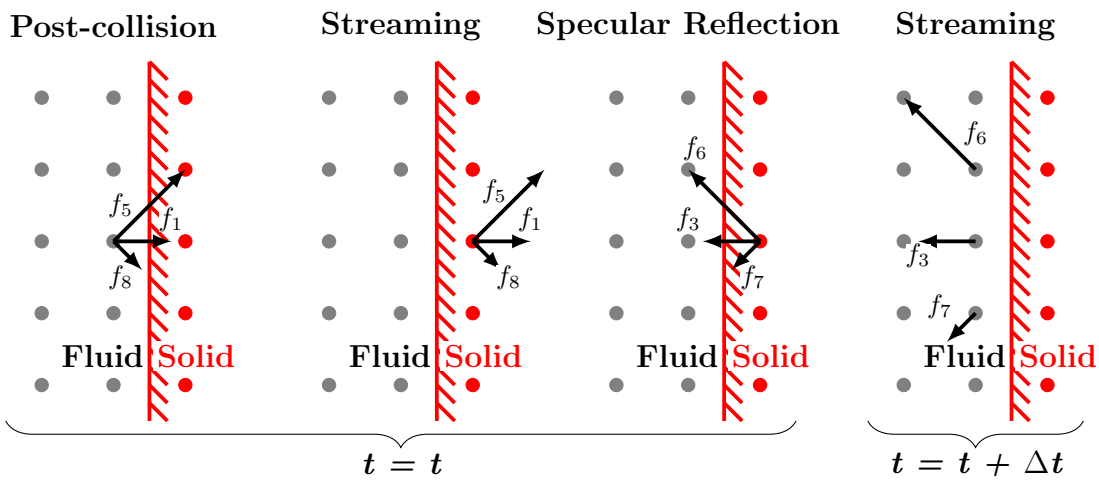


Figure 6.8: The process of specular reflection at boundaries in the D2Q9 model.

6.4 Methodology

The lattice Boltzmann model used in these works is an adapted version of a CUDA GPU code presented by Gray and Boek (2016). As discussed earlier, the D3Q19 lattice is used in these works, as shown in figure 6.3. However, all of the results presented here are only the two-dimensional cases. In these cases the number of lattice nodes in the y-direction is set to 1 and no driving forces have been specified for this direction, such that the system is effectively two-dimensional. The only transport observed in the z-dimension is negligible in comparison to the flow directions and is due to artefacts caused by the model precision.

In these works, initially the specular reflection plus bounce-back combination boundary condition is used. Here both the bounce-back boundary, figure 6.7, and the specular reflection boundary, see figure 6.8, are implemented and the slip length is controlled by the slip coefficient, C_s, via equation 6.23.

In practice, this boundary condition is simple to implement as it involves only an additional specular reflection step during streaming and the addition of the slip coefficient to both the bounce-back and specular reflection steps.

However, issues arise with this boundary condition when surfaces are not aligned with the grid. For instance, if a straight channel is rotated and re-simulated it

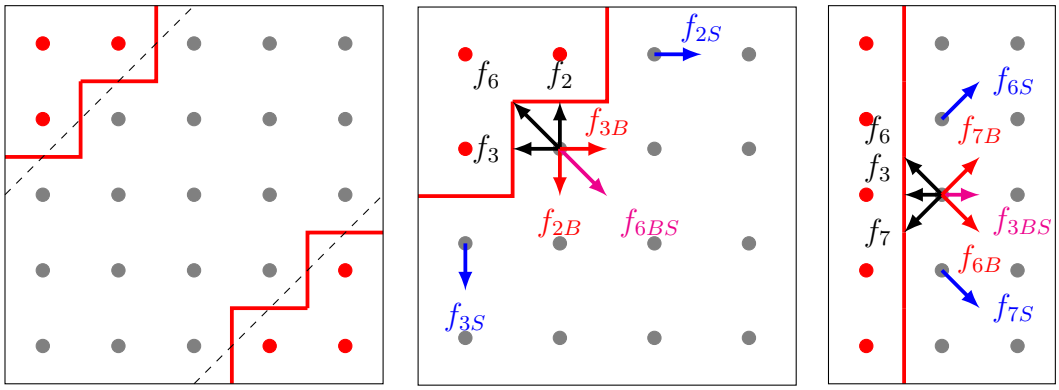


Figure 6.9: The specular reflection bounce-back combination boundary condition for the cases of a channel 45° out of alignment with the lattice and a straight channel. Red dots and the surrounding red lines indicate the discretised location of the solid boundary. The dashed line indicates the represented surface.

will exhibit different slip with each rotation up until it is aligned with the lattice again. When the channel is 45° out of alignment with the grid every surface fluid node is surrounded by two solid nodes. With no additional modification to the mid-grid specular reflection boundary condition, every distribution entering a wall node will be head on with a solid node and therefore only qualify for bounce-back with no specular reflection taking place. Thus a channel out of alignment will exhibit less slip until 45°, where it will exhibit a zero slip velocity. To counter this, cases must be specified depending on the surrounding solid nodes, such that the specular reflection node is selected correctly. The specular reflection and bounce-back combination boundary condition is shown in figure 6.9 including the 45° channel and straight channel cases.

Another example case where specular reflection should be specified separately is when a surface fluid node is bounded in a diagonal direction as well as surrounded on two primary adjacent directions, such as north west, east, and north. Here only distributions heading west and north east should undergo specular reflection.

In this study, the viscosity used in LBM is the bulk phase dynamic viscosity, and any slip length measurements have been made based on this rather than an effective viscosity under confinement. As such, no alteration of the residence time

has been made with channel height.

In order to specify the correct slip lengths, calculated in chapter 5, the slip coefficient can be found using a similar equation to those presented by Švec and Skoček (2013) and Ahmed and Hecht (2009).

The second method used here to specify a slip boundary condition involves the on-site velocity boundary condition presented by Hecht and Harting (2010). In this case, the slip length should be converted to a slip velocity via equation 5.1.

In these works the momentum corrections have been specified as zero, such that with a zero wall velocity supplied the bounce-back boundary condition is exactly produced. These terms would normally vanish at equilibrium.

The only missing step is to calculate the shear rate in the fluid nodes adjacent to the boundary. This can be performed in multiple ways, including direct calculation of the shear rate tensor at boundary nodes locally or via fitting of the velocity profile across two or more fluid nodes in line normal to the surface and parallel to the flow direction, i.e. with a finite difference approach. For the D2Q9 lattice, equation 6.26 can be used to calculate the shear rate tensor. For the D3Q19 and any other lattice, the general equation for the shear rate tensor is (Krüger et al. 2009):

$$S_{\alpha\beta} = -\frac{3}{2\tau\rho}\sum_i \left(e_{i\alpha}e_{i\beta} - \frac{\delta_{\alpha\beta}}{D}\mathbf{c_i}\cdot\mathbf{c_i}\right) f_i^{neq} \tag{6.30}$$

where D is the dimensionality of the system, which is 3 in the case of the D3Q19 lattice.

In these works, straight, diagonal, and cylindrical geometries are simulated using LBM with the specular-bounce-back combination boundary condition and the on-site velocity boundary condition. The diagonal channels are identical to the straight channels except that the surface is not in alignment with the lattice grid.

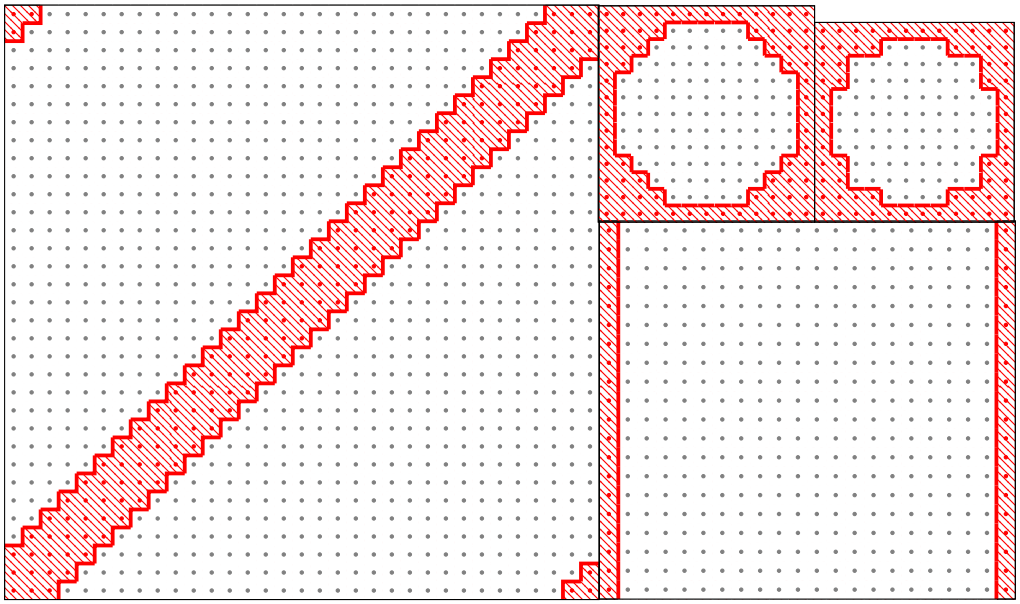


Figure 6.10: Sample of geometries used in LBM flow calculations. Red signifies solid nodes whilst grey signifies fluid nodes. (Left) 20 lu wide channel 45° out of alignment. (Bottom right) 20 lu wide channel aligned with lattice. (Top right) 11 lu and 10 lu diameter cylindrical geometries.

An ideal method for slip implementation would result in identical fluid dynamics for both the straight and diagonal cases, and at the very least could be tuned to do so. A sample of the geometries investigated here are shown in figure 6.10.

Here four channel widths are used for the straight geometries, these are 20, 40, 80, and 200 lu. For the diagonal channels, due to the discrete nature of LBM, the lattice dimensions have been chosen such that the channel widths are as close to the straight channel values as possible. The channel length is 20 lu in all straight channel cases and the widths shown here are the surface-surface distances, i.e. the true z-dimension is the channel width plus 2 lu as there are two solid nodes along the z-dimension. The geometry is periodic in all dimensions, as such only one solid node is required in the z-dimension, however two are used here to maintain symmetry for the sole purpose of easing analysis. The impact on the computational time is negligible as no calculations take place at solid nodes. In all cases the y-dimension is set to 1 lu.

The cylindrical geometries are chosen to have on-grid diameters of 5, 6, 10, 11,

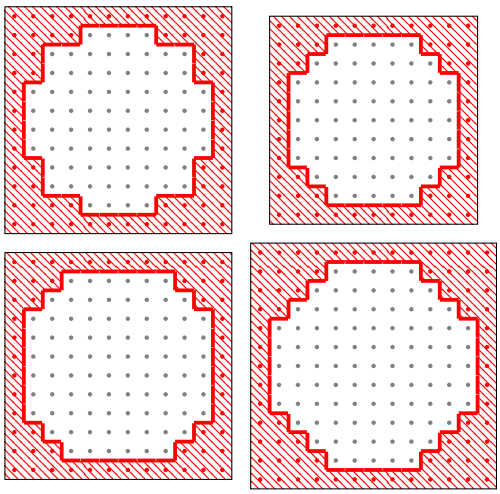


Figure 6.11: Discretised cylindrical geometries, 10 lu (top) and 11 lu (bottom) diameters, with central node either on grid (left) or mid-grid (right).

20, 21, 40, 41, 80, 81, 200, and 201 lu. Here more sizes are selected such that the effect of odd and even lattice dimensions can be investigated. When discretising the cylindrical geometries, the in-line separation between solid surfaces specified as the diameter, such that the distance between opposite mid grid boundaries along the horizontal (or vertical) axis is exactly what is listed here. This causes the centre of cylinders with an even number diameter to be between grid points. The issue with this is that discretisation can cause even diameter cylinders to have a larger diagonal diameter than an odd number set diameter cylinder specified to be larger. This can be seen in figure 6.11 where the 11 lu cylinder has a diagonal diameter of $7\sqrt{2}$ whilst the 10 lu case has a diagonal diameter of $8\sqrt{2}$. The resulting velocity profiles may be more consistent if all cylinders have a central point that is on grid, although this is not the case in any of this work.

6.5 Discussion

6.5.1 Specular-bounce-back boundary condition

Straight and cylindrical geometries are simulated using LBM with a combination of specular reflection and bounce-back boundary conditions, as in equa-

tion 6.23 and figure 6.9. The resulting velocity profile is plotted for 20 lu and 40 lu wide/diameter channels with three slip coefficients in figures 6.12 and 6.13. From fitting to Navier-Stokes, equations 5.4 and 5.5, the slip length is found for all channel widths/diameters and is shown in tables 6.12 and 6.13. The result of equation 6.25 is also tabulated for comparison. For the cylindrical pores the fit to Navier-Stokes is performed along the z-axis across the centre of the cylinder, left to right in figure 6.10, since the discretised wall location is equal to the set diameter along this line. In cylinders with an even number diameter the velocities along the centre are found by fitting each slice to a 2nd order polynomial and interpolating to find the centre velocity. The resulting velocities are fit to Navier-Stokes in the same way as the odd number diameter cylinders. The deviation from Navier-Stokes presented in tables 6.1 to 6.4 is calculated from the difference between the set g/ν and the value obtained from the fit, i.e. it is independent of the measured slip length and is only dependent on the shape of the polynomial. In all cases presented here the body force, g, is set to 1e−6 lu ts^{-1} whilst the kinematic viscosity, ν, is 0.05 lu^2 ts^{-1}. In all cases, LBM simulations are considered converged when the relative change in the average velocity per time step is less than 1$\boldsymbol{e}$−5 %.

The relationship between the measured slip length and channel matches with equation 6.25 presented by Švec and Skoček (2013) for all channel widths simulated here. This confirms that the slip coefficient is independent of the size of the channel when the channel is aligned with the lattice grid and implies that the specular bounce-back combination boundary slip length is only a function of the slip coefficient and the relaxation time in the straight geometry. The error from Navier-Stokes here increases with the channel width which can be attributed to the specification of the condition of convergence. In the widest channels the average velocity converges much slower than in the smaller cases and as such a change of 1$\boldsymbol{e}$−5 % in the average velocity is not small enough to indicate entire convergence and as such the deviation from Navier-Stokes is larger. The

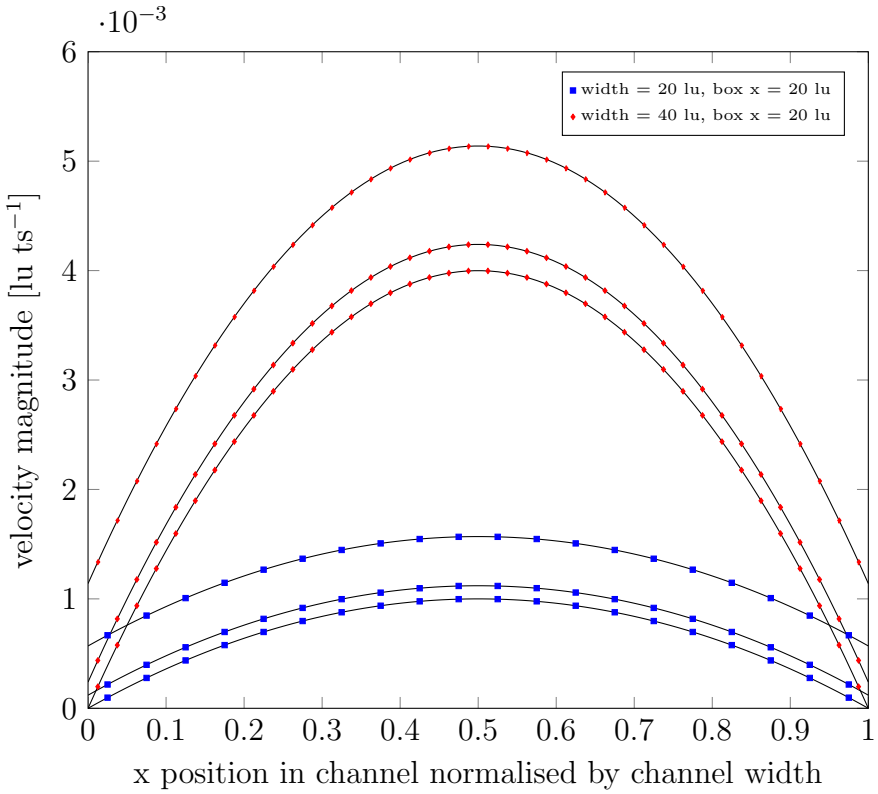


Figure 6.12: Velocity profiles, in straight geometries, calculated from LBM with specular-bounce-back combination boundary condition (marks) and the fit to Navier-Stokes (equation 5.4)(solid lines). From bottom to top for each channel width: $C_s = 0$, 0.8, and 0.95.

Table 6.1: Slip lengths in straight geometries calculated using LBM with specular bounce-back combination boundary condition. Boundaries are in alignment with the grid.

Slip coefficient	Channel width [lu]	Slip length [lu]	Equation 6.25 [lu]	Deviation from analytical solution (%)
0	20	0	0	0
0	40	0	0	0.01
0	80	−0.001	0	0.048
0	200	0.01	0	0.439
0.8	20	0.599	0.6	−0.019
0.8	40	0.599	0.6	0.006
0.8	80	0.599	0.6	0.045
0.8	200	0.612	0.6	0.446
0.95	20	2.851	2.85	0.044
0.95	40	2.851	2.85	0.034
0.95	80	2.852	2.85	0.082
0.95	200	2.865	2.85	0.476

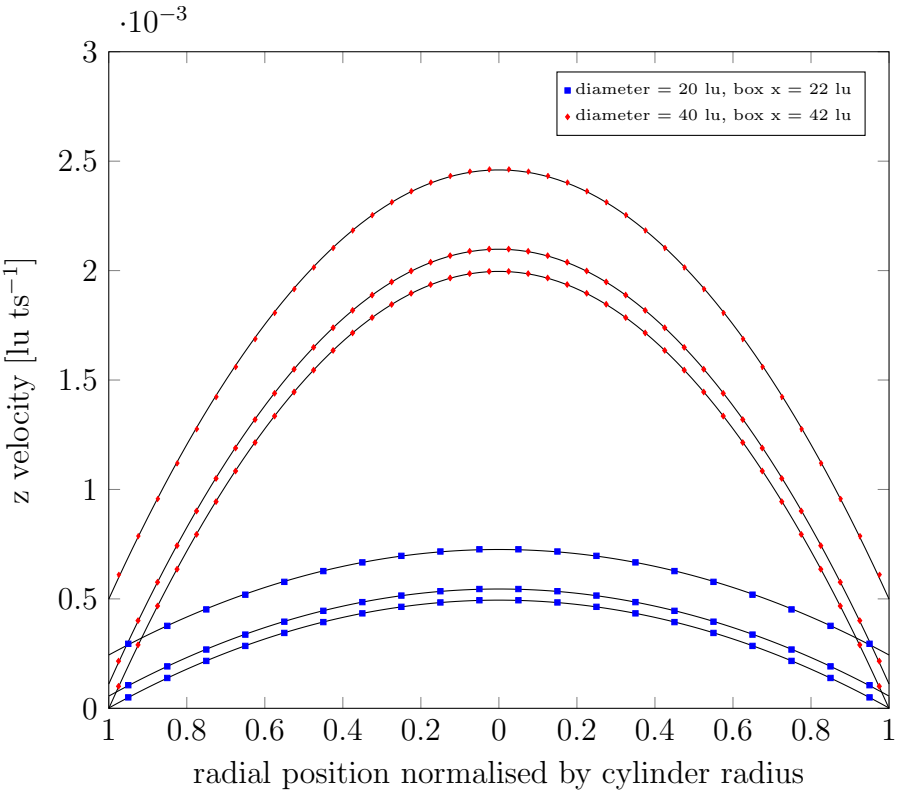


Figure 6.13: Velocity profiles, in cylindrical geometries, calculated from LBM with specular-bounce-back combination boundary condition (marks) and the fit to Navier-Stokes (equation 5.5)(solid lines). From bottom to top for each cylinder diameter: $C_s = 0$, 0.8, and 0.95.

maximum deviation from equation 6.25 for a slip coefficient of 0.8 is 0.17 % for channels smaller than 80 lu and for a slip coefficient of 0.95 it is 0.07 %.

In the cylindrical geometries the error from Navier-Stokes increases with decreasing diameter for all values of the slip coefficient investigated here, as shown in figure 6.14. With the exception of the 5 and 6 lu geometries with bounce-back and the 6 lu geometry with a slip coefficient of 0.8, the error is consistently positive, signifying that the amplitude of the velocity profile is larger than it is expected to be and as such not caused by a lack of convergence.

Furthermore, the slip length calculated here is no longer independent of the size of the geometry for diameters less than 40 lu. The slip length is also heavily dependent on the centre of the cylinder used during discretisation, more-so for cylinders with a diameter of less than 40 lu, as seen in figure 6.15. Above 40 lu

Table 6.2: Slip lengths in cylindrical geometries calculated using LBM with specular bounce-back combination boundary condition.

Slip coefficient	Channel width [lu]	Slip length [lu]	Equation 6.25 [lu]	Deviation from analytical solution (%)
0	5	0.02	0	−1.7
0	6	0.058	0	−6.176
0	10	0.02	0	2.847
0	11	0.042	0	1.15
0	20	0.013	0	1.403
0	21	0.046	0	1.097
0	40	−0.005	0	0.133
0	41	0.01	0	0.864
0	80	−0.004	0	0.26
0	81	0.003	0	0.251
0	200	−0.002	0	0.281
0	201	−0.036	0	0.278
0.8	5	0.585	0.6	1.729
0.8	6	0.666	0.6	−1.886
0.8	10	0.569	0.6	3.363
0.8	11	0.619	0.6	3.554
0.8	20	0.571	0.6	2.148
0.8	21	0.622	0.6	2.44
0.8	40	0.559	0.6	0.67
0.8	41	0.574	0.6	1.364
0.8	80	0.565	0.6	0.57
0.8	81	0.571	0.6	0.553
0.8	200	0.57	0.6	0.415
0.8	201	0.535	0.6	0.408
0.95	5	2.623	2.85	4.5
0.95	6	2.817	2.85	2.162
0.95	10	2.507	2.85	4.258
0.95	11	2.643	2.85	6.131
0.95	20	2.527	2.85	3.587
0.95	21	2.637	2.85	4.619
0.95	40	2.545	2.85	1.953
0.95	41	2.566	2.85	2.688
0.95	80	2.585	2.85	1.511
0.95	81	2.593	2.85	1.493
0.95	200	2.626	2.85	0.912
0.95	201	2.582	2.85	0.883

diameters the calculated slip length is reasonable constant with the cylinder size, however there is still a discretisation dependence in even the largest, 200 and 201 lu, cylinders.

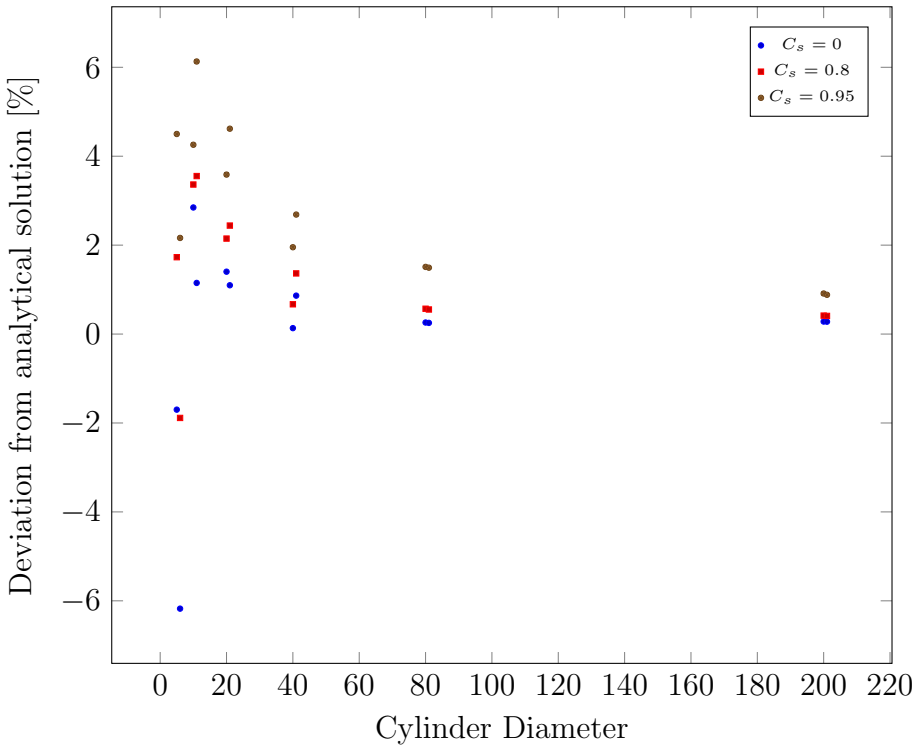


Figure 6.14: Error from Navier-Stokes as a function of cylinder diameter for three values of the slip coefficient.

Moreover, the relationship presented in equation 6.25 is no longer applicable for any discretisation, as can be seen by the increasing deviation, with increasing C_s, of the calculated slip length from the predicted value. The reason for this deviation from the straight channel slip length is likely due to the "pixelation" of the boundary. As such, a new relationship between the slip length and the slip coefficient would be required before implementing the curvature dependent slip length presented in chapter 5, this would entail a parametric study involving a large number of independent simulations with varying diameters and as such is reserved for future investigations.

The average deviation from equation 6.25 is 5.7 % and 8.6 % for slip coefficients of 0.8 and 0.95 respectively. The slip lengths in odd number diameter cylinders are generally larger than for the even diameter cylinders. This is likely due to large differences between the diameter approximated by the in-line boundary separation along the horizontal and vertical axes and the real average diameter. In the largest pores the deviation from equation 6.25 is reasonably constant and

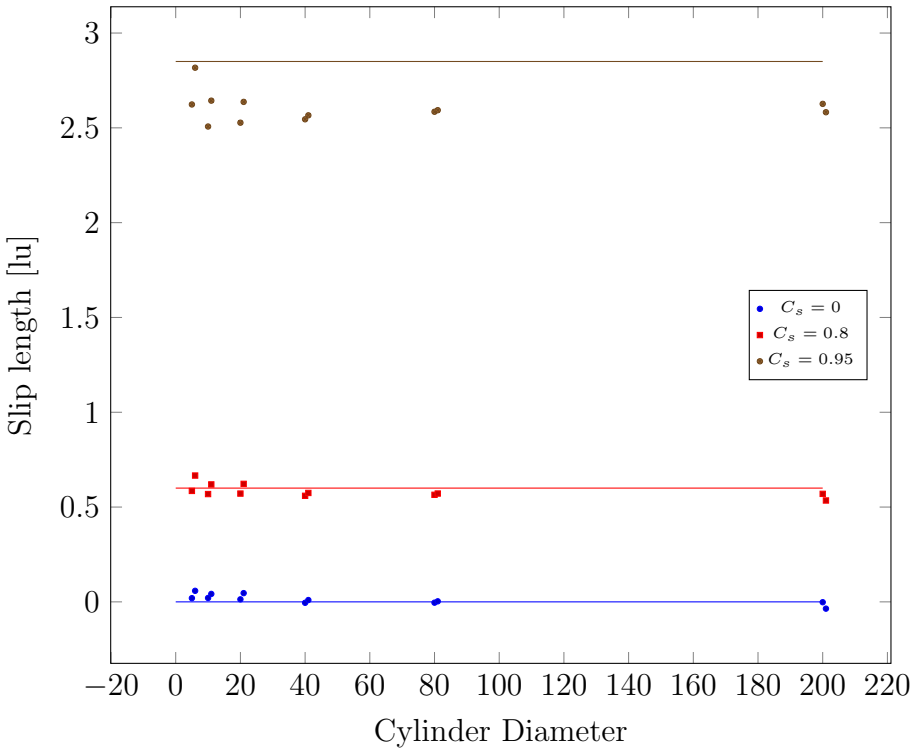


Figure 6.15: Calculated (marks) slip length and prediction from equation 6.25 (solid lines) as a function of cylinder diameter for three values of the slip coefficient.

is on average 9.4 % for the 0.95 slip coefficient case.

This method of introducing the slip length into LBM appears promising based on the results presented here. However, the boundary condition has yet to be implemented for flow in a direction not aligned with the lattice. As such, the last step before being able to perform simulations on complex geometries is to implement and test the method represented in figure 6.9 for diagonal boundaries.

6.5.2 Velocity boundary condition

Similarly, as for the specular-bounce-back boundary condition, the velocity boundary condition of Hecht and Harting (2010) is implemented here. Again, straight and cylindrical geometries are simulated and the resulting velocity profiles are fitted to Navier-Stokes and the slip length extracted. For comparison with the specular-bounce-back boundary condition, the same geometries have been con-

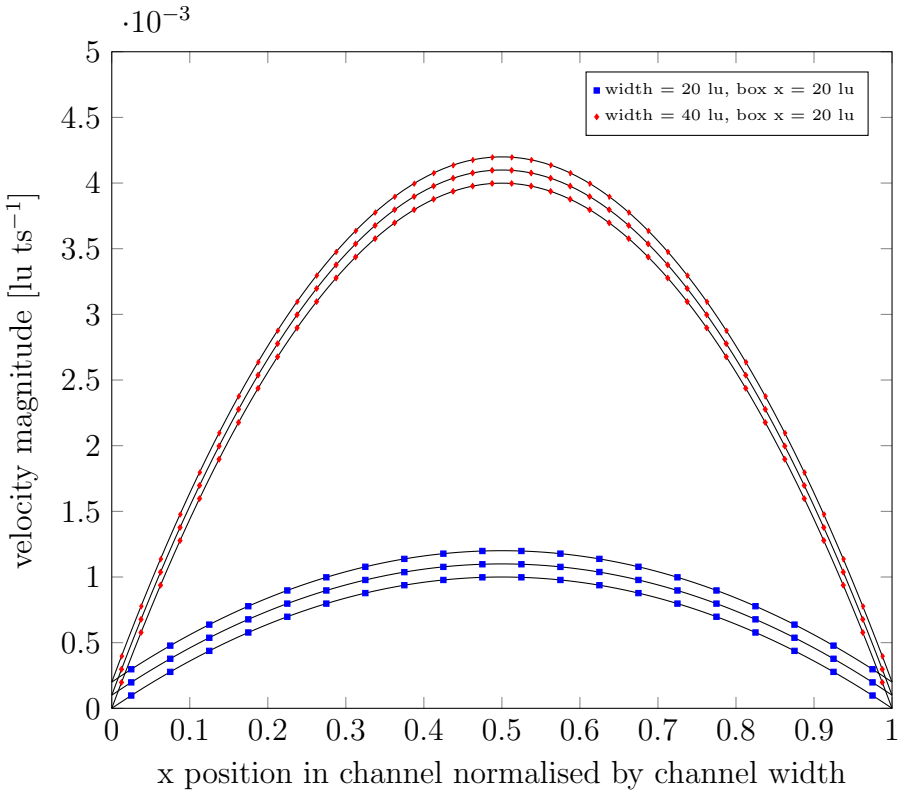


Figure 6.16: Velocity profiles, in straight geometries, calculated from LBM with velocity boundary condition (marks) and the fit to Navier-Stokes (equation 5.4)(solid lines). From bottom to top for each channel width: $u_{wall} = 0$, 0.0001, and 0.0002 lu ts^{-1}.

sidered.

Figure 6.16 shows the velocity profile for the 20 lu and 40 lu channels and table 6.3 shows the calculated wall velocity, slip length, and error from Navier-Stokes, calculated in the same way as previously. Here, for a wall velocity of 0 lu ts^{-1} the results match exactly with those for the specular-bounce-back boundary, as in both cases the implementation reduces exactly to the standard bounce-back boundary condition.

The wall velocity reaches a maximum deviation of 4 % from the specified value for the largest channel widths and is generally larger for lower wall velocities.

Again the velocity profiles for cylindrical geometries are plotted in figure 6.17 and the entire sample results are tabulated in table 6.4.

Here the error from Navier-Stokes, as shown in figure 6.18, is much larger than for

Table 6.3: Slip lengths in straight geometries calculated using LBM with velocity boundary condition. Boundaries are in alignment with the grid.

Wall velocity [lu ts^{-1}]	Channel width [lu]	Calculated wall velocity [lu ts^{-1}]	Slip length [lu]	Deviation from analytical solution (%)
0	20	9.99e−17	0	0
0	40	−1.01e−7	0	0.014
0	80	−1.69e−6	−0.002	−0.027
0	200	2.57e−6	0.001	0.092
0.0001	20	1.00e−4	0.501	0.036
0.0001	40	9.98e−5	0.249	0.008
0.0001	80	9.85e−5	0.123	−0.027
0.0001	200	1.03e−4	0.052	0.091
0.0002	20	2.00e−4	0.998	−0.064
0.0002	40	2.00e−4	0.5	0.01
0.0002	80	1.99e−4	0.248	−0.026
0.0002	200	2.04e−4	0.102	0.094

the specular-bounce-back boundary condition in the same cylindrical geometries. Here the deviation is too large to be considered appropriate in pores smaller than 40 lu, reaching a staggering maximum deviation of 228 % for the 5 lu cylinder with a specified wall velocity of $2\boldsymbol{e}-4$ lu ts^{-1}. In this case, the velocity profile is no longer comparable to Navier-Stokes as the wall velocity is larger than the velocity in the centre of the channel. This is likely due to the specification of an unrealistically large wall velocity for such a small channel. Since the wall velocity is specified here rather than a parameter proportional to the slip length, the driving force is not large enough to account for the large wall velocity as quickly as the wall velocity increases. This issue would likely disappear if the wall velocity was specified to be proportional to the shear rate, such that the slip length is supplied rather than the wall velocity. This is reflected in figure 6.19 where the calculated slip length deviates from the expected value given the wall velocities specified. It should be noted here that by specifying the wall velocity rather than the slip length, given that the system could fully equilibrate, the slip length would rapidly increase with decreasing diameter, as shown in figure 6.19. The shear rate dependence has not been implemented in these works, however it

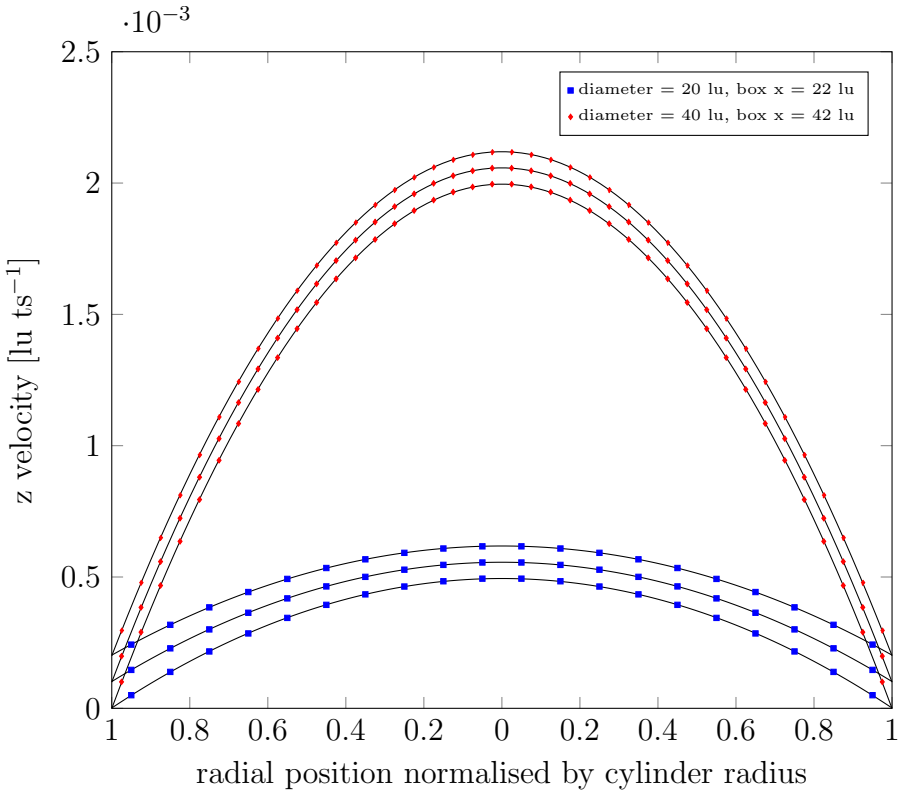


Figure 6.17: Velocity profiles, in cylindrical geometries, calculated from LBM with velocity boundary condition (marks) and the fit to Navier-Stokes (equation 5.5)(solid lines). From bottom to top for each cylinder diameter: $u_{wall} = 0$, 0.0001, and 0.0002 lu ts^{-1}.

would be a likely next step.

Unlike for the specular-bounce-back boundary condition, the case of flow along a surface out of alignment with the lattice grid is handled naturally by the velocity boundary condition. Here the x and z components of the body force are chosen to give a resulting body force of $1\boldsymbol{e}-6$ parallel to the boundary, to match all other geometries.

Figure 6.20 shows the velocity profiles whilst table 6.5 shows the entire sample results. The results match very well with the prediction from Navier-Stokes, and the calculated velocity is at most 1 % out from the specified value. This natural ability to accurately apply a slip velocity for any geometry is a clear advantage of this method over the specular-bounce-back method. However, the shear rate is still required in order for this method to be usable for the purposes

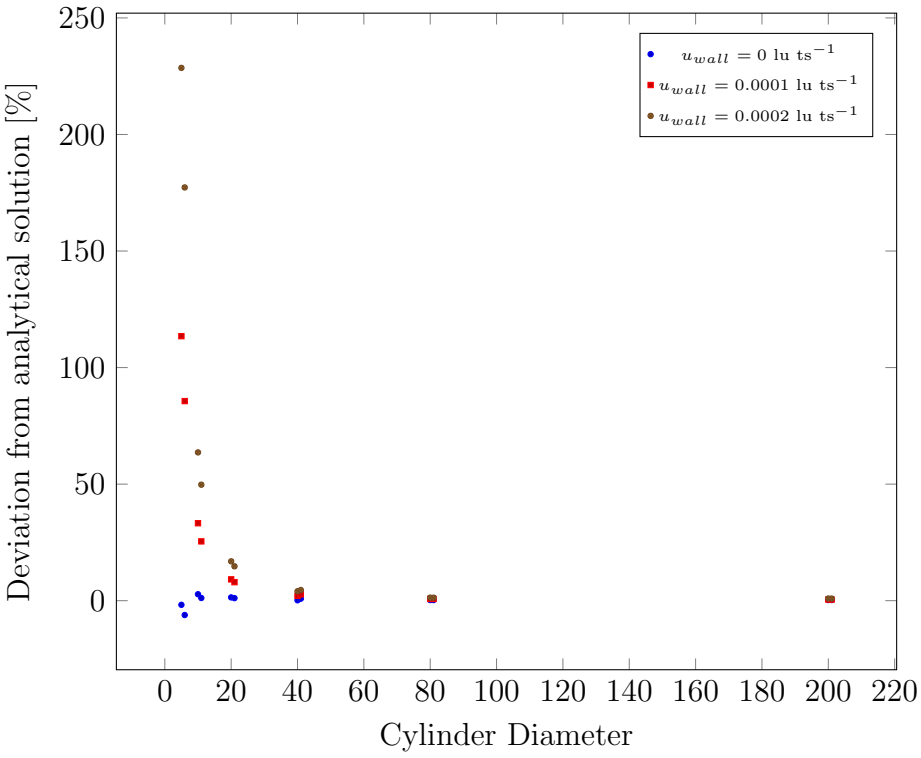


Figure 6.18: Error from Navier-Stokes as a function of cylinder diameter for three values of the wall velocity.

of implementing the correct curvature dependence of the slip length and in order to perform simulations on complex geometries with varying pore sizes present.

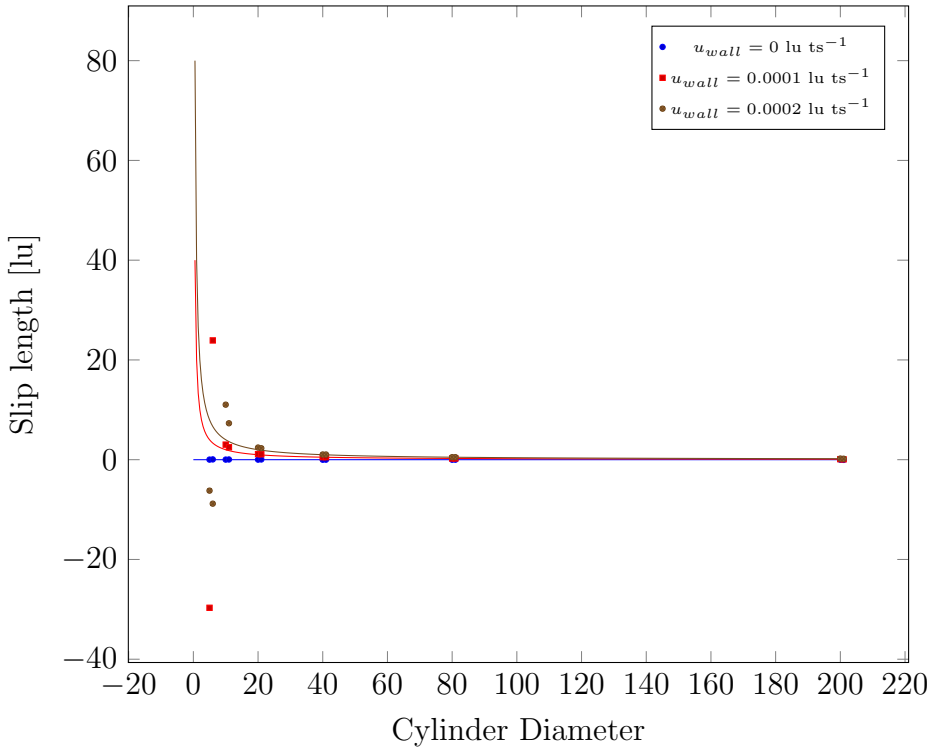


Figure 6.19: Calculated (marks) slip length and prediction from equation 5.5 (solid lines) as a function of cylinder diameter for three values of the wall velocity.

Table 6.4: Slip lengths in cylindrical geometries calculated using LBM with velocity boundary condition.

Wall velocity [lu ts^{-1}]	Channel width [lu]	Calculated wall velocity [lu ts^{-1}]	Slip length [lu]	Deviation from analytical solution (%)
0	5	4.80e−7	0.019	−1.771
0	6	1.86e−6	0.058	−6.154
0	10	9.65e−7	0.02	2.766
0	11	2.31e−6	0.042	1.152
0	20	1.30e−6	0.013	1.404
0	21	4.78e−6	0.046	1.098
0	40	−6.98e−7	−0.003	0.171
0	41	1.92e−6	0.009	0.866
0	80	−1.55e−6	−0.004	0.27
0	81	1.23e−6	0.003	0.258
0	200	−2.92e−6	−0.003	0.285
0	201	−3.50e−5	−0.035	0.288
0.0001	5	10.00e−5	−29.69	113.471
0.0001	6	1.03e−4	23.911	85.62
0.0001	10	1.01e−4	3.021	33.23
0.0001	11	1.02e−4	2.489	25.441
0.0001	20	1.02e−4	1.122	9.14
0.0001	21	1.05e−4	1.089	7.938
0.0001	40	9.96e−5	0.509	2.088
0.0001	41	1.02e−4	0.514	2.715
0.0001	80	9.93e−5	0.25	0.77
0.0001	81	1.02e−4	0.254	0.748
0.0001	200	1.06e−4	0.106	0.499
0.0001	201	7.22e−5	0.072	0.481
0.0002	5	2.00e−4	−6.207	228.571
0.0002	6	2.04e−4	−8.816	177.277
0.0002	10	2.01e−4	11.031	63.612
0.0002	11	2.02e−4	7.305	49.758
0.0002	20	2.03e−4	2.436	16.879
0.0002	21	2.06e−4	2.298	14.755
0.0002	40	2.00e−4	1.043	4.041
0.0002	41	2.03e−4	1.039	4.57
0.0002	80	2.00e−4	0.507	1.308
0.0002	81	2.03e−4	0.508	1.278
0.0002	200	2.25e−4	0.227	0.93
0.0002	201	1.92e−4	0.193	0.92

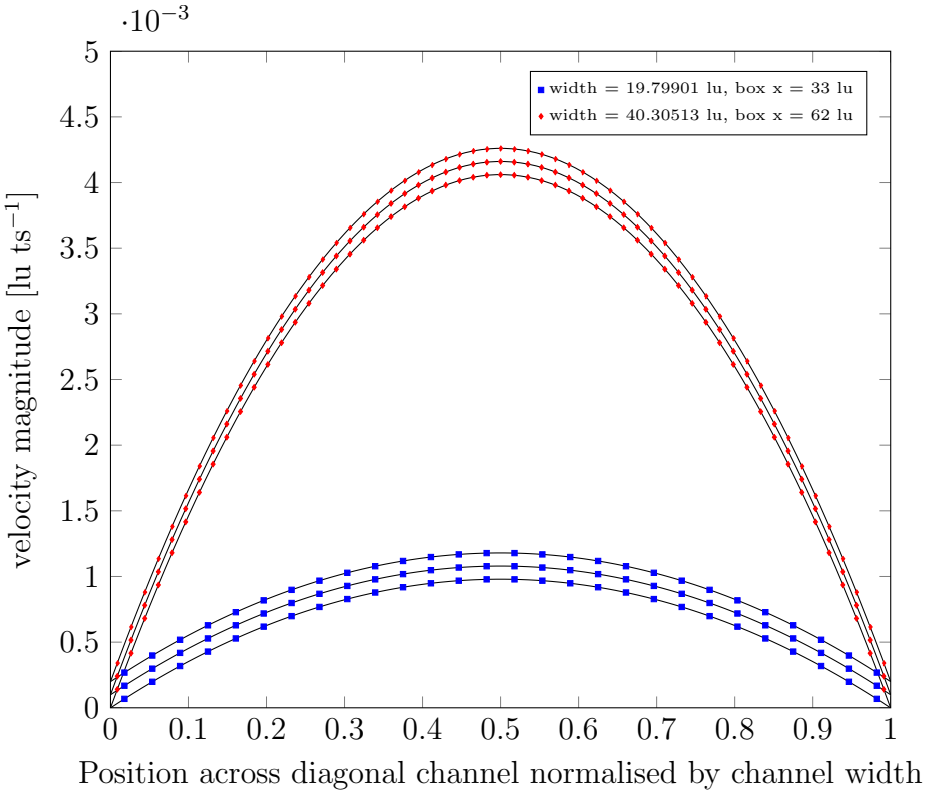


Figure 6.20: Velocity profiles, in straight geometries 45° out of alignment with the lattice, calculated from LBM with velocity boundary condition (marks) and the fit to Navier-Stokes (equation 5.4)(solid lines). From bottom to top for each channel width: $u_{wall} = 0$, 0.0001, and 0.0002 lu ts^{-1}.

Table 6.5: Slip lengths in diagonal geometries calculated using LBM with velocity boundary condition. Boundaries are 45° out of alignment with the grid.

Wall velocity [lu ts^{-1}]	Channel width [lu]	Calculated wall velocity [lu ts^{-1}]	Slip length [lu]	Deviation from analytical solution (%)
0	9.8995	−6.28e−7	−0.006	−0.006
0	19.79901	−6.24e−7	−0.003	0.004
0	40.30513	−6.66e−7	−0.002	0.001
0	79.90315	−7.54e−7	−0.001	0.006
0.0001	9.8995	9.94e−5	1.004	0.013
0.0001	19.79901	9.94e−5	0.502	0.002
0.0001	40.30513	9.95e−5	0.247	0.008
0.0001	79.90315	9.93e−5	0.124	0.009
0.0002	9.8995	1.99e−4	2.014	−0.003
0.0002	19.79901	1.99e−4	1.007	−0.002
0.0002	40.30513	1.99e−4	0.495	0.002
0.0002	79.90315	2.00e−4	0.25	0.017

6.6 Conclusions

Two methods of implementing a slip boundary condition into LBM are presented here. Both the specular-bounce-back boundary condition and the velocity boundary condition show promise in this area. However, the specular-bounce-back boundary condition appears more robust based on these results, however this is before the addition of the momentum corrections into the velocity boundary condition implementation that may correct some of it's issues.

Additional work is required in order for both of these boundary conditions to be used in complex geometries. The specular-bounce-back boundary can already deal with a system of pores of varying sizes, however currently it relies on there being few (to no) concave corners along the flow direction, which is unrealistic. Contrary to this, the velocity boundary condition is already able to simulate complicated geometries with any level of curvature and discretisation, however the dependence of the wall velocity on the slip length is not yet implemented. This results in an even less realistic scenario whereby the wall velocity is constant everywhere whilst slightly reduced at curved boundaries. Although the real slip length is a function of surface curvature, the relationship exhibited by this boundary condition is far from the real relationship without further adaptation. Implementation of the shear rate calculation, and as such the slip length to slip velocity conversion, is straightforward given the methods described here.

One key advantage of the velocity boundary condition over the specular-bounce-back boundary condition is that, once a shear rate dependence has been implemented, a negative slip length can be used since the velocity can be specified in any direction. This is important in geometries where the solid-fluid interactions are extremely high, such that fluid does not move in the first few fluid layers. As such the velocity at the wall, after extrapolation from the bulk velocity profile, would appear to be negative. This phenomena cannot be reflected with the specular-bounce-back boundary condition as the limiting case is that of 100 %

bounce-back, which results in a zero wall velocity.

Although not yet performed here, in order to implement the curvature dependent slip length a preprocessing step can be performed on the lattice grid. In this step the local curvature in each direction can be calculated by fitting the surrounding solid nodes to a 2^{nd} order polynomial. Based on this curvature the actual directional dependent slip length at each surface node is specified and an equivalent slip coefficient can be selected locally. This is trivial to implement into the existing model, however due to time constraints this has not been done here and should be included in any future work.

Additional future work would include performing a parametric study of the curvature dependence of the slip length on the slip coefficient in an analogous manner to Švec and Skoček (2013). Additionally, a further investigation into the effect of cylinder discretisation on the relationship between the slip length and the slip coefficient is necessary along with a better fitting process involving averaging around the entire radius and calculating the actual average diameter in order for calculation of the correct slip length.

A completely different approach to introducing slip along with additional nanoscale phenomena could also be implemented in place of / addition to the boundary conditions discussed here. For instance, Lennard-Jones parameters could be represented directly into LBM, such that solid and fluid nodes exhibit either an attractive or repulsive force on fluid which can be implemented in an analogous manner to body forces and would depend on the fluid density. This could theoretically be coupled with a maximum fluid node density which would allow for a fluid layering effect as is seen in molecular dynamics simulations. However, this would require much further study and could be the subject of an entire thesis in itself.

Chapter 7

Conclusion

In this thesis both molecular dynamics and lattice Boltzmann simulations have been performed for slip in nanopores. Particular emphasis has been put on water and n-heptane in graphitic slit pores and carbon nanotubes, however the methods presented here are applicable for any fluid-solid combination.

Through combination of the works presented here, a procedure now exists for implementing an accurate slip length in LBM, along with other continuum scale simulation packages. The final step of integrating the curvature dependent slip into LBM has not been performed here, although a description of the methods required to do this have been included.

Initially, TIP4P water and OPLS-AA n-heptane models have been validated against literature data for the bulk density, the saturated vapour pressure, the surface tension, and the liquid-vapour coexistence curves. In addition, density-temperature isobars were presented.

After confirming the applicability of the water and n-heptane models for both vapour and liquid phase systems, the adsorption in carbon nanotubes and graphitic slit pores has been studied. Observations have been made with regards to the rate and mechanisms of adsorption in slit and cylindrical pores of varying separation

and radii.

The process of adsorption has been shown to be dependent on the interactions between the fluid and solid pore surfaces. Water is shown to enter the pores studied here in a plug like manner, whilst n-heptane initially fills the surface in a single molecule thick layer before the central pore fluid enters in a similar fashion to water. The driving force for n-heptane adsorption also change with confinement from a pressure dominated to a pull-dominated force. For pull-dominated filling, the rate of fluid adsorption in the pores matched that of spontaneous imbibition given a zero pressure gradient. For n-heptane in CNTs, it has been observed that there is a transition between push-dominated and pull-dominated filling at a critical pore size.

Confinement is an important factor for the rate of adsorption of n-heptane, whilst it has little effect for water other than in the most extreme cases in cylindrical pores where single file flow occurs. For both water and n-heptane, the varying confinement caused a fluid layering effect that resulted in large discontinuities in the density as separation was varied.

For vapour phase water and n-heptane filling the same pores, the mechanisms of adsorption are drastically different. n-Heptane is adsorbed in a single fluid layer at the pore surfaces, whilst water in most pores does not exhibit any significant surface adsorption and remains in a vapour phase inside the pore space. For the smallest pores, a clear third n-heptane layer forms in the centre of the pore that is caused by an overlap in the potential from fluid molecules in the first fluid layers at opposite surfaces.

The time taken for n-heptane to adsorb from vapour phase reservoirs is shown to take O(100) times longer than for the liquid reservoirs case due to the slow rate of diffusion inside the pore.

Density-temperature isobars were also generated for water and n-heptane within

1 nm and 5 nm slit and cylindrical pores.

Starting with the equilibrated pores generated whilst investigating adsorption, the slip length was then calculated with both equilibrium and non-equilibrium methods. It was found that the average slip length is independent of separation for flat surfaces. However, when there is strong solid-fluid attraction, the fluid layering and confinement cause increasingly large deviations from the average that are dependent on the pore density.

It has also been shown that there is a clear functional relationship between the slip length and curvature that differs depending on whether the surface is concave or convex. Functions are proposed here which depend on two currently unknown parameters over the entire slip range of radii. The slip length has been shown to increase with decreasing radii for both water and n-heptane inside CNTs, whilst it decreases for fluid on the outside of the same CNTs.

The slip length is also much larger for vapour phase water in the same geometries as liquid phase water, whilst for n-heptane the opposite is observed due to the large solid-fluid attractive forces.

It has been shown here that the method of filling the pore is important for gaining accurate insight into the fluid arrangement in the pore, and as such calculate accurate slip lengths. By filling from an equilibrated reservoir of fluid the pore naturally fills to the correct density and proper layering is observed.

Finally, slip has been implemented into the lattice Boltzmann method using two different slip boundary conditions, specular-bounce-back and velocity. These have been validated for straight, cylindrical, and off-grid straight channels.

Both boundary conditions are shown to produce accurate slip flow, however the velocity boundary condition requires less parameter fitting before accurate slip lengths, such as those calculated in chapter 5, can be integrated.

7.1 Future work

There are several improvements that can be made to both the molecular dynamics and the lattice Boltzmann models, as well as further studies and investigations that would benefit the applications of this work. These are listed below, starting with improvements to the MD models.

The OPLS-AA forcefield is parametrised for a fixed cut-off length with a long-range dispersion correction. This means that longer cut-off lengths cannot be used, even when a correction is not included. This leads to difficulty when studying inhomogeneous systems, as the dispersion correction relies on an isotropic radial distribution function beyond the cut-off. A better model would be able to reproduce experimental data for interfacial properties, such as surface tension, without having to perform separate single phase simulations, such as Gibbs ensemble Monte-Carlo. This is possible by parametrising a model with PME summation used for calculation of the dispersion forces beyond the cut-off.

The temperature, in these works, has been coupled directly to the fluid molecules. By coupling the temperature to the solid surface atoms, the rate and mechanisms of adsorption may change. This could be introduced by artificially bonding atoms to lattice sites at the solid surface and controlling the temperature via bond oscillations. This could also be introduced by allowing the solid surface to move freely, in the same way that the piston has been defined. This would require a large number of individual simulations though, as the random motion of the pore will affect adsorption.

The slip length is also highly dependent on surface roughness, however only atomistically smooth surfaces have been modelled here. The procedures described here are applicable for all surfaces; however no other surfaces than those presented here have yet been tested.

Further investigation into hysteresis effects on isobars within CNTs and graphitic

slit pores should be performed. For a pore that is already filled with liquid phase fluid, gradually reducing the temperature of the fluid will result in a phase transition point that is higher than the bulk transition point. This is of importance for adsorption in engine deposits, as the engine temperature is initially cold during start-up.

In terms of LBM, there are still several steps that have not yet been implemented into the models. For the specular-bounce-back boundary condition, surfaces that are not aligned with the lattice have not been tested with the methods described here. The slip length as a function of the slip coefficient for cylindrical geometries also currently does not exist and is required before the true curvature dependent slip length can be introduced.

For the velocity boundary condition, the shear rate calculation and momentum correction terms have not been included and should be before continuing with this model.

In addition, a preprocessing step, for complex geometries, is still required for calculation of the local curvature and consequently the local slip length.

Finally, a completely different direction can be taken for implementing slip, along with other nanoscale phenomena, in LBM via Lennard-Jones interaction potentials. Fluid-fluid and fluid-solid potentials can be included, based on node density, in order to allow for realisation of fluid layering and friction naturally. However, this would be a time consuming task and could be the subject of an entire thesis in itself. The intricacies may also prove this to be impossible, although it would be interesting to investigate this.

Bibliography

Abascal, J. L. and Vega, C. (2005). "A general purpose model for the condensed phases of water: TIP4P/2005." *The Journal of chemical physics* 123.23, p. 234505. DOI: 10.1063/1.2121687.

Ahmed, N. K. and Hecht, M. (2009). "A boundary condition with adjustable slip length for Lattice Boltzmann simulations". *Journal of Statistical Mechanics: Theory and Experiment* 2009, p. 13. DOI: 10.1088/1742-5468/2009/09/P09017.

Alder, B. J. and Wainwright, T. E. (1959). "Studies in Molecular Dynamics. I. General Method". *The Journal of Chemical Physics* 31.2, pp. 459–466. DOI: 10.1063/1.1730376.

Alejandre, J., Tildesley, D. J., and Chapela, G. A. (1995). "Molecular dynamics simulation of the orthobaric densities and surface tension of water". *The Journal of Chemical Physics* 102.11, pp. 4574–4583. DOI: 10.1063/1.469505.

Baidakov, V. G. and Sulla, I. I. (1985). "Surface tension of propane and isobutane at near critical temperatures." *Rus. J. Phys. Chem.* 59.4, pp. 551–552.

Barrat, J. L. and Bocquet, L. (1999). "Large slip effect at a nonwetting fluid-solid interface". *Physical Review Letters* 82.23, pp. 4671–4674. DOI: 10.1103/PhysRevLett.82.4671.

Benson, J. D. (1975). *Some factors which affect octane requirement increase*. Society of Automotive Engineers. DOI: 10.4271/750933.

Berendsen, H. J. C., Postma, J. P. M., Gunsteren, W. F. van, DiNola, a, and Haak, J. R. (1984). "Molecular dynamics with coupling to an external bath". *The Journal of Chemical Physics* 81.8, pp. 3684–3690. DOI: 10.1063/1.448118.

Bhatnagar, P. L., Gross, E. P., and Krook, M. (1954). "A model for collision processes in gases. I. Small amplitude processes in charged and neutral one-component systems". *Physical Review* 94.3, pp. 511–525. DOI: 10.1103/PhysRev.94.511.

Bocquet, L. and Barrat, J.-L. (2007). "Flow boundary conditions from nano- to micro-scales". *Soft Matter* 3.6, pp. 685–693. DOI: 10.1039/B616490K.

Bocquet, L. and Barrat, J.-L. (2013). "On the Green-Kubo relationship for the liquid-solid friction coefficient". *Journal of Chemical Physics* 139.4, p. 044704. DOI: 10.1063/1.4816006.

Boek, E. S. and Venturoli, M. (2010). "Lattice-Boltzmann studies of fluid flow in porous media with realistic rock geometries". *Computers and Mathematics with Applications* 59.7, pp. 2305–2314. DOI: 10.1016/j.camwa.2009.08.063.

Boek, E. S., Zacharoudiou, I., Gray, F., Shah, S. M. K., Crawshaw, J. P., and Yang, J. (2014). "Multiphase flow and reactive transport at the pore scale using lattice-Boltzmann computer simulations". *SPE Annual Technical Conference and Exhibition*. DOI: 10.2118/170941-MS.

Bussi, G., Donadio, D., and Parrinello, M. (2007). "Canonical sampling through velocity rescaling". *Journal of Chemical Physics* 126.1, p. 014101. DOI: 10.1063/1.2408420.

Calado, J. C., McLure, I. A., and Soares, V. A. (1978). "Surface tension for octafluorocyclobutane, n-butane and their mixtures from 233 K to 254 K, and vapour pressure, excess Gibbs function and excess volume for the mixture at 233 K". *Fluid Phase Equilibria* 2.3, pp. 199–213. DOI: 10.1016/0378-3812(78)80009-0.

Caleman, C., Maaren, P. J. van, Hong, M., Hub, J. S., Costa, L. T., Spoel, D. van der, Maaren, P. J. V., Hong, M., Hub, J. S., Costa, L. T., and Spoel, D. V. D.

(2012). "Force Field Benchmark of Organic Liquids: Density, Enthalpy of Vaporization, Heat Capacities, Surface Tension, Isothermal Compressibility, Volumetric Expansion Coefficient, and Dielectric Constant." *Journal of chemical theory and computation* 8.1, pp. 61–74. DOI: 10.1021/ct200731v.

Cercignani, C. (1969). *Mathematical Methods in Kinetic Theory*. Plenum Press New York, pp. 1–233. DOI: 10.1007/978-1-4899-5409-1.

Chen, B. and Siepmann, J. I. (1999). "Transferable Potentials for Phase Equilibria. 3. Explicit-Hydrogen Description of Normal Alkanes". *Journal of Physical Chemistry B* 103.25, pp. 5370–5379. DOI: 10.1021/jp990822m.

Chen, L., Zhang, L., Kang, Q., Viswanathan, H. S., Yao, J., and Tao, W. (2015). "Nanoscale simulation of shale transport properties using the lattice Boltzmann method: permeability and diffusivity". *Scientific Reports* 5, p. 8089. DOI: 10.1038/srep08089.

Chen, S. and Doolen, G. D. (1998). "Lattice Boltzmann Method for Fluid Flows". *Annual Review of Fluid Mechanics* 30, pp. 329–364. DOI: 10.1146/annurev.fluid.30.1.329.

Chen, S., Chen, H., Martinez, D., and Matthaeus, W. (1991). "Lattice Boltzmann Model for Simulation of Magnetohydrodynamics". *Physical Review Letters* 67.27, p. 5. DOI: 10.1103/PhysRevLett.67.3776.

Chen, W., Zhang, R., and Koplik, J. (2014). "Velocity slip on curved surfaces". *Physical Review E - Statistical, Nonlinear, and Soft Matter Physics* 89.2, p. 023005. DOI: 10.1103/PhysRevE.89.023005.

Cieplak, M., Koplik, J., and Banavar, J. R. (2001). "Boundary conditions at a fluid-solid interface". *Physical Review Letters* 86.5, pp. 803–806. DOI: 10.1103/PhysRevLett.86.803.

Coffin, C. C. and Maass, O. (1928). "The Preparation and Physical Properties of α-, β- and γ-Butylene and Normal and Isobutane". *Journal of the American Chemical Society* 50.5, pp. 1427–1437. DOI: 10.1021/ja01392a028.

Cornell, W. D., Cieplak, P., Bayly, C. I., Gould, I. R., Merz, K. M., Ferguson, D. M., Spellmeyer, D. C., Fox, T., Caldwell, J. W., and Kollman, P. A. (1995). "A second generation force field for the simulation of proteins, nucleic acids, and organic molecules". *Journal of the American Chemical Society* 117.19, pp. 5179–5197. DOI: 10.1021/ja00124a002.

Cummings, P. T., Docherty, H., Iacovella, C. R., and Singh, J. K. (2010). "Phase transitions in nanoconfined fluids: The evidence from simulation and theory". *AIChE Journal* 56.4, pp. 842–848. DOI: 10.1002/aic.12226.

Di Pierro, M., Elber, R., and Leimkuhler, B. (2015). "A Stochastic Algorithm for the Isobaric-Isothermal Ensemble with Ewald Summations for All Long Range Forces". *Journal of Chemical Theory and Computation* 11.12, pp. 5624–5637. DOI: 10.1021/acs.jctc.5b00648.

Diaby, M., Sablier, M., Le Negrate, A., El Fassi, M., and Bocquet, J. (2009). "Understanding carbonaceous deposit formation resulting from engine oil degradation". *Carbon* 47.2, pp. 355–366. DOI: 10.1016/j.carbon.2008.10.014.

Dietrich, O. (2002). *Diffusion Coefficients of Water*.

Docherty, H. and Cummings, P. T. (2010). "Direct evidence for fluidsolid transition of nanoconfined fluids". *Soft Matter* 6.8, p. 1640. DOI: 10.1039/c000821d.

Dymond, J. H. and O/ye, H. A. (1994). "Viscosity of Selected Liquid n-Alkanes". *Journal of Physical and Chemical Reference Data* 23.1, pp. 41–53. DOI: 10.1063/1.555943.

Dysthe, D. K., Fuchs, a. H., and Rousseau, B. (2000). "Fluid transport properties by equilibrium molecular dynamics. III. Evaluation of united atom interaction potential models for pure alkanes". *The Journal of Chemical Physics* 112.17, pp. 7581–7590. DOI: 10.1063/1.481353.

English, N. J. (2005). "Molecular dynamics simulations of liquid water using various long-range electrostatics techniques". *Molecular Physics* 103.October, pp. 1945–1960. DOI: 10.1080/00268970500105003.

Esaki, Y., Ishiguru, T., Suzuki, N., and Nakada, M. (1990). "Mechanism of intake valve deposit formation: Part 1 Characterization of deposits". *SAE Technical Paper* 900151. DOI: 10.4271/900151.

Falk, K., Sedlmeier, F., Joly, L., Netz, R. R., and Bocquet, L. (2010). "Molecular origin of fast water transport in carbon nanotube membranes: Superlubricity versus curvature dependent friction". *Nano Letters* 10.10, pp. 4067–4073. DOI: 10.1021/nl1021046.

Falk, K., Sedlmeier, F., Joly, L., Netz, R. R., and Bocquet, L. (2012). "Ultralow liquid/solid friction in carbon nanotubes: Comprehensive theory for alcohols, alkanes, OMCTS, and water". *Langmuir* 28.40, pp. 14261–14272. DOI: 10.1021/la3029403.

Fishman, E. (1955). "SELF-DIFFUSION IN LIQUID n-PENTANE AND n-HEPTANE". *The Journal of Physical Chemistry* 59.5, pp. 469–472.

Frisch, U., Hasslacher, B., and Pomeau, Y. (1986). "Lattice-gas automata for the Navier-Stokes equation". *Physical Review Letters* 56.14, pp. 1505–1508. DOI: 10.1103/PhysRevLett.56.1505.

Galea, T. M. and Attard, P. (2004). "Molecular dynamics study of the effect of atomic roughness on the slip length at the fluid-solid boundary during shear flow." *Langmuir : the ACS journal of surfaces and colloids* 20.8, pp. 3477–3482. DOI: 10.1021/la035880k.

Gao, J., Luedtke, W. D., and Landman, U. (1997). "Layering transitions and dynamics of confined liquid films". *Physical Review Letters* 79.4, pp. 705–708. DOI: 10.1103/PhysRevLett.79.705.

Gardiner, C. W. (1985). *Handbook of stochastic methods*. Third. Vol. 55. 1, p. 101. DOI: 10.1016/0001-8708(85)90015-5.

Ghoufi, A., Goujon, F., Lachet, V., and Malfreyt, P. (2008). "Expressions for local contributions to the surface tension from the virial route". *Physical Review E - Statistical, Nonlinear, and Soft Matter Physics* 77.3, pp. 1–4. DOI: 10.1103/PhysRevE.77.031601.

González, M. A. and Abascal, J. L. (2010). "The shear viscosity of rigid water models". *Journal of Chemical Physics* 132.9, pp. 1–5. DOI: 10.1063/1.3330544.

Gray, F. and Boek, E. (2016). "Enhancing Computational Precision for Lattice Boltzmann Schemes in Porous Media Flows". *Computation* 4.1, p. 11. DOI: 10.3390/computation4010011.

Guo, Z. and Zheng, C. (2008). "Analysis of lattice Boltzmann equation for microscale gas flows: Relaxation times, boundary conditions and the Knudsen layer". *International Journal of Computational Fluid Dynamics* 22.7, pp. 465–473. DOI: 10.1080/10618560802253100.

Guo, Z., Zheng, C., and Shi, B. (2002). "Discrete lattice effects on the forcing term in the lattice Boltzmann method". *Physical Review E - Statistical, Nonlinear, and Soft Matter Physics* 65.4, pp. 1–6. DOI: 10.1103/PhysRevE.65.046308.

Guo, Z., Zhao, T. S., and Shi, Y. (2006). "Physical symmetry, spatial accuracy, and relaxation time of the lattice Boltzmann equation for microgas flows". *Journal of Applied Physics* 99.7, p. 074903. DOI: 10.1063/1.2185839.

Haneveld, J., Tas, N. R., Brunets, N., Jansen, H. V., and Elwenspoek, M. (2008). "Capillary filling of sub- 10 nm nanochannels". *Journal of Applied Physics* 104.1. DOI: 10.1063/1.2952053.

Hansen, J. S., Todd, B. D., and Daivis, P. J. (2011). "Prediction of fluid velocity slip at solid surfaces". *Physical Review E - Statistical, Nonlinear, and Soft Matter Physics* 84.1, p. 016313. DOI: 10.1103/PhysRevE.84.016313.

Hardy, J., Pomeau, Y., and De Pazzis, O. (1973). "Time evolution of a two-dimensional classical lattice system". *Physical Review Letters* 31.5, pp. 276–279. DOI: 10.1103/PhysRevLett.31.276.

Harvey, S. C., Tan, R. K. Z., and Cheatham, T. E. (1998). "The flying ice cube: Velocity rescaling in molecular dynamics leads to violation of energy equipartition". *Journal of Computational Chemistry* 19.7, pp. 726–740. DOI: 10.1002/(SICI)1096-987X(199805)19:7<726::AID-JCC4>3.0.CO;2-S.

He, X. Y. and Doolen, G (1997). "Lattice Boltzmann method on curvilinear coordinates system: Flow around a circular cylinder". *Journal of Computational Physics* 134.2, pp. 306–315. DOI: 10.1103/PhysRevE.55.R6333.

Hecht, M. and Harting, J. (2010). "Implementation of on-site velocity boundary conditions for D3Q19 lattice Boltzmann simulations". *Journal of Statistical Mechanics: Theory and Experiment* 2010.01, P01018. DOI: 10.1088/1742-5468/2010/01/P01018.

Heffelfinger, G. S., Tan, Z., Gubbins, K. E., Marini Bettolo Marconi, U., and Swol, F. van (1988). "Fluid mixtures in narrow cylindrical pores: Computer simulation and theory". *International Journal of Thermophysics* 9.6, pp. 1051–1060. DOI: 10.1007/BF01133272.

Hess, B. (2002). "Determining the shear viscosity of model liquids from molecular dynamics simulations". *Journal of Chemical Physics* 116.1, pp. 209–217. DOI: 10.1063/1.1421362.

Hess, B., Kutzner, C., Van Der Spoel, D., and Lindahl, E. (2008). "GROMACS 4: Algorithms for highly efficient, load-balanced, and scalable molecular simulation". *Journal of Chemical Theory and Computation* 4.3, pp. 435–447. DOI: 10.1021/ct700301q.

Heywood, J. B. (1988). *Internal Combustion Engine Fundamentals*. Vol. 930. McGraw-Hill New York, pp. 491–566. DOI: 10.1036/007028637X.

Ho, T. A., Papavassiliou, D. V., Lee, L. L., and Striolo, A. (2011). "Liquid water can slip on a hydrophilic surface". *Proceedings of the National Academy of Sciences* 108.39, pp. 16170–16175. DOI: 10.1073/pnas.1105189108.

Hoover, W. G. (1985). "Canonical dynamics: Equilibrium phase-space distributions". *Physical Review A* 31.3, pp. 1695–1697. DOI: 10.1103/PhysRevA.31.1695.

Huang, K. and Szlufarska, I. (2014). "Green-Kubo relation for friction at liquid-solid interfaces". *Physical Review E - Statistical, Nonlinear, and Soft Matter Physics* 89.3, pp. 1–10. DOI: 10.1103/PhysRevE.89.032119.

IAPWS (1994). "Viscosity and thermal conductivity of heavy water substance". *Physical Chemistry of Aqueous Systems: Proceedings of the 12th International Conference on the Properties of Water and Steam*, a107–a138.

IAPWS (1997). *Revised Release on the IAPS Formulation 1985 for the Viscosity of Ordinary Water Substance*. Tech. rep. Erlangen, Germany: International Association for the Properties of Water and Steam.

Irving, J. H. and Kirkwood, J. G. (1950). "The Statistical Mechanical Theory of Transport Processes. IV. The Equations of Hydrodynamics". *Journal of Chemical Physics* 18.6, pp. 817–829. DOI: 10.1063/1.1747782.

Jorgensen, W. L. and Tirado-Rives, J. (1988). "The OPLS [optimized potentials for liquid simulations] potential functions for proteins, energy minimizations for crystals of cyclic peptides and crambin". *Journal of the American Chemical Society* 110.6, pp. 1657–1666. DOI: 10.1021/ja00214a001.

Jorgensen, W. L., Chandrasekhar, J., Madura, J. D., Impey, R. W., and Klein, M. L. (1983). "Comparison of simple potential functions for simulating liquid water". *The Journal of Chemical Physics* 79.2, p. 926. DOI: 10.1063/1.445869.

Kalghatgi, G. T. (1995). "Combustion Chamber Deposits in Spark-Ignition Engines: A Literature Review". *SAE Technical Paper*, p. 952443. DOI: 10.4271/952443.

Kalghatgi, G. T. (1990). "Deposits in Gasoline Engines - A Literature Review". *SAE Technical Paper*, p. 902105. DOI: 10.4271/902105.

Kalra, A., Garde, S., and Hummer, G. (2003). "Osmotic water transport through carbon nanotube membranes". *Proceedings of the National Academy of Sciences* 100.18, pp. 10175–10180. DOI: 10.1073/pnas.1633354100.

Kannam, S. K., Todd, B. D., Hansen, J. S., and Daivis, P. J. (2013). "How fast does water flow in carbon nanotubes?" *Journal of Chemical Physics* 138.9, p. 094701. DOI: 10.1063/1.4793396.

Kannam, S. K., Daivis, P. J., and Todd, B. D. (2017). "Modeling slip and flow enhancement of water in carbon nanotubes". *MRS Bulletin* 42.4, pp. 283–288. DOI: 10.1557/mrs.2017.61.

Katz, D. L., Saltman, W., and Iutz, D. L. (1939). "Surface tension of Hydrocarbons". *Industrial & Engineering Chemistry* 31.1, pp. 91–94. DOI: 10.1021/ie50349a019.

Kiss, P. T. and Baranyai, A. (2011). "Sources of the deficiencies in the popular SPC / E and TIP3P models of water". *The Journal of chemical physics* 054106.5, p. 54106. DOI: 10.1063/1.3548869.

Klein, J. and Kumacheva, E. (1998). "Simple liquids confined to molecularly thin layers. I. Confinement-induced liquid-to-solid phase transitions". *Journal of Chemical Physics* 108.16, pp. 6996–7009. DOI: 10.1063/1.476114.

Koelman, J. M.V. A. (1991). "A Simple Lattice Boltzmann Scheme for Navier-Stokes Fluid Flow". *Europhysics Letters (EPL)* 15.6, pp. 603–607. DOI: 10.1209/0295-5075/15/6/007.

Kofke, D. A. (1993). "Direct evaluation of phase coexistence integration along the saturation line". *Journal of Chemical Physics* 98.5, pp. 4149–4162. DOI: 10.1063/1.465023.

Koplik, J., Banavar, J., and Willemsen, J. (1989). "Molecular dynamics of fluid flow at solid surfaces". *Physics of Fluids A: Fluid Dynamics* 1.5, pp. 781–794.

Krüger, T., Varnik, F., and Raabe, D. (2009). "Shear stress in lattice Boltzmann simulations". *Physical Review E - Statistical, Nonlinear, and Soft Matter Physics* 79.4, p. 15. DOI: 10.1103/PhysRevE.79.046704.

Kumacheva, E. and Klein, J. (1998). "Simple liquids confined to molecularly thin layers. II. Shear and frictional behavior of solidified films". *Journal of Chemical Physics* 108.16, pp. 7010–7022. DOI: 10.1063/1.476115.

Kuznetsova, T. and Kvamme, B. (2002). "Thermodynamic properties and interfacial tension of a model watercarbon dioxide system". *Physical Chemistry Chemical Physics* 4.6, pp. 937–941. DOI: 10.1039/b108726f.

Lallemand, P. and Luo, L.-S. (2000). "Theory of the lattice Boltzmann Method: Dispersion, Dissipation, Isotropy, Galilean Invariance, and Stability". *Physical Review E* 61.6, pp. 6546–6562. DOI: 10.1103/PhysRevE.61.6546.

Leadbetter, A. J., Taylor, D. J., and Vincent, B. (1964). "The Densities and Surface Tensions of Liquid Ethane and Nitrous Oxide". *Canadian Journal of Chemistry* 42.12, pp. 2930–2932. DOI: 10.1139/v64-439.

Li, X., Ross, D. A., Trusler, J. P. M., Maitland, G. C., and Boek, E. S. (2013). "Molecular dynamics simulations of CO2 and brine interfacial tension at high temperatures and pressures". *Journal of Physical Chemistry B* 117.18, pp. 5647–5652. DOI: 10.1021/jp309730m.

Lim, C. Y., Shu, C., Niu, X. D., and Chew, Y. T. (2002). "Application of lattice Boltzmann method to simulate microchannel flows". *Physics of Fluids* 14.7, pp. 2299–2308. DOI: 10.1063/1.1483841.

Lisal, M., William, W., and Nezbeda, I. (2001). "Accurate vapour-liquid equilibrium calculations for complex systems using the reaction Gibbs-Ensemble Monte Carlo simulation method". *Fluid Phase Equilibria* 181.1-2, pp. 127–146. DOI: 10.1016/S0378-3812(01)00489-7.

Liu, J. and Monson, P. A. (2005). "Does Water Condense in Carbon Pores ? ". 15, pp. 10219–10225.

López-Lemus, J. and Alejandre, J. (2002). "Thermodynamic and transport properties of simple fluids using lattice sums: bulk phases and liquid-vapour interface". *Molecular Physics* 100.18, pp. 2983–2992. DOI: 10.1080/00268970210121669.

Lumley, J. L. (1999). *Engines: an introduction*. Cambridge University Press.

MacKerell, A. D., Bashford, D, Bellott, M, Dunbrack, R. L., Evanseck, J. D., Field, M. J., Fischer, S, Gao, J, Guo, H, Ha, S, Joseph-McCarthy, D, Kuchnir, L, Kuczera, K, Lau, F. T. K., Mattos, C, Michnick, S, Ngo, T, Nguyen, D. T., Prodhom, B, Reiher, W. E., Roux, B., Schlenkrich, M, Smith, J. C., Stote, R, Straub, J, Watanabe, M, Wiorkiewicz-Kuczera, J, Yin, D, and Karplus, M.

(1998). "All-atom empirical potential for molecular modeling and dynamics studies of proteins". *Journal of Physical Chemistry B* 102.18, pp. 3586–3616. DOI: 10.1021/jp973084f.

Mahoney, M. W. and Jorgensen, W. L. (2001). "Diffusion constant of the TIP5P model of liquid water". *Journal of Chemical Physics* 114.1, pp. 363–366. DOI: 10.1063/1.1329346.

Markesteijn, A. P., Hartkamp, R., Luding, S., and Westerweel, J. (2012). "A comparison of the value of viscosity for several water models using Poiseuille flow in a nano-channel". *Journal of Chemical Physics* 136.13. DOI: 10.1063/1.3697977.

Martin, M. G. (2006). "Comparison of the AMBER, CHARMM, COMPASS, GROMOS, OPLS, TraPPE and UFF force fields for prediction of vapor-liquid coexistence curves and liquid densities". *Fluid Phase Equilibria* 248.1, pp. 50–55. DOI: 10.1016/j.fluid.2006.07.014.

Martin, M. G. and Siepmann, J. I. (1998). "Transferable Potentials for Phase Equilibria. 1. United-Atom Description of n-Alkanes". *The Journal of Physical Chemistry B* 102.97, pp. 2569–2577. DOI: 10.1021/jp972543+.

MATLAB (2010). *version 8.3 (R2014a)*. Natick, Massachusetts: The MathWorks Inc.

Matsumoto, M. and Kataoka, Y. (1988). "Study on Liquid Vapor Interface of Water .1. Simulational Results of Thermodynamic Properties and Orientational Structure". *J. Chem. Phys.* 88.5, pp. 3233–3245. DOI: 10.1063/1.453919.

McCabe, C., Bedrov, D., Borodin, O., Smith, G. D., and Cummings, P. T. (2003). "Transport Properties of Perfluoroalkanes Using Molecular Dynamics Simulation: Comparison of United- and Explicit-Atom Models". *Industrial & Engineering Chemistry Research* 42, pp. 6956–6961. DOI: 10.1021/ie034012f.

McCracken, M. E. and Abraham, J. (2005). "Multiple-relaxation-time lattice-Boltzmann model for multiphase flow". *Physical Review E - Statistical, Nonlinear, and Soft Matter Physics* 71.3. DOI: 10.1103/PhysRevE.71.036701.

McNamara, G. R. and Zanetti, G. (1988). "Use of the boltzmann equation to simulate lattice-gas automata". *Physical Review Letters* 61.20, pp. 2332–2335. DOI: 10.1103/PhysRevLett.61.2332.

Mendoza, F. N., López-Rendón, R., López-Lemus, J., Cruz, J., and Alejandre, J. (2008). "Surface tension of hydrocarbon chains at the liquidvapour interface". *Molecular Physics* 106.April 2015, pp. 1055–1059. DOI: 10.1080/00268970802119694.

Michaelides, A. (2016). "Nanoscience: Slippery when narrow". *Nature* 537.7619, pp. 171–172. DOI: 10.1038/537171a.

Miyamoto, S. and Kollman, P. (1992). "Settle - an Analytical Version of the Shake and Rattle Algorithm for Rigid Water Models". *Journal of Computational Chemistry* 13.8, pp. 952–962. DOI: 10.1002/jcc.540130805.

Moore, J. W. and Wellek, R. M. (1974). "Diffusion coefficients of n-heptane and n-decane in n-alkanes and n-alcohols at several temperatures". *Journal of Chemical & Engineering Data* 19.2, pp. 136–140. DOI: 10.1021/je60061a023.

Müller, E. A. and Gubbins, K. E. (1998). "Molecular simulation study of hydrophilic and hydrophobic behavior of activated carbon surfaces". *Carbon* 36.10, pp. 1433–1438. DOI: 10.1016/S0008-6223(98)00135-3.

Navier, C. L.M. H. (1823). "Memoire sur les lois du mouvement des fluides". *Memoires de l'Academie Royale des Sciences de l'Instit de France* 6, pp. 389–440.

O'Connell, S. T. and Thompson, P. A. (1995). "Molecular dynamics-continuum hybrid computations: A tool for studying complex fluid flows". *Physical Review E* 52.6, pp. 5792–5795. DOI: 10.1103/PhysRevE.52.R5792.

Parrinello, M. and Rahman, A. (1981). "Polymorphic transitions in single crystals: A new molecular dynamics method". *Journal of Applied Physics* 52.12, pp. 7182–7190. DOI: 10.1063/1.328693.

Payal, R. S., Balasubramanian, S., Rudra, I., Tandon, K., Mahlke, I., Doyle, D., and Cracknell, R. F. (2012). "Shear viscosity of linear alkanes through molecu-

lar simulations: quantitative tests for n-decane and n-hexadecane". *Molecular Simulation* 38.14-15, pp. 1234–1241. DOI: 10.1080/08927022.2012.702423.

Perumal, D. A. and Dass, A. K. (2015). "A Review on the development of lattice Boltzmann computation of macro fluid flows and heat transfer". *Alexandria Engineering Journal* 54.4, pp. 955–971. DOI: 10.1016/j.aej.2015.07.015.

Peterson, B. K., Gubbins, K. E., Heffelfinger, G. S., Marconi, U. M. B., and Swol, F. van (1988). "Lennard-Jones fluids in cylindrical pores: Nonlocal theory and computer simulation". en. *The Journal of Chemical Physics* 88.10, pp. 6487–6500. DOI: 10.1063/1.454434.

Petravic, J. and Harrowell, P. (2007). "On the equilibrium calculation of the friction coefficient for liquid slip against a wall". *Journal of Chemical Physics* 127.17, p. 174706. DOI: 10.1063/1.2799186.

Pinto Da Costa, J. M. C., Cracknell, R. F., Sarkisov, L., and Seaton, N. A. (2009). "Structural characterization of carbonaceous combustion-chamber deposits". *Carbon* 47.14, pp. 3322–3331. DOI: 10.1016/j.carbon.2009.07.053.

Pinto Da Costa, J. M. C., Cracknell, R. F., Seaton, N. A., and Sarkisov, L. (2011). "Towards predictive molecular simulations of normal and branched alkane adsorption in carbonaceous engine deposits". *Carbon* 49.2, pp. 445–456. DOI: 10.1016/j.carbon.2010.09.041.

Qian, Y. H. and Orszag, S. A. (1993). "Lattice BGK Models for the Navier-Stokes Equation: Nonlinear Deviation in Compressible Regimes". *Europhysics Letters (EPL)* 21.3, pp. 255–259. DOI: 10.1209/0295-5075/21/3/001.

Ramos-Alvarado, B., Kumar, S., and Peterson, G. P. (2016). "Hydrodynamic slip length as a surface property". *Physical Review E* 93.2, p. 023101. DOI: 10.1103/PhysRevE.93.023101.

Rappe, A. K., Casewit, C. J., and Colwell, K. S. (1992). "UFF, a full periodic table force field for molecular mechanics and molecular dynamics simulations". *J. Am. Chem. Soc.* 2, pp. 10024–10035. DOI: 10.1021/ja00051a040.

Reiter, G, Demirel, A. L., and Granick, S (1994). "From static to kinetic friction in confined liquid films." *Science (New York, N.Y.)* 263.5154, pp. 1741–1744. DOI: 10.1126/science.263.5154.1741.

Ross, D. A. and Boek, E. S. (2016). "Molecular Dynamics Simulations of Slip on Curved Surfaces". *Oil & Gas Science and Technology – Revue d'IFP Energies nouvelles* 71.4. Ed. by C. David and N. Sallee, p. 46. DOI: http://dx.doi.org/10.2516/ogst/2016004.

Roy, S., Raju, R., Chuang, H. F., Cruden, B. A., and Meyyappan, M. (2003). "Modeling gas flow through microchannels and nanopores". *Journal of Applied Physics* 93.8, pp. 4870–4879. DOI: 10.1063/1.1559936.

Scott, W. R. P., Hünenberger, P. H., Tironi, I. G., Mark, A. E., Billeter, S. R., Fennen, J., Torda, A. E., Huber, T., Krüger, P., and Gunsteren, W. F. van (1999). "The GROMOS Biomolecular Simulation Program Package". *The Journal of Physical Chemistry A* 103.19, pp. 3596–3607. DOI: 10.1021/jp984217f.

Shen, V., Siderius, D., Krekelberg, W., and Hatch, H. *NIST Standard Reference Simulation Website*.

Sides, S. W., Grest, G. S., and Lacasse, M. D. (1999). "Capillary waves at liquid-vapor interfaces: a molecular dynamics simulation." *Physical review. E, Statistical physics, plasmas, fluids, and related interdisciplinary topics* 60.6 Pt A, pp. 6708–6713. DOI: 10.1103/PhysRevE.60.6708.

Smith, E. R., Heyes, D. M., Dini, D., and Zaki, T. A. (2012). "Control-volume representation of molecular dynamics". *Physical Review E - Statistical, Nonlinear, and Soft Matter Physics* 85.5. DOI: 10.1103/PhysRevE.85.056705.

Smolyanitsky, A., Kazakov, A. F., Bruno, T. J., and Huber, M. L. (2013). *Mass diffusion of organic fluids : a molecular dynamics perspective*. Tech. rep. National Institute of Standards and Technology Technical Note 1805. DOI: 10.6028/NIST.TN.1805.

Soares, V. A. M., de J.V.S. Almeida, B., McLure, I. A., and Higgins, R. A. (1986). "Surface tension of pure and mixed simple substances at low temperatures". *Fluid Phase Equilibria* 32.1, pp. 9–16. DOI: 10.1016/0378-3812(86)87002-9.

Sokhan, V. P., Nicholson, D., and Quirke, N. (2001). "Fluid flow in nanopores: An examination of hydrodynamic boundary conditions". *Journal of Chemical Physics* 115.8, pp. 3878–3887. DOI: 10.1063/1.1387976.

Sokhan, V. P., Nicholson, D., and Quirke, N. (2002). "Fluid flow in nanopores: Accurate boundary conditions for carbon nanotubes". *Journal of Chemical Physics* 117.18, pp. 8531–8539. DOI: 10.1063/1.1512643.

Somayajulu, G. R. (1988). "A generalized equation for surface tension from the triple point to the critical point". *International Journal of Thermophysics* 9.4, pp. 559–566. DOI: 10.1007/BF00503154.

Span, R. (2000). "Multiparameter Equations of State: An Accurate Source of Thermodynamic Property Data", p. 367.

Spoel, D. van der, Lindahl, E., Hess, B., and The GROMACS development team (2013). "GROMACS User Manual version 4.6". *Www.Gromacs.Org*. DOI: 10.1007/SpringerReference_28001.

Srivastava, R., Docherty, H., Singh, J. K., and Cummings, P. T. (2011). "Phase transitions of water in graphite and mica pores". *Journal of Physical Chemistry C* 115.25, pp. 12448–12457. DOI: 10.1021/jp2003563.

Steele, W. A. (1973). "The physical interaction of gases with crystalline solids. I. Gas-solid energies and properties of isolated adsorbed atoms". *Surface Science* 36.1, pp. 317–352. DOI: 10.1016/0039-6028(73)90264-1.

Striolo, A., Gubbins, K. E., Gruszkiewicz, M. S., Cole, D. R., Simonson, J. M., Chialvo, A. A., Cummings, P. T., Burchell, T. D., and More, K. L. (2005a). "Effect of temperature on the adsorption of water in porous carbons". *Langmuir* 21.21, pp. 9457–9467. DOI: 10.1021/la051120t.

Striolo, A., Chialvo, A. A., Gubbins, K. E., and Cummings, P. T. (2005b). "Water in carbon nanotubes: Adsorption isotherms and thermodynamic properties

from molecular simulation". *Journal of Chemical Physics* 122.23. DOI: 10.1063/1.1924697.

Striolo, A., Chialvo, A. A., Cummings, P. T., and Gubbins, K. E. (2003). "Water adsorption in carbon-slit nanopores". *Langmuir* 19.20, pp. 8583–8591. DOI: 10.1021/la0347354.

Striolo, A., Gubbins, K. E., Chialvo, A. A., and Cummings, P. T. (2004). "Simulated water adsorption isotherms in carbon nanopores". *Molecular Physics* 102.3 PART II, pp. 243–251. DOI: 10.1080/00268970410001668507.

Stukan, M. R., Ligneul, P., Crawshaw, J. P., and Boek, E. S. (2010). "Spontaneous imbibition in nanopores of different roughness and wettability". *Langmuir* 26.16, pp. 13342–13352. DOI: 10.1021/la101995t.

Succi, S. (2002). "Mesoscopic modeling of slip motion at fluid-solid interfaces with heterogeneous catalysis." *Physical review letters* 89.6, p. 064502. DOI: 10.1103/PhysRevLett.89.064502.

Succi, S. (2001). *Lattice Boltzmann Equation*. Vol. 240. Oxford University Press on Demand, pp. 221–228.

Sukop, M. C. and Thorne, D. T. (2013). *Lattice Boltzmann modeling-an introduction for geoscientists and engineers*. Vol. 53. 9, pp. 1689–1699. DOI: 10.1017/CBO9781107415324.004.

Sun, H. (1998). "COMPASS: An ab Initio Force-Field Optimized for Condensed-Phase ApplicationssOverview with Details on Alkane and Benzene Compounds". *Journal of Physical Chemistry B* 5647.98, pp. 7338–7364. DOI: 10.1021/jp980939v.

Supple, S. and Quirke, N. (2005). "Molecular dynamics of transient oil flows in nanopores. II. Density profiles and molecular structure for decane in carbon nanotubes". *Journal of Chemical Physics* 122.10, pp. 1–9. DOI: 10.1063/1.1856927.

Švec, O. and Skoček, J. (2013). "Simple Navier's slip boundary condition for the non-Newtonian Lattice Boltzmann fluid dynamics solver". *Journal of Non-*

Newtonian Fluid Mechanics 199, pp. 61–69. DOI: 10.1016/j.jnnfm.2013.06.003.

Taherian, F., Marcon, V., Van Der Vegt, N. F. A., and Leroy, F. (2013). "What is the contact angle of water on graphene?" *Langmuir* 29.5, pp. 1457–1465. DOI: 10.1021/la304645w.

Thompson, P. A. and Robbins, M. O. (1989). "Simulations of contact-line motion: Slip and the dynamic contact angle". *Physical Review Letters* 63.7, pp. 766–769. DOI: 10.1103/PhysRevLett.63.766.

Thompson, P. A. and Troian, S. M. (1997). "A general boundary condition for liquid flow at solid surfaces". *Nature* 389.September, pp. 360–362. DOI: 10.1038/38686.

Vega, C. and De Miguel, E. (2007). "Surface tension of the most popular models of water by using the test-area simulation method". *Journal of Chemical Physics* 126.15, pp. 1–10. DOI: 10.1063/1.2715577.

Vega, C., Abascal, J. L. F., and Nezbeda, I. (2006). "Vapor-liquid equilibria from the triple point up to the critical point for the new generation of TIP4P-like models: TIP4P/Ew, TIP4P/2005, and TIP4P/ice". *Journal of Chemical Physics* 125.3, pp. 1–9. DOI: 10.1063/1.2215612.

Verlet, L. (1967). "Computer Experiments on Classical Fluids .I. Thermodynamical Properties of Lennard-Jones Molecules". *Phys. Rev.* 159.1, p. 98. DOI: http://dx.doi.org/10.1103/PhysRev.159.98.

Wagner, W. and Pruss, A. (2002). "The IAPWS formulation 1995 for the thermodynamic properties of ordinary water substance for general and scientific use". *Journal of Physical and Chemical Reference Data* 31.2, pp. 387–535. DOI: 10.1063/1.1461829.

Washburn, E. W. (1921). "The dynamics of capillary flow". *Physical Review* 17.3, pp. 273–283. DOI: 10.1103/PhysRev.17.273.

Watanabe, K. and Klein, M. L. (1989). "Effective pair potentials and the properties of water". *Chemical Physics* 131.2-3, pp. 157–167. DOI: 10.1016/0301-0104(89)80166-1.

Wennberg, C. L., Murtola, T., Hess, B., and Lindahl, E. (2013). "Lennard-Jones lattice summation in bilayer simulations has critical effects on surface tension and lipid properties". *Journal of Chemical Theory and Computation* 9.8, pp. 3527–3537. DOI: 10.1021/ct400140n.

Yang, J. and Boek, E. S. (2013). "A comparison study of multi-component Lattice Boltzmann models for flow in porous media applications". *Computers and Mathematics with Applications* 65.6, pp. 882–890. DOI: 10.1016/j.camwa.2012.11.022.

Yang, J., Crawshaw, J. P., and Boek, E. S. (2013). "Quantitative determination of molecular propagator distributions for solute transport in homogeneous and heterogeneous porous media using lattice Boltzmann simulations". *Water Resources Research* 49.12, pp. 8531–8538. DOI: 10.1002/2013WR013877.

Yongli, S., Minhua, S., Weidong, C., Congxiao, M., and Fang, L. (2007). "The examination of water potentials by simulating viscosity". *Computational Materials Science* 38.4, pp. 737–740. DOI: 10.1016/j.commatsci.2006.05.007.

Yue, X., Wu, Y., Huang, X., Ma, Y., Pang, Y., Bao, X., and Hao, J. (2012). "Impact of gasoline engine deposits on light duty vehicle emissions: In-use case study in Beijing, China". *Frontiers of Environmental Science and Engineering in China* 6.5, pp. 717–724. DOI: 10.1007/s11783-012-0438-3.

Zahariev, T. K., Slavchov, R. I., Tadjer, A. V., and Ivanova, A. N. (2014). "Fully atomistic molecular-mechanical model of liquid alkane oils: Computational validation". *Journal of Computational Chemistry* 35.10, pp. 776–788. DOI: 10.1002/jcc.23546.

Zerda, T. W., Yuan, X., and Moore, S. M. (2001). "Effects of fuel additives on the microstructure of combustion engine deposits". *Carbon* 39.10, pp. 1589–1597. DOI: 10.1016/S0008-6223(00)00287-6.

Zerda, T., Yuan, X., Moore, S., and Leon y Leon, C. (1999). "Surface area, pore size distribution and microstructure of combustion engine deposits". *Carbon* 37.12, pp. 1999–2009. DOI: 10.1016/S0008-6223(99)00068-8.

Zhang, X., Xiao, L., Shan, X., and Guo, L. (2014). "Lattice Boltzmann simulation of shale gas transport in organic nano-pores." *Scientific reports* 4, p. 4843. DOI: 10.1038/srep04843.

Zhao, L., Cheng, T., and Sun, H. (2008). "On the accuracy of predicting shear viscosity of molecular liquids using the periodic perturbation method." en. *J.Chem.Phys* 129.14, p. 144501. DOI: 10.1063/1.2936986.

Zielkiewicz, J. (2012). "Structural properties of water : Comparison of the SPC , SPCE , TIP4P , and TIP5P models of water". *The Journal of chemical physics* 104501.2005, p. 104501. DOI: 10.1063/1.2018637.

Zubillaga, R. A., Labastida, A., Cruz, B., Martinez, J. C., Sanchez, E., and Alejandre, J. (2013). "Surface tension of organic liquids using the OPLS/AA force field". *Journal of Chemical Theory and Computation* 9.3, pp. 1611–1615. DOI: 10.1021/ct300976t.

Zwanzig, R. (1965). "Time-correlation functions and transport coefficients in statistical mechanics". *Annual Review of Physical Chemistry* 16.1, pp. 67–102. DOI: 10.1146/annurev.pc.16.100165.000435.

Appendix A

Models for molecular simulations

A.1 Simulation options and summary of interaction parameters

Most simulation options, including some that have not already been discussed, are summarised in table A.1. These options are specific to GROMACS and the GROMACS manual should be referred to for more details on how these options work. The purpose of providing these options is to aid in reproducibility of the results. These options are used in most simulations presented here unless otherwise mentioned or implied.

Run input files, matlab scripts, and bash scripts along with instructions for reproducing these results can be found at dx.doi.org/10.6084/m9.figshare.5258077.

Table A.1: Simulation options for use with GROMACS.

Option (units)	Value	Section	Notes
dt (fs)	0.002	3.2.6	Time-step
comm-mode	none / Linear	–	Centre of mass motion removal. For avoiding build up of overall translation in a system. Used in all fluid only systems.
nstcomm	1	–	Number of steps for centre of mass motion removal.
pbc	xyz	3.2.3	Dimensions in which periodic boundary conditions are applied.
nstlist	10	3.2.2	Frequency for updating the neighbour list.
rlist (nm)	1.0	3.2.2	Cut-off distance, within which the neighbour list is determined at each time step.
coulombtype	PME	3.2.2	Algorithm used for calculating coulomb interactions.
rcoulomb (nm)	1.0	3.2.2	Direct-space interaction radius when used with coulombtype = PME.
vdw-type	Cut-off	3.2.2	Algorithm used for calculating van der Waals interactions.
rvdw (nm)	1.0	3.2.2	Cut-off distance, within which van der Waal interactions are calculated.
DispCorr	no / EnerPres	3.2.2	Type of long-range dispersion correction to use. Either not used or both energy and pressure corrections done, depending on whether the system is homogeneous or not.
fourierspacing (nm)	0.12	3.2.2	Approximate grid separation used in determining the number of Fourier-space grid points.
tcoupl	v-rescale	3.2.9	Type of temperature coupling algorithm used.
nsttcouple	10	3.2.9	Frequency for coupling the temperature.
tau-t	0.1 ps / 2 ps	3.2.9	Time constant for temperature coupling (v-rescale / Langevin).
Pcoupl	no / Parrinello-Rahman	3.2.10	Type of pressure coupling algorithm used.
nstpcouple		3.2.10	Frequency for coupling the pressure.
tau-p	1 ps	3.2.10	Time constant for pressure coupling. With Parrinello-Rahman pressure coupling this is the period of pressure fluctuations at equilibrium.
compressibility (bar^{-1})	4.5e-5	3.2.10	Chosen as the compressibility of water at standard conditions. This has no effect on the average pressure, only on the size of the pressure fluctuations.

constraints	h-bonds	3.4	Bonds/angles that are constrained. Here all hydrogen bonds are constrained to allow for a higher time-step.
constraint-algorithm	LINCS	–	Algorithm used for applying constraints.
pull	constant force	3.5.2	Type of pulling. Used for moving pistons. Pistons are pulled with a constant force towards the open pore.
freezegrps	SOLIDS	3.5	Groups which are frozen in place, i.e. only the solid pore surface atoms.
freezedim	Y Y Y	3.5	Dimensions in which to freeze the aforementioned freeze groups.

Table A.2: Summary of non-bonded interactions.

Molecule	Forcefield	Atom	Atom ID	Description	Number	Mass	Charge	$*\sigma$ (nm)	$*\epsilon$ (kJ mol^{-1})
Water	TIP4P[†]	O	opls_113	Oxygen	1	15.9994	0	3.15365e-1	6.48520e-1
		H	opls_114	Hydrogen	2	1.0080	0.52	0	0
		D	opls_115	Dummy atom	1	0	-1.04	0	0
n-Heptane	OPLSAA[‡]	C	opls_135	Carbon end group	2	12.0110	-0.18	3.50000e-1	2.76144e-1
		C	opls_136	Carbon	5	12.0110	-0.12	3.50000e-1	2.76144e-1
		H	opls_140	Hydrogen	16	1.0080	0.06	2.50000e-1	1.25520e-1
Solid Carbon	OPLSAA[‡]	C	opls_147	Carbon (naphthalene)	∞	12.0110	-0.18	3.55000e-1	2.92880e-1

[*] Parameters for equation 3.1

[†] Jorgensen et al. (1983)

[‡] Jorgensen and Tirado-Rives (1988)

Table A.3: Summary of bonded interactions.

Molecule	Forcefield	Type	i-j(-k(-l))	Equation	Number	length (nm) / angle (°)	k^b / k^θ / C_0	C_1	C_2	C_3
Water	TIP4P†	Settle	O-H	–	–	0.09572	–	–	–	–
		Settle	H-H	–	–	0.15139	–	–	–	–
		Bond	O-H	3.8	2	0.09572	502416.0	–	–	–
		Angle	H-O-H	3.9	1	104.520	628.02	–	–	–
		Virt. Site	O-D	–	1	0.015	–	–	–	–
		Virt. Site	D-O-H	–	1	52.26	–	–	–	–
n-Heptane*	OPLSAA‡	Bond	C-C	3.8	6	0.15290	224262.4	–	–	–
		Bond	C-H	3.8	16	0.10900	284512.0	–	–	–
		Angle	C-C-C	3.9	5	112.700	488.273	–	–	–
		Angle	C-C-H	3.9	26	110.700	313.800	–	–	–
		Angle	H-C-H	3.9	11	107.800	276.144	–	–	–
		Dihedral	C-C-C-C	3.10	4	–	2.92880	-1.46440	0.20920	-1.67360
		Dihedral	C-C-C-H	3.10	22	–	0.62760	1.88280	0	-2.51040
		Dihedral	H-C-C-H	3.10	28	–	0.62760	1.88280	0	-2.51040
Piston**	OPLSAA‡	Bond	C-C	3.8	∞	0.142	392459.2	–	–	–
		Angle	C-C-C	3.9	∞	120.000	527.184	–	–	–
		Dihedral	C-C-C-C	3.10	∞	–	30.33400	0	-30.33400	0

* Bonds, angles and dihedrals parameters are from CHARM22 forcefield.
** Bonds and angles parameters are from phenol and dihedral parameters are from an aromatic ring.
† Jorgensen and Tirado-Rives (1988)
‡ Jorgensen et al. (1983)

Appendix B

Calculation of slip lengths and friction coefficients via molecular simulation

B.1 Navier-Stokes

The Navier-Stokes equations are a set of equations that describe the motions of a continuum fluid under laminar flow conditions. Equations B.1 – B.3 and B.4 – B.6 are the Navier-Stokes equations for Cartesian and cylindrical coordinates respectively (Navier 1823).

$$\rho\left(\frac{\partial u_x}{\partial t}+u_x\frac{\partial u_x}{\partial x}+u_y\frac{\partial u_x}{\partial y}+u_z\frac{\partial u_x}{\partial z}\right)= \\ -\frac{\partial p}{\partial x}+\mu\left(\frac{\partial^2 u_x}{\partial x^2}+\frac{\partial^2 u_x}{\partial y^2}+\frac{\partial^2 u_x}{\partial z^2}\right)-\mu\frac{\partial}{\partial x}\left(\frac{\partial u_x}{\partial x}+\frac{\partial u_y}{\partial y}+\frac{\partial u_z}{\partial z}\right)+\rho g_x \quad \text{(B.1)}$$

$$\rho\left(\frac{\partial u_y}{\partial t}+u_x\frac{\partial u_y}{\partial x}+u_y\frac{\partial u_y}{\partial y}+u_z\frac{\partial u_y}{\partial z}\right)= -\frac{\partial p}{\partial y}+\mu\left(\frac{\partial^2 u_y}{\partial x^2}+\frac{\partial^2 u_y}{\partial y^2}+\frac{\partial^2 u_y}{\partial z^2}\right)-\mu\frac{\partial}{\partial y}\left(\frac{\partial u_x}{\partial x}+\frac{\partial u_y}{\partial y}+\frac{\partial u_z}{\partial z}\right)+\rho g_y \quad \text{(B.2)}$$

$$\rho\left(\frac{\partial u_z}{\partial t}+u_x\frac{\partial u_z}{\partial x}+u_y\frac{\partial u_z}{\partial y}+u_z\frac{\partial u_z}{\partial z}\right)= -\frac{\partial p}{\partial z}+\mu\left(\frac{\partial^2 u_z}{\partial x^2}+\frac{\partial^2 u_z}{\partial y^2}+\frac{\partial^2 u_z}{\partial z^2}\right)-\mu\frac{\partial}{\partial z}\left(\frac{\partial u_x}{\partial x}+\frac{\partial u_y}{\partial y}+\frac{\partial u_z}{\partial z}\right)+\rho g_z \quad \text{(B.3)}$$

$$\rho\left(\frac{\partial u_r}{\partial t}+u_r\frac{\partial u_r}{\partial r}+\frac{u_\phi}{r}\frac{\partial u_r}{\partial \phi}+u_z\frac{\partial u_r}{\partial z}-\frac{u_\phi^2}{r}\right)= -\frac{\partial p}{\partial r}+\mu\left[\frac{1}{r}\frac{\partial}{\partial r}\left(r\frac{\partial u_r}{\partial r}\right)+\frac{1}{r^2}\frac{\partial^2 u_r}{\partial \phi^2}+\frac{\partial^2 u_r}{\partial z^2}-\frac{u_r}{r^2}-\frac{2}{r^2}\frac{\partial u_\phi}{\partial \phi}\right]+\rho g_r \quad \text{(B.4)}$$

$$\rho\left(\frac{\partial u_\phi}{\partial t}+u_r\frac{\partial u_\phi}{\partial r}+\frac{u_\phi}{r}\frac{\partial u_\phi}{\partial \phi}+u_z\frac{\partial u_\phi}{\partial z}+\frac{u_r u_\phi}{r}\right)= -\frac{1}{r}\frac{\partial p}{\partial \phi}+\mu\left[\frac{1}{r}\frac{\partial}{\partial r}\left(r\frac{\partial u_\phi}{\partial r}\right)+\frac{1}{r^2}\frac{\partial^2 u_\phi}{\partial \phi^2}+\frac{\partial^2 u_\phi}{\partial z^2}-\frac{u_\phi}{r^2}+\frac{2}{r^2}\frac{\partial u_\phi}{\partial \phi}\right]+\rho g_\phi \quad \text{(B.5)}$$

$$\rho\left(\frac{\partial u_z}{\partial t}+u_r\frac{\partial u_z}{\partial r}+\frac{u_\phi}{r}\frac{\partial u_z}{\partial \phi}+u_z\frac{\partial u_z}{\partial z}\right)= -\frac{\partial p}{\partial z}+\mu\left[\frac{1}{r}\frac{\partial}{\partial r}\left(r\frac{\partial u_z}{\partial r}\right)+\frac{1}{r^2}\frac{\partial^2 u_z}{\partial \phi^2}+\frac{\partial^2 u_z}{\partial z^2}\right]+\rho g_z \quad \text{(B.6)}$$

Here, u_i is the velocity in direction i and g_i is a driving force which is typically gravity.

The above equations can be reduced by assuming steady state has been reached and unidirectional flow. For flow in a slit geometry, with flow in the z-direction and surfaces normal to the x-axis, equation B.3 reduces to:

$$0=\mu\frac{\partial^2 u_z}{\partial x^2}+\rho g_z. \quad \text{(B.7)}$$

Integrating twice with respect to x, with the slip boundary condition defined in equation 5.1, this becomes:

$$u_z = \frac{\rho g_z}{2\mu}\left(Hx - x^2 + bH\right). \tag{B.8}$$

Where $du_z/dx|_{wall}$ is the shear rate at a wall. Similarly, for flow in a cylindrical geometry aligned with the z-axis, equation B.6 reduces to equation B.9 and upon integration produces equation B.10.

$$0 = \frac{\mu}{r}\frac{\partial}{\partial r}\left(r\frac{\partial u_z}{\partial r}\right) + \rho g_z \tag{B.9}$$

$$u_z = \frac{\rho g_z}{4\mu}\left(R^2 - r^2 + 2bR\right) \tag{B.10}$$

From equations B.8 and B.10 it is easy to see that the slip length simply shifts the velocity up by a constant amount. This indicates that the shape of the velocity profile is independent of the slip length as would be expected.

Appendix C

Adsorption in nanopores via molecular simulation

C.1 Full page sized graphs of liquid water and n-heptane adsorption against a vacuum

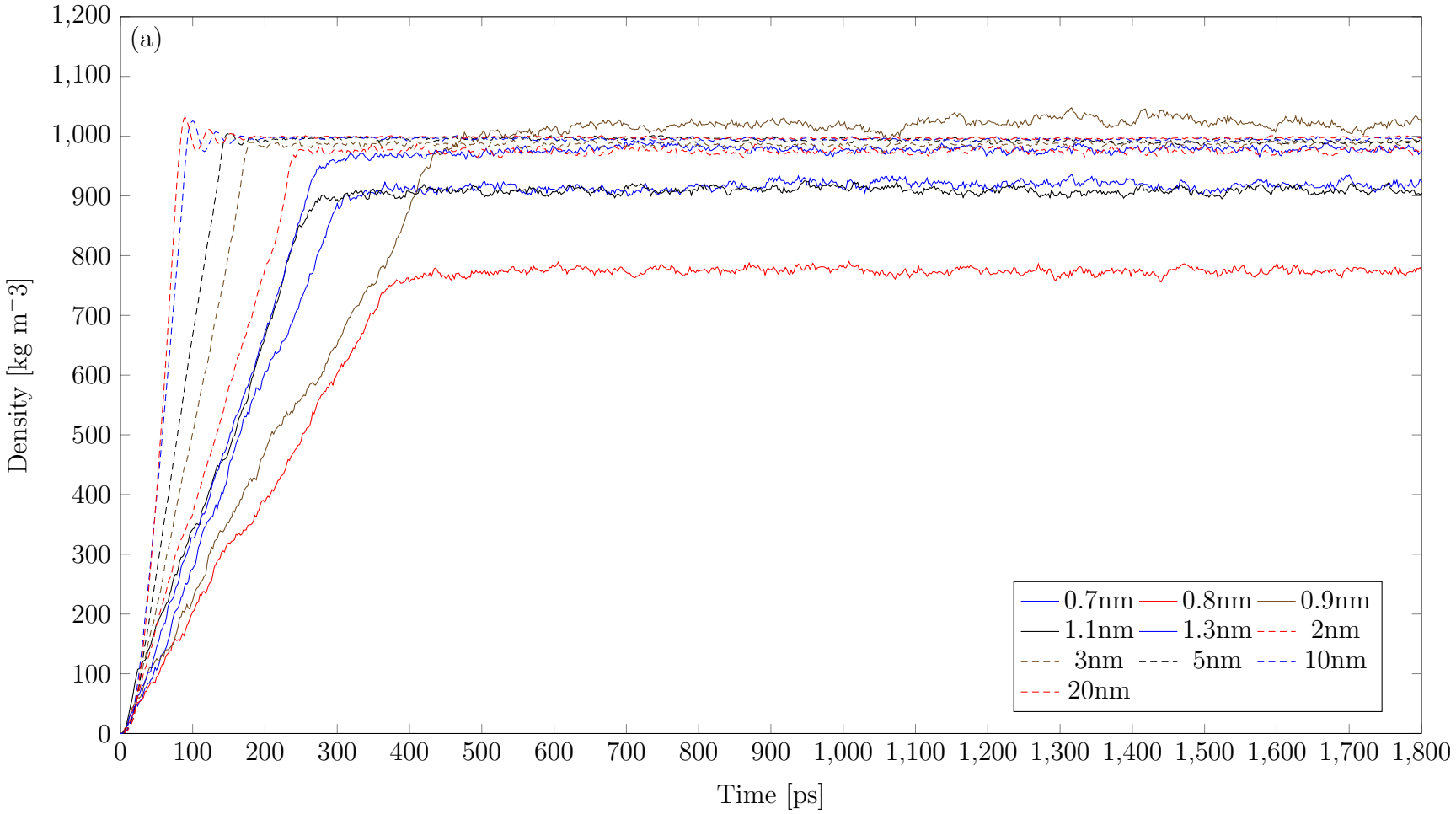


Figure C.1: Liquid water at 300 K filling various slit pores. a) Pore density against time.

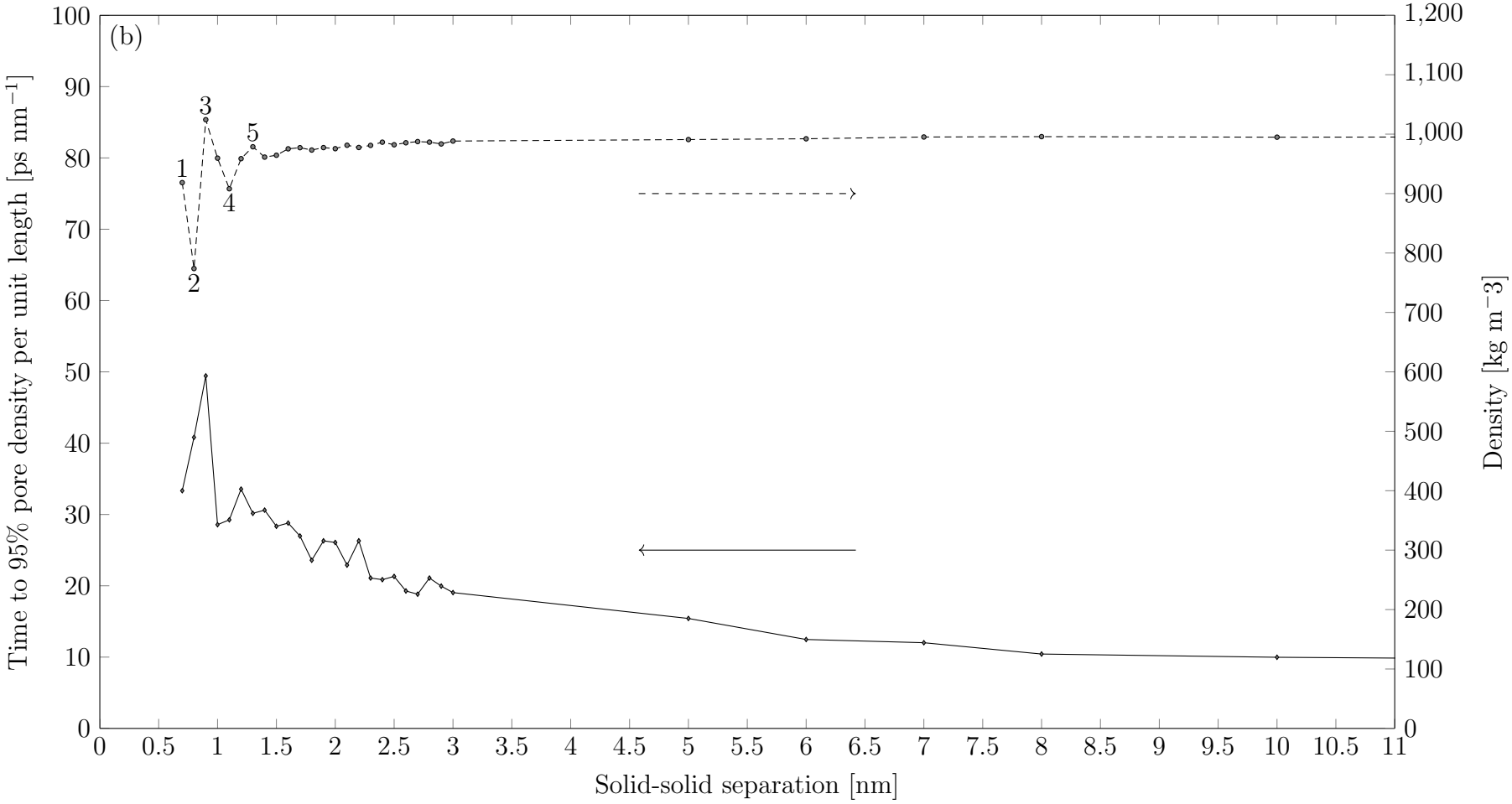


Figure C.2: Liquid water at 300 K filling various slit pores. b) Comparison between pore fill time and the mean density calculated over the final 500 ps of (a). The labels correspond to the density extremes in the smallest pores. The matching pore geometries are shown in figure 4.25.

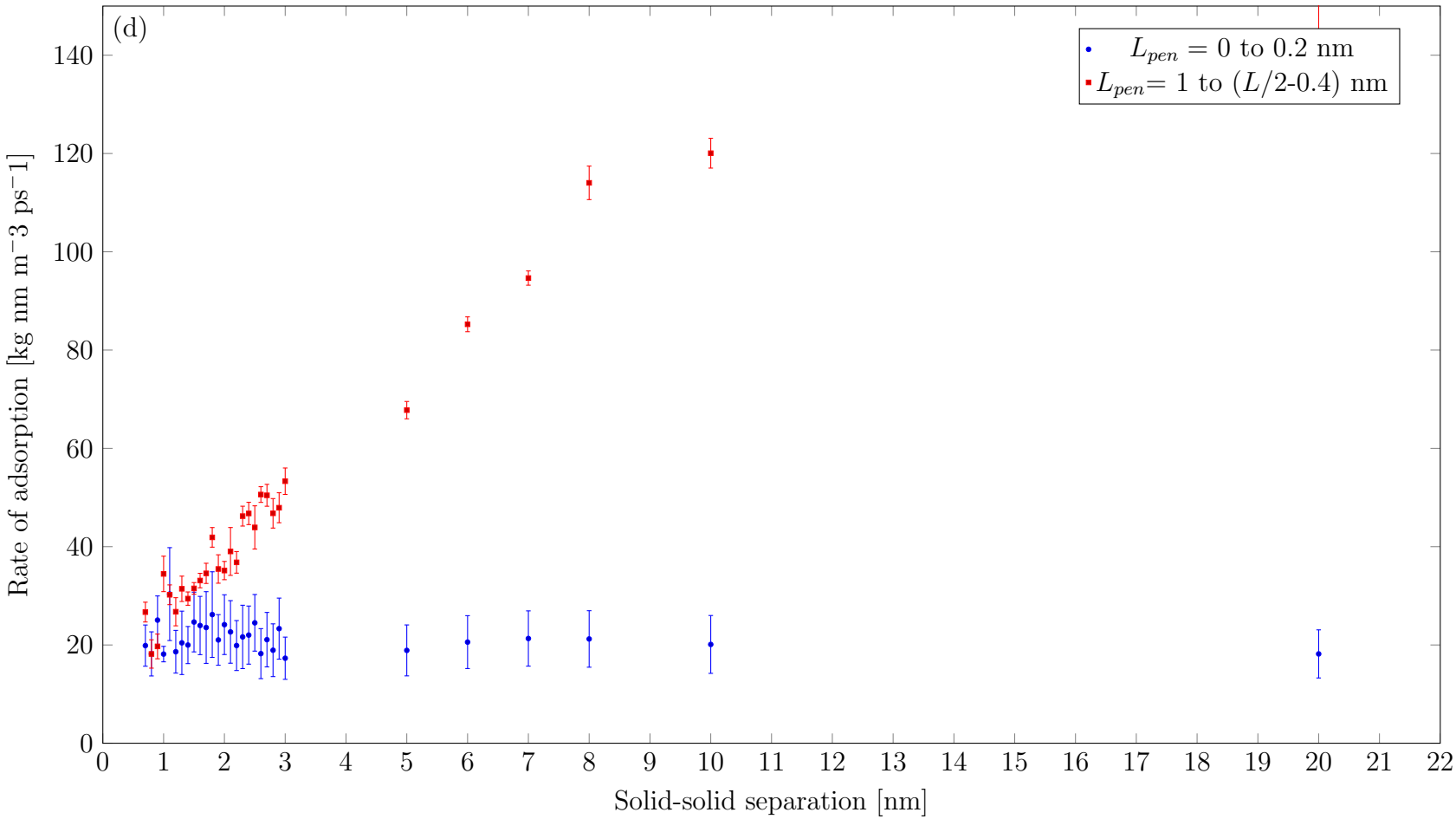


Figure C.3: Liquid water at 300 K filling various slit pores. c) Pore density * pore length against time, for use in calculating initial fill rate of pore.

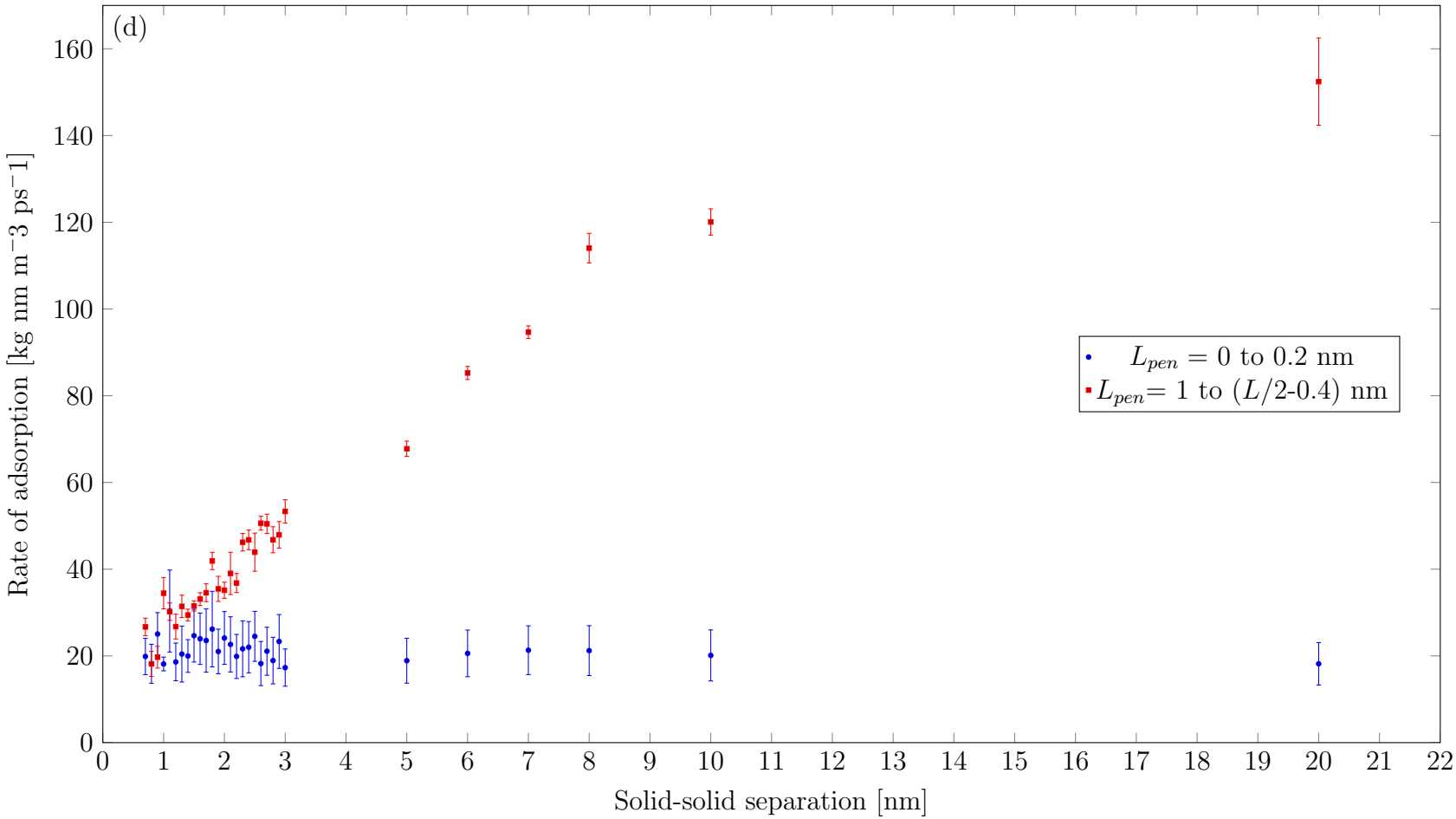


Figure C.4: Liquid water at 300 K filling various slit pores. d) Initial and secondary rates of adsorption, extracted from (c). The lengths stated in (d) are the equivalent pore penetration lengths, given that the fluid were to enter the pore in a plug fashion at the same local density as the final pore density.

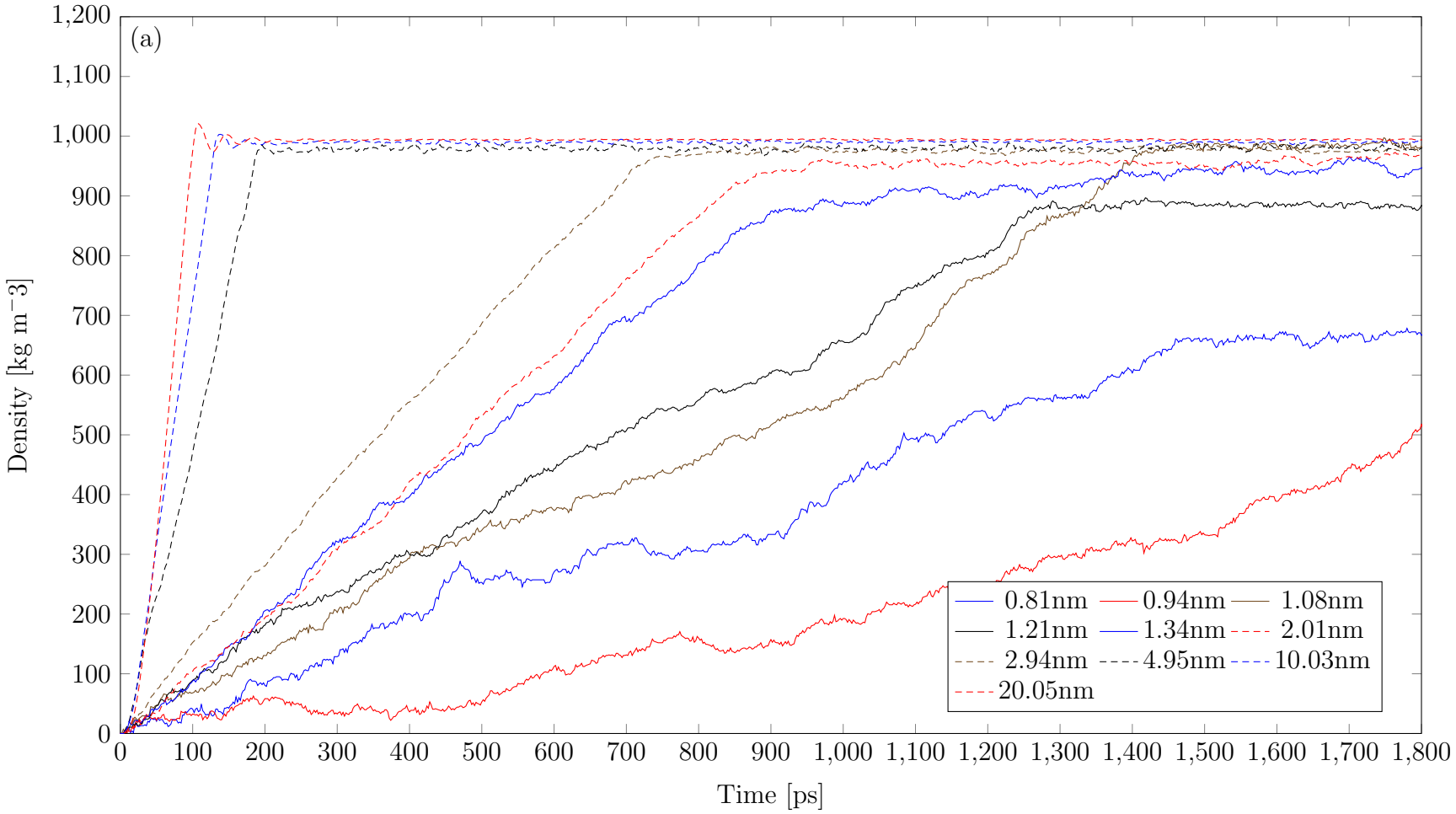


Figure C.5: Liquid water at 300 K filling various cylindrical pores. a) Pore density against time.

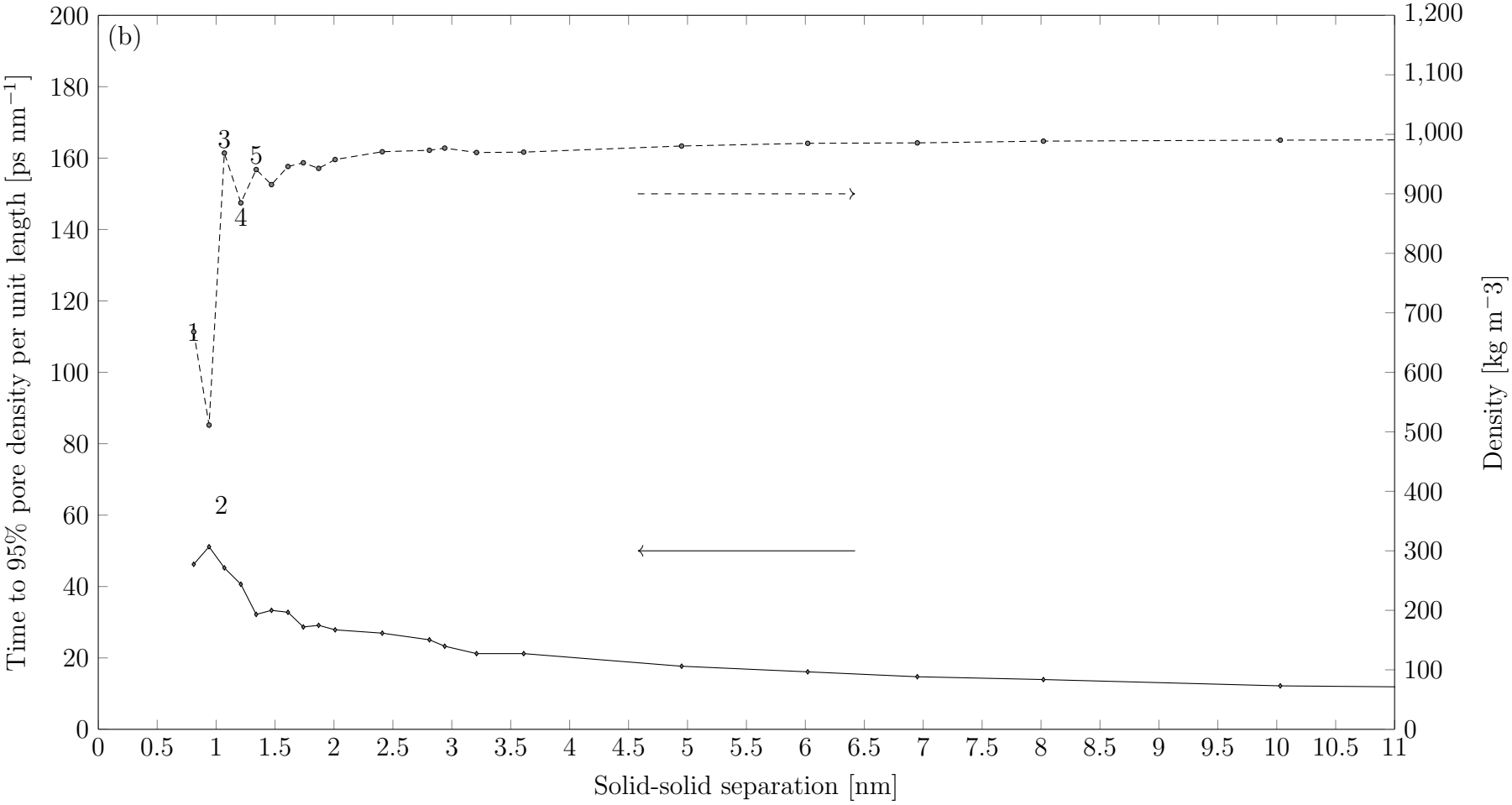


Figure C.6: Liquid water at 300 K filling various cylindrical pores. b) Comparison between pore fill time and the mean density calculated over the final 500 ps of (a). The labels correspond to the density extremes in the smallest pores. The matching pore geometries are shown in figure 4.25.

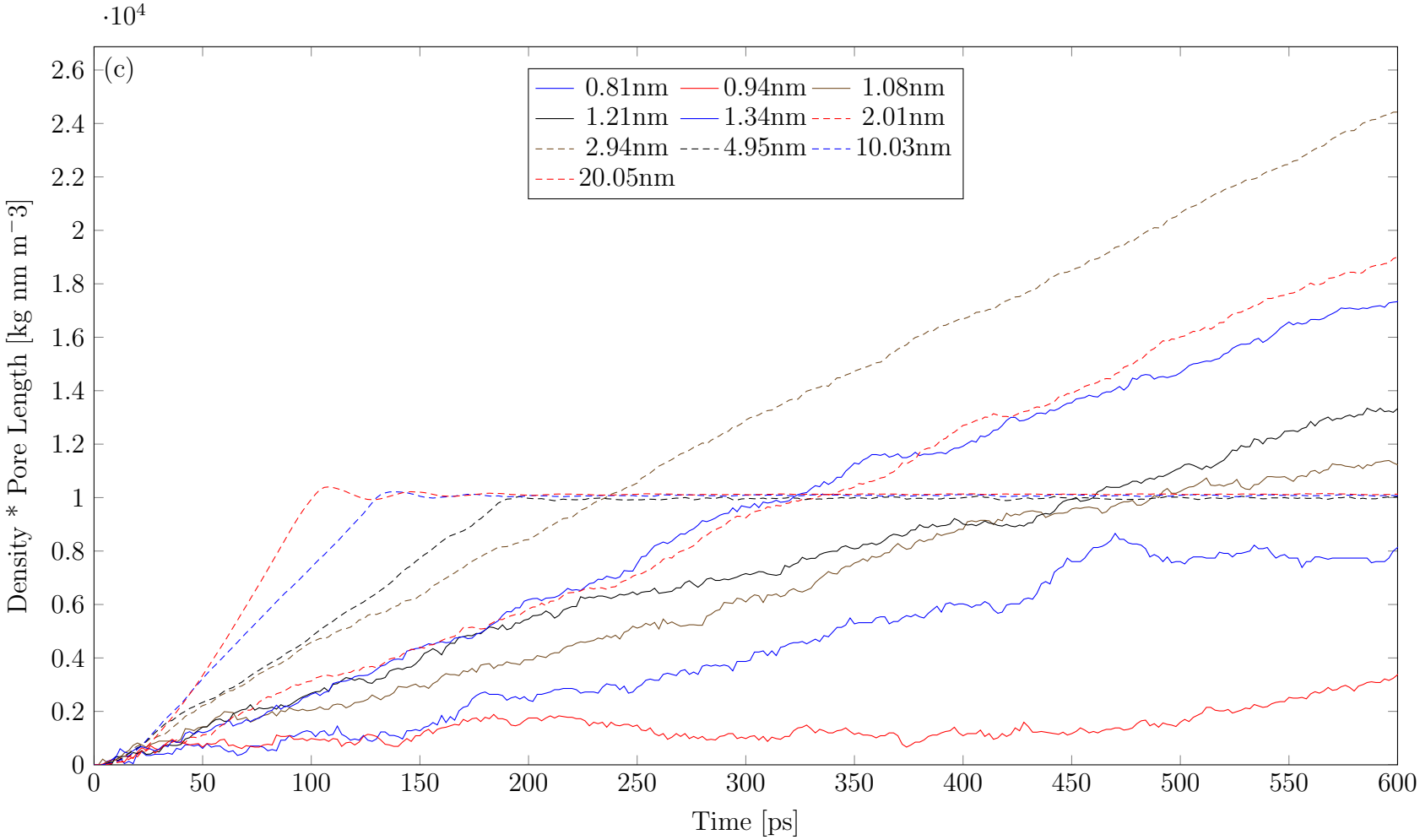


Figure C.7: Liquid water at 300 K filling various cylindrical pores. c) Pore density * pore length against time, for use in calculating initial fill rate of pore.

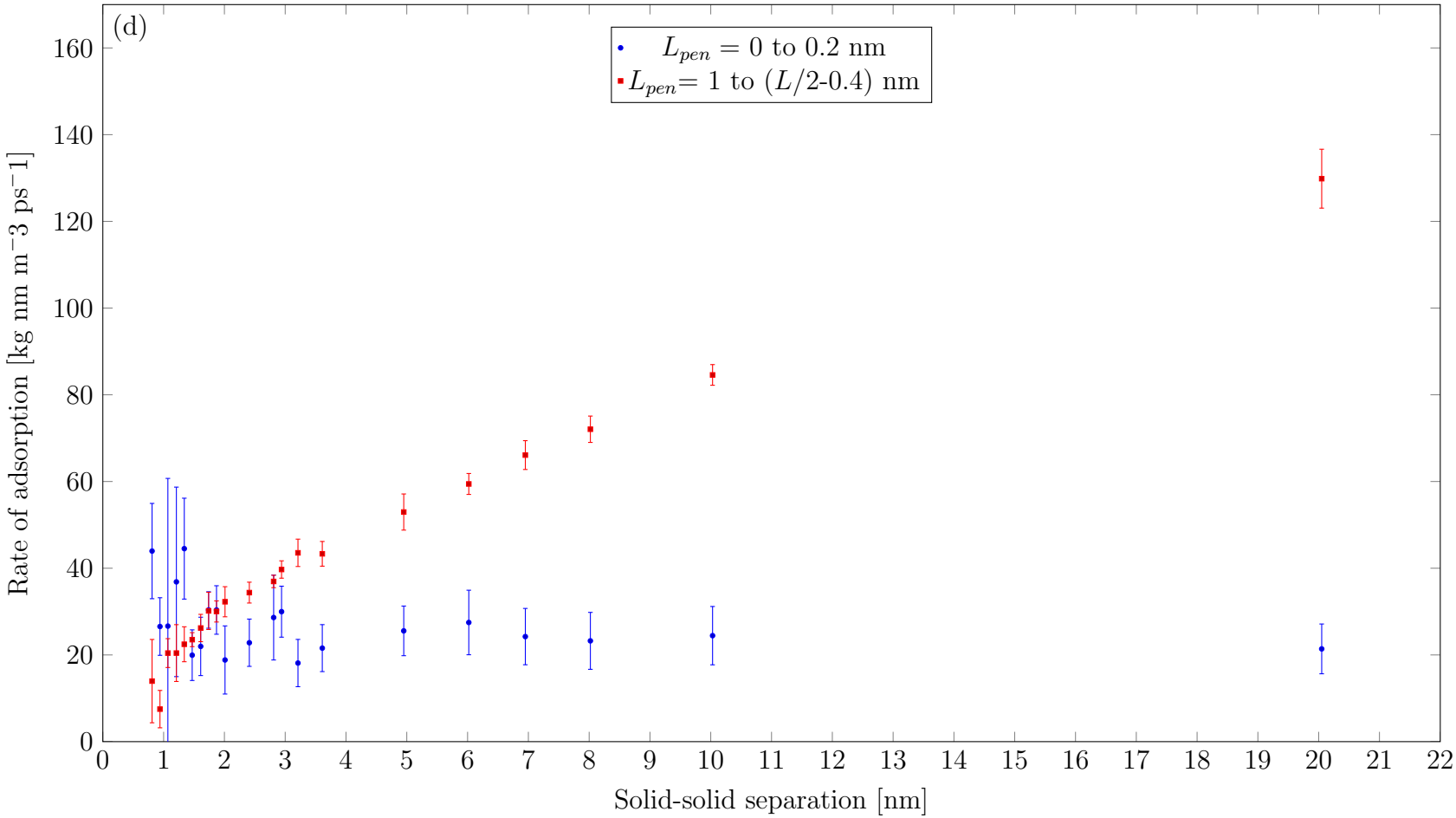


Figure C.8: Liquid water at 300 K filling various cylindrical pores. d) Initial and secondary rates of adsorption, extracted from (c). The lengths stated in (d) are the equivalent pore penetration lengths, given that the fluid were to enter the pore in a plug fashion at the same local density as the final pore density.

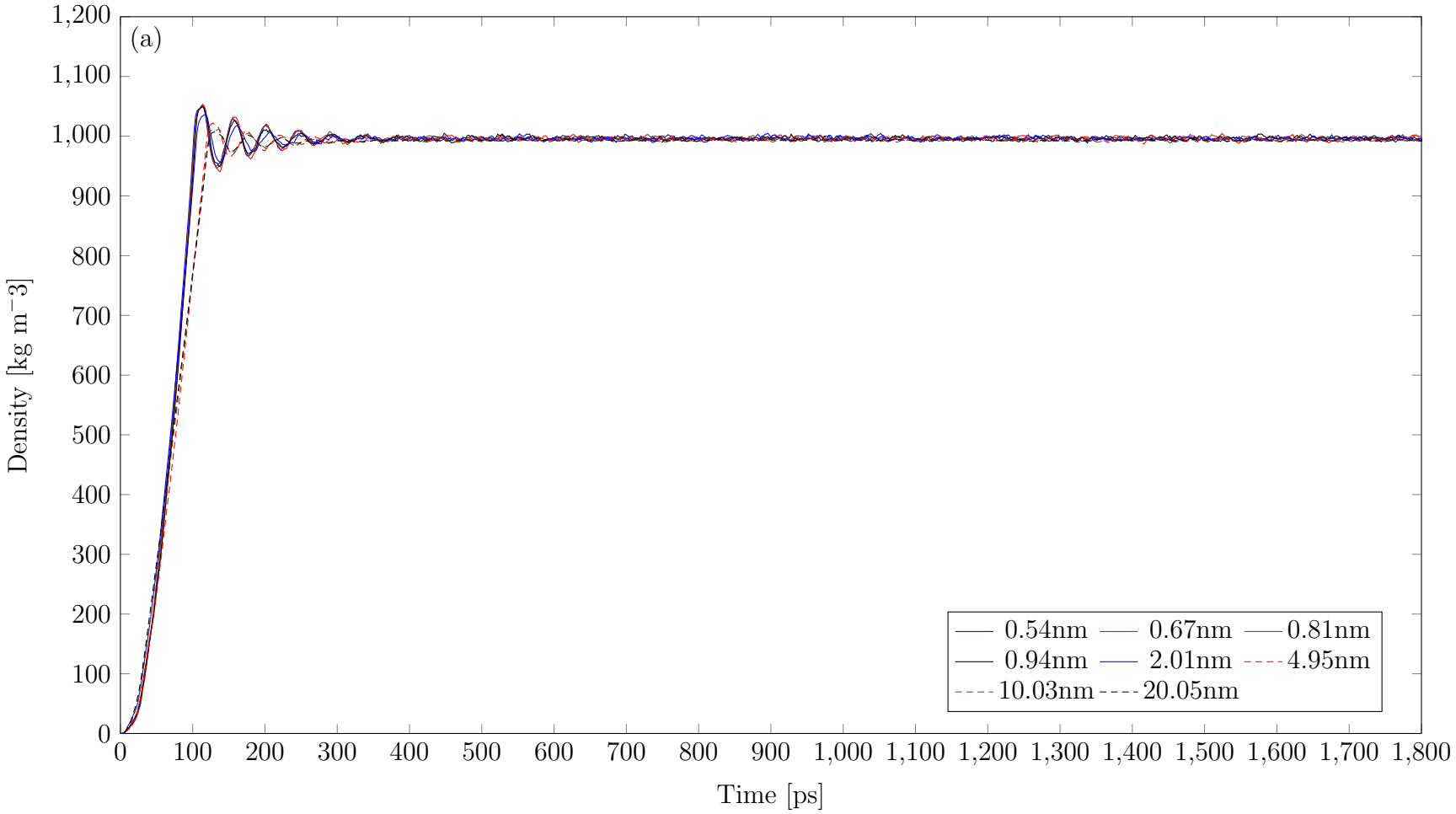


Figure C.9: Liquid water at 300 K filling the outside of various cylindrical pores. a) Pore density against time.

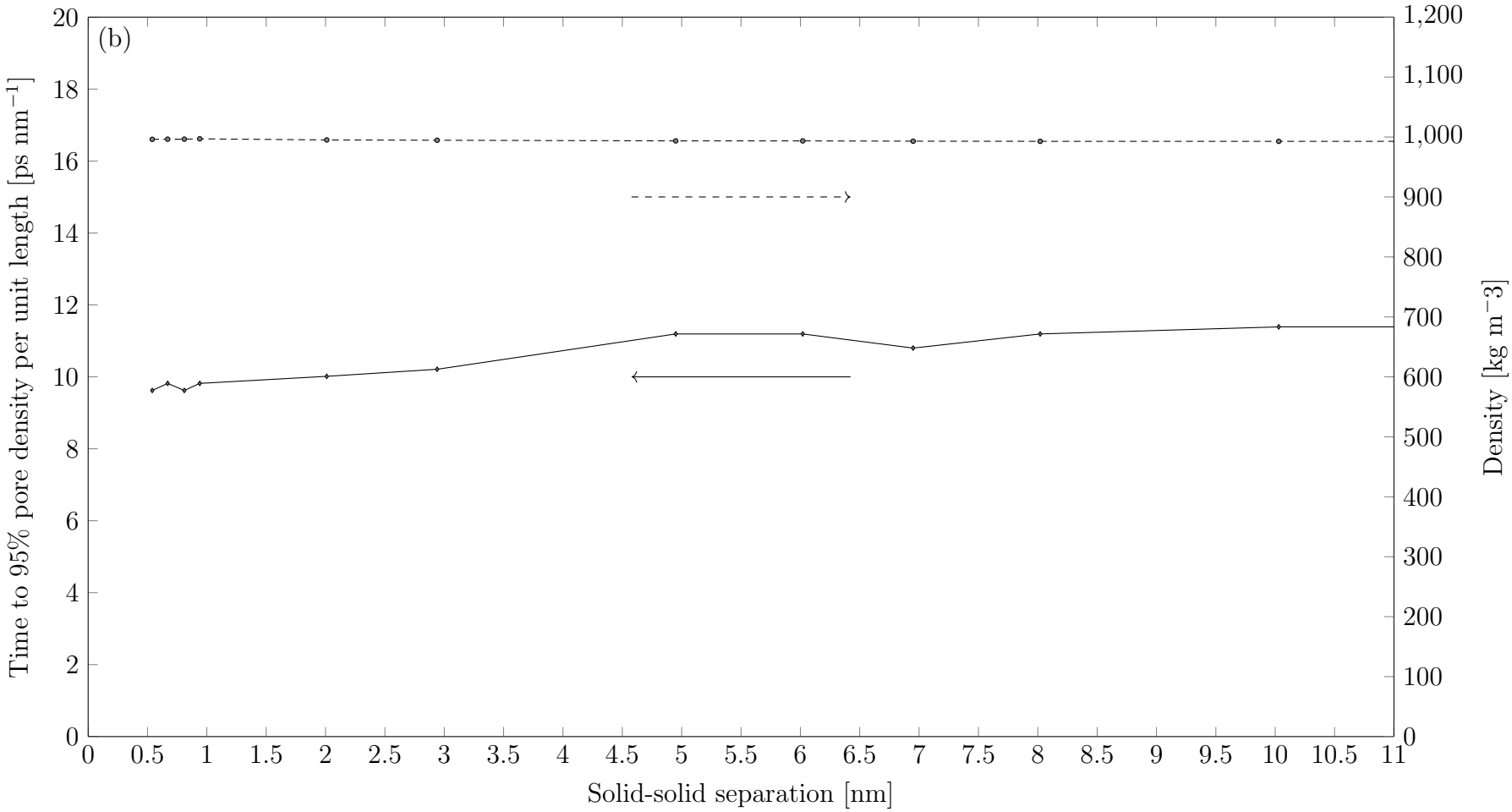


Figure C.10: Liquid water at 300 K filling the outside of various cylindrical pores. b) Comparison between pore fill time and the mean density calculated over the final 500 ps of (a). The labels correspond to the density extremes in the smallest pores. The matching pore geometries are shown in figure 4.25.

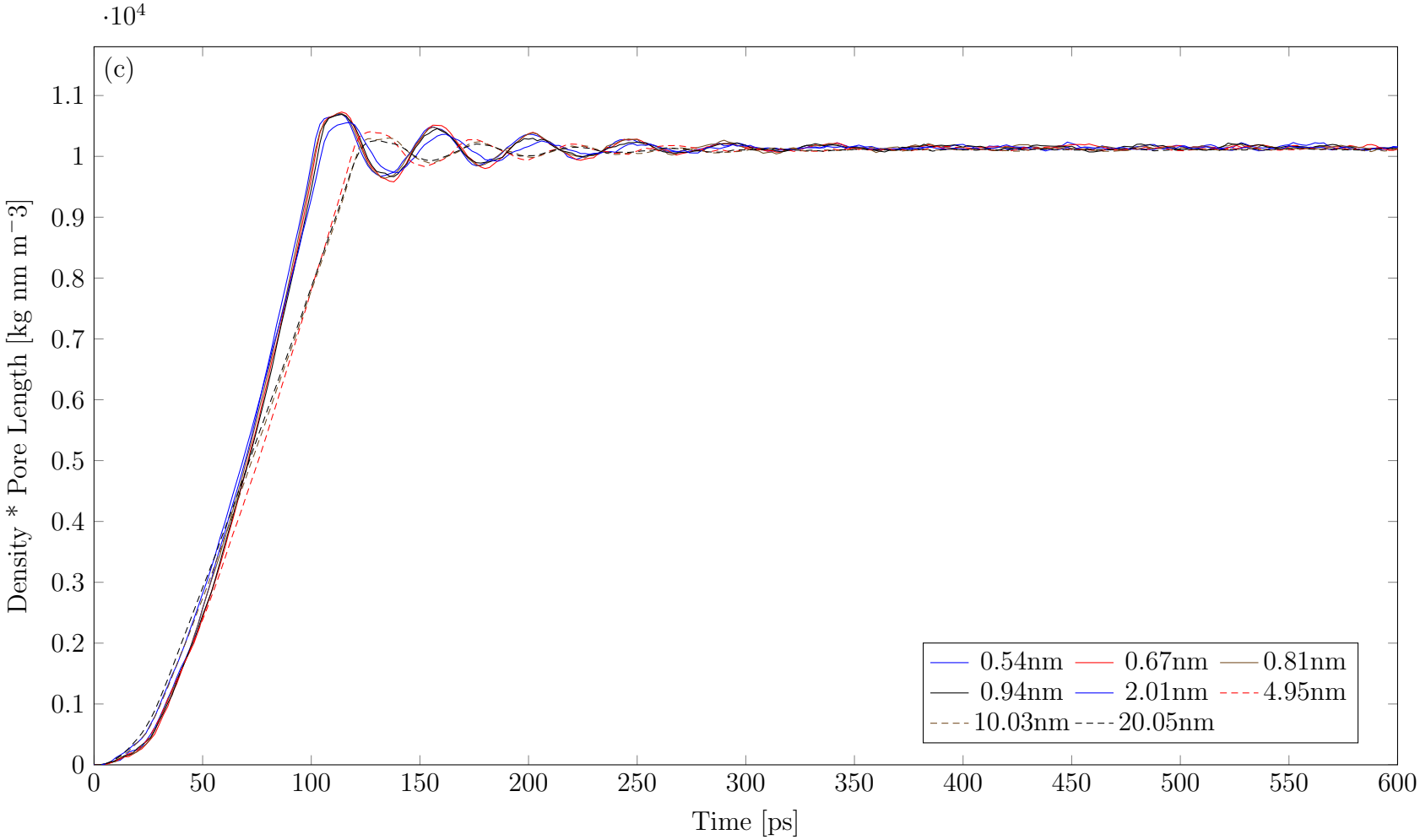


Figure C.11: Liquid water at 300 K filling the outside of various cylindrical pores. c) Pore density * pore length against time, for use in calculating initial fill rate of pore.

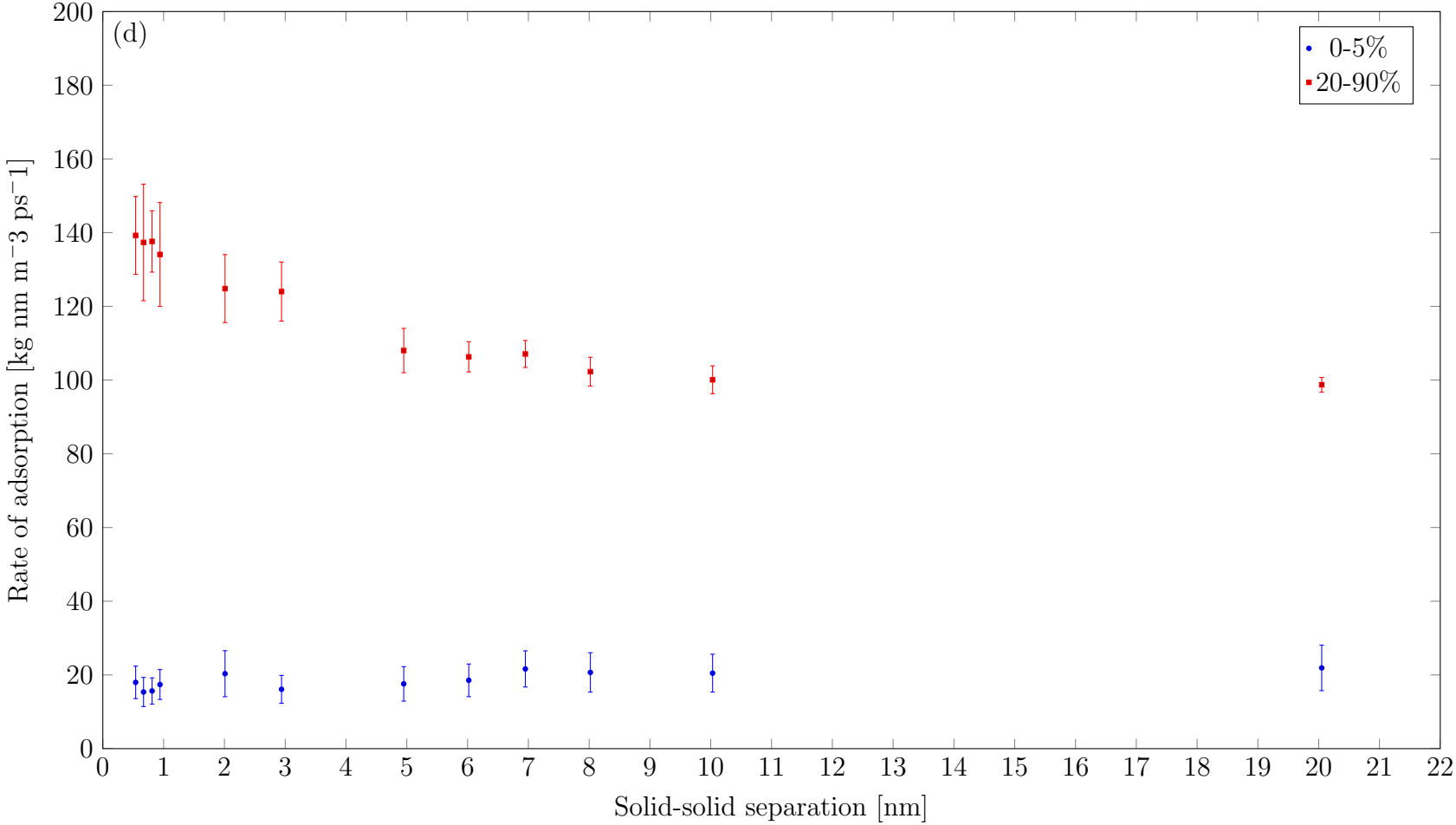


Figure C.12: Liquid water at 300 K filling the outside of various cylindrical pores. d) Initial and secondary rates of adsorption, extracted from (c). The lengths stated in (d) are the equivalent pore penetration lengths, given that the fluid were to enter the pore in a plug fashion at the same local density as the final pore density.

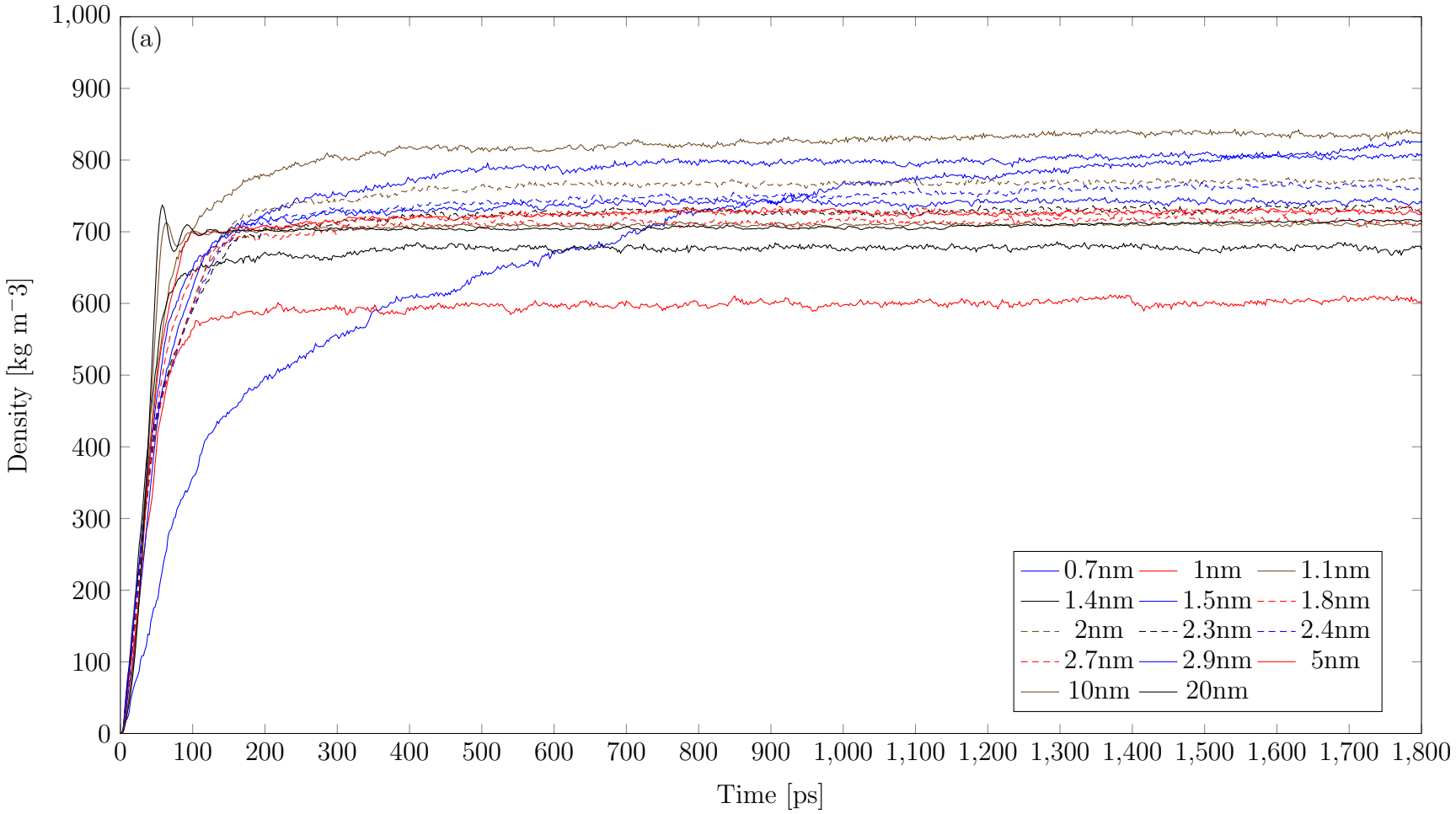


Figure C.13: Liquid n-heptane at 300 K filling various slit pores. a) Pore density against time.

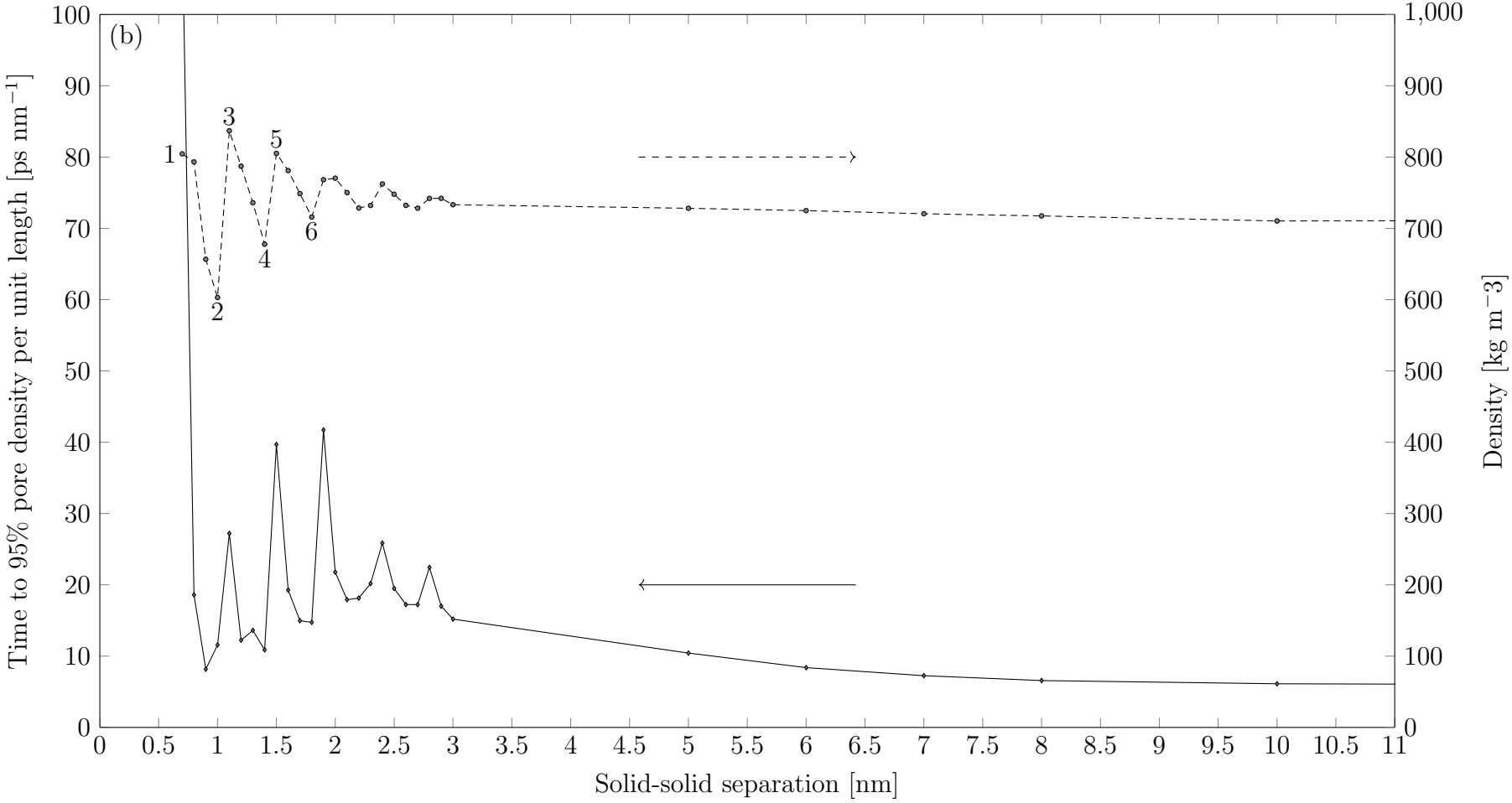


Figure C.14: Liquid n-heptane at 300 K filling various slit pores. b) Comparison between pore fill time and the mean density calculated over the final 500 ps of (a). The labels correspond to the density extremes in the smallest pores. The matching pore geometries are shown in figure 4.45.

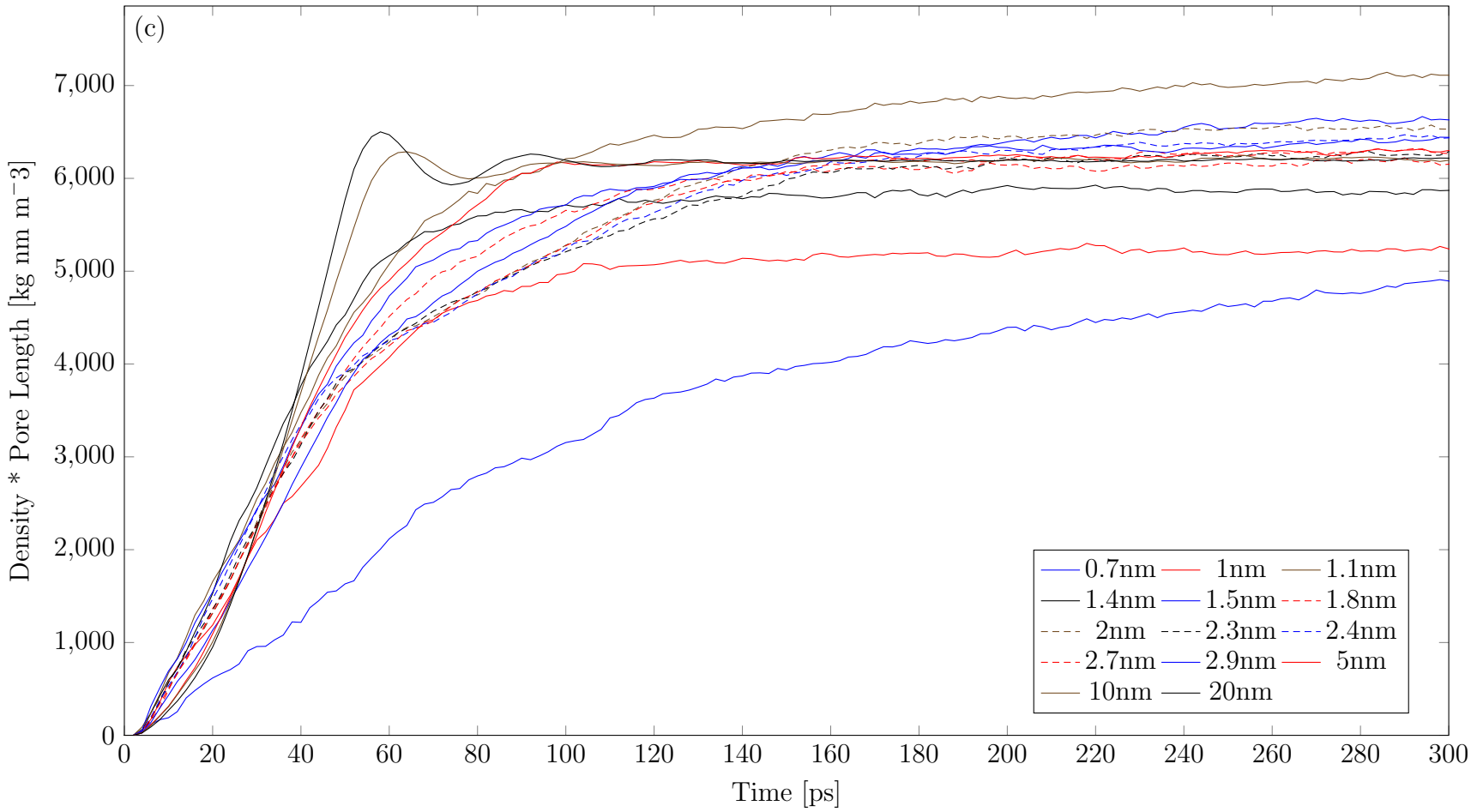


Figure C.15: Liquid n-heptane at 300 K filling various slit pores. c) Pore density * pore length against time, for use in calculating initial fill rate of pore.

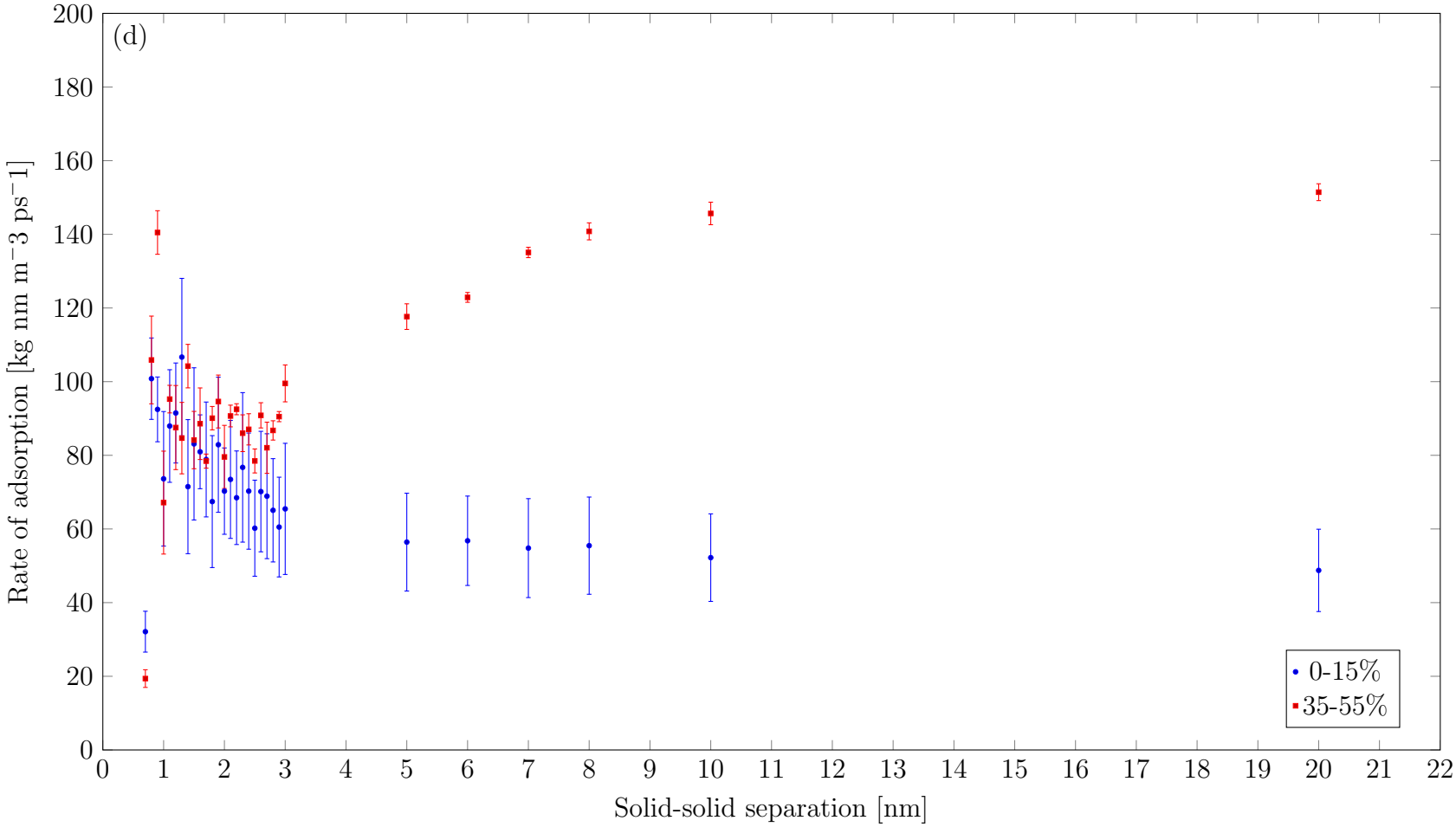


Figure C.16: Liquid n-heptane at 300 K filling various slit pores. d) Initial and secondary rates of adsorption, extracted from (c). The percentage ranges in (d) are of the final maximum fluid density in the pore.

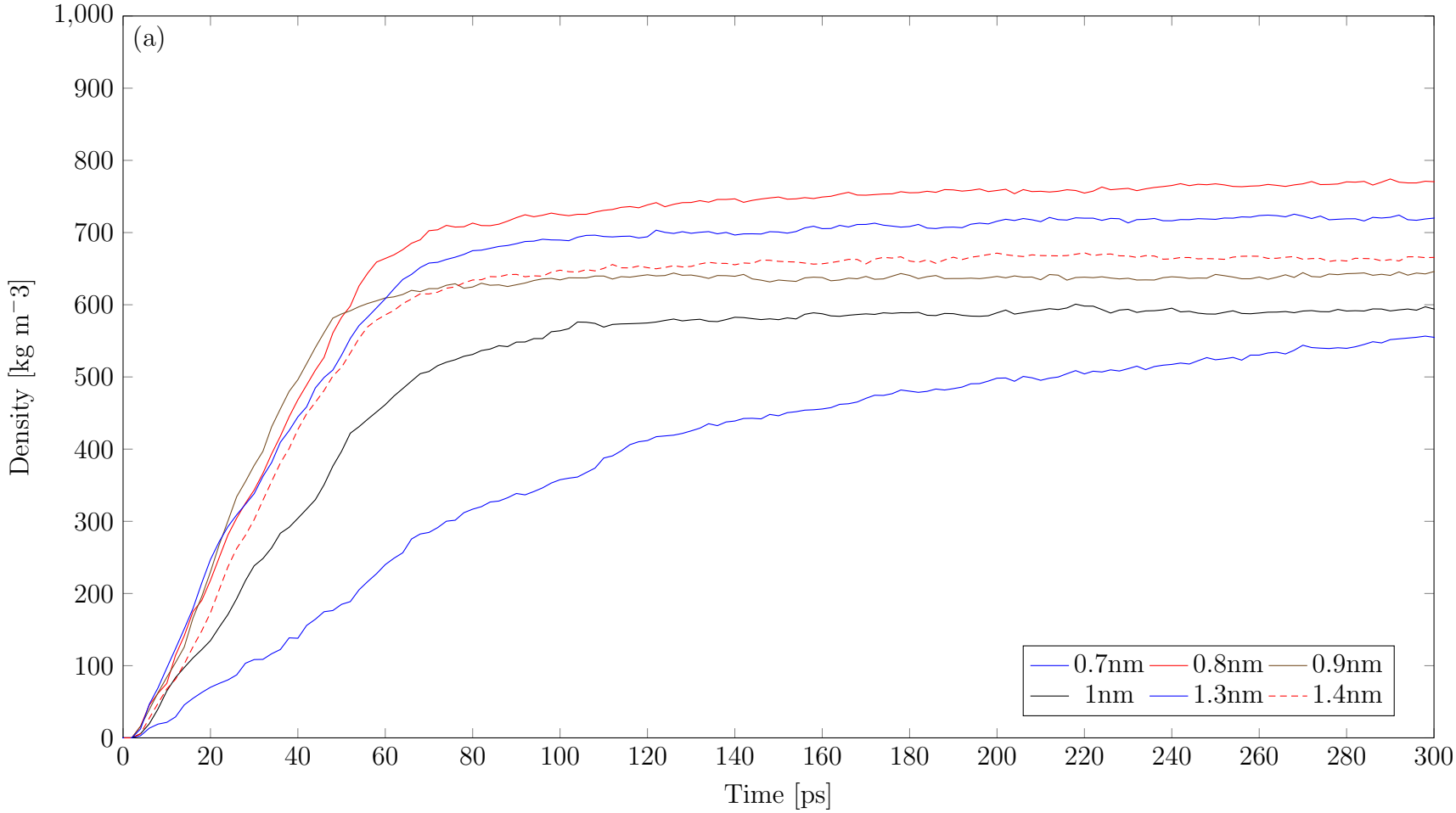


Figure C.17: As in figure C.13 (a), separated into groups, based on the shape of the data.

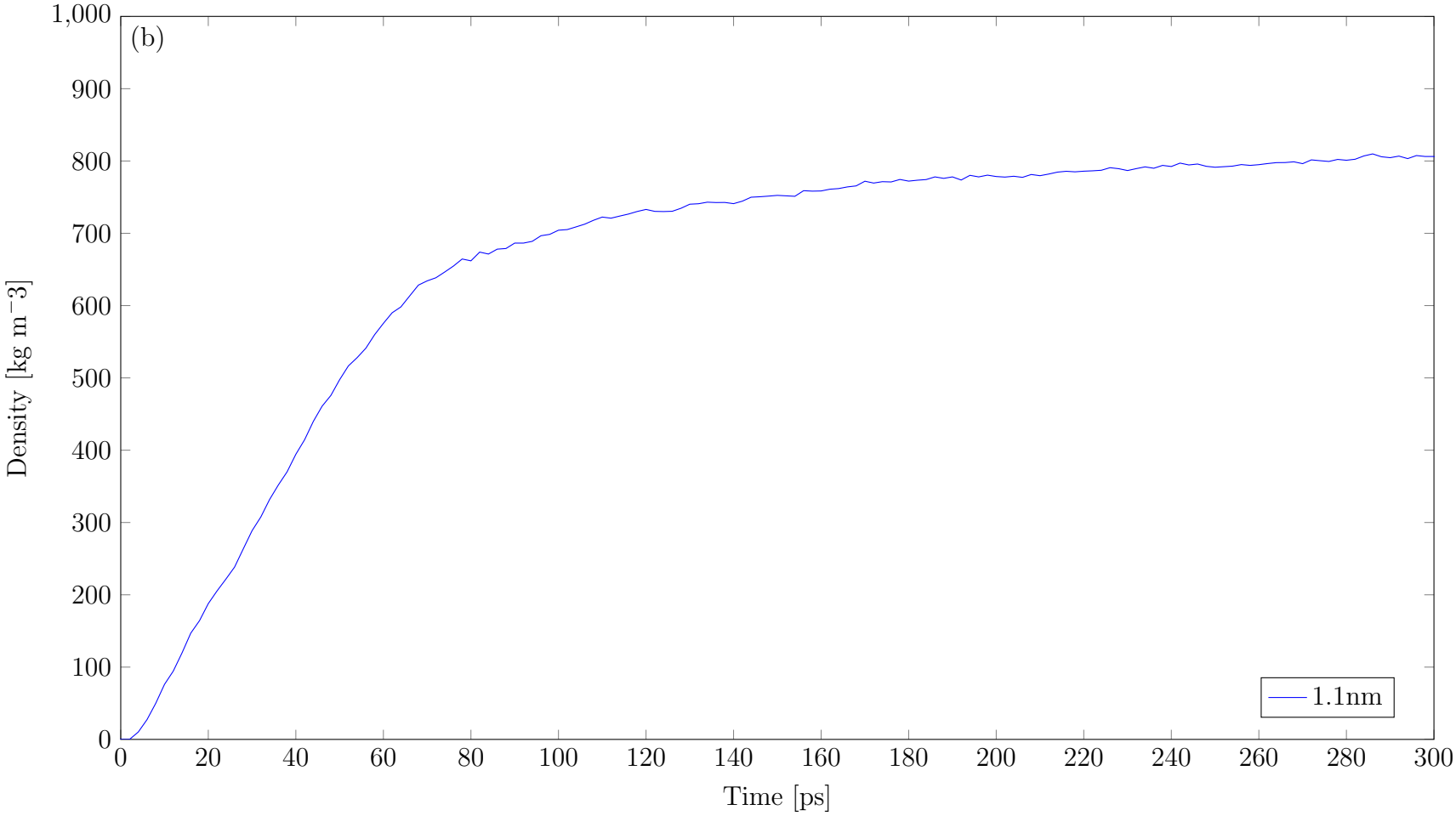


Figure C.18: As in figure C.13 (a), separated into groups, based on the shape of the data.

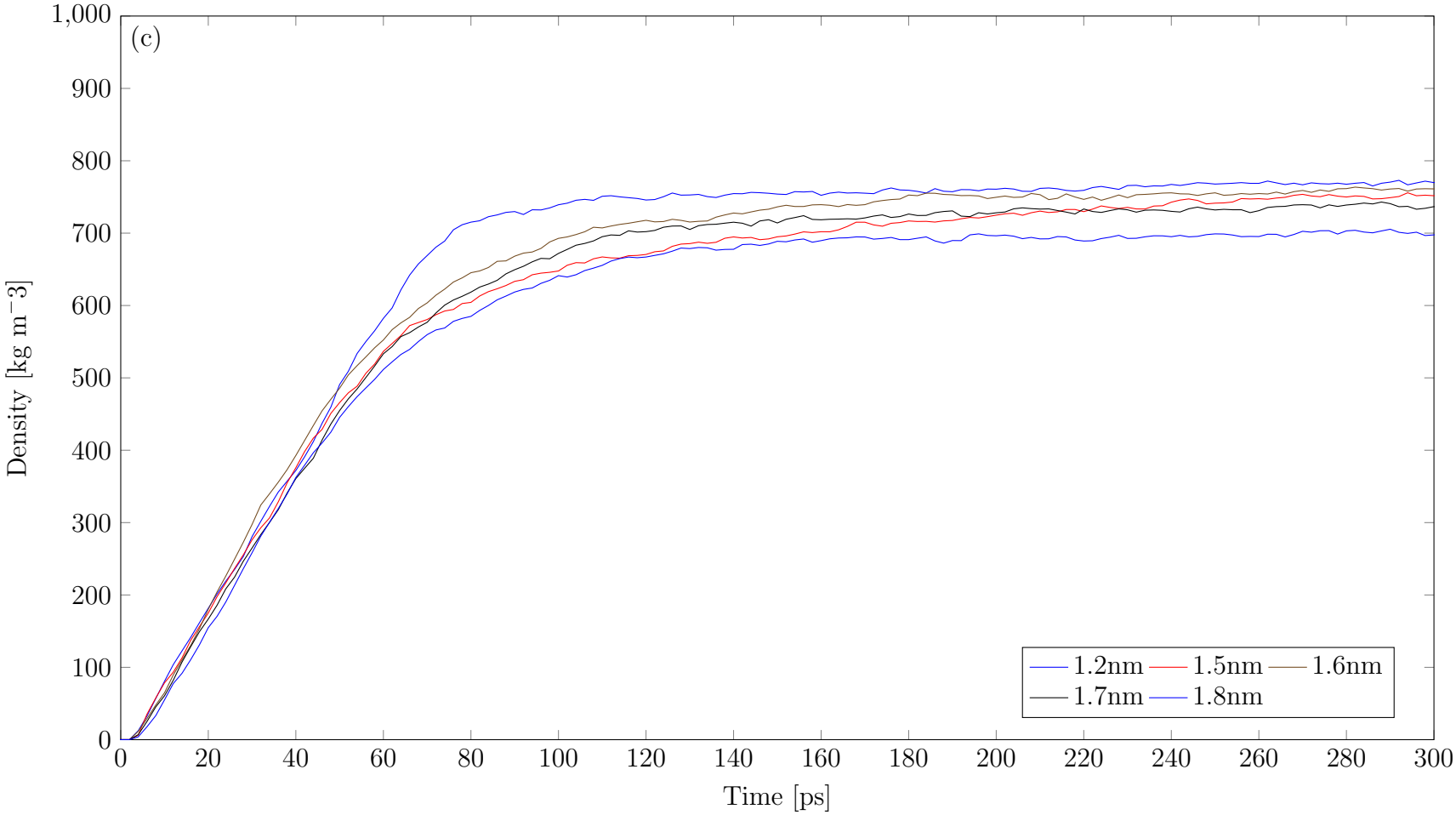


Figure C.19: As in figure C.13 (a), separated into groups, based on the shape of the data.

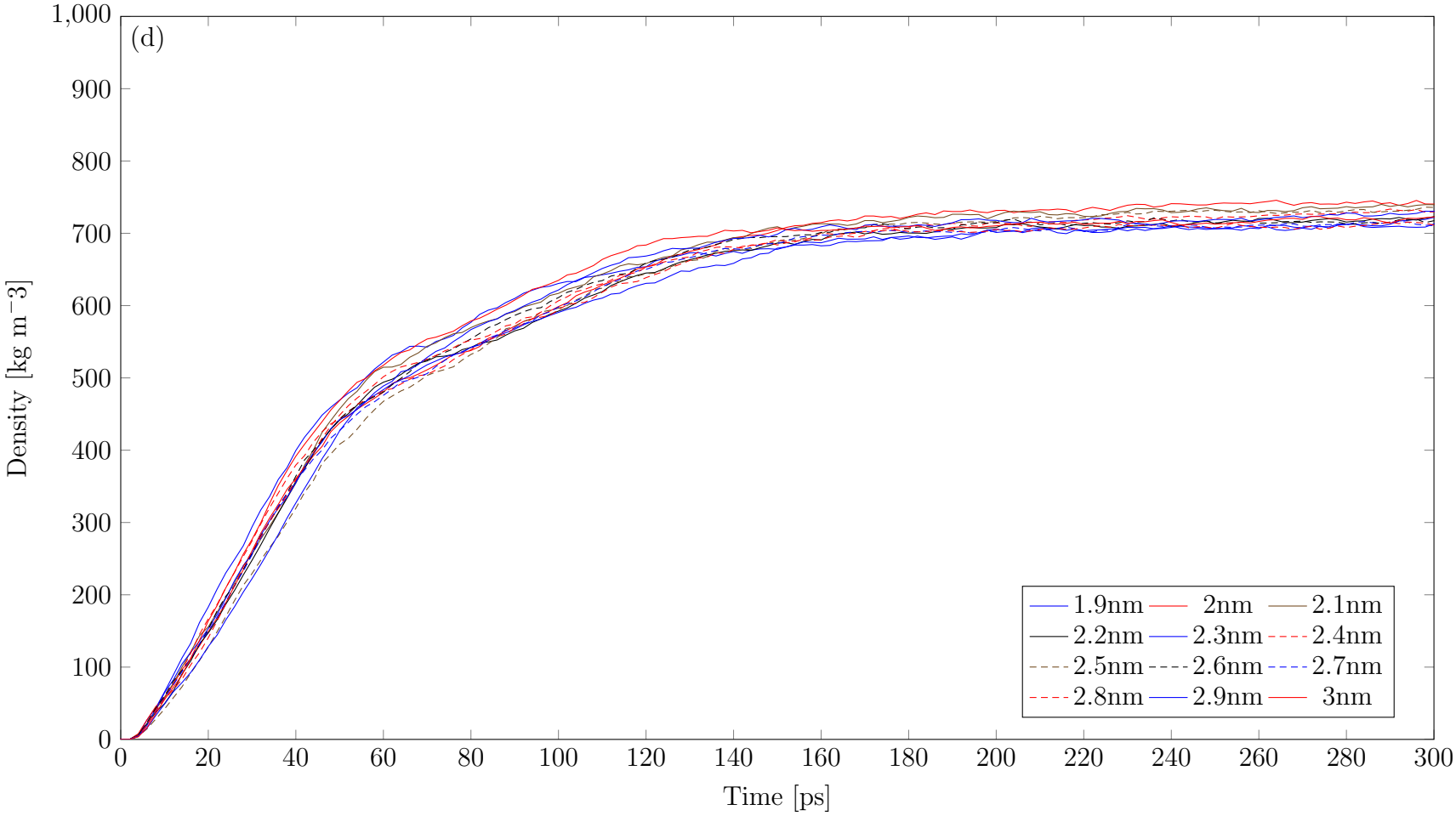


Figure C.20: As in figure C.13 (a), separated into groups, based on the shape of the data.

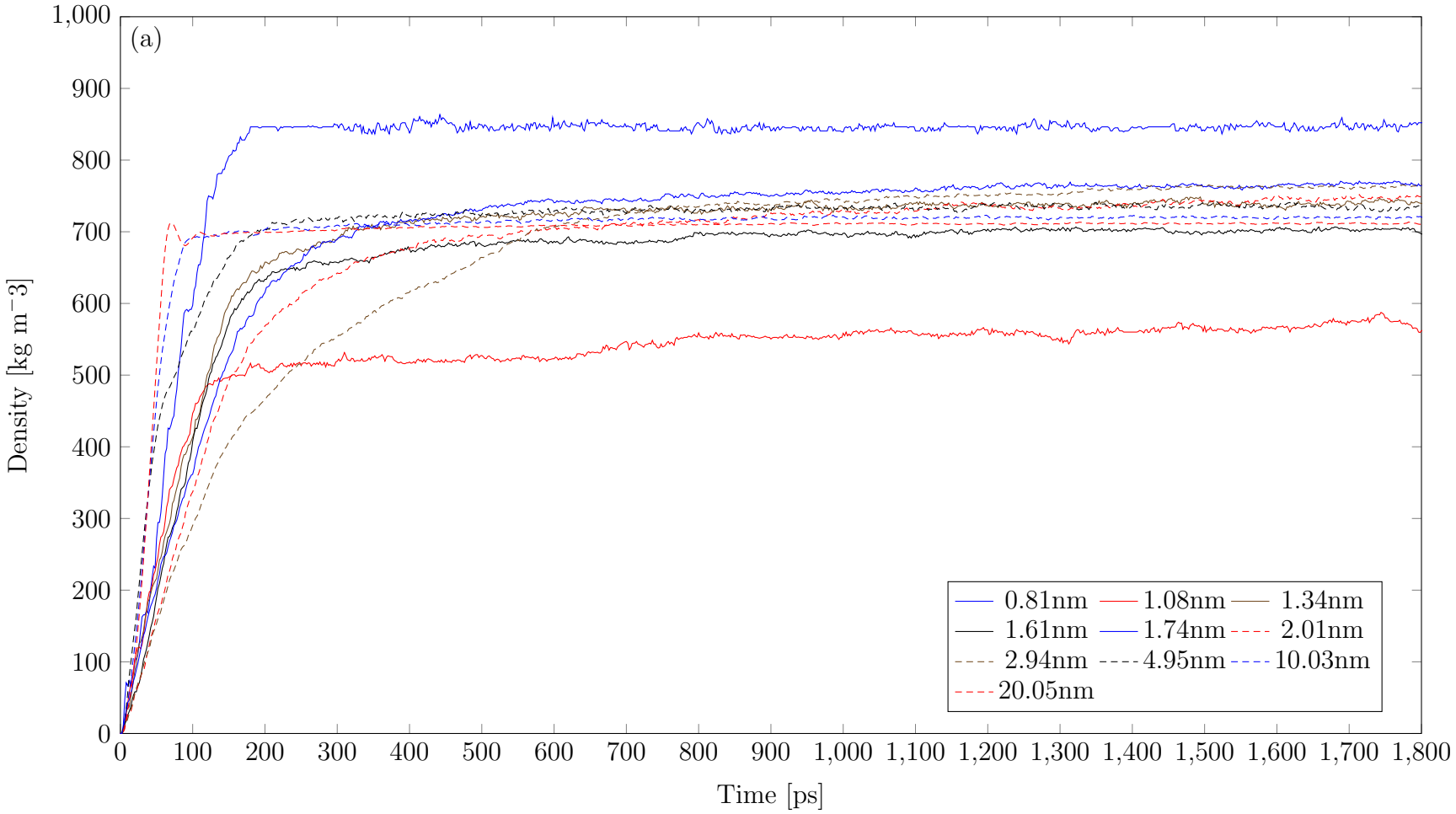


Figure C.21: Liquid n-heptane at 300 K filling various cylindrical pores. a) Pore density against time.

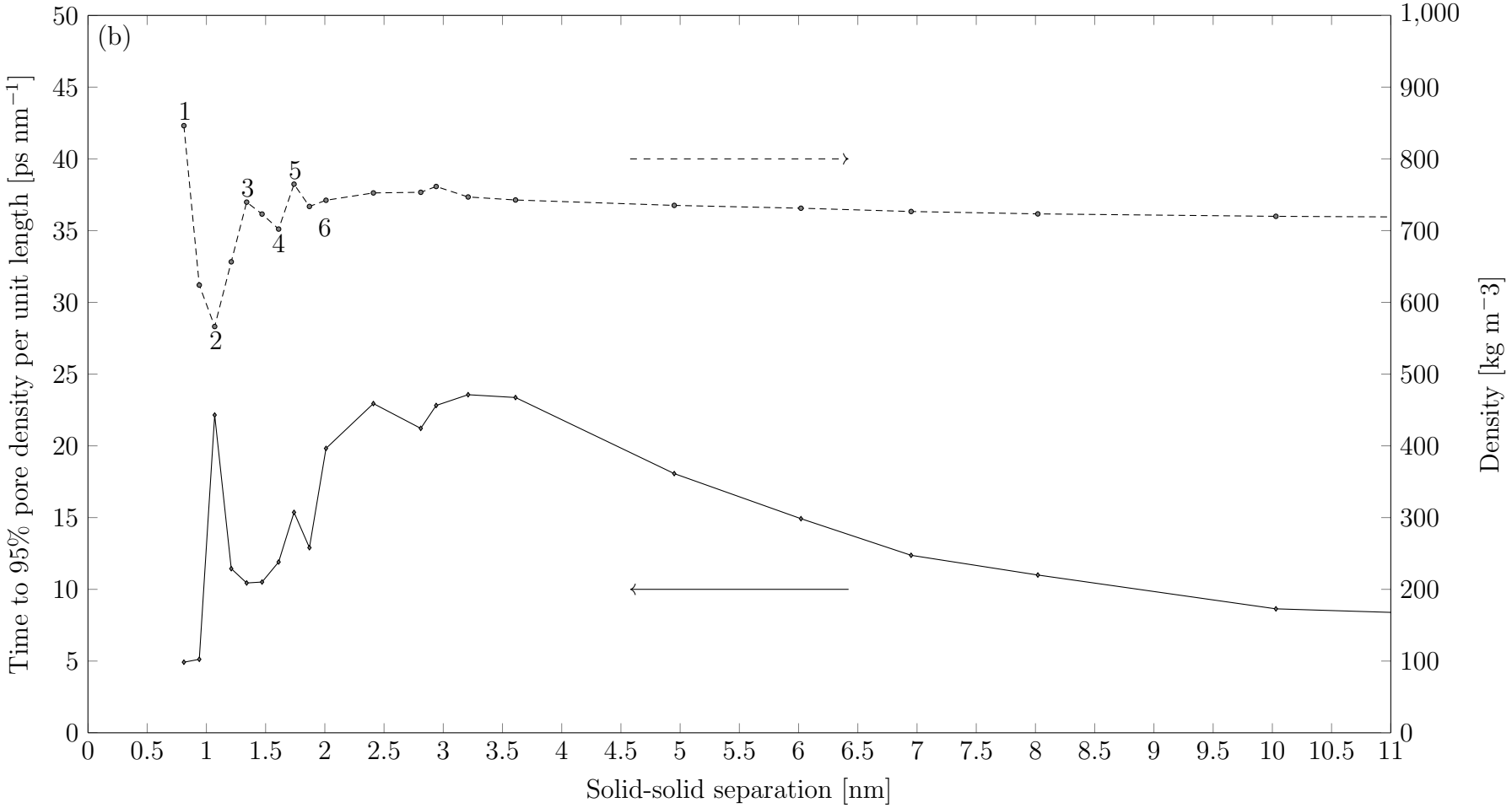


Figure C.22: Liquid n-heptane at 300 K filling various cylindrical pores. b) Comparison between pore fill time and the mean density calculated over the final 500 ps of (a). The labels correspond to the density extremes in the smallest pores. The matching pore geometries are shown in figure 4.45.

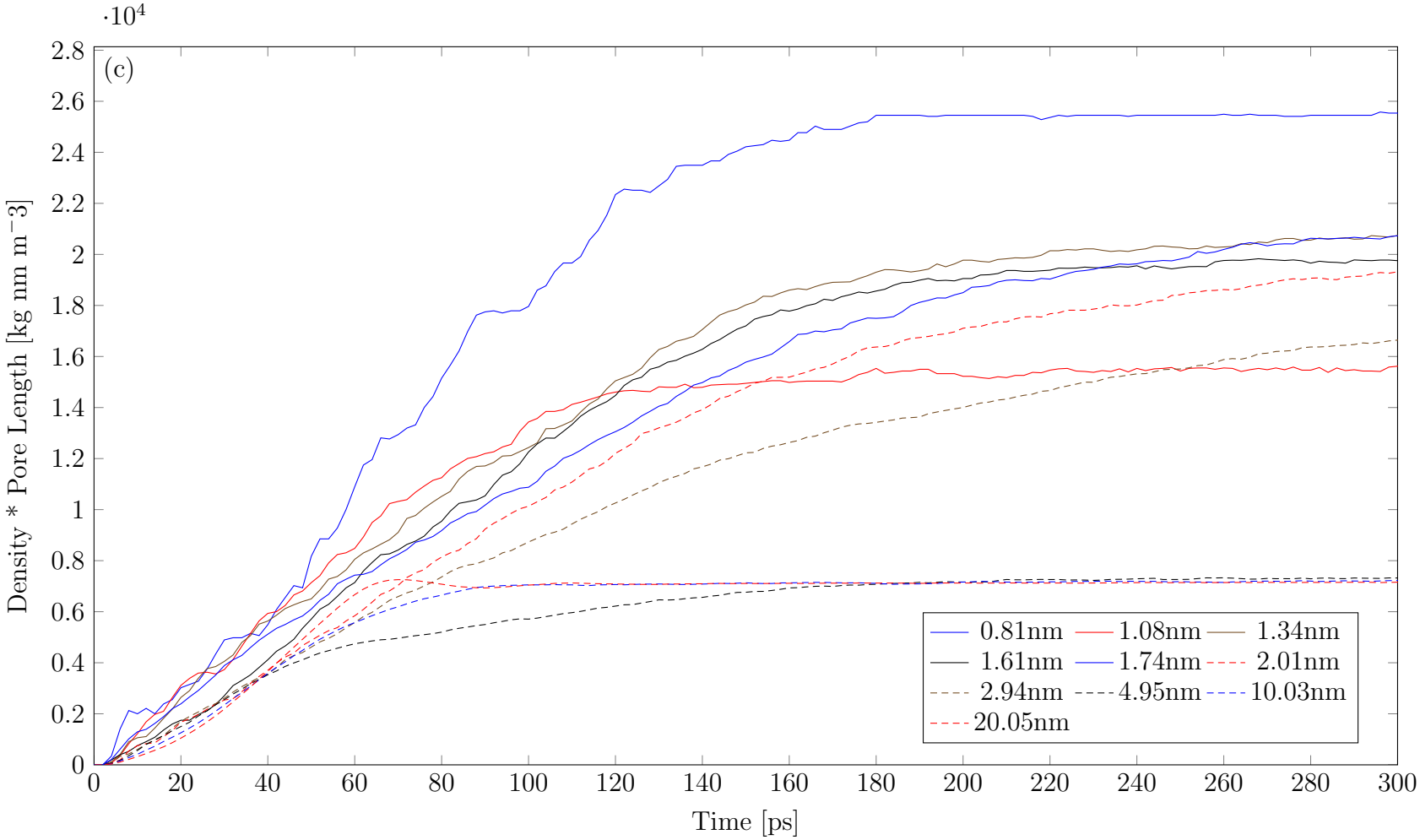


Figure C.23: Liquid n-heptane at 300 K filling various cylindrical pores. c) Pore density * pore length against time, for use in calculating initial fill rate of pore.

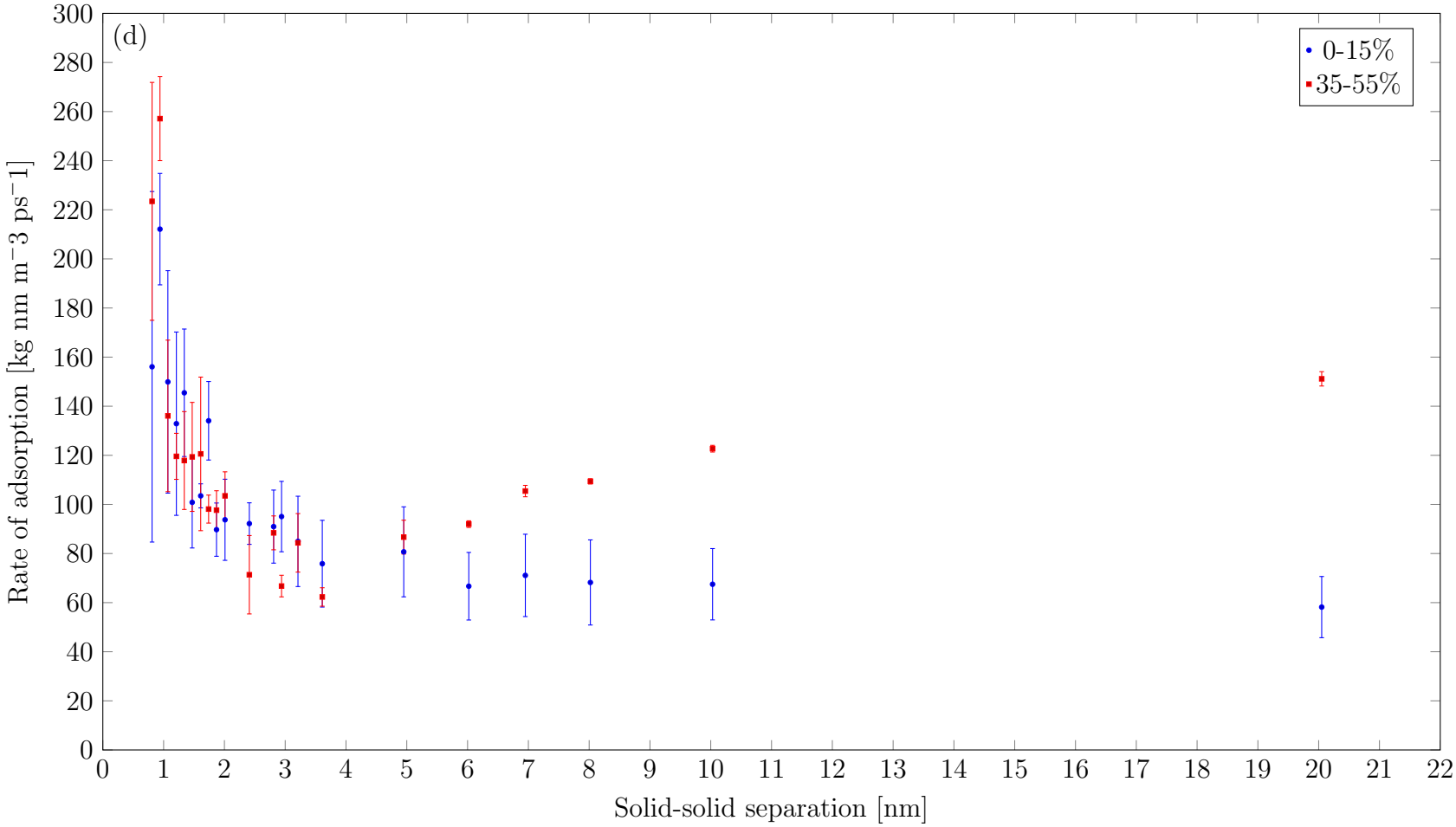


Figure C.24: Liquid n-heptane at 300 K filling various cylindrical pores. d) Initial and secondary rates of adsorption, extracted from (c). The percentage ranges in (d) are of the final maximum fluid density in the pore.

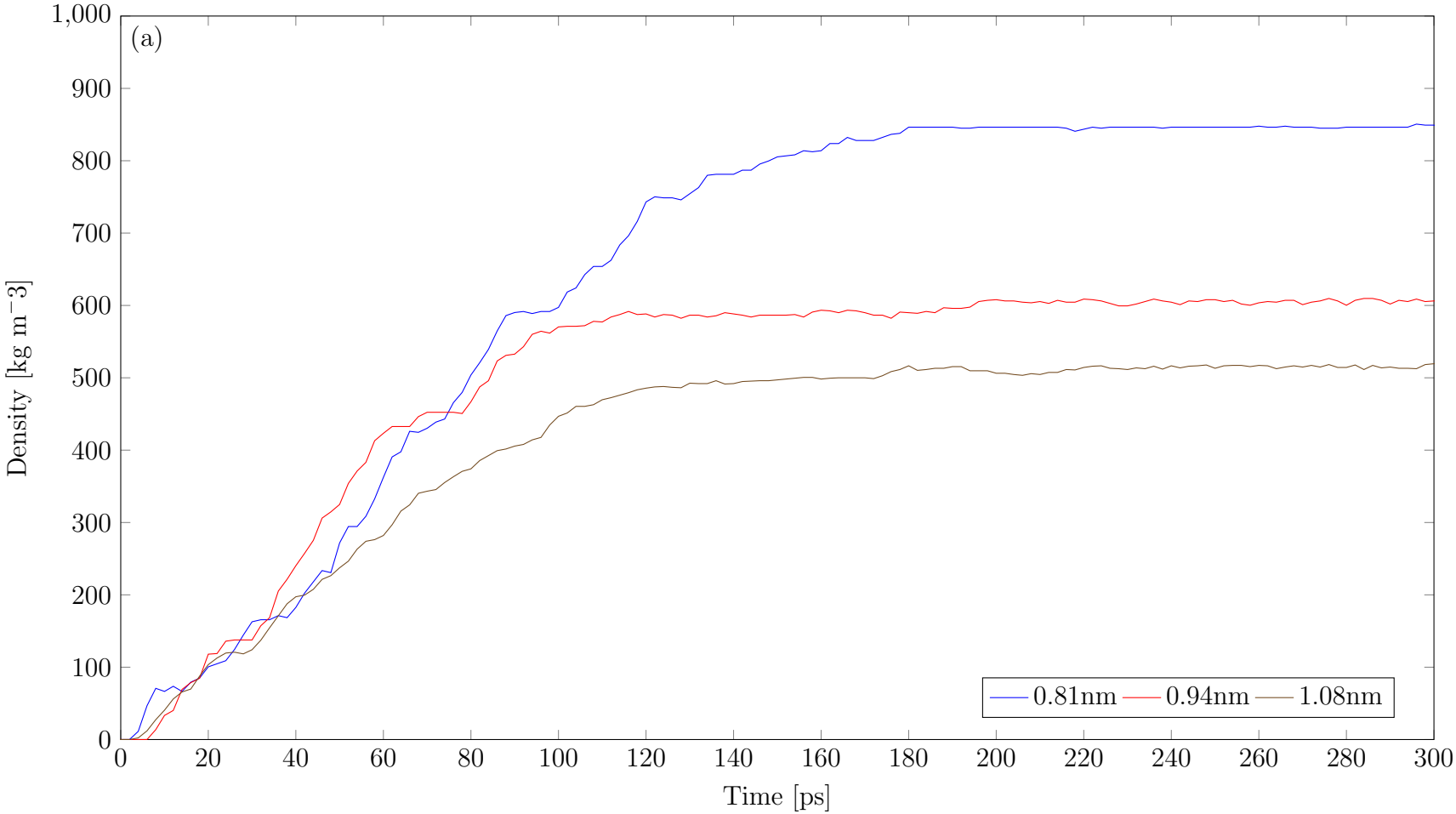


Figure C.25: As in figure C.21 (a), separated into groups, based on the shape of the data.

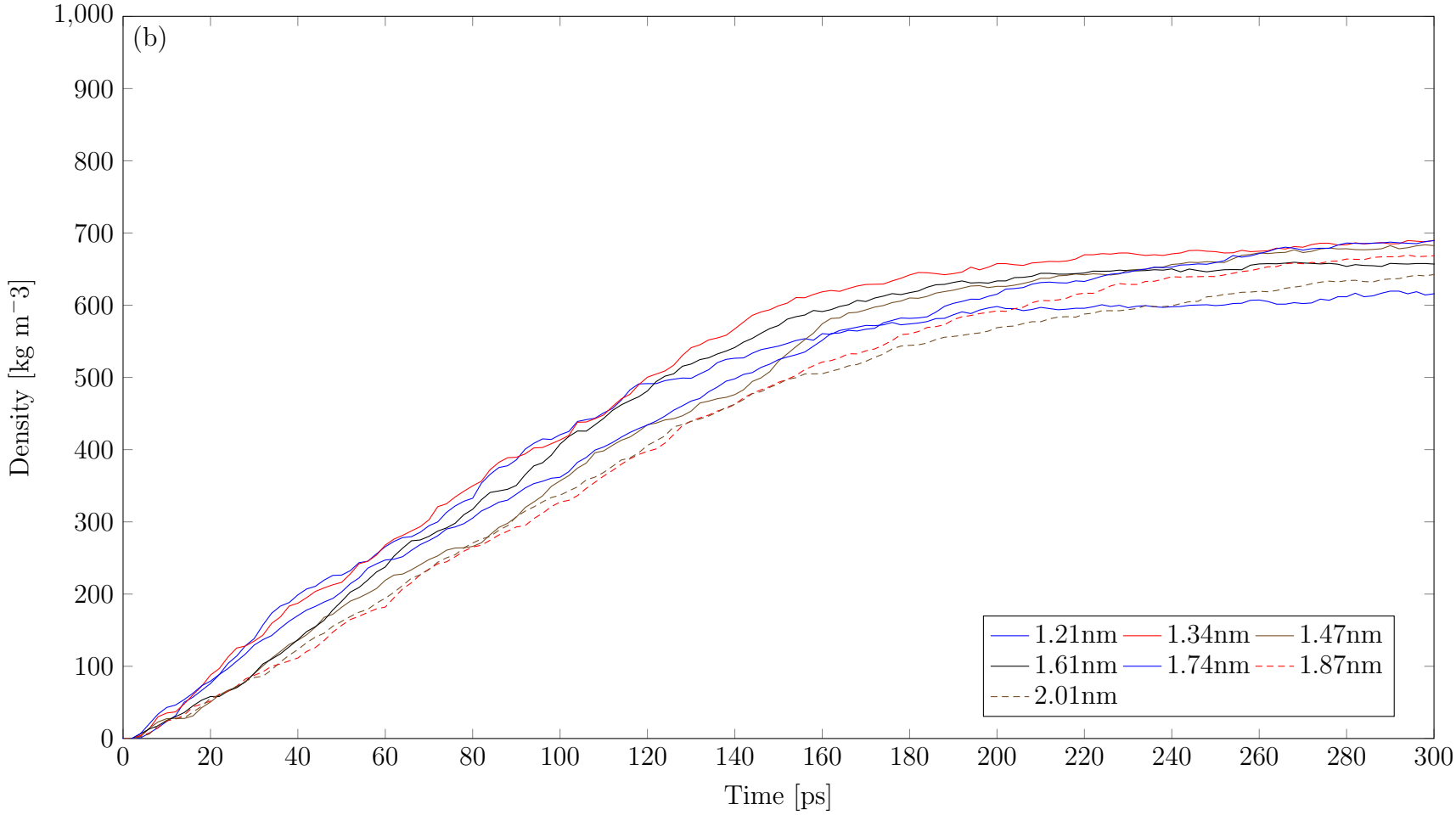


Figure C.26: As in figure C.21 (a), separated into groups, based on the shape of the data.

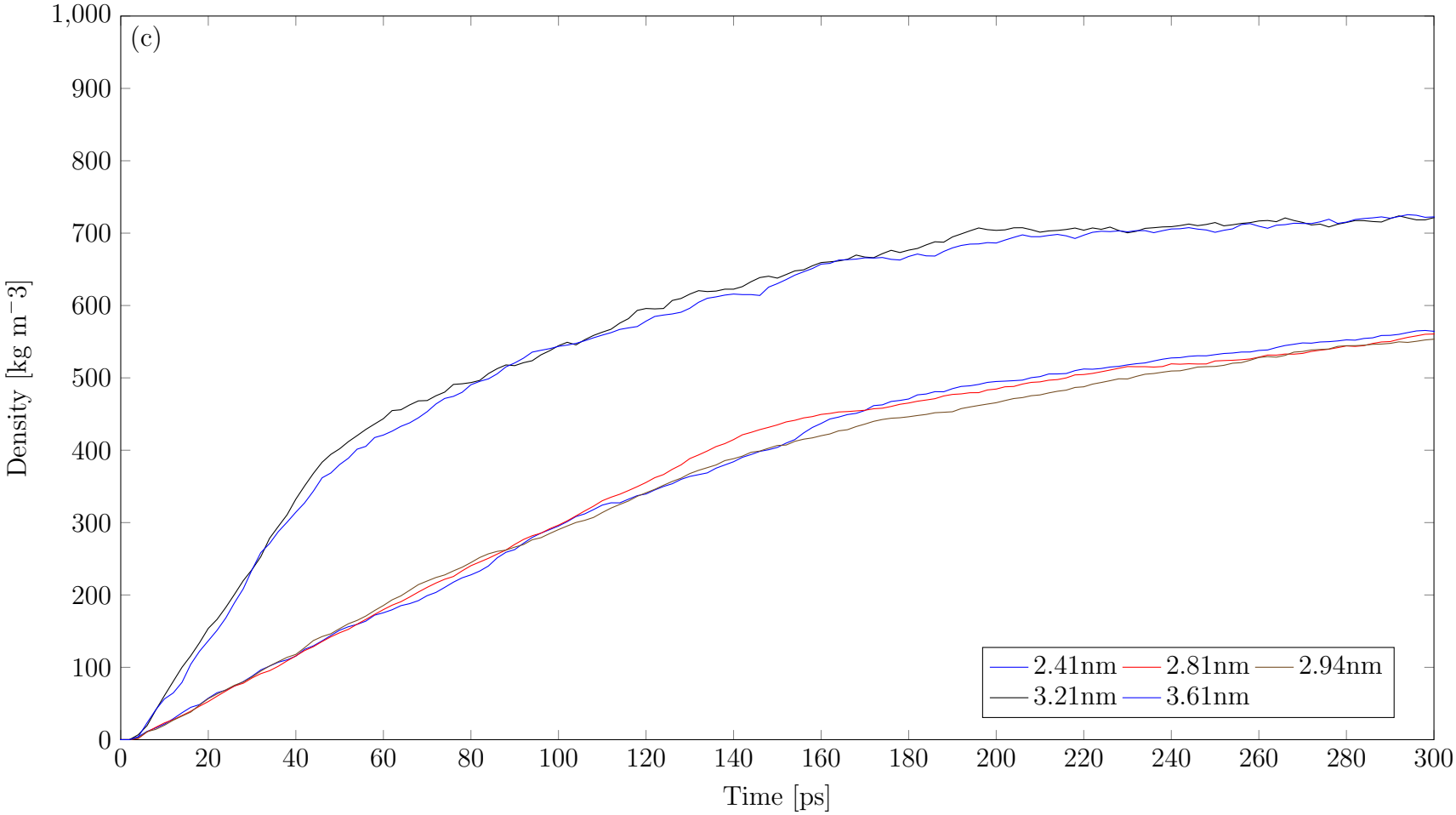


Figure C.27: As in figure C.21 (a), separated into groups, based on the shape of the data.

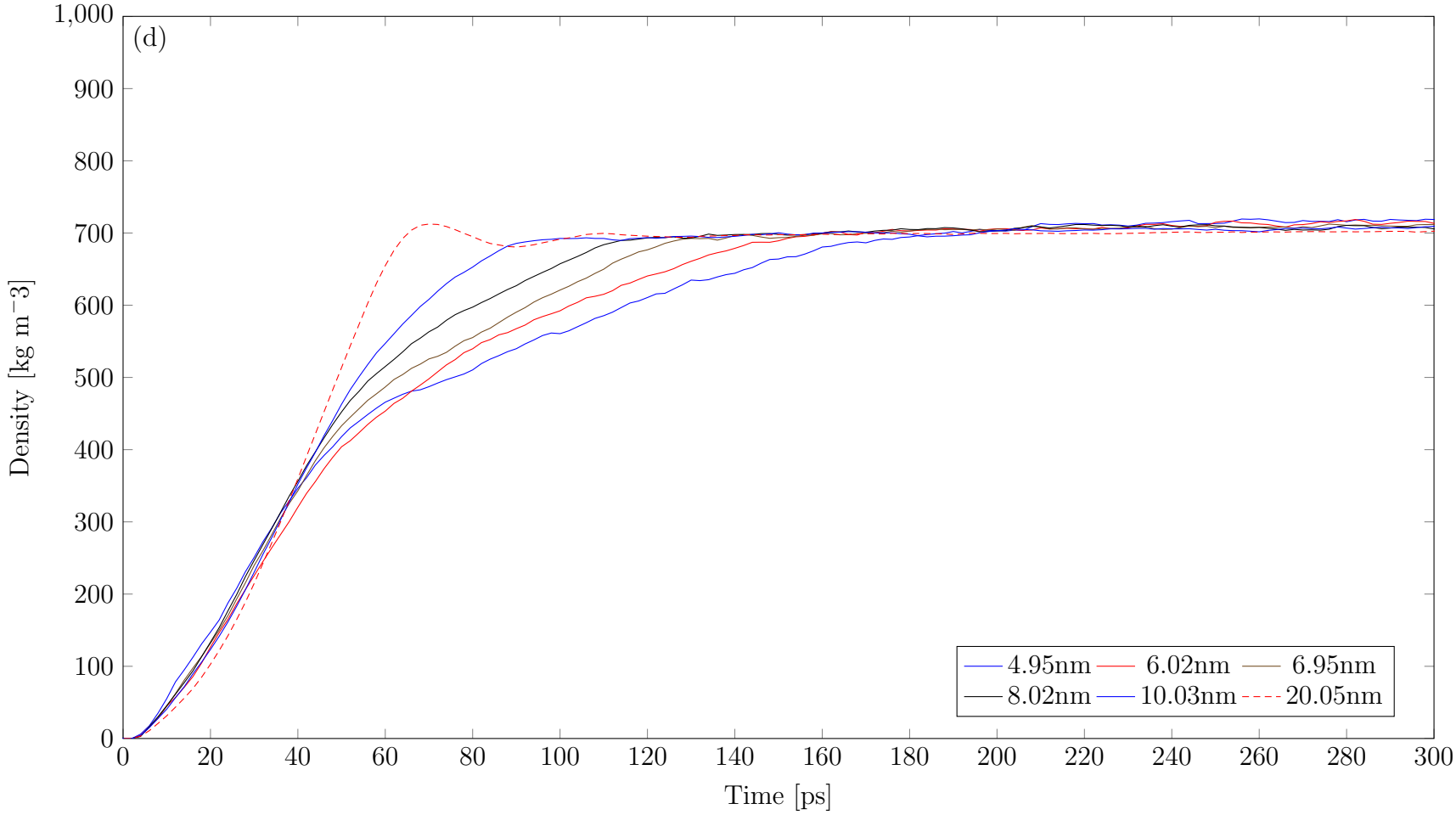


Figure C.28: As in figure C.21 (a), separated into groups, based on the shape of the data.

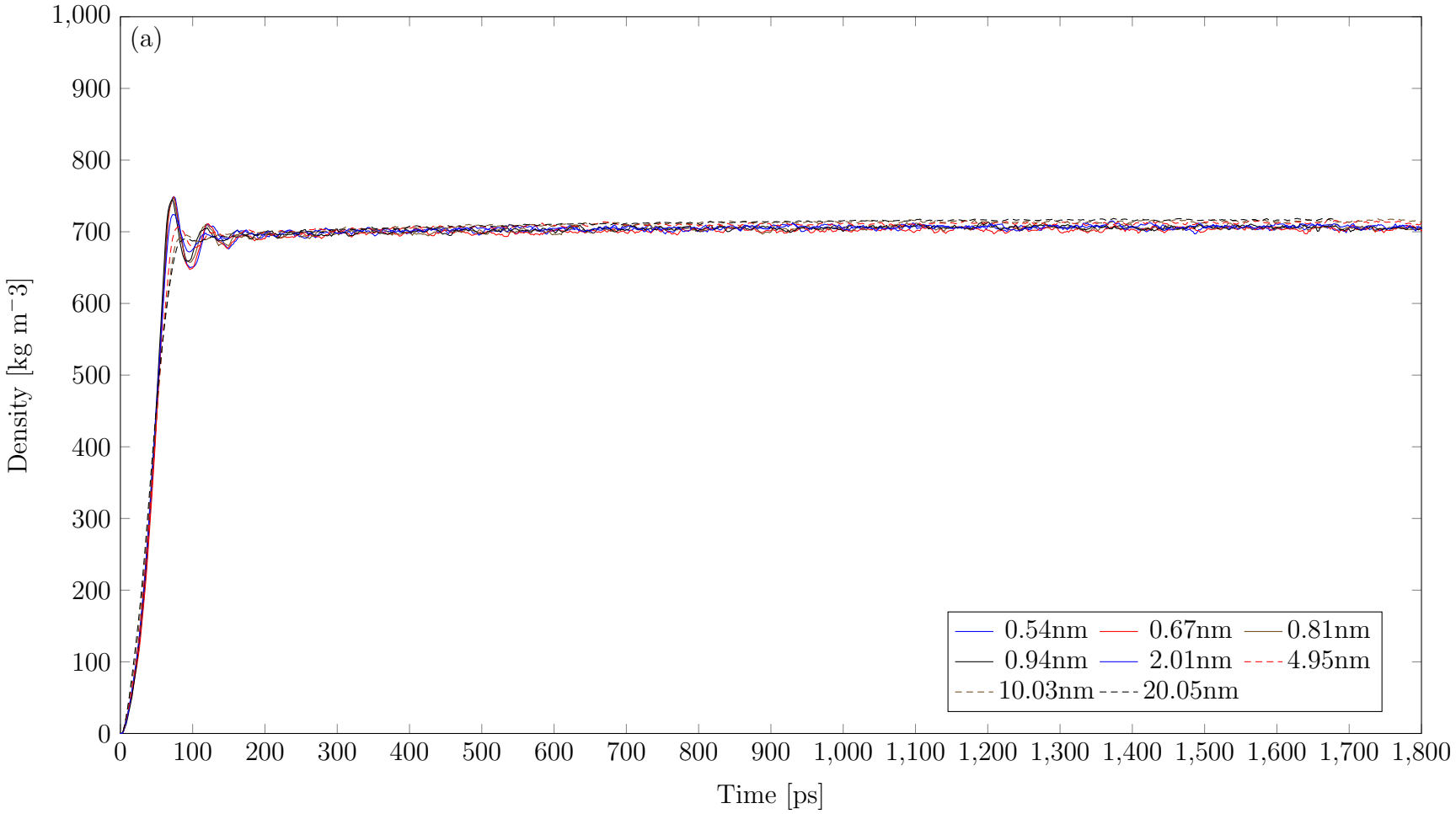


Figure C.29: Liquid n-heptane at 300 K filling the outside of various cylindrical pores. a) Pore density against time.

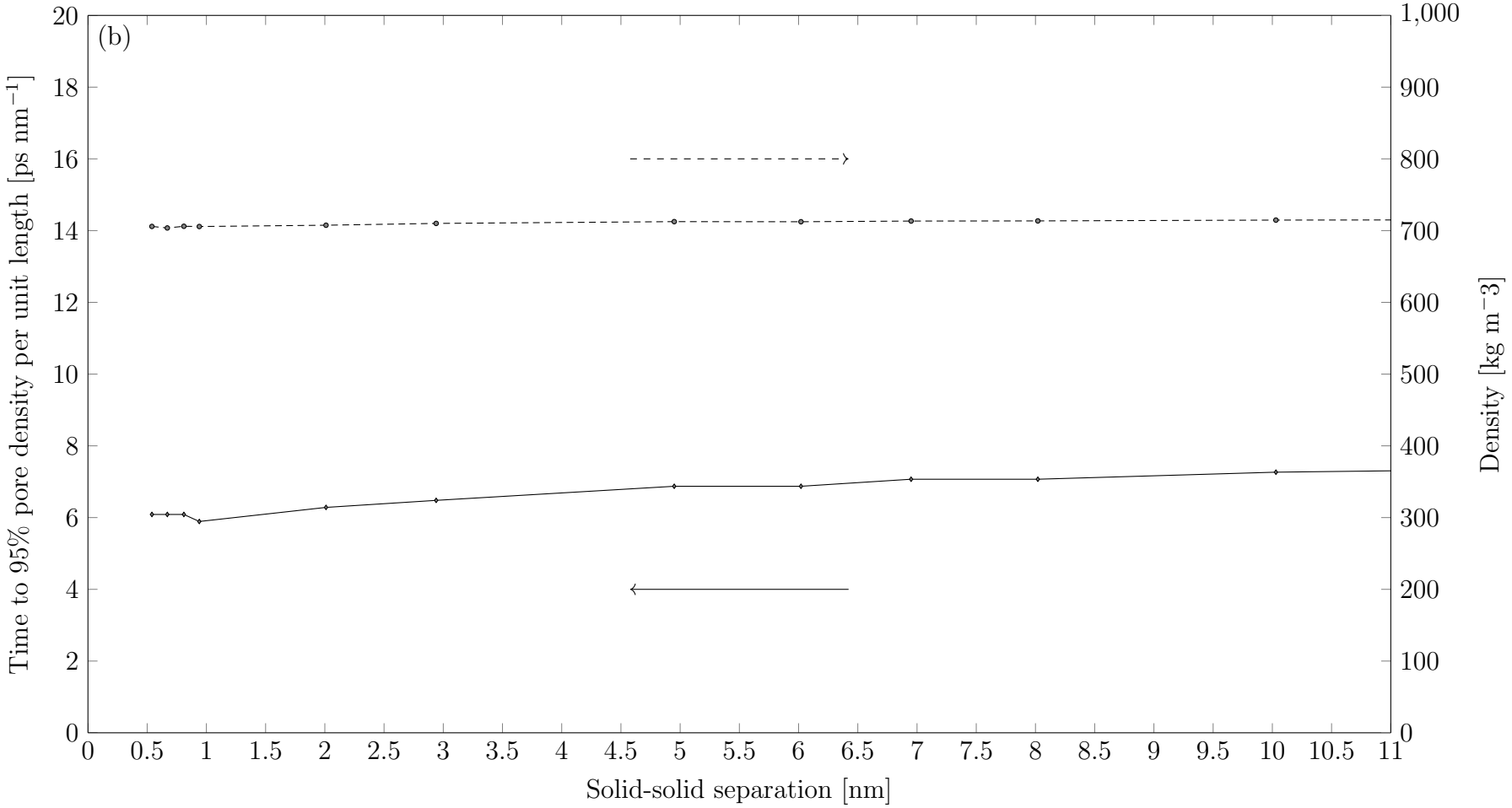


Figure C.30: Liquid n-heptane at 300 K filling the outside of various cylindrical pores. b) Comparison between pore fill time and the mean density calculated over the final 500 ps of (a). The labels correspond to the density extremes in the smallest pores. The matching pore geometries are shown in figure 4.45.

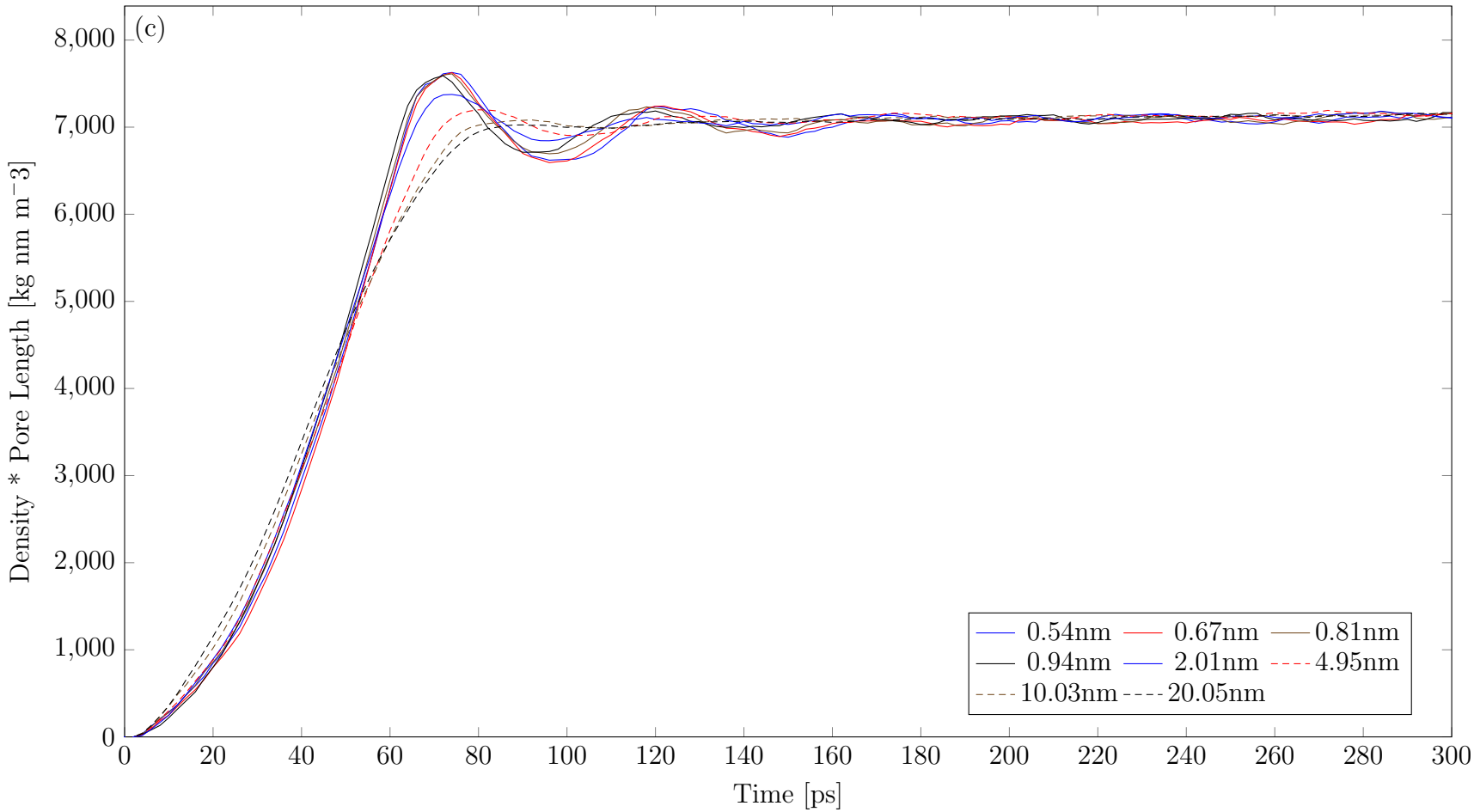


Figure C.31: Liquid n-heptane at 300 K filling the outside of various cylindrical pores. c) Pore density * pore length against time, for use in calculating initial fill rate of pore.

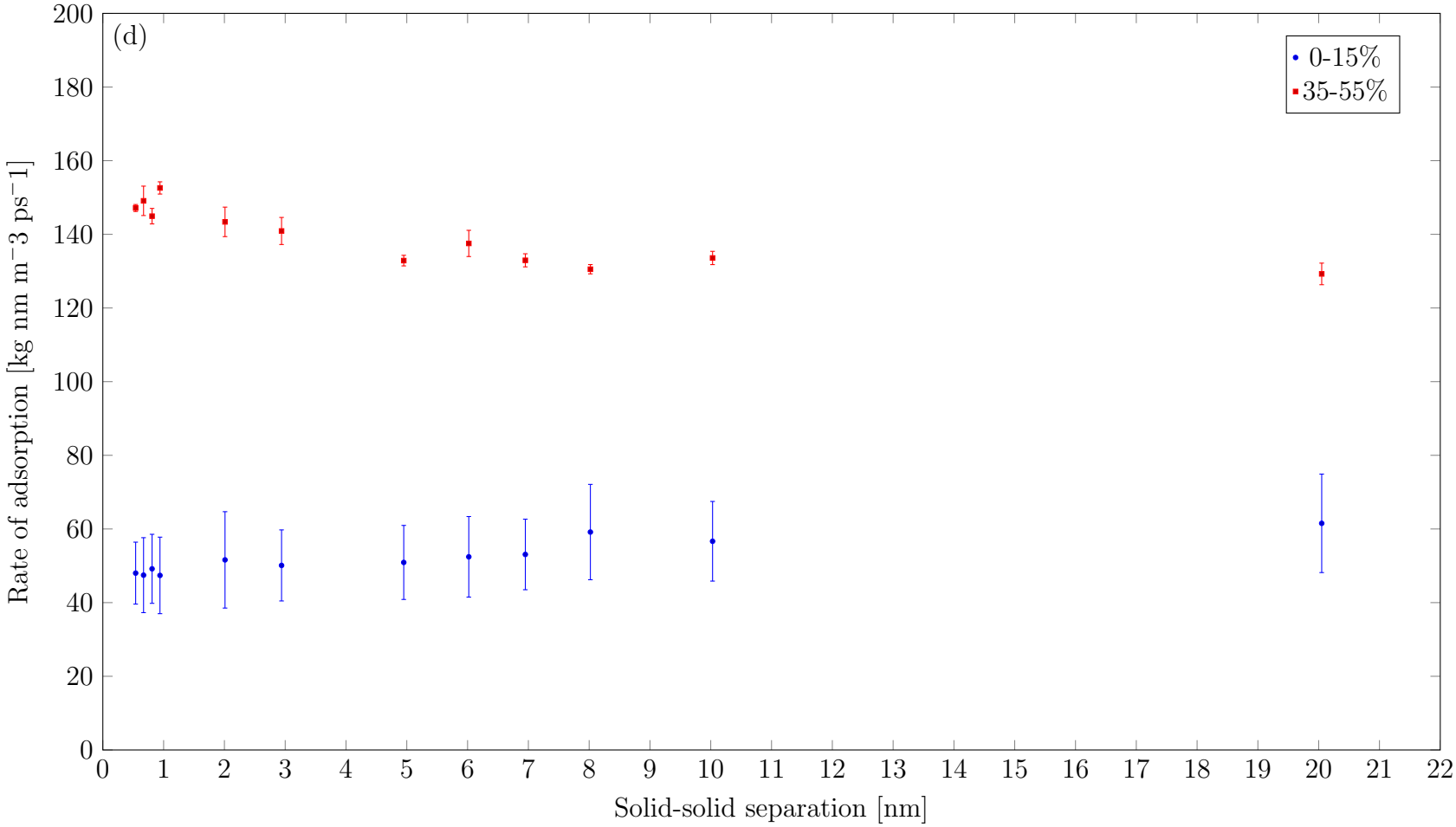


Figure C.32: Liquid n-heptane at 300 K filling the outside of various cylindrical pores. d) Initial and secondary rates of adsorption, extracted from (c). The percentage ranges in (d) are of the final maximum fluid density in the pore.